Numerical Modelling for Hydrodynamic Impact and Power Assessments of Tidal Current Turbine Arrays

MARINE
SCIENCE
& ENGINEERING
WITH
PLYMOUTH
UNIVERSITY

by

Thomas Roc

A thesis submitted to the University of Plymouth

in partial fulfilment for the degree of

DOCTOR OF PHILOSOPHY

School of Marine Science & Engineering

September 2012

This copy of the thesis has been supplied on condition that anyone who consults it is understood to recognize that its copyright rests with its author and that no quotation from the thesis and no information derived from it may be published without the author's prior consent.

Abstract

Channel constrictions in which strong currents are mainly driven by tidal processes represent sites with high potential for harvesting renewable and predictable tidal stream energy. Tidal Current Turbines (TCTs) deployed in arrays appear to be the most promising solution to efficiently capturing this carbon neutral energy resource. However to ensure the sustainable character of such projects, the balance between power extraction maximization and environmental impact minimization must be found so that device layout optimization takes into account environmental considerations. This is particularly appropriate since both resource and impact assessments go intrinsically hand in hand. The present method proposes the use and adaptation of ocean circulation models as an assessment tool framework for tidal current turbine (TCT) array-layout optimization. By adapting both momentum and turbulence transport equations of an existing model, the present TCT representation method is proposed to extend the actuator disc concept to 3-D large scale ocean circulation models. Through the reproduction of physical experiments to reasonable accuracy, grid and time dependency tests and an up-scaling exercise, this method has shown its numerical validity as well as its ability to simulate accurately both momentum and turbulent turbine-induced perturbations in the wake. These capabilities are demonstrated for standalone devices and device arrays, and are achieved with a relatively short period of computation time. Consequently the present TCT representation method is a very promising basis for the development of a TCT array layout optimization tool. By applying this TCT representation method to realistic cases, its capability is demonstrated for power capture assessment and prediction of hydrodynamic interactions as would be required during the layout deployment optimization process. Tidal energy has seen considerable development over the last decade and the first commercial deployments are likely to take place within the next 5 years. It is hoped that this new tool and the numerical approaches described herein will contribute to the development of TCT array power plants around the world.

Contents

List of Figures

List of Tables

Acknowledgments

It would not have been possible to write this doctoral thesis without the help and support of the kind people around me, to only some of whom it is possible to give particular mention here. Above all, I would like to thank my parents, brother and friends for having given me their unequivocal support throughout, as always, for which my mere expression of thanks likewise does not suffice.

This thesis would not have been possible without the help, support and patience of my principal supervisor, Dr. Daniel C. Conley, not to mention his advice and knowledge of coastal processes. The good advice and support of my second supervisor, Prof. Deborah Greaves, has been invaluable, for which I am extremely grateful. I would like to acknowledge the IT support services of the University of Plymouth, particularly Peter Mills and its staff that provided the necessary technical support for this research.

I am most grateful to Dr. Kristen M. Thyng for collaborating with me on the applications of this research project and sharing the publication efforts. Last, but by no means least, I would also like to thank my colleagues and friends from the University of Plymouth, the University of Washington, the University of Bristol, the INORE group and all the beautiful people I met in Plymouth during these past 4 years.

For any errors or inadequacies that may remain in this work, of course, the responsibility is entirely my own.

In memory of Vincent.

Author's Declaration

At no time during the registration for the degree of Doctor of Philosophy has the author been registered for any other University award without prior agreement of the Graduate Committee

This study was financed with aid of a student sponsorship from the Great Western Research and International Power Marine Developments Limited, and carried out in collaboration with the University of Bristol and the University of Exeter.

Relevant scientific seminars and conferences were regularly attended at which work was often presented; external institutions were visited for consultation purposes and several papers prepared for publication. Two papers have been submitted for publication in refereed journals.

Publications:

Roc, T., Conley, D. C. & Greaves, D., **2013**. Methodology for Tidal Turbine Representation in Ocean Circulation Model. *Renewable Energy (In Press)*

Roc, T., Conley, D. C. & Greaves, D., **2012**. Tidal Turbine Representation in an Ocean Circulation Model: Towards Realistic Applications. *Ocean Engineering (Under review).*

Conference Posters, Presentations and Proceedings:

2009:

PMSP conference, *Plymouth*. Oral presentation: "*Tidal Energy Extraction Modelled by Drag Coefficient: Advantages & Limitations*"

GWR sustainability conference, *Exeter*. Oral presentation: "*Hydrodynamic Tool for Assessing Tidal Current Turbine Arrays*"

2010:

INORE symposium, *Dartmouth*. Poster and oral presentation: "*A Regional Numerical Model for Tidal Current Turbine Farm Planning*"

ICOE conference, *Bilbao*. Poster and proceeding: "*Accounting for Turbulence in a Regional Numerical Model for Tidal Current Farm Planning*"

Primare conference, *Plymouth*. Poster and oral presentation: "*A Regional Numerical Model for Tidal Current Turbine Farm Planning*"

AGU conference, *Portland*. Oral presentation: "*Calibration of a Tidal Current Array Planning Tool*"

2011:

RCUK conference, *Oxford*. Poster: "*Accounting for Turbulence in a Regional Numerical Model for Tidal Current Farm Planning*"

2012:

ISOPE conference, Maui. Oral presentation and proceeding: "*Turbulence Correction Terms for Representing Tidal Current Turbines in a Regional Ocean Model for Array Planning and Impact Assessment*"

EWTEC conference, *Southampton.* Oral presentation and proceeding*: "Applying a decision-making tool for tidal current turbine (TCT) planning projects to the Puget Sound estuary - Early results*"

Word count of main body of thesis: 31,103

Signed: _____

Date: _____

Nomenclature

$\vec{e}_{(i,j,k)} \equiv$ Numerical basis vector

$\vec{e}_{(x,y,z)} \equiv$ Cartesian basis vector

$\vec{v}_{[\dots]} \equiv$ Velocity vector $(\mathrm{m.\,s^{-1}})$

$\Delta_{[\dots]} \equiv$ Numerical resolution step

$\Upsilon_{[\dots]} \equiv$ Mean kinetic density $(\mathrm{kW.\,m^{-2}})$

$\chi_{[\dots]} \equiv$ Kantha & Clayson's stability function

$C_{[\dots]} \equiv$ Scalar concentration $(\mathrm{Mol.\,m^{-3}})$

$C_{Chezy} \equiv$ Chezy friction coefficient $(\mathrm{m^{1/2}.\,s^{-1}})$

$C_D \equiv$ Drag coefficient

$C_p \equiv$ Power coefficient

$C_t \equiv$ Thrust coefficient

$D_{[\dots]} \equiv$ Diffusion tensor

$E_{[\dots]} \equiv$ Energy yield $(\mathrm{W.\,h})$

$F_{[\dots]} \equiv$ Force (N)

$K_{[\dots]} \equiv$ Vertical viscosity/diffusivity $(\mathrm{m^2.\,s^{-1}})$

$M_{[\dots]} \equiv$ Matrix

$P_{er} \equiv$ Wetted perimeter (m)

$P_x \equiv$ Power extraction rate $(\mathrm{W.\,m^{-1}})$

$Q_{[\dots]} \equiv$ Discharge/flux $(\mathrm{m^3.\,s^{-1}})$

$Rey_{num} \equiv$ "Numerical" Reynolds number

$R_{ig} \equiv$ Bulk Richardson number

$S_{[\dots]} \equiv$ Source/sink term

$Z_0 \equiv$ Bottom roughness height (m)

$\vec{n} \equiv$ Unitary normal vector

$n_{Maning} \equiv$ Maning coefficient $(\mathrm{m^{-\frac{1}{3}}.\,s})$

$p_{[\dots]} \equiv$ Pressure $(\mathrm{kg.\,m^{-1}.\,s^{-2} = N.\,m^{-2}})$

$\zeta_{Smago} \equiv$ Smagorinsky viscosity/diffusivity $(\mathrm{m^2.\,s^{-1}})$

$\zeta_{bi} \equiv$ Biharmonic viscosity/diffusivity $(\mathrm{m^2.\,s^{-1}})$

$\nu_\theta \equiv$ Molecular diffusivity $(\mathrm{m^2.\,s^{-1}})$

$\rho_0 \equiv$ Average density $(\mathrm{kg.\,m^{-3}})$

$\sigma_k \equiv$ Schmidt number

$\tau_{[\dots]} \equiv$ Stress tensor $(\mathrm{kg.\,m.\,s^{-2}})$

$\tau_0 \equiv$ Standard bottom shear stress $(\mathrm{kg.\,m.\,s^{-2}})$

$\tau_{add} \equiv$ Additional bottom shear stress $(\mathrm{kg.\,m.\,s^{-2}})$

$\tau_{eff} \equiv$ Effective bottom shear stress $(\mathrm{kg.\,m.\,s^{-2}})$

$h \equiv$ Total depth (free surface perturbation plus bathymetry) (m)

$\Gamma \equiv$ Canuto's stability function

$\gamma \equiv$ Turbine efficiency

$\Delta V \equiv$ Control volume $(\mathrm{m^3})$

$\Delta\theta \equiv$ Bidirectionality (deg)

$A \equiv$ Rotor disc surface (m^2)

$B \equiv$ Production term of TKE by buoyancy $(\text{m}^2.\text{s}^{-3})$

$Fr \equiv$ Froude number

$H \equiv$ Bathymetry (m)

$I \equiv$ Identity matrix

$N \equiv$ Buoyancy frequency (s^{-1})

$P \equiv$ Production term of TKE by shear $(\text{m}^2.\text{s}^{-3})$

$Pow \equiv$ Instantaneous power (W)

$R \equiv$ Hydraulic radius (m)

$Rey \equiv$ Reynolds number

$U \equiv$ Steady velocity component along the x-direction $(\text{m}.\text{s}^{-1})$ (i.e. Reynolds decomposition)

$V \equiv$ Steady velocity component along the y-direction $(\text{m}.\text{s}^{-1})$ (i.e. Reynolds decomposition)

$W \equiv$ Steady velocity component along the z-direction $(\text{m}.\text{s}^{-1})$ (i.e. Reynolds decomposition)

$X \equiv$ Any given quantity

$a \equiv$ Induction factor

$c \equiv$ Gravitational wave celerity $(\text{m}.\text{s}^{-1})$

$f \equiv$ Coriolis coefficient (s^{-1})

$g \equiv$ Acceleration due to gravity $(\text{m}.\text{s}^{-2})$

$k \equiv$ Turbulent Kinetic Energy (TKE) per unit mass $(\text{m}^2.\text{s}^{-2})$

$l \equiv$ Turbulent length scale (m)

$u' \equiv$ Fluctuating velocity component along the x-direction $(\text{m}.\text{s}^{-1})$ (i.e. Reynolds decomposition)

$u \equiv$ Velocity component along the x-direction $(\text{m}.\text{s}^{-1})$

$v' \equiv$ Fluctuating velocity component along the y-direction $(\text{m}.\text{s}^{-1})$ (i.e. Reynolds decomposition)

$v \equiv$ Velocity component along the y-direction $(\text{m}.\text{s}^{-1})$

$w' \equiv$ Fluctuating velocity component along the z-direction $(\text{m}.\text{s}^{-1})$ (i.e. Reynolds decomposition)

$w \equiv$ Velocity component along the z-direction $(\text{m}.\text{s}^{-1})$

$\alpha \equiv$ permeability (m^2)

$\varepsilon \equiv$ Turbulent energy dissipation rate per unit mass $(\text{m}^2.\text{s}^{-3})$

$\zeta \equiv$ Eddy viscosity/diffusivity $(\text{m}^2.\text{s}^{-1})$

$\eta \equiv$ Total depth (free surface perturbation plus bathymetry) (m)

$\kappa \equiv$ Von Karman's constant

$\lambda \equiv$ Diffusion constant

$\mu \equiv$ Dynamic viscosity $(\text{kg}.\text{m}^{-1}.\text{s}^{-1})$

$\nu \equiv$ Kinematic viscosity $(\text{m}^2.\text{s}^{-1})$

$\rho \equiv$ Density $(\text{kg}.\text{m}^{-3})$

$\sigma \equiv$ Sigma coordinate

$\omega \equiv$ Vorticity (s^{-1})

$\phi \equiv$ Tidal phase (rad)

$n \equiv$ n$^{\text{th}}$ time step index

$neap \equiv$ Associated with neap tide

$s \equiv$ Associated with surface layer

$spring \equiv$ Associated with spring tide

$u.d. \equiv$ Upstream distance

$v \equiv$ Vertical component

$w \equiv$ Located in the wake

Subscripts

$(i, j, k) \equiv$ 3-D numerical multi-index

$(u, v, w) \equiv$ 3-D velocity component index

$(x, y, z) \equiv$ 3-D Cartesian multi-index

$\vec{n} \equiv$ Associated with the normal component of a vector

$\infty \equiv$ Free stream

$h \equiv$ Horizontal component

$C \equiv$ Associated with scalar concentration

$H \equiv$ Depth averaged

$M \equiv$ Associated with momentum component

$T \equiv$ Averaged over a tidal cycle

$b \equiv$ Associated with bottom layer

$d \equiv$ At rotor-disc location

$mean \equiv$ Associated with mean tide

Superscripts

$^{-} \equiv$ Time averaged

$\vec{n} \equiv$ Associated with the normal component of a vector

$\overrightarrow{tan} \equiv$ Associated with the tangential component of a vector

$' \equiv$ Fluctuating component

$* \equiv$ Dynamical component

$C \equiv$ Associated with scalar concentration

$M \equiv$ Associated with momentum component

Operators

$| \quad | \equiv$ Absolut value

$\| \quad \| \equiv$ Vector norm

$\propto \equiv$ Proportional

Chapter 1. Introduction

According to the Renewables Advisory Board, the United Kingdom aims to reach 15% of its energy use from renewable energy sources by 2020. In comparison, in 2009, the percentage of U.K.'s energy consumption from renewable sources reached 3%[1]. Such a national challenge will necessitated an energy production makeover. Since the late 1980's, sustainable development has established itself as a more eco-friendly, economical alternative and in its wake numerous renewable energy solutions have emerged, among them marine emergy converters. The latest study from the Crown Estate (2012) estimates the total theoretical UK resources for marine energy to 69 TWh/year ± 25 % (27 GW) from wave energy, 95 TWh/year ± 25 % (32 GW) from tidal stream and 121 TWh/year ± 25 % (59 GW) from tidal range (i.e. barrage and lagoon schemes). Accordingly, the tidal stream resource itself could potentially provide 4.4% of the energy demand forecasted for 2020 by the UK Government's central projection. Channel constrictions in which strong currents are mainly driven by tidal processes represent sites with high potential for harvesting renewable and predictable energy. Their potential lies mainly in two features. Firstly tidal currents are driven by a well-known phenomenon based on the gravitational interactions between the Earth's hydrosphere, the Moon and the Sun (Boone, 2004). Tidal range and current predictions have been mastered for centuries and can be considered as highly predictable and inexhaustible. Secondly, channel constrictions concentrate this tidal power in narrow areas surrounded by land and, sometimes, pre-existing electrical grids (i.e. Puget Sound, Washingon state, U.S.). As a result, a smartly-designed

---

[1] Department of Energy and Climate Change, http://www.decc.gov.uk/

1. Introduction

power plant running on this well-known resource and deployed in such constrictions should ensure a renewable and sustainable power production. Tidal Current Turbines (TCTs) deployed in arrays appear to be the most promising solution to efficiently capture this carbon neutral energy resource. Indeed, in contrast to tidal barrages, TCT arrays permit a high concentration of devices without entirely blocking the tidal flow and thus avoid drastic perturbations in the hydrodynamics of the site. Nevertheless, to ensure the sustainable character of such projects, the balance between power extraction maximization and impact minimization must be found so that device layout optimization can take into account environmental considerations. The possibility of ecological implications such as the risk of collision, refuge alteration and changing foraging habitats that might drastically perturb marine life symbiosis (Smith and Scott, 2009) has to be considered during the pre-deployment phase. In a similar manner, changes to the hydrodynamic configuration of a site may affect the surrounding fluid and sedimentary dynamics on a regional scale (Ahmadian et al., 2012; Neill et al., 2012).

It has been demonstrated in numerous articles (Pham & Martin, 2009; Salter, 2009; Bryden & Couch, 2004; Bryden & Couch, 2007; Garrett & Cummins, 2005; Blunden & Bahaj, 2007) that assessment methods of tidal energy harvesting based solely on undistributed flow considerations, without integrating any feedbacks due to TCT hydrodynamic influences, misrepresent the real potential of exploitable sites and the potential hydrodynamic impacts of TCT array layouts. In fact the potential for energy extraction can be increased by taking into account and making the use of turbine induced impacts (Salter, 2009; Couch & Bryden, 2006; Bryden & Melville, 2004). For instance, interactions with the free surface can change the nature of the flow (O'Doherty et al., 2009) and, by extension, the head drop in a channel. In consequence the potential resource itself becomes a function of the induced free surface perturbation as the pressure head drop ought to be a parameter in resource estimation (Salter, 2009). Conversely, surface waves generated by tides, swells or winds may affect turbine yield (Turner & Owen, 2009) and structure (Barltrop et al., 2006). This latter consideration can partly be compensated for by optimizing the vertical location of turbine

1. Introduction

hubs in the water column (Turner & Owen, 2009; Khan et al., 2009). An optimum vertical location of the device in the water column decreases structure loading and wake persistence downstream of the device (Myers & Bahaj, 2010). Deployment optimization also includes wake interactions with downstream turbines (Bai et al., 2009). Indeed, wake shapes, extensions and decays are sensitive to internal and surface waves (Maganga et al., 2009; Salter, 2009), flow alignment (O'Doherty et al., 2009) and turbulence intensity (Harrison et al., 2009). For instance, Myers & Bahaj (2012) showed that, in TCT arrays, an adequate device spacing of the upstream row may increase the power capture of the downstream row up to 22% (Myers & Bahaj, 2012). Reciprocally, turbine yields are affected by upstream-turbine wakes through the characteristic velocity deficits and increase in turbulence (Gretton et al., 2009).

When exploited in large-scale arrays, such "green energy" generators could be intrusive and potentially harmful for the marine habitat or sediment dynamics if used without understanding the potential impacts and without precautions (Defne et al., 2011; Ingram et al., 2011; Kadiri et al., 2012; Shields et al., 2009; Neill et al., 2009; Neill et al., 2012). Therefore it is necessary to develop assessment tools for investigating the flow perturbations on a large scale as well as the power yield for any type of TCT device layout in order to find the optimum deployment strategy to minimize the impacts on the physical environment and thus preserve the sustainable character of such renewable energy resources (Defne et al., 2011; Ingram et al., 2011; Kadiri et al., 2012; Shields et al., 2009; Neill et al., 2009). Nonetheless, turbine wake interactions can also have positive impacts on the power harvest (Salter, 2009; Couch & Bryden, 2006; Bryden & Melville, 2004). Therefore, finding the optimum deployment strategy also requires a detailed understanding of the turbine interactions within farms. Thus a relevant device layout optimization must account for all those parameters and at the same time enable the identification of potentially harmful hydrodynamic effects such as those on sediment transport processes induced by the presence of devices in the channel flow (Neill et al., 2009; Neill et al., 2012).

1. Introduction

The ultimate aim of this research is to create an appropriate modelling platform for such optimization investigations. As analytical approaches cannot be utilized for the level of complexity inherent in realistic cases, this thesis focuses on representing tidal current turbines in a numerical model which can be applied to spatial scales sufficient to represent the area of most significant impact. It has been decided to accomplish this through the adaptation of an existing ocean circulation model by including a TCT representation.

The chosen model ought to possess some key numerical features. First of all the model must bear three dimensional domain and baroclinic dynamics. Additionally, most of the investigated sites shall have complex topographies and geometries that necessitate adaptive and/or unstructured grids and the use of relevant coordinate systems. The simulations should also investigate the effects of dynamical oceanic and meteorological forcing and, therefore, permit water height fields which may vary spatially and temporally following the example of waves on shelf flows. One of the most important numerical developments of this project is the investigation of the device impacts over a regional scale through local and depth specific considerations by implementing sinks of momentum and/or sources of turbulence or vorticity. This implies the existence of relevant turbulence models within the code as well as a flexible mixing parameterization of the latter. Additionnaly, the chosen numerical platform should allow future developments in order to investigate further impacts such as sediment transport changes. From that point of view, choosing the most relevant numerical regional hydrodynamic model appeared to be a crucial task, with significant consequences for the project and its potential extension. An inter-comparison has been undertaken between the most popular models (EFDC, MIKE3, TELEMAC 3D, ROMS, POLCOMS, ADCIRC, HELIKE, DEFLT 3D), which all match with the project requirements. This feature analysis was also based on practical and exploitation considerations.Eventually, the open-source numerical platform ROMS (Regional Ocean Modelling System[2]) stood out as one of the preferable base models upon which to build such a tool.

---

[2] https://www.myroms.org/

1. Introduction

The main innovations of the TCT representation presented here lie in the fact that it treats each individual device as a mid-water column perturbation, accounting for both momentum and turbulent hydrodynamic-effects, itself implemented in a regional ocean circulation modelling framework. This has required implementation of techniques borrowed from high resolution Computational Fluid Dynamics (CFD) as well as coarse resolution ocean-circulation models and developed for various research fields such as wind energy or porous media modelisation used, among others, in forest canopy research. The relevancy of the proposed method theory and implementation has been validated against series of standard numerical tests of convergence and dependency as well as the reproduction of experimental results. The so-validated platform has then been used to tackle realistic TCT farm deployment scenarios and initiate a reflection on power assessment strategy for such power plants.

This document is organized as follows. Literature review for this work is laid down in Chapter 2 and overviewes the techniques and methodologies which have been used to model turbine flow-perturbations up to now. Chapter 3 includes a summary of relevant aspects of the model framework, the Regional Ocean Modeling System (ROMS), used in this research as well as an extended description of the actuator disc theory and its limitations. The theory, model modifications and implementation techniques behind the proposed TCT representation method is then described in Chapter 4. Chapter 5 and Chapter 6 gather the results from numerical benchmark and experimental data comparisons for standalone and multiple device cases constituting the validation phase of the proposed numerical tool. A reflection on TCT array layout effects and their implications on power assessment is initiated in Chapter 7. The question of the scale applicability of the model is then answered in Chapter 8. Finally, in Chapter 9, a test case application involving a TCT array deployment in the Puget Sound (Washington state, U.S.) is investigated.

Chapter 2. Existing TCT-Arrays

Assessment Methods

Once a potential site for large-scale tidal current turbine arrays has been chosen considering deployment and exploitation factors (i.e. local facilities for construction and maintenance, grid-connection availability, spare grid capacity, etc), two main aspects of the project have to be considered. The first one involves resource assessment of the considered site and could be summarized as "how much extractable power is available for this site and what is the most efficient way to capture it?". The second deals with the environmental and hydrological impacts and could be formulated as "How much power can be extracted from the flow without critically damaging the surrounding environment?". So far these two issues have been tackled separately and numerically using respectively large-scale coarse-resolution models or fine-scale high-resolution models. However results tend to show that, for such regional-scale planning projects, these two aspects cannot be treated independently and are fundamentally inter-related problems (Pham & Martin, 2009; Salter, 2009; Bryden et al., 2007; Blunden & Bahaj, 2007; Bryden & Couch, 2007; Garrett & Cummins, 2005; Bryden & Melville, 2004).

2.1. Resource Assessment

2.1.1. 1-D Approaches

Resource assessment is a key issue since it is needed to define the profitability of such large-scale planning and is therefore an important decision-making index for investors and stakeholders. Estimates of the available power from a typically exploitable site, namely a tidal channel, from its natural flow, was first approached by assuming the available energy entirely provided by the kinetic energy carried within the flow (Couch & Bryden, 2006). Garrett and Cummins developed a one-dimensional time-averaged model based on flow conservation where the presence of the turbine array is simulated through a power-law term corresponding to the drag force associated with the turbines (Garrett & Cummins, 2005). Let λ be a non-dimensional coefficient which is related to the estimated extracted power and is a function of the number of turbines and their location along the channel. The more turbines deployed, the bigger λ gets. The model of Garrett & Cummins showed the existence of an upper limit to the extractable power, the same limit being a function of the natural flow. In fact, the power extracted increases with the number of deployed turbines up to 71% of the undisturbed flow power and then decreases as too many turbines block the flow. This simplistic approach gives good preliminary assessment of the upper bound on the available power of constricted flows but excludes numerous factors which will turn out to be of high influence in realistic power assessment (Garrett & Cummins, 2005). A number of studies (Bryden & Melville, 2004; Bryden & Couch, 2004; Bryden et al., 2007; Chick et al., 2007), improved this approach by simulating the hydrodynamic turbine effect on the flow by including an additional quadratic bottom shear stress. Accordingly for Bryden and Couch (2007), the flow behaviour follows the standard hydraulic equation for open channel flow (Bryden & Couch, 2007).

2. Existing TCT-Array Assessment Methods

$$\begin{cases} \left(1 - \dfrac{Q^2}{h^3 b^2 g}\right)\dfrac{\partial h}{\partial x} = \dfrac{\partial b}{\partial x}\dfrac{Q^2}{h^2 b^3 g} - \dfrac{1}{\rho g b h}P_{er}\tau_{eff} \\[2ex] \tau_{eff} = \tau_0 = \rho\dfrac{g}{C^2}u_h{}^2 \\[2ex] C_{chezy} = \dfrac{R^{1/6}}{n_{Maning}} \end{cases} \quad (1)$$

where Q is the discharge $(\mathrm{m^3.s^{-1}})$, $h = H + \eta$, g the acceleration due to the gravity $(\mathrm{m.s^{-2}})$, P_{er} the wetted perimeter (m), τ_{eff} the effective bottom shear stress $(\mathrm{kg.m.s^{-2}})$, τ_0 the standard bottom shear stress $(\mathrm{kg.ms^{-2}})$, C_{chezy} the Chezy friction coefficient $(\mathrm{m^{\frac{1}{2}}.s^{-1}})$, R the hydraulic radius (m) and n_{Maning} the Manning coefficient $\left(\mathrm{m^{-\frac{1}{3}}.s}\right)$. In such an approach, instead of searching for the maximum extractable power, the extracted power is assumed equal to 10% of the total available and accordingly dissipated as additional bottom shear stress. Indeed the additional bottom shear stress τ_{add} applied over the location of the device array is, a priori, formulated as a function of the power-extraction rate P_x.

$$\tau_{add} = \frac{P_x R}{\|\overrightarrow{v_H}\|} \quad (2)$$

where $\overrightarrow{v_H}$ is the depth averaged flow velocity vector. Thus over the device array the effective shear stress is:

$$\tau_{eff} = \tau_0 + \tau_{add} \quad (3)$$

Surprisingly the actual backward estimation of energy extracted by the turbine array is smaller than 10% (Bryden & Couch, 2004). The explanation proposed by Bryden & Couch (2004) for this counter-intuitive result lies in the fact that a natural flow intrinsically possesses both potential and kinetic energy and, furthermore, the alleged 10% energy extraction is partly balanced between these two components. This consideration raises the question of the relevance of assessing the potential of a site only on kinetic energy considerations (Salter, 2009). Nonetheless, it should be highlighted that the previous models have been built on very restrictive assumptions. In fact they are only relevant for steady flows in single channels of simplified bathymetry driven only by a gradient in sea surface level. In addition, the TCT array effects are assumed uniform across the channel cross-section and

consequently the flow is not free to adjust in order to by-pass the obstructions. Outside of this frame of work, especially regarding the last assumption, these types of power-yield estimations are no longer considered relevant (Sutherland et al., 2007). A realistic interaction between tides and TCT is a multi-dimensional problem (Chick et al., 2007) whose complexity cannot be accurately fully resolved under such a narrow hypothesis (Bryden & Couch, 2007).

2.1.2. 2-D Approaches

The natural progression is to extend the scope of resolution of numerical models to a second dimension. Among the references using 2-D hydrodynamic models for power yield assessment, two different options have been chosen for this task. The first one consists in using industrial software such as MIKE21, Delft-2Dh or Telemac (Lawrence et al., 2009; Pham & Martin, 2009; Carballo et al., 2009), the second one in using academic codes which are more likely to be adapted to a particular problem (Bryden et al., 2007). Loosely, theoretical cores of both model types are based upon the Saint Venant's equation system, namely an equation system covering two different hydrodynamic processes under the hydrostatic and shallow-water assumptions. The first process accounted for is the horizontal depth-integrated momentum balance and the second one is the mass continuity for incompressible flow (Eq. (4)). They are derived from the Navier-Stokes equation system.

$$
\begin{cases}
\left.\begin{aligned}
\frac{\partial u_H}{\partial t} + u_H \frac{\partial u_H}{\partial x} + v_H \frac{\partial u_H}{\partial y} = f v_H - g \frac{\partial \eta}{\partial x} - F_x \\
\frac{\partial v_H}{\partial t} + u_H \frac{\partial v_H}{\partial x} + v_H \frac{\partial v_H}{\partial y} = -f u_H - g \frac{\partial \eta}{\partial y} - F_y
\end{aligned}\right\} \equiv Momentum\ Balance \\
\frac{\partial \eta}{\partial t} = -\frac{\partial}{\partial x}\big(u_H(H+\eta)\big) - \frac{\partial}{\partial y}\big(v_H(h+\eta)\big) \equiv Mass\ Continuity
\end{cases}
\tag{4}
$$

where (u_H, v_H) are the components of the depth averaged flow velocity vector, *H* is the bathymetry (m), η the free surface elevation (m), g the acceleration due to gravity (m.s^{-2}), f the Coriolis coefficient and $F_{(x,y)}$ external forces. The first intuitive method for assessing tidal resources would be to simulate the potential site with accuracy and then apply, on the resulting simulations, the tidal resource assessment formula without incorporating any TCT effects into the computation (Pham & Martin, 2009; Carballo et al., 2009; Trigo-Teixeira & Rebordao, 2009). Commonly for this type of

approach the instantaneous power, Pow, that can be harnessed by a turbine or an array of turbines is expressed as a function of the cubed averaged velocity $\left\|\vec{V}\right\|^3$, the area normal to the flow swept by the turbine blades A, the water density ρ and the power coefficient (also named efficiency) of the turbine γ (5).

$$Pow = \frac{1}{2}\gamma\rho A\left\|\vec{V}\right\|^3 \tag{5}$$

In order to assess more realistic yield estimations, the previous formula has to be applied to the time varying tidal regimes representative of the examined site. According to Pham & Martin (2009), the schematic tides method appears to be one way to evaluate the energy yield E [GWh] over a standard year. This method consists in determining the energy yield for one mean spring, E_{spring}, tide, one "mean tide", E_{mean}, and one mean neap tide, E_{neap}, and then adding them to each other as follows (6) :

$$E = 0.3E_{spring} + 0.4E_{mean} + 0.3E_{neap} \tag{6}$$

Unfortunately, since the volume flux dynamics are essential to properly estimate the potentially extractable energy (Sutherland et al., 2007), ignoring the device effects when assessing the tidal resource from the natural flow, can lead to significant discrepancies in realistic cases (Polagye et al., 2008). Conceptually extracting energy from a flow would slow the mass of fluid passing through the area swept by the turbine blades or rotor discs. Additionally, by design, fluid mass passing through a rotor induces a discontinuity of static pressure (Figure 1) along the rotor-centre line (Burton et al., 2008)
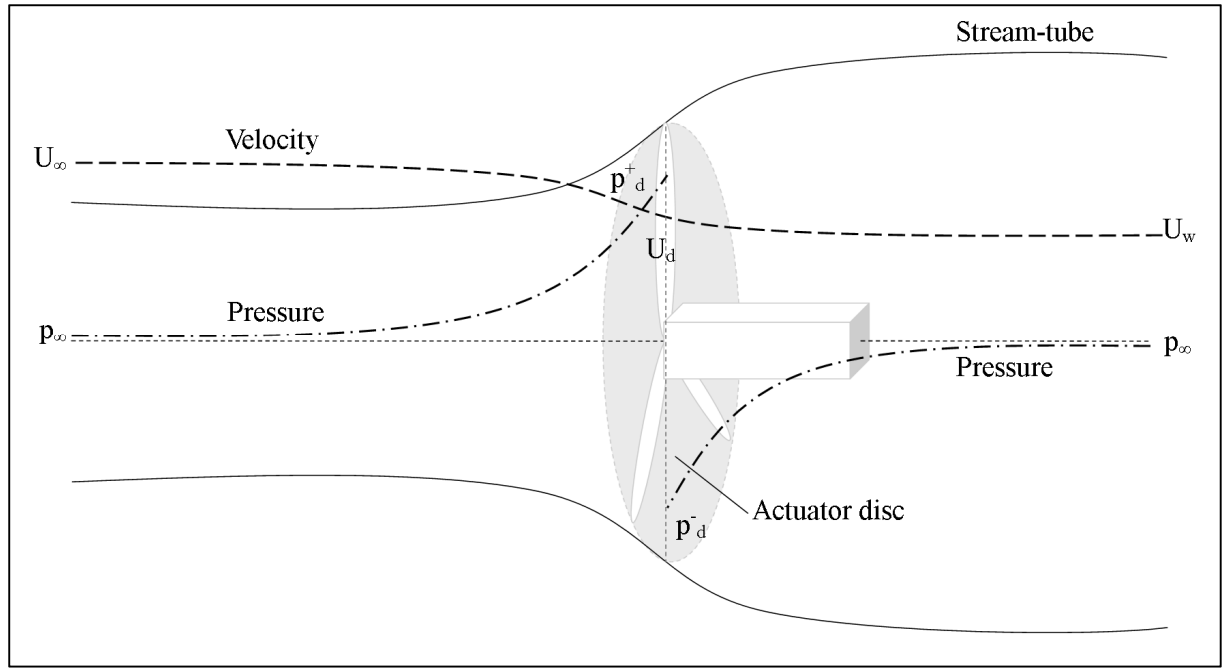
Figure 1: Actuator disc theory - Conceptual diagram. The diagram displays the actuator disc (grey surface), the turbine hub (white box and the white blades), stream-tube (delineated by solid lines), approximated velocity (heavy dashed lines) and pressure magnitudes (heavy dotted-dashed lines). The fluid flows from left to right. After Burton et al. (2008).

This particular dynamics are commonly formalized through the Momentum Theory:

$$(p_d^+ - p_d^-) = (U_\infty - U_w)\rho A_d U_\infty (1 - a) \tag{7}$$

Where p_d^+ represents the static pressure right in front of the disc, p_d^- represents the static pressure right behind the disc, A_d the actuator disc area (m^2) and a the induction factor (i.e. Eq. (40), Section 3.2). Accordingly, a quadratic force $\overrightarrow{F_{add}}$, is injected in the right-hand side of the momentum balance (Draper et al., 2009; Lalander, 2009; Bryden & Couch, 2007) generally in the following form (8).

$$\overrightarrow{F_{add}} = \frac{1}{2}\rho A C_d \overrightarrow{v_h}|\overrightarrow{v_h}| \tag{8}$$

where C_d stands for the drag coefficient. This formulation of the turbine induced force on the flow is also referred as the actuator disc theory (Figure 1).

As 2D models are depth integrated, this new force is, therefore, vertically uniform over the water column. Furthermore, its physical meaning can be equally regarded as a drag force (Draper et al., 2009) or an additional shear stress (Lalander, 2009; Bryden & Couch, 2007). As a consequence, although this type of representation allows a better understanding from a horizontal point of view,

the vertical flow behaviours such as the relation between water column height and corresponding drag coefficient (Sutherland et al., 2007), vertical flow bypassing of the device or distinction between bottom friction and energy extraction (Karsten et al., 2008), are misrepresented and also poorly estimated. Using a 3-D model which utilised the additional bottom shear stress method, Kawase & Thyng highlighted the importance of integrating baroclinic dynamics in the simulation to fully assess the turbine yield (Kawase & Thyng, 2009).

Another induced hydrodynamic effect of turbines which cannot be neglected in a large-scale turbine-farm yield-assessment is the induced wake (Pham & Martin, 2009; Blunden & Bahaj, 2007; Polagye et al., 2008). The extracted flow-energy is converted into useable power thanks to the torque applied on the rotor disc by the water mass passing through; torque itself is induced by the design of the blades. In the opposite reaction, the water flow acquires a swirl-like rotational motion downstream of the turbine. This area of reduced axial momentum and increased angular momentum reaching over several rotor diameter lengths is called the wake. Commonly the wake structure is divided in two parts: the near and the far wake (Vermeer et al., 2003). It has been shown that for wind turbines most of the rotational motion is contained in the near wake and mostly dissipated within five rotor-diameter lengths (Connel & George, 1981; Sforza et al., 1981). Accordingly assuming a regional scope resolution, one could a priori neglect the induced swirl effects from TCT modelling methods as is effectively done in physical scale modelling where turbines are usually represented by non-rotating porous discs (Whelan et al., 2009; Harrison et al., 2009; Sun et al., 2008).

2.1.3. 3-D Approaches

Naturally, and thanks to exponentially increasing computer-power development, to accurately understand wake behaviours at a fine-scale the scientific community leans toward Computational Fluid Dynamics (CFD) models. This allows solution of the complete Navier-Stokes equations at fine enough resolution to accurately simulate the local flow conditions. Different numerical techniques and theories are applied to represent turbines in such tools and are often derived from experience

gained in the wind turbine field. The most common method to tackle interactions of a large-scale turbine farm consist of applying, over the areas swept by the turbine-blades, a retarding force (Whelan et al., 2009; Harrison et al., 2009; Sun et al., 2008; Bai et al., 2009; Blunden et al., 2009) on the flow. This retarding force, also called thrust force, $\overrightarrow{F_t}$, is derived from momentum theory (i.e. Section 3.2 and Eq. (7)) and is proportional to the flow velocity squared multiplied by the surface swept by the turbine blades, A_d:

$$\overrightarrow{F_t} \propto -A_d(\vec{v}.|\vec{v}|) \tag{9}$$

Thanks to this approach and the use of high resolution CFD models, induced wakes as well as wake-induced turbulence and mixing are quantifiable. It has been shown that their impacts in terms of resource assessment are significant (Gretton et al., 2009) and therefore non-negligible. Furthermore, a layout optimization based on wake interactions within a farm is possible (Bai et al., 2009). More specific techniques have also been developed employing the Blade Element Momentum theory (BEM) (O'Doherty et al., 2009; Mc Combes et al., 2009; Bai et al., 2009). Basically BEM theory involves the decomposition of blades in small parts and considers that the forces applied on those elements are solely responsible for the change of momentum in the fluid (Burton et al., 2008). By integrating those forces along the rotating blades and combining them with momentum theory, one can obtain very accurate simulations of the fluid interactions with the device. Another promising method is developed in McCombes et al. (2009). Traditionally, CFD models resolve Navier-Stokes equations through their primitive form, also called velocity-pressure formulation (10)):

$$\begin{cases} \dfrac{\partial \vec{v}}{\partial t} + \vec{v}.\nabla \vec{v} = -\dfrac{1}{\rho} + \upsilon \nabla^2 \vec{v} \\ \nabla.\vec{u} = 0 \end{cases} \tag{10}$$

Where $\vec{v}$ is the flow velocity vector $(\mathrm{m.s^{-1}})$ and υ the kinematic viscosity $(\mathrm{m^2.s^{-1}})$. This formulation carries three main issues. The first issue related with this formulation is the necessity to compute this equation system in all the cells constituting the numerical domain even if resolving certain parts of this domain possesses no immediate interest. The second of these issues lies in the requirement of mesh resolution to be applied on the rotor blades in order to resolve the boundary layer. In order

not to truncate local instabilities due to small-scale fluid phenomena, high density of surface cells on the mesh is compulsory. These two issues often lead to prohibitively high requirements of computational time. Finally, the third issue concerns the artificial diffusion of the wake. This numerical artefact emerges from the grid-based nature of the solution itself and requires, to be contained, the use of higher order discretisation scheme and artificially enhanced viscosity. McCombes et al. (2009) used a specific treatment of a vorticity conservative formulation of the Navier-Stokes (NS) equations combined with limited high resolution finite volume method in order to avoid those issues. This treatment is also called the velocity-vorticity formulation (11)):

$$\begin{cases} \dfrac{\partial \omega}{\partial t} + \vec{v}.\nabla\omega = \omega.\nabla\vec{v} + \upsilon\Delta\omega + S \\ \quad\quad \nabla\times\vec{v} = \omega \end{cases} \tag{11}$$

Where ω is the vorticity (s^{-1}), S a source term vorticity and υ the kinematic viscosity (m^2.s^{-1}). The turbine is then represented as a source of vorticity through S which seems to be the most realistic way to account for turbine effects (Mc Combes et al., 2009). However, all the 3-D numerical methods discussed here are more relevant and useful for single turbine performance and design investigations since, in the scope of large-scale array deployment and regional scale simulations, their high resolution requirements are excessively expensive. Because of this computational cost of CFD models, they cannot usually be employed for realistic cases (Mc Combes et al., 2009). As a consequence, a 3-D model based on relevant regional-scope hydrodynamic assumptions appears to be the most promising alternative in developing a tool to treat the optimization of large-scale TCT array deployment in realistic environments.

2.2. Impact Assessment

Impact assessment is the other main issue in the pre-deployment phase of the TCT planning project. As Myers & Bahaj emphasize, development of tidal stream generators might have critical effects on wildlife and sea-users (Myers & Bahaj, 2009). In addition extraction of kinetic energy from water flows may have irreversible consequences on transport mechanisms (Bryden & Melville, 2004) and by extension on sediment dynamics (Pingree, 1978; Neill et al., 2009; Neill et al., 2012). Thus it is

necessary to estimate and then monitor these potential side effects to save the project from becoming environmentally and economically counter-productive. Thanks to theoretical studies which have been performed up to now and models presented above, it is possible to account for the complete range of hydrodynamic phenomena involved. The first obvious outcome shall be the reduction of speed confined, downstream, within the wake of a turbine or a turbine farm (Burton et al., 2008). It has been demonstrated that the wake recovers 90% of the free stream velocity around twenty diameters downstream (Mc Combes et al., 2009). As described in the Momentum Theory (Section 3.2), the flow passing through the rotor produces a drop of pressure which will then be partly balanced by the free surface drop (Sun et al., 2008) advected downstream of the device. Those two variations are characteristic of a reduction of flow exchange and, in the case of a realistic site driven by tidal dynamics, are likely to affect the tidal range, the advected energy and the kinetic power density as well as alter the phasing of tides by changing the tidal wave propagation (Polagye et al., 2008).

Turbines generate turbulence and, therefore, enhance the mixing process in the water column which could equally perturb sedimentation of the site (Fettweis et al., 2006; Pingree, 1978; Neill et al., 2012; Neill et al., 2009) or phytoplankton blooms (Ross & Sharples, 2008). So it is clear that the range of potential impacts is broad but more importantly they are site-specific (Sun et al., 2008) and cannot be predicted without performing an accurate simulation of the device deployment (Ahmadian & Falconer, 2012). Key-parameters to take into account for performing relevant and accurate impact assessments include: precise bathymetry (Kawase & Thyng, 2009; Lalander, 2009) and site geometries, baroclinic features (Kawase & Thyng, 2009) and vertical velocity profiles (Salter, 2009; Sun et al., 2008), bottom (Karsten et al., 2008) and wall roughness parameterization (Turner & Owen, 2009), tidal magnitude and phase (Draper et al., 2009; Smith & Scott, 2009), free surface interactions (Barltrop et al., 2006; Sutherland et al., 2007), time-dependent analysis (Polagye et al., 2008) and, of course, realistic TCT array representation.

2. Existing TCT-Array Assessment Methods

The most essential concept which has been discussed here lies in the fact that both resource and impact assessments are inter-related. It has been demonstrated in numerous articles (Pham & Martin, 2009; Salter, 2009; Bryden et al., 2007; Garrett & Cummins, 2005; Bryden & Couch, 2004; Blunden & Bahaj, 2007) that assessing methods of tidal energy harvesting solely based on natural, undisturbed-flow considerations, without integrating any back-corrections due to TCT hydrodynamic influences, misrepresent the real potential of exploitable sites. Even the range of exploitable site itself can be sized up by taking into account and using turbine induced impacts (Salter, 2009; Couch & Bryden, 2004; Bryden & Melville, 2004). To conclude one can say that in order to ensure the sustainable and renewable characters of a large-scale TCT farm planning project, during the pre-deployment phase, a mutual resource-impact regional assessment must be performed. In order to do so, the use of a 3D meso-scale numerical model spanning multi-scale phenomenon from sub-grid scale turbulences to channel water level perturbations appears to be the most relevant option.

Chapter 3. Background Theory

3.1. Model Framework - Regional Ocean Modelling System (ROMS)

This project is based on an existing numerical model. Furthermore the Existing TCT-Arrays Assessment Methods suggests that a model which is suitable for simulating TCT array operation ought to possess some key numerical features. First of all, the model must bear three dimensional domain and baroclinic dynamics. Additionally, most of the investigated sites have complex bathymetries and geometries that necessitate adaptive and/or unstructured grids and the use of relevant coordinate systems. The simulations should also investigate the effects of dynamical oceanic and meteorological forcing and, therefore, permit water height fields which may vary spatially and temporally following the example of waves on shelf flows. One of the most important numerical developments of this project is the investigation of the device impacts over a regional scale through local and depth specific considerations by implementing sinks of momentum and sources of turbulence or vorticity. The latter requirement implies the existence of relevant turbulence models within the code as well as a flexible mixing parameterization of the latter.

In consequence, choosing the most relevant numerical regional hydrodynamic model is a crucial task, with significant consequences for the present project. An inter-comparison has been undertaken between the most popular models (EFDC, MIKE3, TELEMAC 3D, ROMS, POLCOMS, ADCIRC, HELIKE, DEFLT 3D), which all match with the project requirements. This feature analysis was

also based on practical and exploitation considerations and led to the selection of ROMS[3] (Regional Ocean Modelling System). Additionally ROMS includes additional advantages which will become very interesting for the future development of this project. Among these additional features, one is the ability to couple with numerous models such as wave propagation and sedimentary transport models and so interact the large and dynamic user community involved in this open-source numerical platform. Nonetheless, as with any numerical regional hydrodynamic model, ROMS has been built on theoretical assumptions that set its frame of use and relevance. As any other large-scale hydrodynamic model, the ROMS computational kernel relies on theoretical and numerical assumptions which have to be fully appreciated in order for it to be used properly. Once this scope of relevance is well understood, an analytical description of the ROMS equation system is necessary to perform theoretical analysis and developments of its capabilities. ROMS can be described as a 3-D, split-explicit, free-surface, terrain-following, hydrostatic primitive equation oceanic model integrating a split-mode. However this description barely outlines the complexity as well as the real potential of this well established numerical tool. Some of its features are worth being detailed as they might condition code implementations and computing strategies.

First the concept of the split-explicit time-stepping scheme needs to be clarified. According to the ROMS website[3], this feature has been developed for the sake of computational cost. This scheme allows a special treatment and coupling between barotropic (fast step) and baroclinic (slow step) modes of the hydrostatic primitive equations for momentum. The evolution of the free-surface and vertically integrated momentum equations within each baroclinic step is performed after a finite number of barotropic steps. Additionally, potential errors related to the aliasing of frequencies solved by the barotropic steps but unsolved by the baroclinic step are corrected by averaging the barotropic fields before substituting those values generated by a longer baroclinic step. This barotropic field averaging involves a cosine-shape time filter, centred at the new time level (Shcheptkin & Mc Williams, 2005). At the same time, the preservation of both volume conservation

---

[3] https://www.myroms.org/

and consistency is needed for the tracer equations. In order to ensure those two properties, ROMS constrains the separated time-stepping (Shcheptkin & Mc Williams, 2005). By default, the time-discretization for all 2-D and 3-D equations uses a third-order accurate predictor (leap-Frog) and corrector (Adams-Molton) time-stepping which is known for its stability and robustness. Eventually, thanks to the high stability of the scheme, the larger time steps offset the increased computational cost of the predictor-corrector algorithm, by a factor of about four (Figure 2). This rather complex computational kernel has been synthetized by its developers, Alexander F. Shchepetkin and James C. McWilliams, in their conceptual diagram (Shchepetkin & Mc Williams, 2009). Consequently, and most of all because no-one can more aptly explain the complexity of this kernel than its own developers, the following diagram and its caption are quoted directly from the latter reference.
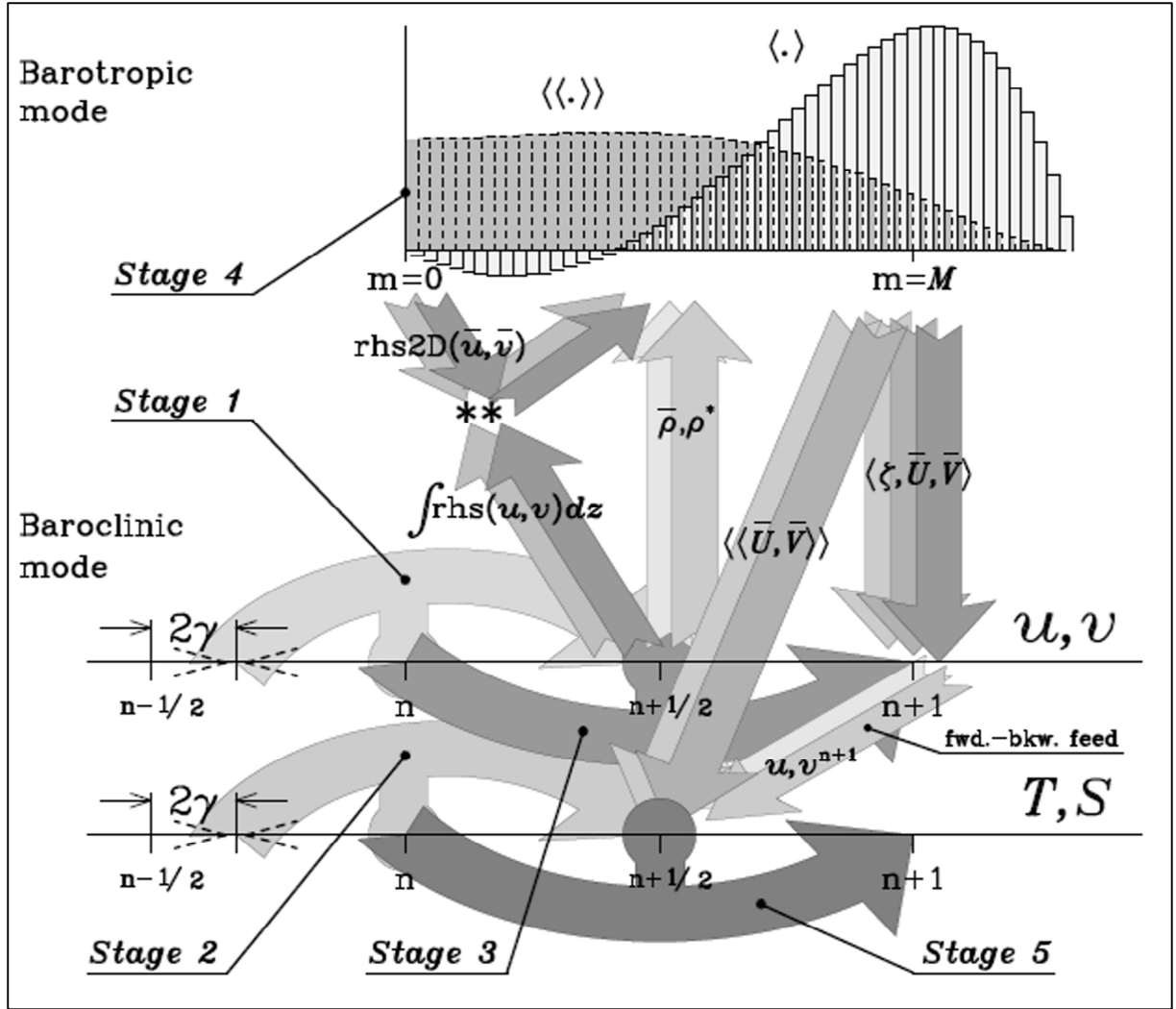
Figure 2: Schematic diagram of main time stepping procedure of ROMS hydrodynamic kernel – third-order Adams-Moulton (LF–AM3) predictor-corrector step for the baroclinic (3D) mode with mode coupling during the corrector stage. The arcs (curved arrows) represent "steps", i.e., updates of either momenta or tracers that involve computation of right hand side (rhs) terms (shown as circles attached to the arcs). Straight arrows indicate exchange of data between the modes. Each arrow originates at the time when the corresponding variable becomes logically available, regardless of its actual temporal placement. Arcs and arrows are drawn in the sequence that matches the sequence of operations in the actual code: whenever arrows overlap, the operation occurring later corresponds to the arc or arrow on top. Note that labels Stage 1 ... Stage 5 correspond to the actual computational stages described in Sec. 5 of Shchepetkin & McWilliams (2005). The four ascending arrows denote the vertically integrated rhs terms for 3D momentum equations; and the 2-way, vertically averaged densities, $\bar{\rho}$ and $\rho*$ which participate in computation of pressure gradient terms for the barotropic mode. The two descending arrows of smaller size on the left symbolize rhs terms computed from barotropic variables. The asterisks (* *) where the two pairs of ascending and descending arrows meet denote the computation of baroclinic-to-barotropic forcing terms, two smaller arrows ascending diagonally to the right. The five large descending arrows symbolize 2-way fast-time-averaged barotropic variables for backward coupling; fwd.-bkw. feed stands for forward-backward feedback between momentum and tracer equations – the update of tracers is delayed until the new-time-step velocities u, v_{n+1} become available, so that they can participate in computation of rhs terms for tracers; M is mode splitting ratio [number of barotropic time steps per one baroclinic]. After (Shchepetkin & Mc Williams, 2009)

3.1. Model Framework

Horizontally, ROMS equations are discretized on the C-Arakawa "staggered" grid (Arakawa & Lamb, 1977). On this type of grid, the horizontal velocity (u, v) are located at the west/east and south/north edges of the cell, respectively, while in contrast the free-surface, the density and active/passive tracers are located at the center of the cell (ρ points on Figure 3). ROMS use of orthogonal curvilinear grid coordinates allows Cartesian, polar and spherical coordinates applications. This type of horizontal grid system is especially suited for ocean circulation applications since it reduces numerical artefacts related to wave dispersion and facilitates adaptation to irregular site geometry.
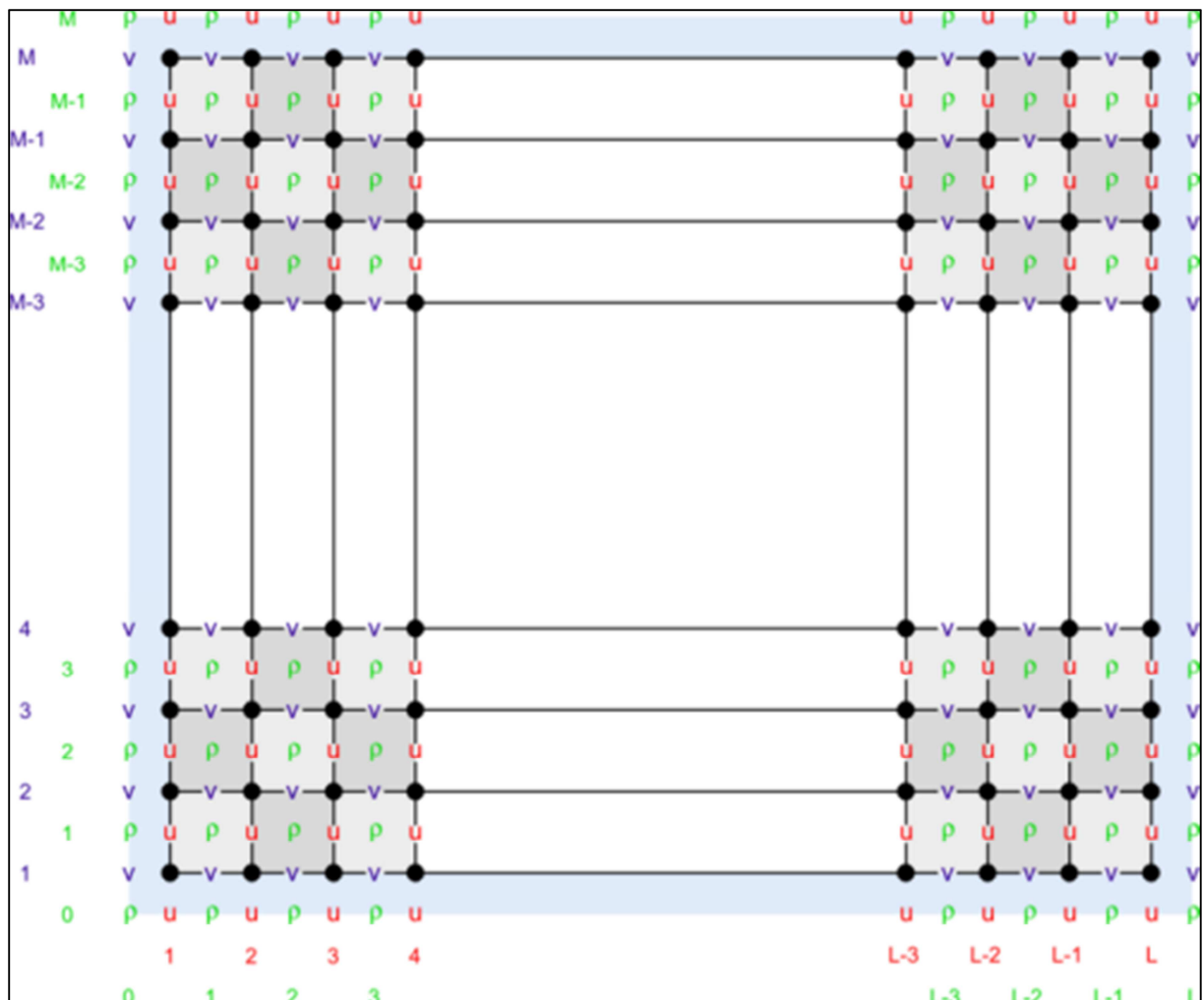
Figure 3: C Arakawa grid. Diagram after https://www.myroms.org/wiki

3.1. Model Framework

ROMS use a topography-following vertical coordinate system (Figure 4) where vertical coordinate sigma, σ, is a function of the actual depth z and the horizontal Cartesian coordinates x and y through the nonlinear stretching function $Stretch$ (12).

$$\begin{cases} -1 \leq \sigma \leq 0 \\ \sigma = 0 \equiv z = \eta \\ \sigma = -1 \equiv z = -h(x,y) \\ z(x.y.\sigma) = Stretch(\sigma).h(x.y) \end{cases} \tag{12}$$

where η represents the free surface elevation (m), $h(x,y)$ the water depth (m). As a result, cell level thickness and volume may vary with the site bathymetry. As in the horizontal equations and for the sake of consistency and numerical robustness, a staggered vertical grid is used to discretize the ROMS equation system (Figure 4). Accordingly, horizontal momentum components (u,v), the density (ρ) and active/passive tracers (Eq. (13)) are located at the centre of the grid cell whereas the vertical velocity (w) and vertical mixing variables (Eq. (22)) are located at the bottom and top faces of cell.
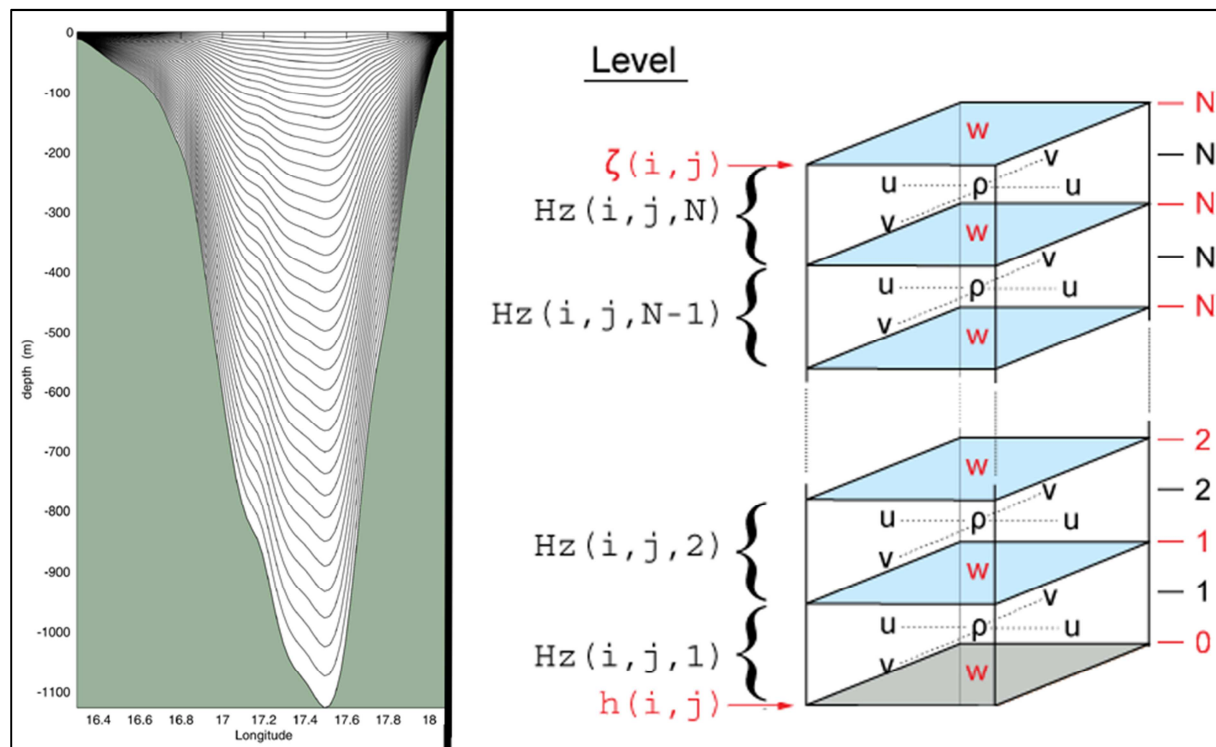
Figure 4: Topography-following vertical coordinate (left) and staggered vertical levels (right). Diagrams adapted from https://www.myroms.org/wiki

3.1. Model Framework

ROMS is a partly hydrostatic model based on the combination of the Boussinesq approximation (Boussinesq, 1903) and a UNESCO-type compressible equation of state (EOS) (Fofonoff & Millard, 1983). The Boussinesq assumptions (Boussinesq, 1903) can be simply formulated through two statements. First the principal cause of density variation in a flow motion is due to the variations in temperature and salinity and not the pressure variations. Secondly the density variation can be neglected except in the buoyancy force term. Specifically, the equation of state links the state variables of a fluid (density, salinity, temperature, pressure). This type of equation is useful in ocean models to compute pressure gradient force (PGF), evaluate the stratification stability and buoyancy flux and participate in the computation of the PGF in barotropic-baroclinic mode splitting (Shcheptkin & Mc Williams, 2005). However the combination of the full EOS and the Boussinesq assumption implied reformulations and modifications of the classic forms of the EOS and the Boussinesq assumption since it first led to spurious vertical shear in the pressure gradient forcing, numerical instability and both inaccuracy and mode-splitting errors (Shchepetkin & Mc Williams, 2003). The PGF for the barotropic mode is defined to account for perturbations in the free-surface elevation $\eta(x, y, t)$ by computing the variational derivative of the hydrostatic PGF, itself vertically integrated. Therefore the barotropic PGF is a function of η, but also of the vertically averaged dynamical density ρ^* and the vertically averaged density $\bar{\rho}$, both stored in the 3-D fields and maintained constant over the barotropic time-stepping. As a result, even with a significant difference between baroclinic and barotropic time-steps in the split-modes, accuracy and stability computations are guaranteed (Shchepetkin & Mc Williams, 2009).

At the same time, the baroclinic PGF computational method is based on monotonised cubic polynomial fitting against the vertical profiles of density and geopotential height. This type of scheme is well known for reducing errors in hydrostatic balance (Shchepetkin & Mc Williams, 2009). Advection schemes are key in ocean models as, in addition to the simple advection of scalar quantities, they ensure monotonicity, low implicit diffusion and conservation of invariants such as energy, entropy and tracer variance (Haidvogel & Beckmann, 1999). Among other options, ROMS

23

3.1. Model Framework

uses a third-order upstream-biased scheme for horizontal advection and a fourth-order centred scheme for vertical advection for both tracer and momentum equations (Smith & Scott, 2009). It may be worth noting that the Coriolis and curvilinear metric terms are included in the advection of momentum in an energy-conserving manner.

Now that the numerical background has been set, the ROMS theoretical kernel has to be related with classical hydrodynamic equations. Let's define C a scalar concentration which can represent, respectively or simultaneously, salinity, temperature or nutrient concentrations. Let's define $\rho^*(x,y,z,t)$ as the dynamic density. Finally, the total in situ density is equal to $\rho = (\rho_0 + \rho^*(x,y,z,t))$ where ρ_0 is defined as the averaged density value of the sea-water, also called background density. The equation system used in ROMS is the following

$$
\begin{cases}
\dfrac{\partial u}{\partial t} + \vec{v}.\nabla u - fv = -\dfrac{\partial p}{\partial x} - \dfrac{\partial}{\partial z}\left(\overline{u'w'} - \nu\dfrac{\partial u}{\partial z}\right) + F_u + D_u \\[2mm]
\dfrac{\partial v}{\partial t} + \vec{v}.\nabla v + fu = -\dfrac{\partial p}{\partial y} - \dfrac{\partial}{\partial z}\left(\overline{v'w'} - \nu\dfrac{\partial v}{\partial z}\right) + F_v + D_v
\end{cases} (A) \\[3mm]
\begin{cases}
\dfrac{\partial C}{\partial t} + \vec{v}.\nabla C = -\dfrac{\partial}{\partial z}\left(\overline{C'w'} - \nu_\theta\dfrac{\partial C}{\partial z}\right) + F_C + D_C \quad\quad (B) \\[2mm]
\rho = \rho(T,S,P) \quad\quad\quad\quad\quad\quad\quad\quad\quad\quad\quad\quad\quad\quad (C) \\[2mm]
\dfrac{\partial p}{\partial z} = -\dfrac{\rho g}{\rho_0} \quad\quad\quad\quad\quad\quad\quad\quad\quad\quad\quad\quad\quad (D) \\[2mm]
\dfrac{\partial u}{\partial x} + \dfrac{\partial v}{\partial y} + \dfrac{\partial w}{\partial z} = 0 \quad\quad\quad\quad\quad\quad\quad\quad (E)
\end{cases}
\tag{13}
$$

Where:

- (A) is the momentum balance in the x and y directions
- (B) is the time evolution of a scalar concentration field
- (C) is the equation of state
- (D) is the Boussinesq approximation (density variations neglected except for the vertical buoyancy force contribution)
- (E) is the continuity equation for an incompressible fluid
- $f(x,y)$ is the Coriolis parameter
- ν is the kinematic molecular viscosity
- ν_θ molecular diffusivity
- g is the acceleration of gravity

3.1. Model Framework

The terms $F_{u,v,C}$ and $D_{u,v,C}$ represent respectively the effects of forcing and horizontal dissipation. Because of the complexity of the $D_{u,v,C}$ term, a particular treatment is dedicated for its explanation further on. To close this system, parameterizations are needed for the horizontal dissipation for momentum and tracers, the Reynolds stresses as well as the turbulent tracer fluxes.

There are three main horizontal dissipation parameterizations available on ROMS, the harmonic eddy viscosity/diffusivity, the biharmonic eddy viscosity/diffusivity and the Smagorinsky dissipation scheme. The following paragraphs give a basic idea of the physics involved in these methods. The equations will be developed in Cartesian coordinates although, in ROMS, another coordinate basis can be chosen. Assuming a linear dependence on Reynolds stress parameterization for large-scale flow and the gradients of large scale fields, we have:

$$\nabla.\left(\overrightarrow{v'v'}\right) = -\nabla.\left(\zeta\nabla\vec{v}\right) \tag{14}$$

where ζ is the turbulent harmonic eddy coefficient. The ratio between horizontal-scale and vertical-scale suggest that ζ could be divided into two different contributions, a horizontal one ζ_h and a vertical one ζ_v. Generally it is assumed that $\zeta_h \gg \zeta_v$ and

$$\zeta = I \times \begin{vmatrix} \zeta_h.\overrightarrow{e_x} \\ \zeta_h.\overrightarrow{e_y} \\ \zeta_v.\overrightarrow{e_z} \end{vmatrix} \tag{15}$$

where I is a 3×3 identity matrix. Because of the high variability of vertical mixing in the ocean, the vertical dissipation components are treated separately. In consequence, these components keep their general formulations $\left\{\frac{\partial\overline{u'w'}}{\partial z}; \frac{\partial\overline{v'w'}}{\partial z}\right\}$ in Eq. (13). It's also worth noticing here that ζ includes the sub-grid scale parameterization for both momentum and scalar concentration effects. These two aspects can be separated as well. The effects on momentum are represented by $\zeta_{h,h}^M$ and called horizontal harmonic eddy viscosity while the effects on scalar concentrations are represented by $\zeta_{h,h}^C$ and called horizontal harmonic eddy diffusivity. Thus by comparison with Eq. (14) & Eq. (15), the horizontal contribution becomes:

3.1. Model Framework

$$
\begin{cases}
D_u = \zeta_{h,h}^{M}\left(\dfrac{\partial^2 \bar{u}}{\partial x^2} + \dfrac{\partial^2 \bar{v}}{\partial y^2}\right) \\[2ex]
D_v = \zeta_{h,h}^{M}\left(\dfrac{\partial^2 \bar{v}}{\partial x^2} + \dfrac{\partial^2 \bar{u}}{\partial y^2}\right) \\[2ex]
D_C = \zeta_{h,h}^{C}\left(\dfrac{\partial^2 \bar{C}}{\partial x^2} + \dfrac{\partial^2 \bar{C}}{\partial y^2}\right)
\end{cases}
\tag{16}
$$

It has been shown (Haidvogel & Beckmann, 1999) that, for high-resolution simulations in which part of the meso-scale eddy spectrum is already incorporated, the harmonic dissipation terms are too dissipative. To limit this erroneous behaviour, higher-order eddy diffusive and viscous operators have been developed, such as biharmonic operators $\zeta_{bi}^{M,C}$. Then $D_{u,v,C}$ is expressed as follows:

$$
\begin{cases}
D_u = \dfrac{\partial}{\partial x}\left(\zeta_{h,bi}^{M}\dfrac{\partial \nabla^2 \bar{u}}{\partial y}\right) \\[2ex]
D_v = \dfrac{\partial}{\partial y}\left(\zeta_{h,bi}^{M}\dfrac{\partial \nabla^2 \bar{v}}{\partial x}\right) \\[2ex]
D_C = \dfrac{\partial}{\partial x}\left(\zeta_{h,bi}^{C}\dfrac{\partial \nabla^2 \bar{C}}{\partial y}\right)
\end{cases}
\tag{17}
$$

Although horizontal biharmonic operators are not easily justified on physical grounds, they provide an interesting compromise between increased scale selectivity and computational requirements (Haidvogel & Beckmann, 1999). Obviously in more realistic flows, the sub-grid scale dissipation is not uniform over the domain and is likely to depend on both grid size variation and deformation of the velocity field. Smagorinsky developed a nonlinear lateral dissipation scheme accounting for these dual effects (Smagorinsky, 1963). This scheme has been built on the form of the horizontal harmonic eddy terms. However here $\zeta_h^{M,C}$ is not a constant anymore and is defined as follows:

$$
\zeta_{h,Smago}^{M,C} = \lambda \Delta x \Delta y \sqrt{\left(\frac{\partial u}{\partial x} - \frac{\partial v}{\partial y}\right)^2 + \left(\frac{\partial u}{\partial y} - \frac{\partial v}{\partial x}\right)^2}
\tag{18}
$$

Where λ is a diffusion constant, Δx is the grid size in the x direction and Δy is the grid size in the y direction

The vertical dissipation terms for Reynolds stresses and turbulent tracer flux have been implemented in ROMS around one unique form:

3.1. Model Framework

$$\begin{cases} \overline{u'w'} = -K_M \dfrac{\partial u}{\partial z} \\ \overline{v'w'} = -K_M \dfrac{\partial v}{\partial z} \\ \overline{C'w'} = -K_C \dfrac{\partial C}{\partial z} \end{cases} \tag{19}$$

where K_M is the vertical eddy viscosity and K_C the vertical eddy diffusivity. Nonetheless, three models are available on ROMS to parameterize these components, the generic length scale closure model, the Mellor-Yamada 2.5 closure model and the K-profile parameterization. The following paragraphs give a basic idea of the physics involved in these schemes. Again, the equations will be developed in Cartesian coordinates even though other coordinate bases can be used in ROMS. Thanks to the parameterizations of third-order moments and pressure strain correlations for the transport equations for the Reynolds stresses, the vertical eddy viscosity K_M and diffusivity K_c can be expressed as

$$\begin{cases} K_M = \Gamma\sqrt{2k}l\chi_M + \vartheta \\ K_C = \Gamma\sqrt{2k}l\chi_C + \vartheta_\theta \end{cases} \tag{20}$$

Where ϑ is the background vertical viscosity, ϑ_θ is the background vertical diffusivity, k is the turbulent kinetic energy (TKE) per unit mass, l is the length scale related to size of eddies that dominate the mixing, Γ is the stability function (Canuto et al., 2001), and χ_M and χ_C are two stability functions depending on the set of tuning parameters A_1, A_2, B_1, B_2 and the buoyancy parameter G (Kantha & Clayson, 1994). Prandtl argued that vertical eddy viscosity K_M (cf. (26) & (27)) is proportional to the length scale, l, multiplied by a characteristic velocity, $k^{\frac{1}{2}}$ (Prandtl, 1945) as given here,

$$\begin{cases} K_M \propto k^{\frac{1}{2}}l \\ k = \dfrac{1}{2}\left(\overline{u'^2} + \overline{v'^2} + \overline{w'^2}\right) \end{cases} \tag{21}$$

Generally two-equation models are composed of one transport equation for advection, diffusion, production and dissipation of k and one equation to prescribe the local value of l. There has been uncertainty and debate about the nature of this latter closure equation. Thus a generic length scale (GLS) equation form has been developed in order to cover most of popular closure

3.1. Model Framework

equations by specifying a few parameters (Umlauf & Burchard, 2001; Warner et al., 2005). In the GLS

model the standard equation for transport of k is:

$$
\begin{cases}
\dfrac{\partial k}{\partial t} + \bar{\vec{v}}.\nabla k = \dfrac{\partial}{\partial z}\left(\dfrac{K_M}{\sigma_k}\dfrac{\partial k}{\partial z}\right) + P + B - \varepsilon \\
P = K_M\left[\left(\dfrac{\partial \bar{u}}{\partial z}\right)^2 + \left(\dfrac{\partial \bar{v}}{\partial z}\right)^2\right] \\
B = -K_c N^2 \\
\varepsilon = \left(c_\mu^0\right)^{3+\frac{p}{n}} k^{3-2+\frac{m}{n}} \psi^{-\frac{1}{n}} \\
\psi = \left(c_\mu^0\right)^p k^m l^n
\end{cases}
\tag{22}
$$

Where:

- σ_k is the turbulent Schmidt number

- P represents the production of TKE by shear

- B represents the production of TKE by buoyancy

- $N = -\dfrac{g}{\rho_0}\dfrac{\partial \rho}{\partial z}$ is the buoyancy frequency

- ε is TKE dissipation

- ψ is a generic parameter

- c_μ^0, m, n, p is a parameterization set

To close the GLS model, a second equation is needed to drive the evolution of the generic parameter

ψ:

$$
\frac{\partial \psi}{\partial t} + \bar{\vec{v}}.\nabla \psi = \frac{\partial}{\partial z}\left(\frac{K_M}{\sigma_\psi}\frac{\partial \psi}{\partial z}\right) + \frac{\psi}{k}(c_1 P + c_3 B - c_3 \varepsilon F_{wall})
\tag{23}
$$

Where:

- c_1, c_3, c_3 is a parameterization set

- Fct_{wall} account for the effects of wall proximity

- σ_ψ is the turbulent Schmidt number for ψ

To conclude, by choosing the correct set of parameters for $c_\mu^0, m, n, p, \sigma_k, \sigma_\psi, c_1, c_2, c_3$ and Fct_{wall},

ROMS can recover the exact formulation of the standard $k - kl$, $k - \varepsilon$ or $k - \omega$ models. Firstly, it's

worth noting that the Mellor-Yamada level 2.5 scheme (MY2.5) expression refers to the original

formulation proposed by Mellor and Yamada (Mellor & Yamada, 1974) whereas the $k - kl$ closure

model notation refers to the GLS implementation of the same closure model. Here the set of

3.1. Model Framework

parameters is the following $\psi = kl$, $c_\mu^0 = 0.5544$, $p = 0.0$, $m = 1.0$, $n = 1.0$, $\sigma_k = \sigma_\psi = 2.44$, $c_1 = 0.9$, $c_2 = 0.5$, $c_3 = 1.0$ and the standard wall proximity function is defined as:

$$Fct_{wall} = \left(1 + 1.33\left(\frac{1}{\kappa}\frac{d_b + d_s}{d_b d_s}\right)^2\right) \tag{24}$$

Where κ is von Karman's constant, d_b and d_s are respectively the distances to the bottom and surface. The enhanced K-profile parameterization for vertical mixing allows both the surface and bottom boundary layers and the ocean interior to be matched. This method is based on boundary layer similarity and accounts for local shear and internal wave effects. Conceptually the vertical eddy viscosity and diffusivity $K_{M,C}$ is expressed differently for the surface boundary layer $K_{M,C}{}^{surf}$ and bottom boundary layer $K_{M,C}{}^{bot}$, as follows:

$$\begin{cases} K_{M,C}{}^{surf} = h_{sbl}w_{sf}G_f \\ K_{M,C}{}^{bot} = h_{bbl}w_{bf}G_f \end{cases} \tag{25}$$

Where:

- h_{sbl} and h_{bbl} are respectively the surface and bottom boundary length scale calculated as the minimum between the Ekman layer (Ekman, 1905) and the shallowest depth at which a critical bulk Richardson number Ri_g (27)is reached

- w_{sf} and w_{bf} are respectively the velocity length scale for surface and bottom layers and, under the neutral forcing assumption (i.e. no heat or salinity fluxes), are equal respectively to the products of the bottom u_b^* and surface u_s^* friction velocities and the Von Karman constant.

- G_f is defined as a shape function based on a third order polynomial. Its four coefficients are computed to match with the surface dissipative terms at the bottom of the boundary layer and the Monin-Obukov theory (Monin & Obukhov, 1954).

Finally the interior viscosity/diffusivity is defined by adding the shear mixing and internal wave-generated mixing. The shear mixing component ϑ^{sh} is computed using a gradient Richardson number (115) formulation:

$$Ri_g = \frac{N^2}{Sh^2} \; ; Ri_0 = 0.7 \tag{26}$$

3.1. Model Framework

$$\vartheta^{sh} = \begin{cases} \vartheta_0 & ; & Ri_g < 0 \\ \vartheta_0 \left[1 - \left(\dfrac{Ri_g}{Ri_0} \right)^2 \right]^3 & ; & 0 < Ri_g < Ri_0 \\ 0 & ; & Ri_0 < Ri_g \end{cases} \tag{27}$$

where Sh is the vertical shear in the horizontal velocity and N is the Brunt-Väisälä frequency. On the other hand internal wave-generated mixing is considered as background mixing. In others terms it is specified as a uniform value for each momentum and scalar. This value can be estimate through field measurement considerations (Large et al., 1994; Ledwell et al., 1993; Peters et al., 1988)

Consequently eq. (13) can be rewritten

$$\begin{cases} \dfrac{\partial u}{\partial t} + \vec{v}.\nabla u - fv = -\dfrac{\partial \varphi}{\partial x} - \dfrac{\partial}{\partial z}\left(-K_M \dfrac{\partial u}{\partial z} - v \dfrac{\partial u}{\partial z} \right) + F_u + A_M \left(\dfrac{\partial^2 \bar{u}}{\partial x^2} + \dfrac{\partial^2 \bar{v}}{\partial y^2} \right) \\[2mm] \dfrac{\partial v}{\partial t} + \vec{v}.\nabla v + fu = -\dfrac{\partial \varphi}{\partial y} - \dfrac{\partial}{\partial z}\left(-K_M \dfrac{\partial v}{\partial z} - v \dfrac{\partial v}{\partial z} \right) + F_v + A_M \left(\dfrac{\partial^2 \bar{v}}{\partial x^2} + \dfrac{\partial^2 \bar{u}}{\partial y^2} \right) \\[2mm] \dfrac{\partial C}{\partial t} + \vec{v}.\nabla C = -\dfrac{\partial}{\partial z}\left(-K_C \dfrac{\partial C}{\partial z} - v_\theta \dfrac{\partial C}{\partial z} \right) + F_C + A_C \left(\dfrac{\partial^2 \bar{C}}{\partial x^2} + \dfrac{\partial^2 \bar{C}}{\partial y^2} \right) \\[2mm] \rho = \rho(T,S,P) \\[2mm] \dfrac{\partial \varphi}{\partial z} = -\dfrac{\rho g}{\rho_0} \\[2mm] \dfrac{\partial u}{\partial x} + \dfrac{\partial v}{\partial y} + \dfrac{\partial w}{\partial z} = 0 \end{cases} \tag{28}$$

with the harmonic form of horizontal dissipation, and

$$\begin{cases} \dfrac{\partial u}{\partial t} + \vec{v}.\nabla u - fv = -\dfrac{\partial \varphi}{\partial x} - \dfrac{\partial}{\partial z}\left(-K_M \dfrac{\partial u}{\partial z} - v \dfrac{\partial u}{\partial z} \right) + F_u + \dfrac{\partial}{\partial x}\left(A_{bi}^M \dfrac{\partial \nabla^2 \bar{u}}{\partial y} \right) \\[2mm] \dfrac{\partial v}{\partial t} + \vec{v}.\nabla v + fu = -\dfrac{\partial \varphi}{\partial y} - \dfrac{\partial}{\partial z}\left(-K_M \dfrac{\partial v}{\partial z} - v \dfrac{\partial v}{\partial z} \right) + F_v + \dfrac{\partial}{\partial y}\left(A_{bi}^M \dfrac{\partial \nabla^2 \bar{v}}{\partial x} \right) \\[2mm] \dfrac{\partial C}{\partial t} + \vec{v}.\nabla C = -\dfrac{\partial}{\partial z}\left(-K_C \dfrac{\partial C}{\partial z} - v_\theta \dfrac{\partial C}{\partial z} \right) + F_C + \dfrac{\partial}{\partial x}\left(A_{bi}^C \dfrac{\partial \nabla^2 \bar{C}}{\partial y} \right) \\[2mm] \rho = \rho(T,S,P) \\[2mm] \dfrac{\partial \varphi}{\partial z} = -\dfrac{\rho g}{\rho_0} \\[2mm] \dfrac{\partial u}{\partial x} + \dfrac{\partial v}{\partial y} + \dfrac{\partial w}{\partial z} = 0 \end{cases} \tag{29}$$

with the biharmonic form of horizontal dissipation.

Generally numerical domains possess rigid or open boundaries and/or unsteady interfaces which of course need a particular numerical treatment since they literally define the spatial limits of the numerical domain but also close the equation system by defining the boundary values. Defining

3.1. Model Framework

$\eta(x, y, t)$ as the surface elevation and $h(x, y)$ the bottom depth, the vertical boundary conditions are needed at the water/sea bed interface and at the atmosphere/water interface. At the atmosphere/water interface, $z = \eta(x, y, t)$:

$$\begin{cases} K_M \dfrac{\partial u}{\partial z} = \tau_s^x(x, y, t) \\ K_M \dfrac{\partial v}{\partial z} = \tau_s^y(x, y, t) \\ K_C \dfrac{\partial C}{\partial z} = \dfrac{X_s}{\rho_0} \\ w = \dfrac{\partial \eta}{\partial t} \end{cases} \tag{30}$$

At the water/sea bed interface where $z = -h(x, y)$:

$$\begin{cases} K_M \dfrac{\partial u}{\partial z} = \tau_b^x(x, y, t) \\ K_M \dfrac{\partial v}{\partial z} = \tau_b^y(x, y, t) \\ K_C \dfrac{\partial C}{\partial z} = 0 \\ -w + \vec{v}.\nabla h = 0 \end{cases} \tag{31}$$

where X_s is the surface concentration flux, $\tau_s^{x,y}$ is the surface wind stress and $\tau_b^{x,y}$ is the bottom stress. ROMS has four different methods for expressing the bottom shear stress depending on the option chosen. It can be defined as linear (32.A), quadratic (32.B), or logarithmic (32.C). It can also be fully defined by the user through an analytical expression,

$$\vec{\tau_b} = \begin{cases} \rho C_{D,0} \vec{v} & (A) \\ \rho C_{D,1} (\vec{v})^2 & (B) \\ \left(\dfrac{\kappa}{\log\left(\frac{z}{Z_0}\right)} \right)^2 (\vec{v})^2 & (C) \end{cases} \tag{32}$$

where $C_{D,0}$, $C_{D,1}$ and Z_0 are set by the user and defined respectively as linear bottom drag coefficient, quadratic bottom drag coefficient and bottom roughness height. There are seven main options for horizontal boundary conditions available on ROMS. They can be spilt in two distinct groups: closed boundary condition and open boundary condition. Considering first closed boundary conditions, let's define the "wall conditions". These conditions differ if slip effects on the wall are taken into account or not. The formulation for the "no-slip" option is:

31

$$\begin{cases} X_{C.B.}^{tan} = 0 \\ X_{C.B.}^{n} = 0 \end{cases} \tag{33}$$

and for the "free-slip" option:

$$\begin{cases} \dfrac{\partial X_{C.B.}^{\overrightarrow{tan}}}{\partial n} = 0 \\ X_{C.B.}^{\vec{n}} = 0 \end{cases} \tag{34}$$

where $X_{C.B.}$ defines any quantity at the closed boundary, the indice $\vec{n}$ refers to the normal direction

to the closed boundary and $\overrightarrow{tan}$ to the tangential direction (Robertson et al., 2004). Secondly ROMS

integrates five different open boundary condition types. The so called "clamped" conditions provide

as boundary values, values fixed by the user:

$$X_{boundary} = X_{fixed} \tag{35}$$

The "gradient conditions" compute the boundary values $X_{O.B.}$ as follows:

$$\frac{\partial X_{O.B.}}{\partial n} = 0 \tag{36}$$

where n represents the normal direction to the boundary. The "radiation conditions" generally

called Sommerfeld conditions calculate boundary values using the following propagation equation:

$$\frac{\partial X_{O.B.}}{\partial t} + c\frac{\partial X_{O.B.}}{\partial n} = 0 \tag{37}$$

where c is wave phase speed. The "Chapman conditions" (Chapman, 1985) are applicable only for

the free surface boundary and derive from the latter equation (37) with $X_{O.B.} = \eta$ and $c =$

$\sqrt{g(\eta + h)}$ the classic form of gravity wave velocity:

$$\frac{\partial \eta}{\partial t} + \sqrt{g(\eta + h)}\,\frac{\partial \eta}{\partial n} = 0 \tag{38}$$

The final option for an open boundary is based on a combination of radiation conditions for long

wave phase speed and a one-dimensional approximation of the continuity equation. This last option

is called "Flather conditions":

$$\frac{\partial \eta}{\partial t} + h\,\frac{\partial \overrightarrow{v_{\vec{n}}}}{\partial n} = 0 \tag{39}$$

where $\overrightarrow{v_{\vec{n}}}$ is the velocity vector normal to the open boundary (Carter & Merrifield, 2007).

3.2. Actuator Disc Theory – Introduction and Limitations

The installation of a TCT is intended to harness a portion of the energy contained in the flow. The energy extracted from the flow is converted into useable power from the torque applied on the rotor by the fluid flow and the torque itself is induced by the design of the blades. In the opposite reaction, the fluid acquires a swirl-like rotational motion downstream of the turbine. This area of reduced axial momentum and increased angular momentum extending several rotor diameter lengths is called the wake. Commonly the wake structure is divided in two parts: the near and the far wake (Pham & Martin, 2009). The near wake is characterized by flow which exhibits high turbulence levels mainly generated by the axial velocity shear, blade related vortices and wake rotation (Réthoré et al., 2009; Kasmi & Masson, 2008). Assuming a regional scale focus, the details of the induced swirl effects in the near wake region are not of great relevance to TCT modelling (Salter, 2009; Bryden & Couch, 2007). As mentioned in Chapter 2, this assumption is inherent in the physical scale modelling practice in which turbines are represented by non-rotating porous discs (Bryden & Couch, 2004; Bryden & Couch, 2007; Garrett & Cummins, 2005). This experimental approach is often compared to the actuator disc concept (Myers & Bahaj, 2010), itself commonly used in numerical simulation and analytical models (Harrison et al., 2009).

According to the actuator disc concept (Figure 1), extracting energy from a fluid flow requires a reduction in the momentum of the fluid passing through the area swept by the turbine blades, often referred to as an actuator disc. Simultaneously, fluid passing through the rotor experiences a discontinuity in static pressure *p* along the rotor-centre line (Figure 1), namely at the rotor location $p_d^+ \neq p_d^-$ (Burton et al., 2008). These particular dynamics are commonly formalised through Momentum Theory (Burton et al., 2008) in which the mass flow rate is considered the same everywhere along the stream-tube (Figure 1). Accordingly, the pressure drop induced by the presence of a TCT can be expressed as follows:

$$(p_d^+ - p_d^-) = (U_\infty - U_w)\rho U_\infty (1 - a) \tag{40}$$

where a is the induction factor $(= \frac{U_\infty - U_d}{U_\infty})$, p_d^+ the pressure preceding the disk and p_d^- the pressure

following the disk, U_w the velocity in the wake, ρ the water density, U_∞ the velocity far upstream of

the disc and U_d the velocity at the disc location. From equation (40) and the definition of the wake

velocity as $U_w = (1 - 2a)U_\infty$ (Burton et al., 2008), the force on the fluid can be defined as follows:

$$Force = (p_d^+ - p_d^-)A_d = 2\rho A_d U_\infty{}^2 a(1 - a) \tag{41}$$

The actuator disc area (m^2) A_d is equivalent to the area swept by the turbine blades. By normalizing

this force, one can introduce a standard non-dimensional quantity called the coefficient of thrust C_t

(Burton et al., 2008):

$$C_t = \frac{Force}{\frac{1}{2}\rho A_d U_\infty{}^2} = 4a(1 - a) \tag{42}$$

In the field of physical scale modelling the coefficient C_t is related to disc porosity (Harrison et al.,

2009). The induction factor a is a dimensionless quantity, ranging from 0 to 1, which represents the

strength of the reduction in fluid velocity. From equation (42), the force on the fluid induced by the

presence of a turbine, also called the thrust force $\overrightarrow{F_t}$, can be expressed as follows:

$$\begin{cases} \overrightarrow{F_t} = -\frac{1}{2}\rho A_d C_t (|\overrightarrow{v_\infty}|\overrightarrow{v_\infty}).\vec{n} = -\frac{1}{2}\rho A_d C_t \begin{cases} (|u_\infty|u_\infty).(\vec{n}.\overrightarrow{e_x}) = \overrightarrow{F_{t,u}} \\ (|v_\infty|v_\infty).(\vec{n}.\overrightarrow{e_y}) = \overrightarrow{F_{t,v}} \end{cases} \\ \vec{n} = unitary\ normal\ vector\ to\ the\ disc\ surface \end{cases} \tag{43}$$

The force being concentrated at the actuator disc, the power extraction from the fluid is equivalent

to the rate of work done by the force ($Work = Force \times U_d$). According to the definition of the

induction factor, the extracted power is given by

$$Power = Force \times U_d = 2\rho A_d U_\infty{}^3 a(1 - a)^2 \tag{44}$$

The induction factor can also be linked to the power coefficient C_{power}, which has the value of the

ratio between extracted power and available power, and can be expressed as follows:

$$C_{power} = \frac{Power}{\frac{1}{2}\rho A_d U_\infty{}^3} = 4a(1 - a)^2 \tag{45}$$

Equations (43) and (45) constitute the core of the actuator disc concept (Burton et al., 2008). The

limit of this theory is set for a value of $a \leq \frac{1}{2}$ above which the velocity in the wake U_w becomes zero,

or even negative. Beyond this limit the momentum theory needs to be adapted to be relevant (Burton et al., 2008).

Draper et al. (2009), Lalander & Leijon (2009) and Bryden & Couch (2007) used the actuator disc concept in large scale 2-D models in order to assess the power available in a realistic flow. However, as 2D models are depth integrated, the implemented thrust force is, therefore, vertically uniform over the water column. This brings confusion in its physical meaning since it can be equally regarded as a drag force (Draper et al., 2009) or an additional shear stress (Lalander & Leijon, 2009). As a consequence, the vertical flow behaviour such as the relation between water column height and corresponding drag coefficient (Sutherland et al., 2007), vertical flow bypassing of the device or distinction between bottom friction and energy extraction (Karsten et al., 2008), are misrepresented and thus wrongly estimated. Kawase & Thyng (2009) highlighted, through a 3-D model using the additional bottom shear stress method, the importance of integrating baroclinic dynamics in the simulation to assess fully the turbine yield (Kawase & Thyng, 2009). The actuator disc concept has been successfully applied to 3D CFD wake models by Harrison et al. (2009) and Sun & Bryden (2008). Thanks to the high resolution of CFD methods and despite the assumption that TCTs can be approximated as non-rotating objects, the actuator disc concept seems to accurately compute the wake decay (Harrison et al., 2009; Sun et al., 2008). Unfortunately, because of their high grid resolution and significant computational cost, CFD models cannot be used for simulating realistic flows with large spatial coverage and complex bathymetry and forcing. Since TCT array optimization has to account for a wide range of scales going from wake interactions to large hydrodynamic impacts, ocean-circulation type models have a practical advantage over CFD models.

Réthoré et al. (2009) and El Kasmi et al. (2008) raised the problem of applying the actuator disc concept to 3D ocean-circulation models. Indeed, the grid resolution and the turbulence closure models used in most of the large-scale 3-D models set an arbitrary threshold of time and scale below which flow fluctuations are considered as turbulence. Since the length and time scales of the turbulence induced by a turbine are several times smaller than the length and time scales of

turbulence considered by the turbulence closure models of large-scale models, correction terms need to be injected into the closure model in order to account for the turbulence activity induced by the turbine (Réthoré & Sorensen, 2008; Kasmi & Masson, 2008; Rados et al., 2009). Moreover, it is even more important to account for turbine induced turbulence since, in most realistic cases, the limit value of $a \leq \frac{1}{2}$ will be exceeded and, accordingly, device induced turbulences will have a major role in the spatial wake decay as described in Chapter 5.3.3 (Roc et al., 2010; Roc et al., 2011). From a physical point of view this threshold marks the point where the wake becomes turbulent and where the flow separates at the disc's edge and spreads radially, generating a virtual radial expansion of the rotor disc (Burton et al., 2008). These phenomena combined with the proximity of the free-surface and the sea-bottom, above and beneath the rotor disc, may also lead to an enhanced horizontal expansion of the virtual rotor disc (Daly et al., 2010). The flow separation is characterized by a slow moving region of low pressure straight after the disc and a fast moving region of high pressure at the front of the disc and around the edge of the device as the fluid surges then flows around the turbine. The induced static pressure drop cannot be balanced by the kinetic energy; therefore the energy loss is compensated by the mixing process taking place in the turbulent wake (Burton et al., 2008). By analogy with a flat plate, this slow moving area is referred to as the stagnation area even though part of the flow still passes through the rotor-disc (i.e. area swept by the turbine blades). Furthermore, this phenomenon is amplified by the blockage effect inherent to constrained flows (Whelan et al., 2007). In summary using the actuator disc concept in large-scale numerical models without adapting the models to account for the turbine induced turbulence occurring in the near wake region would lead to a misrepresentation of the wake recovery and impacts in realistic scenarios.

3.3. Accounting for Turbulence Perturbations

Although empirical approaches have been attempted by Buhl (2005) and Whelan (2007) to adapt the actuator disc theory beyond its limit of validity by artificially enhancing the thrust

coefficient (Buhl, 2005; Whelan et al., 2007), empirical parameterizations of the thrust coefficient present difficulties for developing a TCT array optimisation tool. Such empirical approaches require large sets of data for almost every scenario and, most importantly, miss the turbulence aspect of the problem. In order to improve the discrepancies in the near wake performance, and by extension wake recovery, of large-scale simulations it may be important to recognize that the fluid passing through a rotor results in a local disturbance of the turbulence equilibrium (Blunden & Bahaj, 2007).

Regarding turbulence, the presence of a turbine in a flow generates shear, itself created by the velocity gradient of the wake. This type of turbulence is handled by the turbulence production term P common to any 2-equation turbulence closure model used in large-scale models. On the contrary, blade root and tip vortices as well as some of the blade shed vortices induce turbulence downstream of the device are not accounted for in closure models as an active contribution in the turbulent dynamics (Réthoré et al., 2009). Likewise, after breaking down a few rotor diameters beyond the turbine, wake rotational motion and vortices also contribute to the wake dissipation but are not accounted for in closure models (Réthoré et al., 2009). In the respective areas of wind turbine and forest canopy research, Sanz (2003) and Rethore et al. (2009) proposed a technique to account for these turbine induced turbulences. It consists of adding a source term, S_P, into the turbulent kinetic energy (TKE) transport equation of 2-equation turbulence closure models (Sanz, 2003). S_P is defined as being proportional to the cube of flow-velocity in the turbulent kinetic energy (TKE) and is only active at the rotor-disc location.

$$S_p \propto \|\vec{v}\|^3 \tag{46}$$

Furthermore, turbines (or porous discs) transfer some kinetic energy harnessed from larger scale turbulence into finer scale turbulence (Harrison et al., 2009; Réthoré et al., 2009; Kasmi & Masson, 2008), perturbing the natural turbulence cascade described by Kolmogorov (Kolmogorov, 1941). In contrast to porous discs, turbines extract part of this transferred energy as mechanical power (Réthoré et al., 2009). This phenomenon is referred as the "short-circuiting of the turbulence cascade" (Sanz, 2003; Réthoré et al., 2009; Kasmi & Masson, 2008; Rados et al., 2009). Sanz (2003)

and Rethore et al. (2009) proposed adding a sink term S_d in the TKE transport equation of 2-equation turbulence closure models to account for this energy transfer. S_d is defined as being proportional to the flow-velocity multiplied by the TKE and only active at the rotor-disc location.

$$S_d \propto -\|\vec{v}\|.k \tag{47}$$

At the same time, the turbulence field present in the near wake will exhibit a reduced spectrum of length scales as it is partially generated by direct fluid interactions with the rotor (or porous disc) (Bryden & Melville, 2004; Bryden & Couch, 2004). In the area of wind turbine research, Kasmi & Mason (2008) and Rados (2009) proposed injection of a new time-scale related to the energy transfer rate from large to small-scale turbulence in the turbulent length-scale (TLS) transport equation of 2-equation turbulence closure models to account for this length-scale transfer. Accordingly, they added an extra term, S_ψ, as described by Chen & Kim (1987) to the TLS transport equation of 2-equaton turbulence closure models, at the rotor-disc location. S_ψ is defined as being proportional to the quadratic production of TKE by shear and only active at the rotor-disc location.

$$S_\psi \propto P^2 \tag{48}$$

The thrust force (43) combined with the three terms of the turbulence corrections (Eq. (46), (47) and (48)) compose the theoretical core of the present TCT representation method.

Chapter 4. General Methods

4.1. Review of Tidal Energy Extraction modelling

The following section deals with the modelling of energy extraction in a simple channel by a linear device array of tidal current turbines. This case has been developed and resolved by Bryden (Bryden et al., 2004; Bryden et al., 2007). In the framework of the PhD, this idealized case has been used as a first step in the background analysis as well as base reflexion material for the development of the proposed method. The approach was to recreate a referenced 1-D simulation and then progressively increase the complexity of the TCT representation by moving to 2-D and 3-D parameterisations. By doing so, the advantages and limitations of the existing numerical representation of TCT are highlighted and the best suited TCT representation for creating TCT layout optimisation tool can be found. From a practical point of view, it implies transporting a 1-D numerical approach into a 2-D depth-averaged and then 3-D environment without losing its consistency.

The idealised case studied by Bryden et al. (2004, 2007) is a simple straight channel of constant depth and width over its four kilometres of length. This east-west channel links two infinite oceans. The device array is located across the channel at two kilometres from its western boundary. The free surface elevation difference between the west and the east boundaries is equal to 0.4 meters and steady in time (Figure 5). The sea bed roughness is homogenous and the friction along the north and south sides of the channel are neglected.

Figure 5: Simplified-channel diagram

where $b = 1000\text{m}$, $L = 4000\text{m}$, $H = 39.6\text{m}$, $\eta = \eta(x)$; $\begin{cases} \eta(0) = 0.4\text{m} \\ \eta(L) = 0\text{m} \end{cases}$. In the depth averaged

version of ROMS, the standard hydraulic equation for open channel flow (i.e. Chapter 2, Eq. (1))

amounts to the following equation system:

$$\begin{cases} u_H \dfrac{du_H}{dx} = -g\dfrac{d\eta}{dx} - C_{D,1}\dfrac{u_H{}^2}{h} \\ \dfrac{dhu_H}{dx} = \dfrac{d(H+\eta)u_H}{dx} = 0 \end{cases} \tag{49}$$

where u_H is the velocity in the x direction averaged over the depth (m.s^{-1}) and $C_{D,1}$ a drag coefficient. This system is valid for a steady solution of a barotropic flow perturbed by a constant free surface elevation and subject to homogenous bottom shear stress under the shallow water assumptions. In Bryden & Couch (2007), energy extraction on the flow is be modelled by an additional bottom shear stress (i.e. Eq. (2)). Equation (2) can be rewrite as follows to meet the quadratic formulation of ROMS' bottom shear stress:

$$\tau_{add} = \frac{1}{2}\rho \varsigma u_H^2 \frac{R}{\Delta x} \tag{50}$$

where ς is the fraction of kinetic flux being extracted $(\varsigma = 0.1)$ and Δx the length over which the energy is being extracted (m). As remainder (i.e. Chapter 2), over the device array the effective shear stress is:

$$\tau_{eff} = \tau_0 + \tau_{add} \tag{51}$$
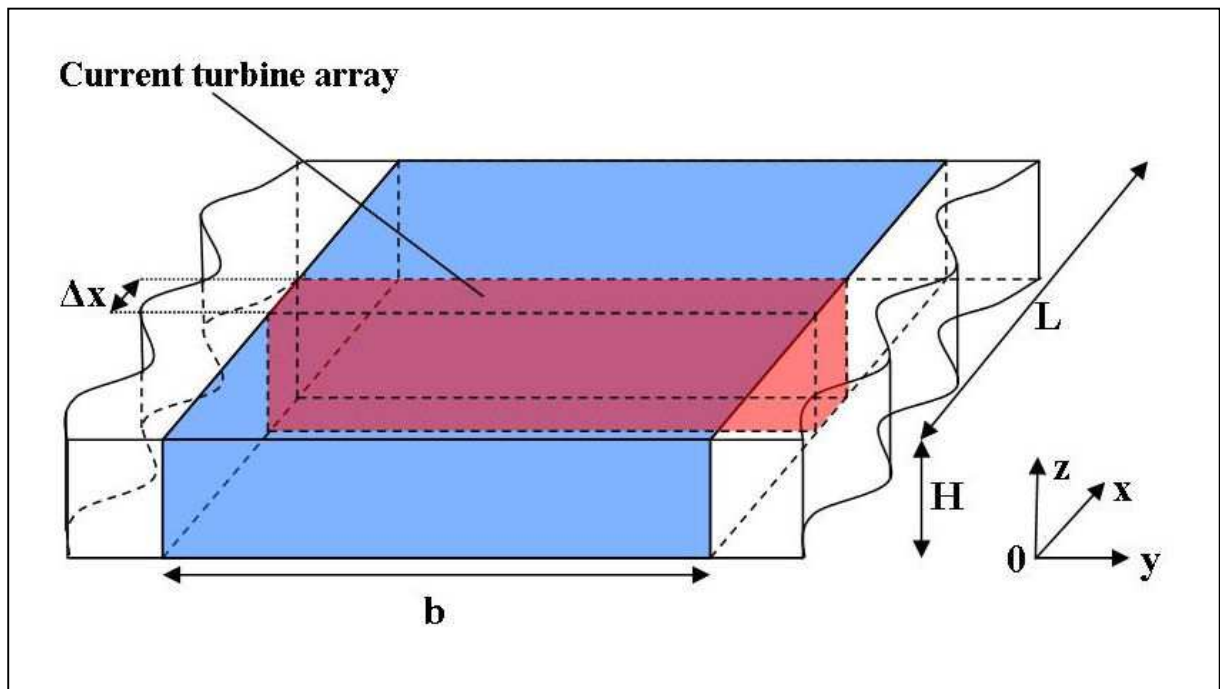
Figure 6: Uniform array case, domain diagram. Current turbine array is represented by the red volume across the channel.

In order to define the ROMS numerical parameters, the equivalence between both discharge conservation equation and ROMS 2-D depth averaged equation systems has to be demonstrated.

Particularly the demonstration will allow us to define the drag coefficient used in ROMS for the computation of the quadratic bottom shear stress. According to (Bryden et al., 2007) and the standard expression of the discharge, we have:

$$\begin{cases} u_H * h * b = Q \\ h * u_H = constant = \dfrac{Q}{b} \\ \dfrac{dh}{dx} = \dfrac{d(H+\eta)}{dx} = \dfrac{d\eta}{dx} \end{cases} \tag{52}$$

Therefore eq.(49) can be rewritten:

$$\left(1 - \frac{Q^2}{gh^3b^2}\right)\frac{dh}{dx} = -C_{D,1}\frac{u_H{}^2}{gh} \tag{53}$$

Besides, knowing that *b* the width of the channel is constant and that the total depth *h = h(x)*, we can reformulate Eq. (53) as:

$$\left(1 - \frac{Q^2}{gh^3b^2}\right)\frac{dh}{dx} = -\frac{P_{er}\tau_0}{\rho gbh} \tag{54}$$

To validate the equivalence the following equation must be true (53)=(54).

$$C_{D,1}\frac{u_H{}^2}{gh} = \frac{P_{er}\tau_0}{\rho gbh} \tag{55}$$

where $P_{er} = (2 * h) + b$ and $R = \frac{hb}{P_{er}}$. Thus, without the device array, the drag coefficient of ROMS equals to:

$$C_{D,1} = g\frac{n^2(2h+b)^{4/3}}{h^{1/3}b^{4/3}} \tag{56}$$

And, with the device array, this coefficient becomes:

$$C_{D,1} = g\frac{n^2(2h+b)^{4/3}}{h^{1/3}b^{4/3}} + \frac{f}{2b\Delta x}(bh) \tag{57}$$

Now that the theoretical equivalence between both equation systems has been made, Bryden's test case can be reproduced with ROMS using the depth averaged version. The spatial domain used is divided by 40 in the x direction and by 5 in the y direction that is a grid composed of 200 cells with a length of 100m and width of 200m. At the eastern and western open boundaries,

the free surface elevations are respectively set to 0 m and 0.4 m thanks to the "clamped" boundary condition and the velocities are imposed by the Flather condition. The slip effects due to the North-South walls have been neglected by imposing a free slip condition on them (i.e. Section 3.1). In order to kick off the simulation the model needs at least an initial velocity at the west boundary. This initial velocity can be assessed thanks to the major balance of this hydrodynamic system:

$$g\frac{d\eta}{dx} \cong C_{D,1}\frac{u_{H,west}^2}{h_{west}} \tag{58}$$

$$u_{H,west}^{ini} = \sqrt{-g\frac{h_{west}}{C_{D,1}}\frac{d\eta}{dx}} \tag{59}$$

This formulation implies one assumption which is:

$$\frac{d\eta}{dx} \equiv constant \cong -1 * 10^{-4} \tag{60}$$

This assumption is not very important since ROMS will compute and correct the velocity for each tile of the grid and over each time step. It has only been made to perturb the system. The time step Δt fits with the CFL condition:

$$\Delta t \leq \frac{\Delta x}{\sqrt{gH}} \tag{61}$$

This condition ensures that the model converges toward a steady solution. For instance, in the case where the device array is not implanted across the channel, one can observe that u_h and η converge toward a steady state (Figure 7 and Figure 8). For both quantities around t=14000s the errors of the two latter parameters are $\left(\frac{\Delta u_h}{u_h}\right)_{max} < 10^{-4}$ and $\left(\frac{\Delta \eta}{\eta}\right)_{max} < 10^{-2}$. The accuracy of those solutions is sufficient to consider $U_{n=14000}$ and $\eta_{n=14000}$ as our solutions for the equilibrium state.
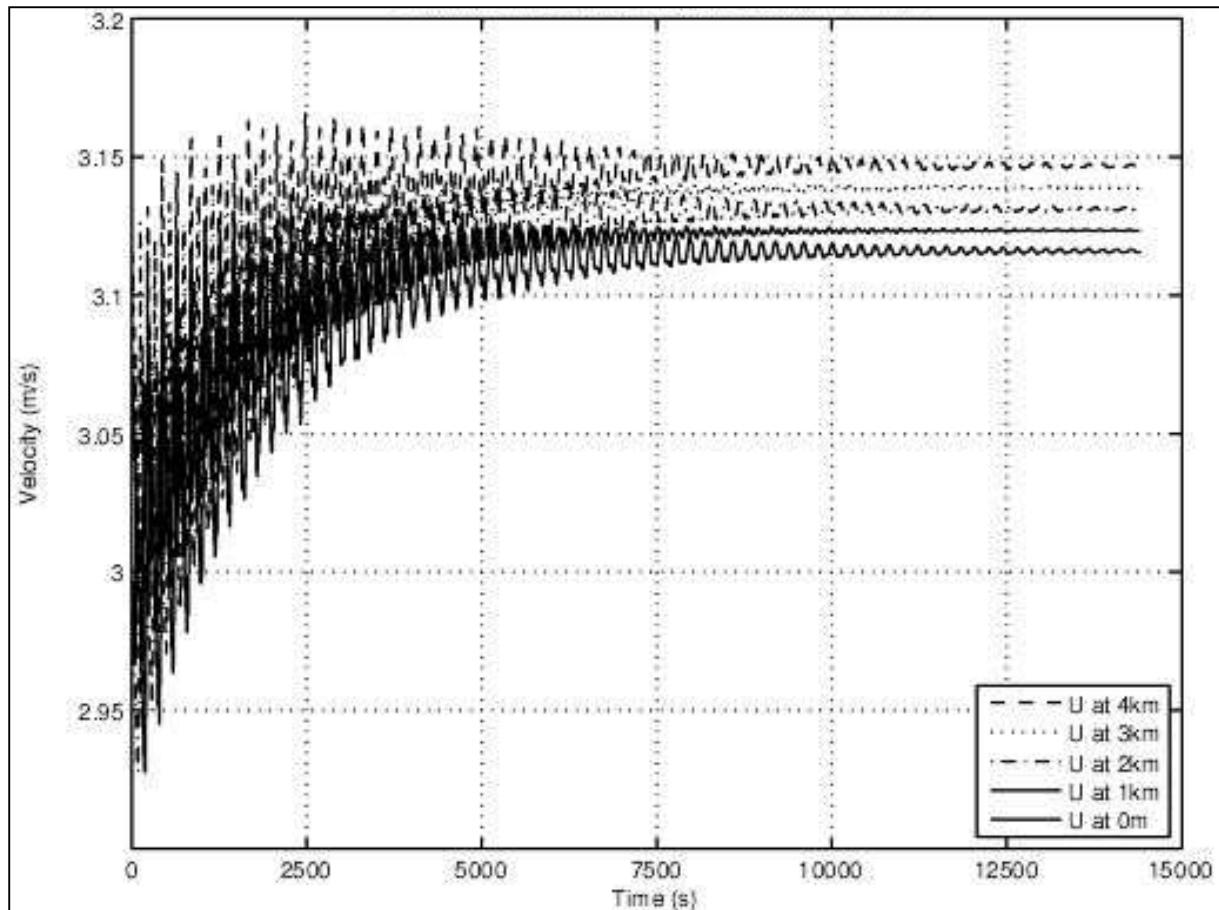
Figure 7: Flow-velocities numerical-convergence. Flow velocities averaged width wise, taken at different locations (represented by different line types) along the channel versus time.
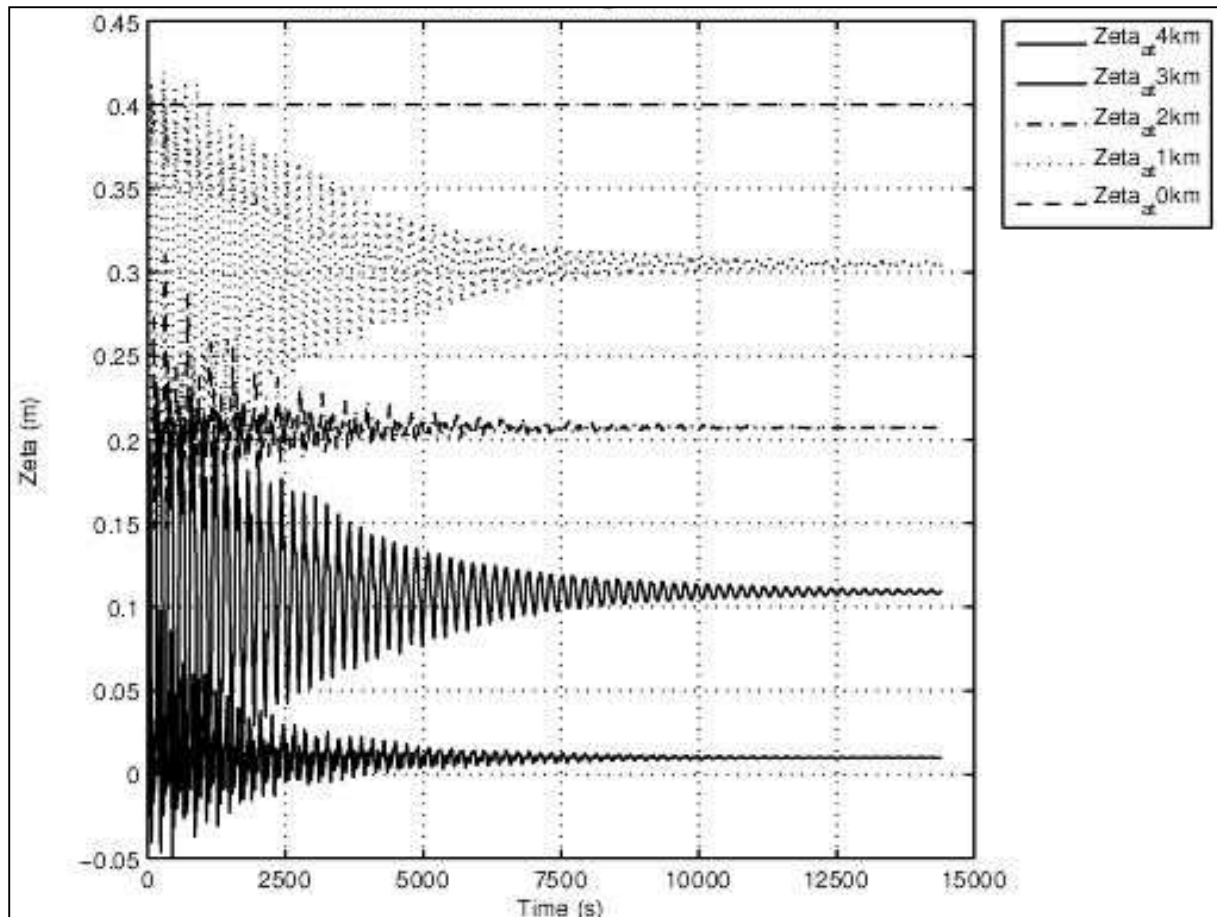
Figure 8: Sea-surface elevation numerical-convergence. Free surface elevation averaged width wise, taken at different locations (represented by different line types) along the channel versus time.

The following figures shows the steady solutions for u_h and η averaged width wise at t=14000s along the channel
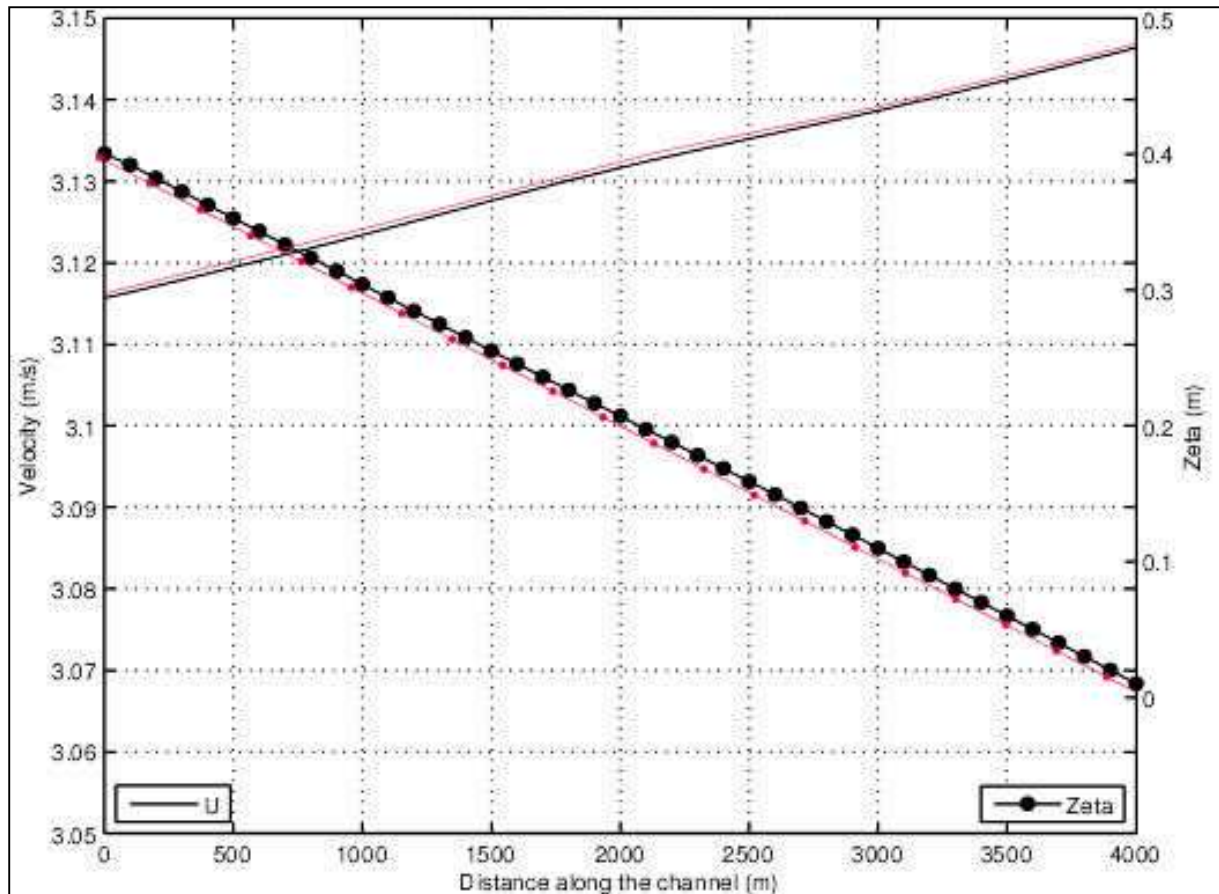
Figure 9: Depth averaged velocity (straight line) and sea-surface elevation (dotted line), both averaged width wise along channel, initial case. (In red the results from Bryden & Couch (2006))

The following figure shows the steady solutions for u_h and η averaged width wise at t=14000s along the channel in the case where the device array is implanted across the channel. The current turbine array has been placed at x=2000m (Figure 6).
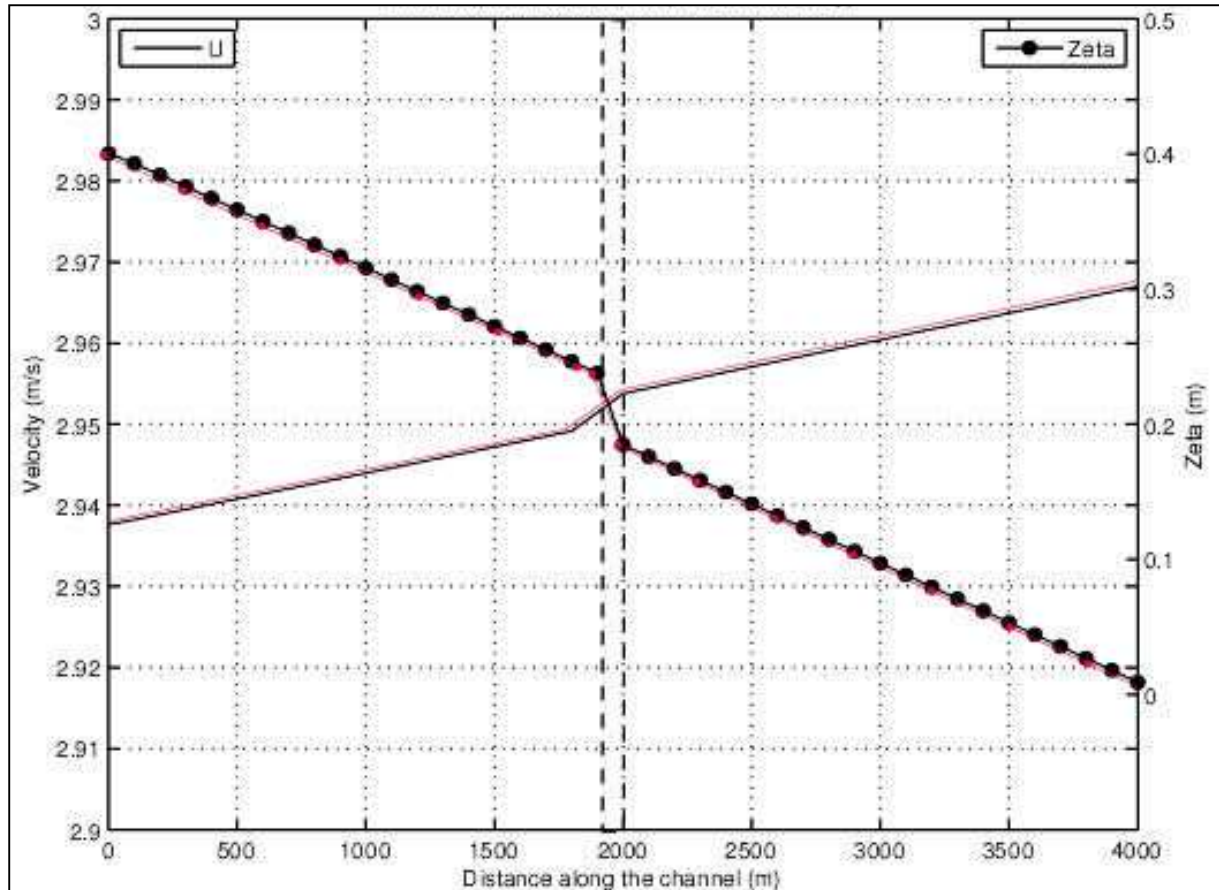
Figure 10: Depth averaged velocity (straight line) and sea-surface elevation (dotted line), both averaged width wise along channel, uniform array case. (In red the results from Bryden & Couch (2006), the dashed lines represent the device array location)

The results from ROMS show a very good agreement with the analytical results. Nonetheless, one expected an energy extraction equal to 10% of the apparent kinetic initial flux. On the contrary, the extraction is equal to 10% of the apparent kinetic modified flux, which is only 8.4% of the initial kinetic flux (Bryden & Couch, 2007). Bryden & Couch explained this counter-intuitive result lies in the fact than a natural flow possesses intrinsically both potential and kinetic energy and, furthermore, the alleged 10% energy extraction is partly balanced between these two energetic components (Bryden & Couch, 2004). Accordingly, a more accurate way to estimate the percentage of energy extracted by such devices would be to measure the change in the total energy, rather than the change in kinetic energy:

$$E_\% = \frac{\Delta E_{Tot,Corrected} \times 100}{E_{Kin,No\ device}} \tag{62}$$

Where:

- $E_{Kin,No\ device}$ kinetic energy available at the location of the intended device for the initial case
- ΔE_{Tot} difference of total energy before and after the device
- $\Delta E_{Tot,Corrected} = \Delta E_{Tot} - bottom\ friction\ loss$
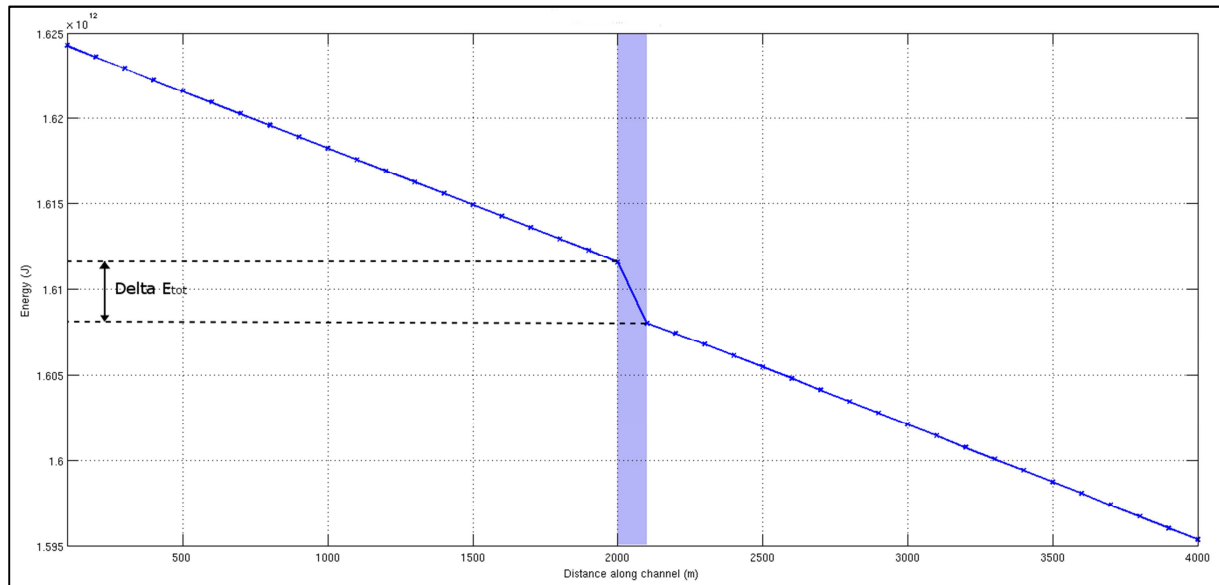
Figure 11: Total energy averaged width wise vs. distance along channel, uniform array case

With this method, $E_\%$ reaches the value of 18.39% which confirms Sutherland's conclusions: the assumption that the TCT array effects are uniform over the channel cross-section and consequently is unavoidable by the inflow, leads to an over-estimate of the real efficiency of the array (Sutherland et al., 2007).

In order to improve the numerical representation of the device array, instead of assuming the additional bottom shear stress as uniform across the channel, the depth averaged strip is split into several "block-turbines" separated by empty gaps.
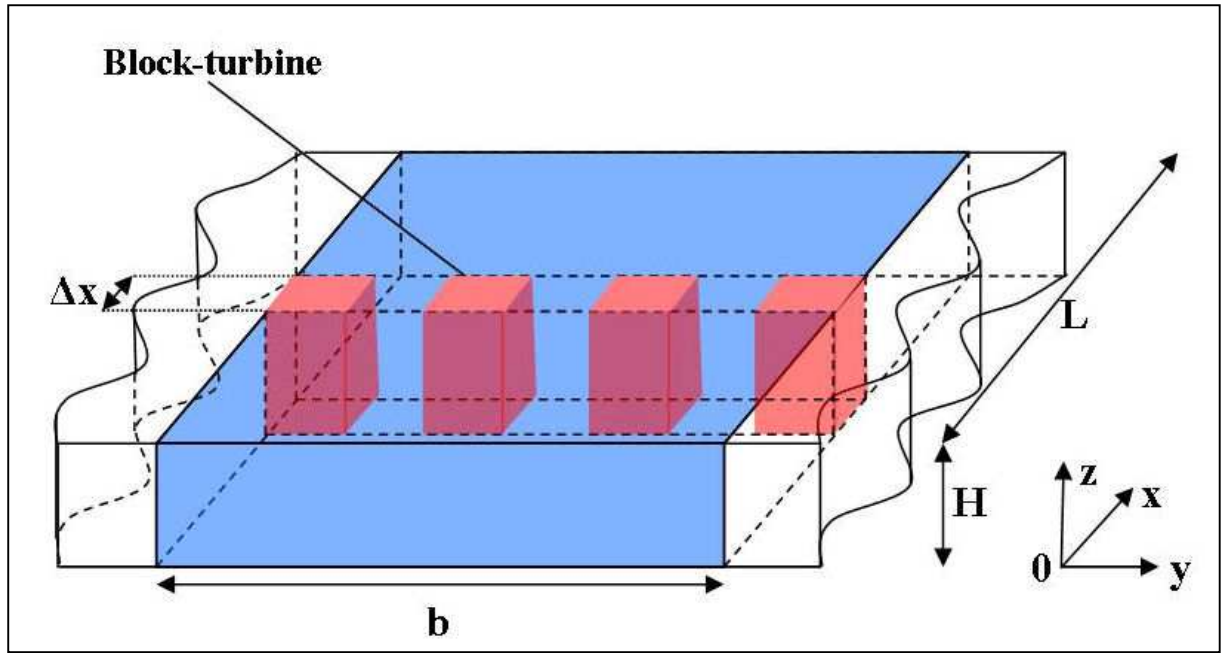
Figure 12: Block turbine case. Domain diagram

where $b = 1000\text{m}$, $L = 4000\text{m}$, $H = 39.6\text{m}$ and $\eta = \eta(x)$; $\begin{cases} \eta(0) = 0.4\text{m} \\ \eta(L) = 0\text{m} \end{cases}$. In addition, the additional shear stress of each block is weighted with a normalization coefficient N in order to extract the same quantity of kinetic energy from the flow as in the last two cases (Eq. (50)).

$$\tau_{add} = N \frac{1}{2} \rho \varsigma u_H^2 \frac{R}{\Delta x} \qquad (63)$$

The model is run with the same set of options as the former simulations. Although the depth and width averaged results for velocities and sea-surface elevation only differ from the uniform array case by an offset (Figure 13), the horizontal flow dynamics are totally different from the uniform case (Figure 14 & Figure 15).
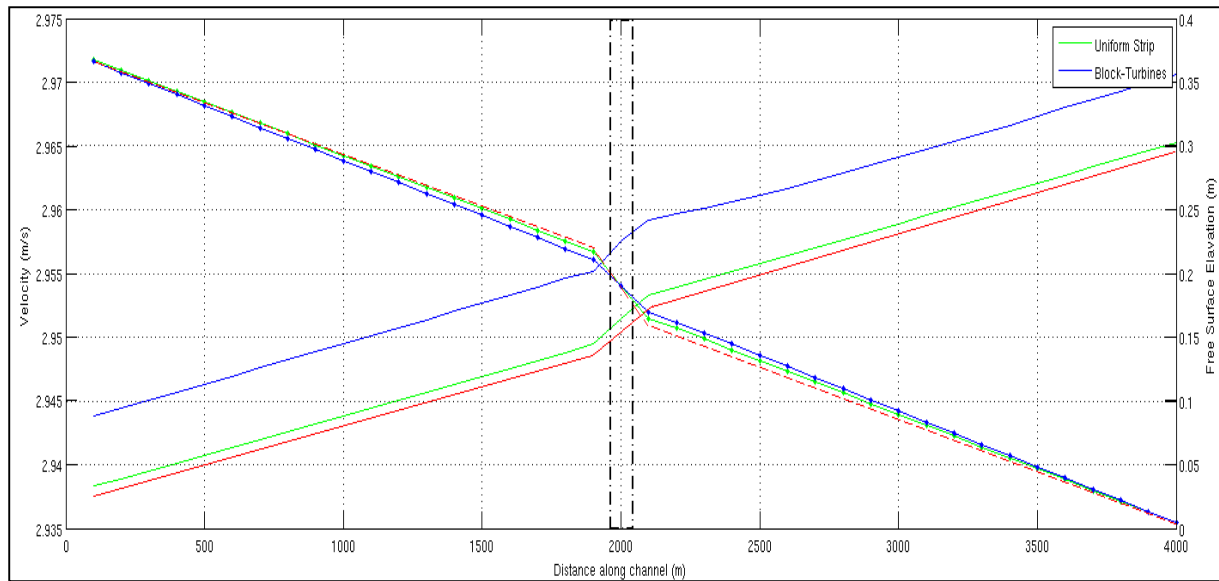
Figure 13: Depth averaged velocity (continuous lines) and sea-surface elevation (dashed lines) along channel for the uniform array case (red & green) and the block turbine case (blue). (In red the results from Bryden & Couch (2006))
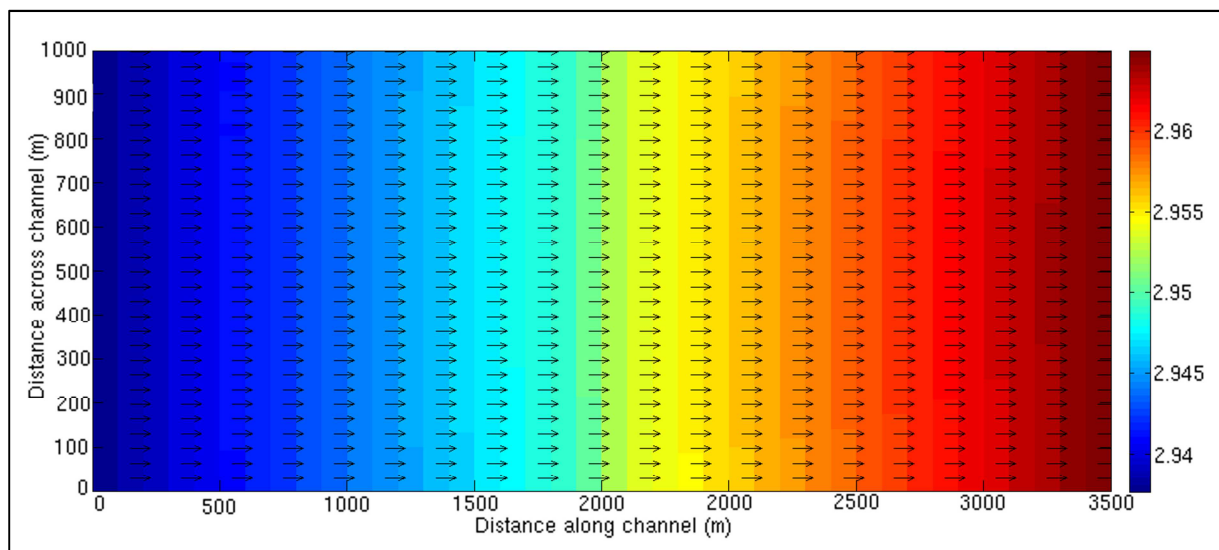
Figure 14: Flow velocity colour-map (bird eye view) for the uniform case
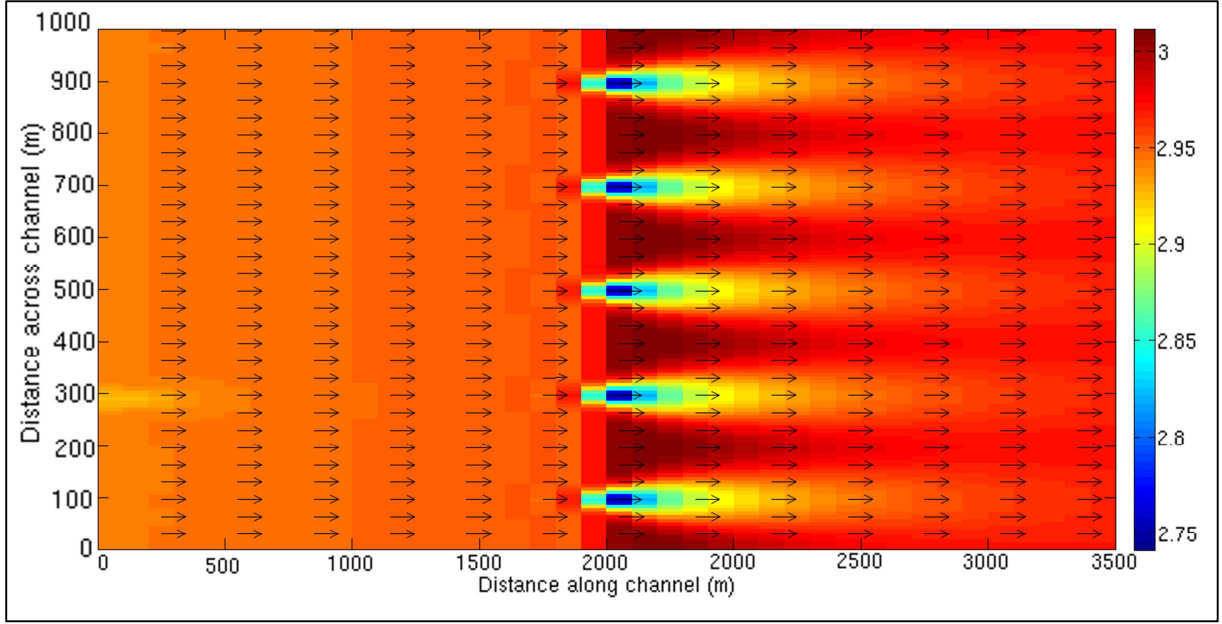
Figure 15: Flow velocity colour-map (bird eye view) for the block-turbine case

Here, contrary to the uniform array case, the velocities are neither uniform across the channel nor

only a function of the distance along

$$\vec{v}_{uniform\ array} = \begin{vmatrix} u(x).\overrightarrow{e_x} \\ 0 \end{vmatrix} \tag{64}$$

Furthermore, the $u(x)$ velocity component of the uniform array case seems to be composed of

three affine functions. In the block turbine case the velocity vectors can be expressed as:

$$\vec{v}_{block\ turbine} = \begin{vmatrix} u(x,y).\overrightarrow{e_x} \\ v(x,y).\overrightarrow{e_y} \end{vmatrix} \tag{65}$$

In addition, the horizontal mixing in ROMS is expressed as follows:

$$D(\vec{v}) = -\nabla.\zeta\overline{\vec{v}} \tag{66}$$

where $D(\vec{v})$ is the horizontal dissipation. As discussed in the section 3.1, two formulations of

horizontal dissipation have been implemented in ROMS commonly called harmonic and biharmonic

eddy viscosities or modes (Eq. (16) & (17)). According to the results, the horizontal mixing parameter

is not negligible but is a significant tuning parameter for the simulation:

$$\begin{cases} D(\vec{v}) = -\nabla.\zeta\vec{\overline{v}} \\ D(\vec{v}_{uniform\ array}) = 0 \\ D(\vec{v}_{block\ turbine}) \neq 0 \end{cases} \qquad (67)$$

To calibrate the parameters, it is crucial to know a priori the order of magnitude of ζ_M and ζ_{bi}^M (i.e.

Eq. (16) & (17)). According to Griffies & Hallberg the maximum values of these parameters can be

estimated as follows (Griffies & Hallberg, 2000):

$$\begin{cases} \zeta_M < \dfrac{[(\Delta x)^{-2} + (\Delta y)^{-2}]^{-1}}{2\Delta t} \\ \zeta_{bi}^M < \dfrac{[(\Delta x)^{-2} + (\Delta y)^{-2}]^{-1}}{4\Delta t} A_{M,max} \end{cases} \qquad (68)$$

where $\Delta x, \Delta y$ are horizontal spatial steps and Δt the time step.

Nonetheless this type of subgrid-scale mixing parameters should be validated against field or

laboratory measurements. As expected, the energy-extraction results are impacted by the change of

device numerical representation, due to the flow surging into the gaps left between the turbines.
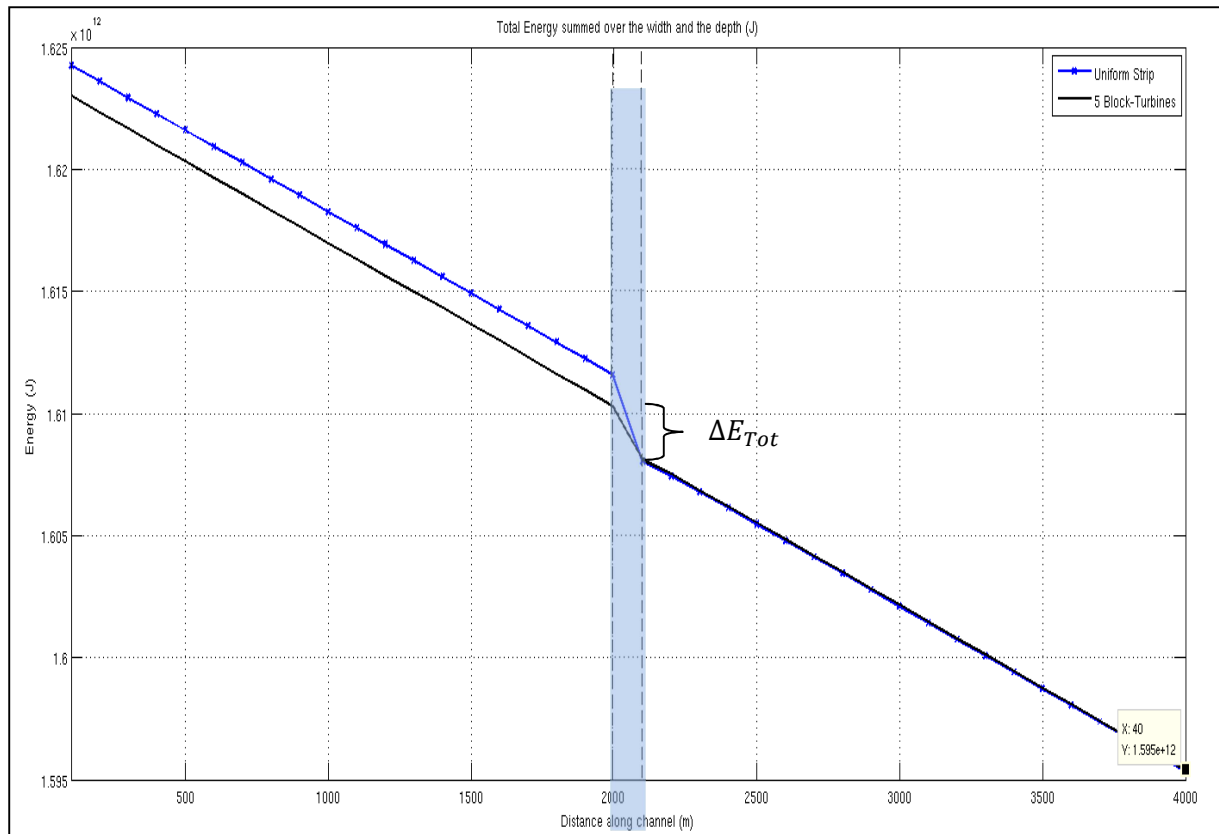
Figure 16: Total energy averaged width wise vs. distance along channel, comparison between uniform array case (blue line) and block turbine array (black line). (Uniform strip in blue; block-turbine in black)

Using the same formula as previously (eq. (62)), one can obtain a percentage of extracted energy of 8.33%. Despite the lack of in-situ validation, what really matters in this last simulation is the quantification of the energy difference between the two representations. With this width-characteristic type of representation, the yield estimation of the array has been divided by 2.2 which demonstrates the importance of the spatial representation of the device and the limit of resolving this problem via a 1-D representation. By extension, one wonders if the latter considerations of numerical representation ought to be applied depth wise as well. Additionally, one can think that the discrepancy between the energy yield of the two representation cases as well as the overestimation of the energy extraction in the first case, are consequences of the non-distinction between energy extracted & energy dissipated by sub-grid scale phenomenon (turbulence, eddies, mixing processes, etc) induced by the simplifications used for the latter turbine parameterizations. The only accurate

method to quantify the efficiency of a turbine is to accurately know the flow velocity distribution

over the area swept by the blades.
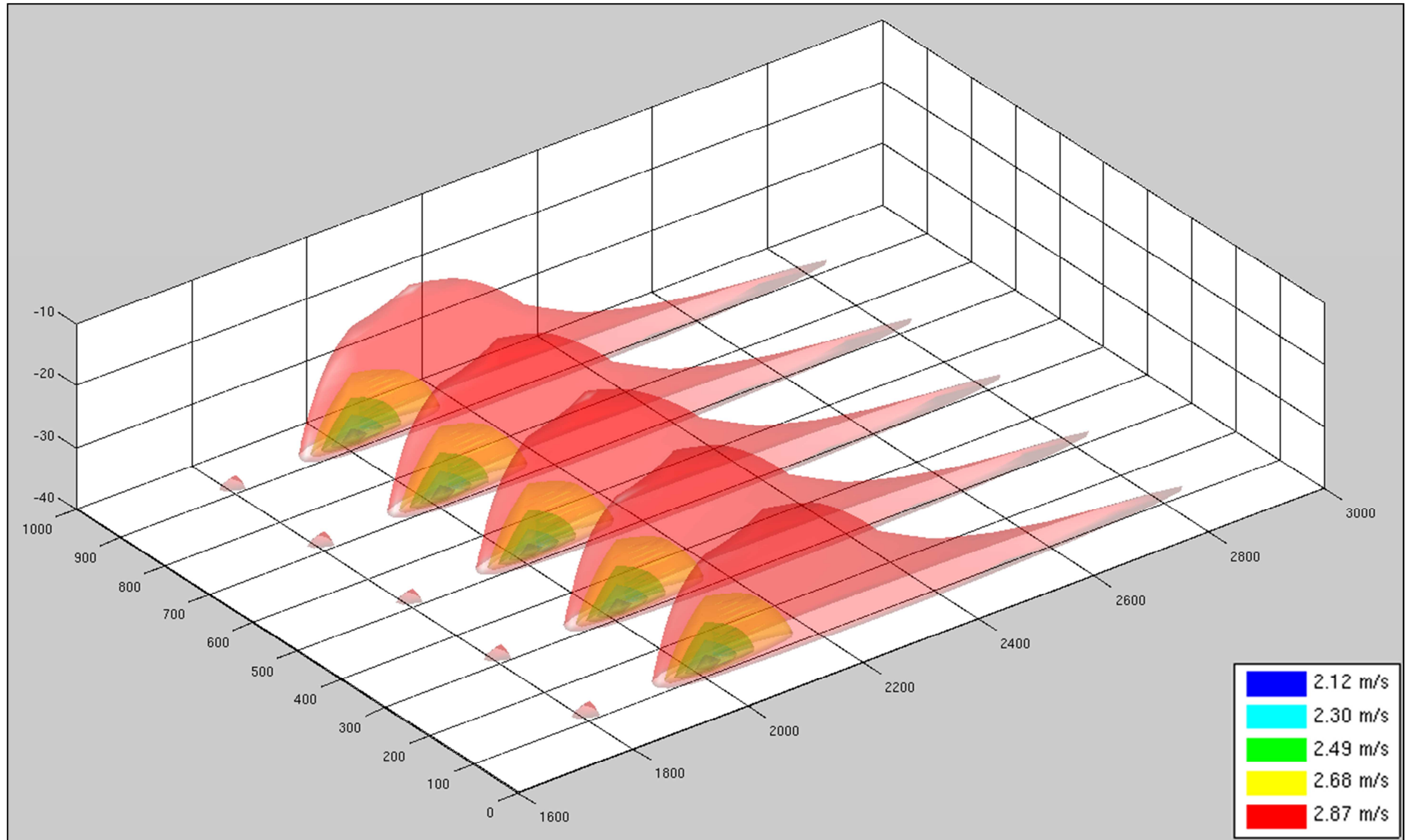
Figure 17: 3-D view, velocity iso surfaces, block turbine case. N.B.: from the highest velocity (red surface) to the lowest (blue surface)
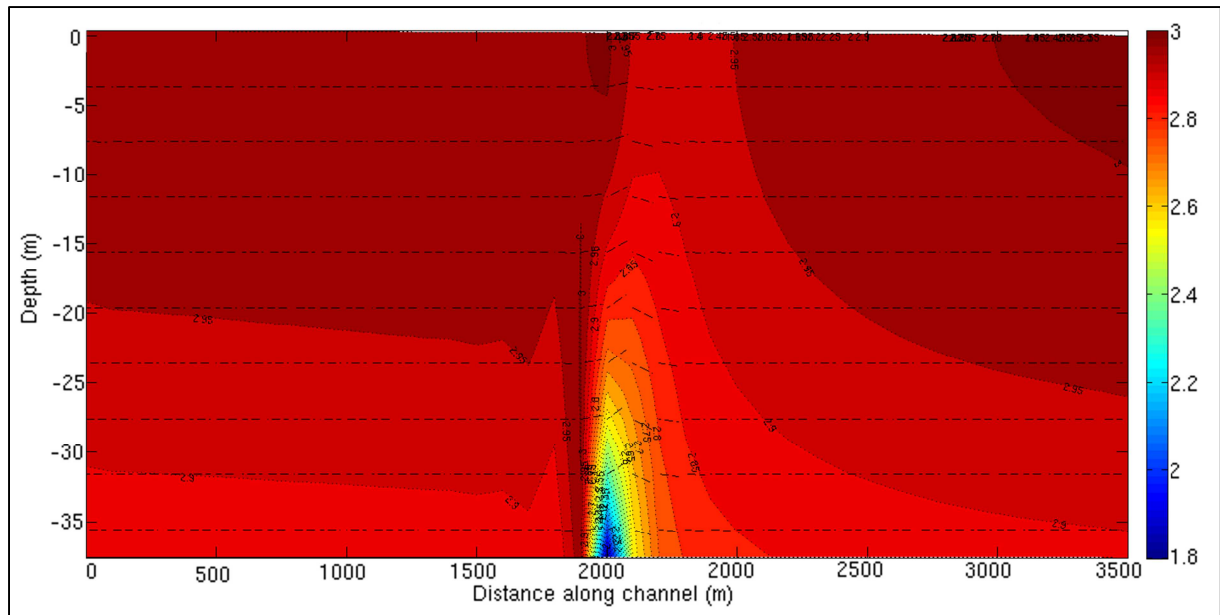
Figure 18: Cross-section of the flow velocity (m/s) along stream

Indeed, the depth characteristic flow dynamics associated with the extra bottom shear stress techniques further reveal their drawbacks. Here the deficit of velocity is concentrated at the bottom, because of the use of additional shear stress in the method, instead of being applied in the middle of the water column. As discussed by Sutherland, it is clear that realistic flow will by-pass above and beneath the turbine rotor (Sutherland et al., 2007). Consequently, a depth-characteristic method may be necessary to improve the energy-extraction assessment. Besides, as has been mentioned in the background chapter, hydrodynamic-impact assessments have to take into account the depth features of perturbed flows.

ROMS contains an option which allows expression of the bottom and surface shear stress as a body-force acting on the fluid. This option works in three steps for each depth level. First the user determines the thickness of the bottom and surface shear layer. Then it transforms the shear expression into a body-force expression and finally injects the latter force in the momentum balance. By mimicking this approach for a mid-depth shear layer in our implementation method, we modified ROMS in order to take into account a mid-depth body-force similar to the flow retarding force induced by a current turbine. From a theoretical point of view, energy extraction by a turbine can be

expressed as a sink of momentum. Let S_i be the momentum sink term in its general Cartesian expression:

$$S_i = \left\{ \begin{array}{c} -\left[\sum_{j=1}^{3} M_{1_{ij}} \mu v_j + \sum_{j=1}^{3} M_{2_{ij}} \frac{1}{2} \rho v_j \left| v_j \right| \right] \\ -[\quad (A) \quad + \quad (B) \quad] \end{array} \right. \tag{69}$$

Where:

- $(A) \equiv$ viscous loss term
- $(B) \equiv$ inertial loss term

According to Sun, for a homogenous porous media $M_{1_{ij}}$ and $M_{2_{ij}}$ can simplified as follows (Sun et al., 2008):

$$M_{1_{ij}} = \begin{bmatrix} \frac{1}{\alpha} & 0 & 0 \\ 0 & \frac{1}{\alpha} & 0 \\ 0 & 0 & \frac{1}{\alpha} \end{bmatrix} ; \ M_{2_{ij}} = \begin{bmatrix} C_D & 0 & 0 \\ 0 & C_D & 0 \\ 0 & 0 & C_D \end{bmatrix} \tag{70}$$

where $\alpha \equiv$ permeability and $C_D \equiv$ constant. In our cases several assumptions can be made. First, according to the geometry of the channel and the orientation of the turbine, S_i possess only one component in the x-direction:

$$S_x = -\left[\frac{\mu}{\alpha} u + \frac{1}{2} \rho C_D |u| u \right] \tag{71}$$

where $\mu \equiv$ dynamic viscosity. The next assumption is not far from the shallow water approximation:

$$\|u\| \cong \|v\| \gg \|w\| \tag{72}$$

This implies that the vertical velocity is only calculated through the continuity equation, the pressure variation and the vertical mixing parameterization. Another assumption is to consider the current turbine as a perforated plate as used in physical modelling. In this way, the viscous loss term (eq.(69)) is equal to zero:

$$S_x = -\frac{1}{2} \rho C_D |u| u \tag{73}$$

It's worth noticing that now the expression of S_x is analogous to a pressure drop or a quadratic drag force. According to Rethore, the coefficient C can be defined as a function of the induction factor and furthermore as a function of the thrust coefficient (Eq. (42)) (Réthoré et al., 2009). The most critical parameter in the sink momentum method defined above is the thrust coefficient C_T. The non-dimensional C_T coefficient featuring any turbine quantifies the upstream-directed force caused by the fluid passing through the virtually porous disc formed by the area swept by the turbine blades.

As highlighted by Polagye (2009), the length scale required to fully understand viscous flow dynamics over a rotating turbine are thousand times smaller than the length scale required to fully understand the potential impacts which might be generated by array of turbines on realistic tidal sites. Therefore, large scale ocean circulation models appear to be the best suited for such investigation. Nonetheless, it has been shown that nonlinear sub-grid scale effects linked to turbine induced turbulence may have non negligible impacts on a large scale (Ahmadian et al., 2012; Thyng, 2012; MacLeod et al., 2002). Moreover, this section shows that simplistic turbine representations lead to unrealistic impact assessment and do not permit accurate resource assessment. As TCT layout optimization requires both accurate impact and resource assessments, it seems clear that the best approach is to inject a mid-depth TCT representation coupled with a sub-grid scale effect parameterization into an ocean circulation model in order to tackle all the issues involved. The following two sections describe such model adaptation.

4.2. Model Modifications

As discussed in Sections 3.2 and 3.3, from a regional scale standpoint, the hydrodynamic perturbations of TCTs can be split in two main components: the momentum balance as represented by the actuator theory (Eq. (74)) and the turbulence balance which will be accounted for in this work by appropriate turbulence-correction terms (Eq. (81)). In the development presented here, several simplifications are made. Firstly, the device supporting structure and its related effects on the flow are neglected. Secondly, the rotor-disc orientation is taken to be normal to the incoming flow. Thus,

the retarding force $\overrightarrow{F_t}$ is always applied in the same direction as the flow, thus equation (43) can be simplified to:

$$\overrightarrow{F_t} = -\frac{1}{2}\rho A_d C_t(|u_\infty|u_\infty).\vec{n} \tag{74}$$

Accordingly, at the rotor-disc location and within the current frame of simplifications, ROMS momentum equation systems (Eq. (29)) are modified as follows:

$$\begin{cases} \dfrac{\partial u}{\partial t} + \vec{v}.\nabla u - fv = -\dfrac{\partial \varphi}{\partial x} - \dfrac{\partial}{\partial z}\left(-K_M\dfrac{\partial u}{\partial z} - v\dfrac{\partial u}{\partial z}\right) + \zeta\left(\dfrac{\partial^2 \bar{u}}{\partial x^2} + \dfrac{\partial^2 \bar{v}}{\partial y^2}\right) + F_t \\[2mm] \dfrac{\partial v}{\partial t} + \vec{v}.\nabla v + fu = -\dfrac{\partial \varphi}{\partial y} - \dfrac{\partial}{\partial z}\left(-K_M\dfrac{\partial v}{\partial z} - v\dfrac{\partial v}{\partial z}\right) + \zeta\left(\dfrac{\partial^2 \bar{v}}{\partial x^2} + \dfrac{\partial^2 \bar{u}}{\partial y^2}\right) \\[2mm] \dfrac{\partial u}{\partial x} + \dfrac{\partial v}{\partial y} + \dfrac{\partial w}{\partial z} = 0 \\[2mm] \dfrac{\partial \varphi}{\partial z} = -\dfrac{\rho g}{\rho_0} \end{cases} \tag{75}$$

One can notice that $\overrightarrow{F_t}$ has been defined as a function of the unperturbed flow speed $\overrightarrow{u_\infty}$ although this force is applied at the location of the turbine blades. Therefore, in order to account for the real nature of the flow perturbation as well as for the sake of implementation, $\overrightarrow{F_t}$ should be defined as function of the flow velocity at the disc location $\overrightarrow{u_d}$. The unperturbed flow speed, $\overrightarrow{u_\infty}$, can be expressed as follows:

$$u_\infty = \frac{u_d}{(1-a)} \tag{76}$$

In this manner the thrust force $\overrightarrow{F_t}$ can be rewritten as follows:

$$\overrightarrow{F_t} = -\frac{1}{2}\rho A_d C_t \frac{|u_d|u_d}{(1-a)^2}.\vec{n} \tag{77}$$

As shown in Hansen et al. (2000), equations (42) and (45) lead to the following expression of the induction factor:

$$a = \frac{1}{2}\left(1 - \sqrt{1 - C_t}\right) \tag{78}$$

Using Eq. (42) and (78), Eq. (77) then becomes:

$$\overrightarrow{F_t} = -\frac{1}{2}\rho A_d\left(4 \times \frac{1 - \sqrt{1 - C_t}}{1 + \sqrt{1 - C_t}}\right)|u_d|u_d.\vec{n} = -\frac{1}{2}\rho A_d C_D|u_d|u_d.\vec{n} \tag{79}$$

where C_D is related to C_t through:

$$C_D = 4 \times \frac{1 - \sqrt{1 - C_t}}{1 + \sqrt{1 - C_t}} \tag{80}$$

As for the turbulence correction terms described in Section 3.3, they required some transformations before being injected in the GLS closure of ROMS. Indeed in their respective sources, S_d, S_p and S_ψ have been developed for either $k - \varepsilon$ or $k - \omega$ closure models and therefore needed to be adapted to fit within the GLS framework. In this way, the user has the option to switch to any kind of 2-equation closure model on demand. Accordingly the three turbulence correction terms are expressed as follows:

$$\begin{cases} S_k = C_p \dfrac{u^3}{\Delta x} - C_d \dfrac{u.k}{\Delta x} = S_p - S_d \\ S_\psi = C_\psi \dfrac{P^2}{\varepsilon} \end{cases} \tag{81}$$

These correction terms, are injected in the GLS closure of ROMS (Eq. (22) & (23)) at the disc location.

$$\begin{cases} \dfrac{\partial k}{\partial t} + \bar{\vec{v}}.\nabla k = \dfrac{\partial}{\partial z}\left(\dfrac{\nu_t}{\sigma_k}\dfrac{\partial k}{\partial z}\right) + P + B - \varepsilon + S_k \\ \dfrac{\partial \psi}{\partial t} + \bar{\vec{v}}.\nabla \psi = \dfrac{\partial}{\partial z}\left(\dfrac{\nu_t}{\sigma_\psi}\dfrac{\partial \psi}{\partial z}\right) + \dfrac{\psi}{k}(c_1 P + c_3 B - c_3 \varepsilon F_{wall} + S_\psi) \\ \varepsilon = \left(c_\mu^0\right)^{3+\frac{p}{n}}k^{3-2+\frac{m}{n}}\psi^{-\frac{1}{n}} \; ; \; \psi = \left(c_\mu^0\right)^p k^m l^n \end{cases} \tag{82}$$

4.3. Numerical Implementation

In order to implement these physical terms into ROMS, several mathematical and numerical adaptations had to be performed. To illustrate these adaptations, consider the case of an orthonormal grid in which the device is defined over a single grid cell-volume (Figure 19).
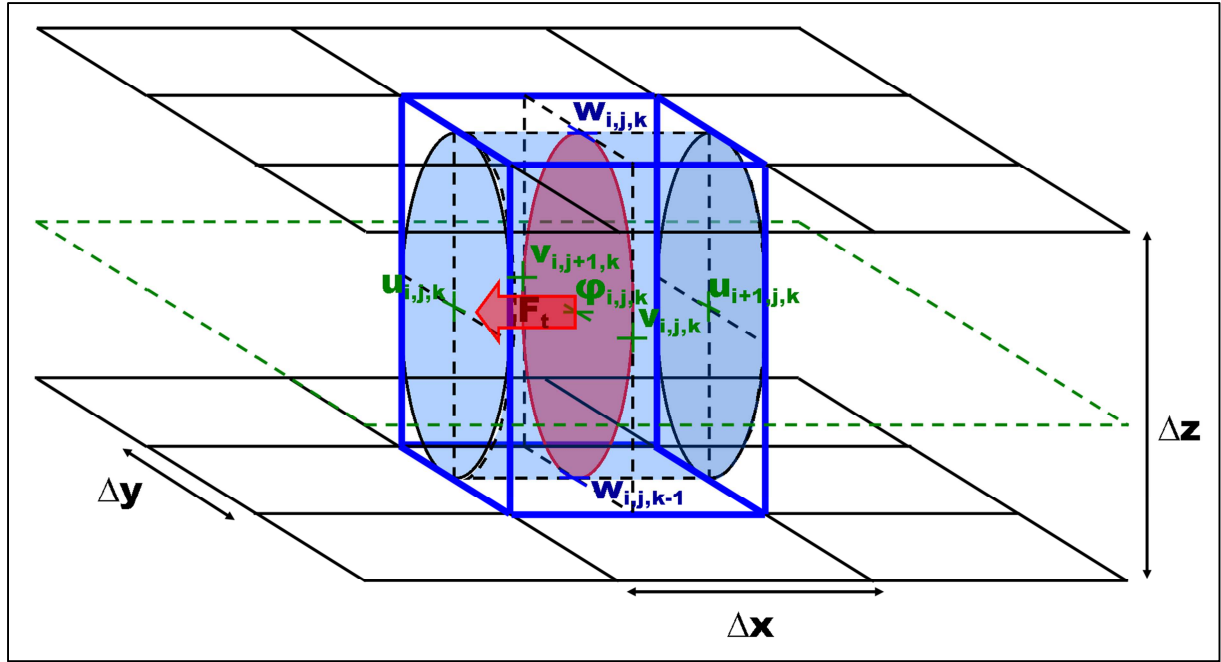
Figure 19: Staggered Grid & Control Volume. The diagram displays staggered horizontal grids at the z_w (N, N+1) levels (black lines), the z_p (N) level (green dashed plane), the actuator disc (red surface), the "smeared" actuator cylinder (light blue volume), the numerical control volume (heavy blue solid lines) and its median planes (dashed black lines). It also displays spatial distribution on ROMS 3-D staggered grid of the velocity components (u,v,w) and the turbulence point (φ).

On such a staggered grid, the components of the flow-velocity (u,v,w) and the turbulent quantities (TKE, TLS) are computed at different locations; the latter being located at the φ-points. For the sake of generalization and further development, the centre of the "real" rotor disc is positioned on a φ-point (i.e. red disc on Figure 19) and thus surrounded by the flow-velocity points. However in ROMS' code, the body-force $\vec{F_t}$ can only be defined on the u/v points and, in this case, more precisely on the u points since $\vec{F_t}$ is aligned with the incoming flow-velocity vector. In other terms, the staggered grid implies that the thrust force is transformed into pressure jumps at each surrounding cell face, namely at the upstream and downstream u-points. Equation (83) ensures the equivalence between the pressure discontinuities and the related force density present in the control volume.

$$\iiint_V \vec{F'}\, dV = \iint_S p\, dS\vec{n} \tag{83}$$

A simplified Rhie-Chow numerical scheme (Réthoré & Sorensen, 2008) is used to calculate the distribution of the force over the neighbouring cells.

61

$$\overrightarrow{F'_{i,J,k}}\Delta V_{i,j,k} = \frac{1}{2}\sum_{j}^{j+1} p_{i,j,k} S_{i,j,k} \overrightarrow{n_{i,J,k}} \tag{84}$$

Here, $\overrightarrow{F'_{i,J,k}}$ symbolizes the force density (N. m^{-3}), $\Delta V_{i,j,k}$ the volume of the control volume (m^3) (i.e. $\Delta V_{i,j,k} = \Delta x \times \Delta y \times \Delta z$)), $\overrightarrow{n_{i,J,k}}$ the normal vector to the cell face, $S_{i,j,k}$ the vertical cell surface (m^2) and $p_{i,j,k}$ the dynamic pressure at the vertical cell surface (N. m^{-2}). The pressure jump, p, corresponds to the dynamic pressure exerted by a moving fluid of velocity $\vec{v}$ on a blocking surface and can be expressed as follows:

$$p = -\frac{1}{2}\rho C_D |\vec{v}| \vec{v}.\vec{n} \tag{85}$$

where C_D is the drag coefficient derived from Eq. (79). Equation (84) gives the following final split expression:

$$\overrightarrow{F'_{i,J,k}}\Delta V_{i,j,k} = \begin{cases} -\frac{1}{4}\rho C_D S_{i,j,k}\left(\sum_{j}^{j+1} u_{i,j,k}|u_{i,j,k}|\right)\overrightarrow{n_{i,J,k}} \; ; \; at \; the \; upstream \; u-point \\[2ex] -\frac{1}{4}\rho C_D S_{i,j,k}\left(\sum_{j-1}^{j} u_{i,j,k}|u_{i,j,k}|\right)\overrightarrow{n_{i,J,k}} \; ; \; at \; the \; downstream \; u-point \end{cases} \tag{86}$$

This implementation has an additional advantage. By splitting the pressure discontinuity generated by the presence of the device into two pressure jump contributions at the two cells adjacent faces, numerical "pressure wiggles" (Réthoré & Sorensen, 2008) may be avoided. However, $\overrightarrow{F'}$ is not the same as the original thrust force $\overrightarrow{F_t}$.

Although they are both body-forces, $\overrightarrow{F'}$ results from the integration of the numerical force density over the control volume ΔV whereas $\overrightarrow{F_t}$ results from the integration of the drag and lift forces over the volume swept by the turbine's blades (Sorensen & Shen, 2002). This volume of integration correspond to the actuator disc surface multiplied by the apparent width of the turbine blades, W. The apparent width can be expressed in function of the blade chord length, L_{chord}, and the blade pitch angle, θ as follows

$$W = L_{chord} \sin\theta \tag{87}$$

62

4.3. Numerical Implementation

Consequently, in order to be consistent with the original thrust force, irrespectively of the width of the numerical control-volume Δx, $\overrightarrow{F'}$ must verify the following equation:

$$\overrightarrow{F_t}\left(\frac{\pi D^2}{4}W\right) = \overrightarrow{F'}\left(\frac{\pi D^2}{4}\Delta x\right) \tag{88}$$

In equation (88), D is the rotor diameter (m). In this manner and by introducing the drag coefficient from Eq. (79), the equivalence between the original thrust force and the smeared numerical force is respected:

$$\overrightarrow{F'_{i,j,k}}\Delta V_{i,j,k} = \begin{cases} -\dfrac{L_{chord}\,sin\,\theta}{4\Delta x}\displaystyle\sum_{j}^{j+1}\overrightarrow{n_{i,j,k}}\,S_{i,j,k}\rho C_D u_{i,j,k}|u_{i,j,k}| \;;\; at\ the\ upstream\ U\ point \\[2em] -\dfrac{L_{chord}\,sin\,\theta}{4\Delta x}\displaystyle\sum_{j-1}^{j}\overrightarrow{n_{i,j,k}}\,S_{i,j,k}\rho C_D u_{i,j,k}|u_{i,j,k}| \;;\; at\ the\ downstream\ U\ point \end{cases} \tag{89}$$

This final formulation is implemented in the "right hand side" (i.e. rhs, Figure 2) of ROMS resolution scheme.

Because of the volumetric implementation method required by the ROMS grid structure, the set of parameters (C_p, C_d, C_ψ), components of the turbulence correction terms (i.e. Eq. (81) and (82)), turns out to be weighted according to the control volume dimensions, as it is the case for $\overrightarrow{F'}$ (i.e. Eq. (89)), and equivalent to Eq. (90):

$$\begin{cases} C_p = C_1\left(C_{pw}\dfrac{L_{chord}\,sin\,\theta}{\Delta x}\right) \\[1.2em] C_d = C_2\left(C_{pw}\dfrac{L_{chord}\,sin\,\theta}{\Delta x}\right) \\[1.2em] C_\psi = C_3\left(C_{pw}\dfrac{L_{chord}\,sin\,\theta}{\Delta x}\right)^2 \end{cases} \tag{90}$$

The relationships between C_d, C_p, C_ψ and $\left(C_{pw}\dfrac{L_{chord}\,sin\,\theta}{\Delta x}\right)$ as well as the magnitude of C_{pw} result from an empirical approach based on the different validation tests performed during the development of the present method (i.e. Sections 5.3.1, 5.3.2, 5.3.4 and Chapter 8). Issuing from this development phase, C_{pw} has been seen to be able to be represented as a function of the design feature C_t as suggested by Réthoré (2009).

$$C_{pw} = C_t \sqrt{1 - C_t} \tag{91}$$

Interestingly and in accordance with the definition of the induction factor and Eq. (45), a parallel can be drawn between C_{power} and C_{pw} since:

$$C_{power} = C_t \frac{U_d}{U_\infty} \; ; \; C_{pw} = C_t \frac{U_w}{U_\infty} \tag{92}$$

The coefficients C_1, C_2 and C_3, however, are given by Réthoré (2009) and Rados *et al.* (2009) yet might be subject to adaptation under specific device design characteristics.

Regarding the integration of the turbulence correction terms (Eq. (82)) on the ROMS grid, the turbulence quantities are computed at the φ-points (Figure 19). Consequently, the volume where the correction terms are injected is bounded by the neighbouring cells faces. As a result of this compulsory volume smearing, the issue raised by Sanz (2002) of delimiting the volume of application of the turbulence balance correction is avoided. The implementation scheme of the three turbulence correction terms (Eq. (81)) can then be expressed as:

$$\begin{cases} S_{k_{i,j,k}} = C_p \dfrac{\left(\frac{1}{2} \left| u_{i+1,j,k} + u_{i,j,k} \right| \right)^3}{\Delta x} - C_d \dfrac{\frac{1}{2} \left| u_{i+1,j,k} + u_{i,j,k} \right| k_{i,j,k}}{\Delta x} = S_{p_{i,j,k}} - S_{d_{i,j,k}} \\ S_{\psi_{i,j,k}} = C_\psi \dfrac{P_{i,j,k}^2}{\varepsilon_{i,j,k}} \; ; \end{cases} \tag{93}$$

where $S_{i,j,k}$ represents the turbulence production by vertical shear (Umlauf et al., 2003) and C_p, C_d and C_ψ come from Equation (90). It is worth noting that the weight applied on S_ψ (i.e. C_ψ) has been empirically validated during the validation and grid-dependency test series which will be presented in the next chapters. The final formulation (Eq. (93)) is implemented in the corrector step of ROMS resolution scheme (Figure 2). The set of $\left(\overrightarrow{F'_{i,j,k}}, S_{p_{i,j,k}}, S_{d_{i,j,k}}, S_{\psi_{i,j,k}} \right)$ constitutes the core of the TCT modeling adaptation implemented in ROMS.

In practice, defining the volume control $\Delta V_{i,j,k}$ as a one cell-cube is too coarse and would generate information loss. Representation of the "rotor cylinder" in the structured grid of ROMS, as shown in Figure 20, is dependent of the grid resolution and will never perfectly match the cylindrical volume. However, after a certain numerical resolution threshold, the resulting discrepancies

between finer resolutions induced by the volume approximation can be neglected as demonstrated

in Section 5.3.1.
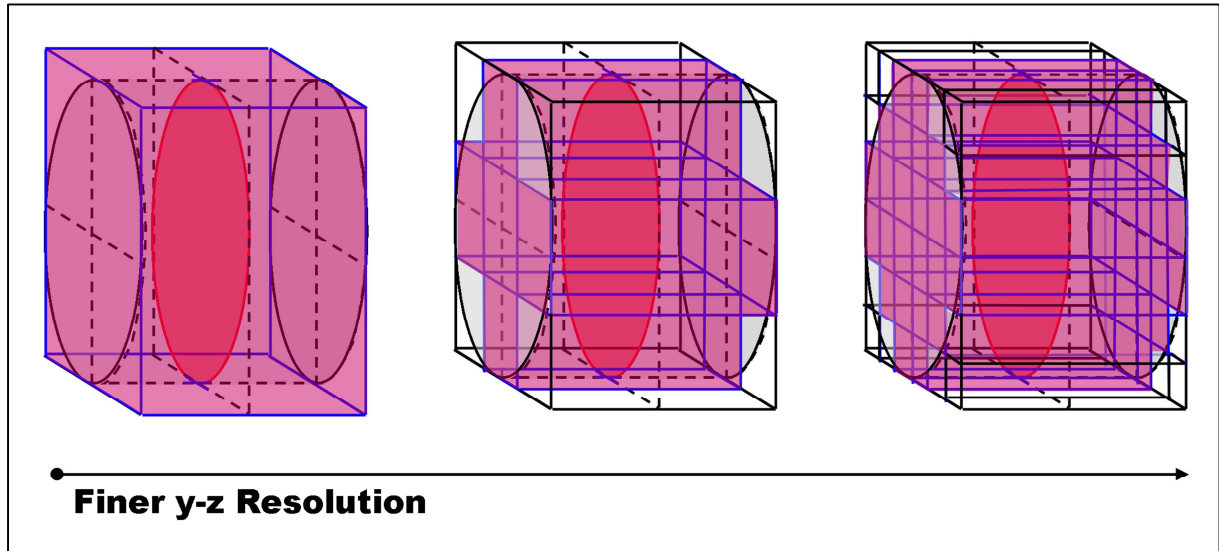
Figure 20: Comparison between numerical control-volume approximations (red volumes) for finer and finer y-z resolutions (left to right) with the exact "smeared" control volume (grey cylinder). The red disc represents the actuator disc.

Chapter 5. Validation-Standalone Device

5.1. Introduction – Validation Phase

This section aims to confront the proposed model with series tests based on a single device deployment. Being able to reproduce accurately flow dynamics perturbed by the presence of a standalone device is key in the development of a numerical tool for TCT array layout optimization. It will condition device interactions within TCT farm and, down the line, resource and impact assessment accuracy. Accordingly, reproduction of a single device deployment in a channel with the proposed model has been performed. Since such in-situ data are not available at the moment, physical scale model experiments from referenced articles have been exploited to constitute the reference data base. In addition, simulations of this standalone device system have been used to test the numerical consistency of the implementation used to inject the proposed TCT representation into ROMS. In summary, standard numerical tests as well as reproduction of referenced physical model results constitute the core material of the validation phase for the proposed TCT representation. In sequence, this section overviews grid dependency tests, time dependency tests, comparison between experimental and simulated results of turbine induced effects on flow momentum and turbulence as well as sensitivity tests to C_t variations.

5.2. Simulation Features and Benchmarks

In order to validate the capability of the proposed TCT modelling method, a comparison between physical scale model and numerical model results has been conducted. The reference physical scale model is described by Myers and Bahaj (2010) and was used by Harrison *et al.* (2009)

as reference data to evaluate the performance of CFD simulations. The experimental features of this flume test are:

- A rectangular channel with a 21000 mm long (L), 1350 mm wide (l) and 300 mm deep (h) working section

- Turbine represented by a 100 mm diameter (d) perforated disc with a porosity corresponding to C_t=0.86

- A constant, depth-averaged inflow of 0.33 m/s whose vertical profile closely matches a (1/7)th power law.

- Bottom roughness length of approximately z_0=8 mm
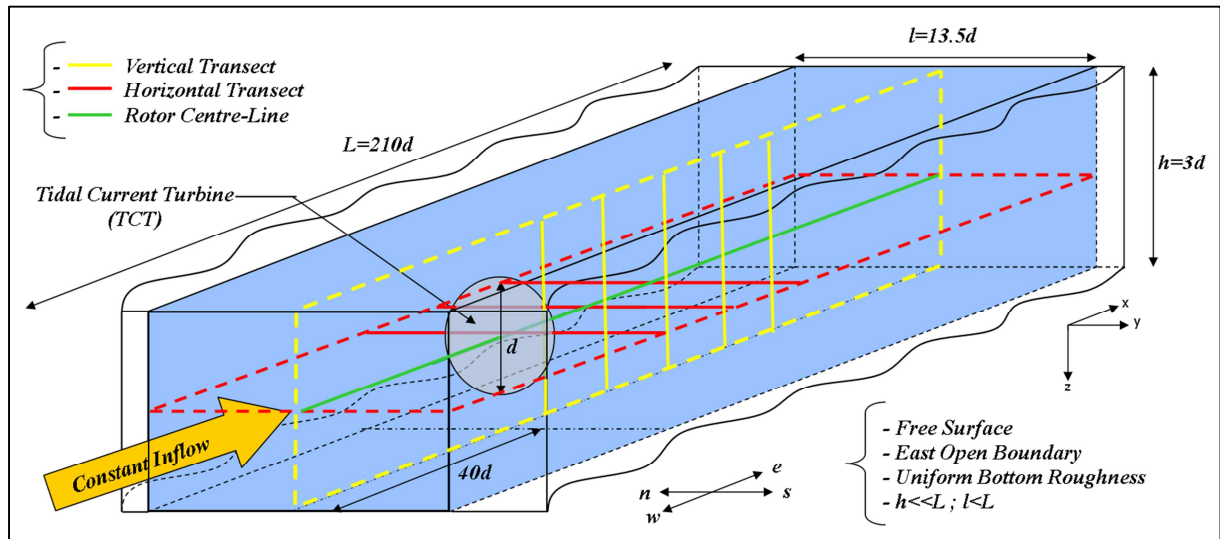
Figure 21: Idealized channel, centre-line, profile and transect locations. This conceptual diagram represents the validation test geometry and dimensions as well as the locations where measurements have been taken.

The numerical grid used for the flume simulation has 420 grid cells in the stream wise direction (equivalent to $\Delta x = 0.05m$ ($\frac{D}{2}$)), 67 grid cells in the cross-stream direction (corresponding to $\Delta y \approx 0.02m$ ($\frac{D}{5}$)) and 30 vertical levels in the grid which are linearly distributed in sigma space in the vertical (equivalent to $\Delta z = 0.01m$ ($\frac{D}{10}$)). Specific grid features for the grid dependency tests are described in §5.3.1. A constant, depth-averaged inflow of 0.33 m/s is imposed at the upstream channel boundary and the free-surface elevation at the downstream boundary is held at 0 m. A free-surface radiation condition, 2D momentum Flather condition and 3D momentum radiation condition are applied on the upstream open boundary; a free-surface clamped condition, 2D momentum

reduced-physics condition and 3D momentum radiation condition are used for the downstream open boundary (Carter & Merrifield, 2007); free-slip conditions are applied on the lateral walls. The model ran until the results indicated that a steady state had been achieved, namely when model averages of velocity, TKE and free surface elevation, taken at the device location, varied by less than 0.1% from one time step to the next. The time step used for the simulation meets CFL (Courant-Friedrichs-Lewy) criterion. It has been verified that using a shorter time step does not change the steady state solution. The simulations have been computed in parallel on 8 processors of 2.5 GHz clock-rate using Message Passing Interface (MPI) libraries. With this set-up, on average, it takes around 6 minutes, real time, for the simulations to reach a steady state.

Prior to model-data comparisons, the simulation results had to be interpolated on a regularly spaced orthogonal grid equivalent to that for which observations were collected. The preferred metric for validation was turbine wake recovery. A conventional method to characterize wake recovery is the rotor velocity deficit $U_{deficit}$ (Eq. (94)).

$$U_{deficit} = 1 - \frac{U_w}{U_\infty} \tag{94}$$

This non-dimensional number is a function of the ratio between free-stream flow velocity U_∞ and the wake velocity U_w, both measured at equivalent vertical and lateral locations in the channel. Direct flow velocities are also used to characterise the momentum behaviours. TKE (or k) and the turbulence intensity (TI) have been chosen as the benchmark quantity for turbulence behaviours (Eq. (95) & (96)). It is worth noting that the TI data have been derived from velocity measurements collected with a conventional Doppler velocimeter (Eq.(95)):

$$TI = \frac{\left(\frac{1}{3}(u'^2 + v'^2 + w'^2)\right)^{\frac{1}{2}}}{(U^2 + V^2 + W^2)^{\frac{1}{2}}} \tag{95}$$

whereas the simulated TIs derive from the simulated k and U (Eq.(97)).

$$TI = \frac{\sqrt{\frac{2}{3}k}}{U} \tag{96}$$

5.2. Simulation Features and Benchmarks

In order to examine the accuracy of the simulation in three dimensions, horizontal and vertical transects have been made at different locations downstream of the turbine (Figure 21). Diagnostic focus is placed on velocity deficits along the rotor-centre line (Figure 23, Figure 24, Figure 26 and Figure 27) although spatial distributions are also examined (Figure 28 and Figure 29). The centre line is defined as the horizontal line normal to the rotor disc passing through its centre. Notice that both reference flume conditions (Figure 22) and velocity deficits along the centre line (Figure 27) are taken from Myers and Bahaj (2010) whereas both reference velocity deficit and TKE horizontal transects and vertical profiles (Figure 26, Figure 28, Figure 29, Figure 30, and Figure 32) are taken from the appendix of Harrison *et al.* (2009). Statistical approaches have been used to assess the accuracy of the numerical method used to replicate the experimental results. The correlation between the reference and simulated data has been investigated by using the standard Pearson product-moment correlation coefficient r^2. The error of magnitude between the physical experiment and simulated values is estimated differently depending if the investigated quantity, q, is normalised (i.e. $U_{deficit}$ & TI) or not (i.e. flow velocity & TKE). In the case of normalised quantities, the root mean square error percentage is then divided by the amplitude of the considered quantity %$_{Nrmse}$ (Eq.(97)).

$$\%_{Nrmse} = \frac{\sqrt{\frac{1}{n}\sum_{i=1}^{n}(X_i - \bar{X})^2}}{X_{max} - X_{min}} \times 100 \tag{97}$$

In the case of non-normalised quantities, q, the root mean square error percentage is then divided by the mean of the considered quantity %$_{Nrmse}$ (Eq. (98)).

$$\%_{Nrmse} = \frac{\sqrt{\frac{1}{n}\sum_{i=1}^{n}(X_i - \bar{X})^2}}{\frac{1}{n}\sum_{i=1}^{n}X_i} \times 100 \tag{98}$$

The first step of the simulation phase was to reproduce the flume conditions without any device deployed in order to obtain the best fit with the experimental data. Several initial inputs, such as the bottom roughness height and the minimum value of specific TKE, had to be set empirically. Notice that discrepancies in model data comparisons arise from locations where the experimental data deviate from smooth profiles (Figure 22). The values of correlation coefficients and error

5.2. Simulation Features and Benchmarks

percentages for both velocity and TI reached for this simulation (namely $r^2 = 0.77$ with $\%_{Nrmse} \cong$ 3.5% for the velocity and $r^2 = 0.88$ for TI $\%_{Nrmse} \cong 10.0\%$) give insight into what level of confidence can be expected for the simulated results but also on the overall uncertainty carried by the physical experiment data performed in the Chilworth flume of the University of Southampton for both momentum and turbulence quantities. Additionally, using a logarithmic analysis of uncertainty propagation applied on the Eq. (96), one can expect $\%_{Nrmse} \cong 17.0\%$ as a satisfying error level for TKE values derived from TI measurements. It is worth noting that, in Figure 22, both experimental and simulated vertical profiles of background flow velocity and turbulence intensity have been measured at channel mid-width and averaged along the channel length.
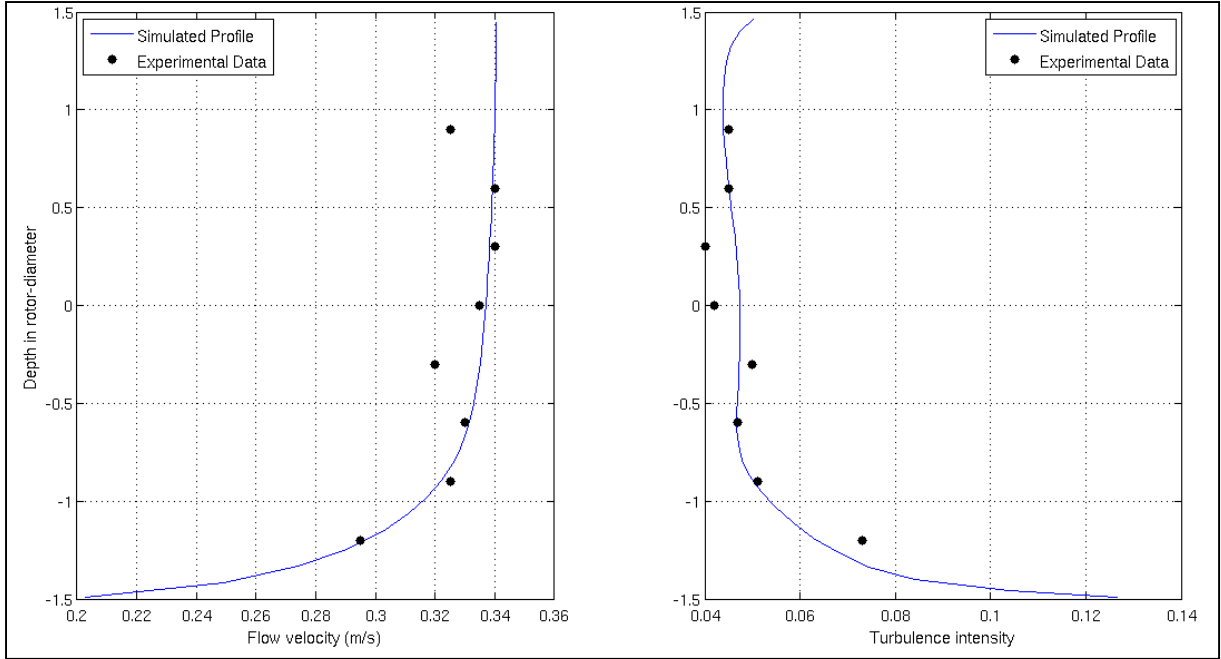
Figure 22: Background conditions – physical experiment data (points) versus simulated results (solid lines). The left hand graph displays velocity profiles and the right hand graph turbulence intensity profiles. Profiles have been measured at channel mid-width and averaged along the channel length.

5.3. Results – Standalone Device

5.3.1. Grid Dependency

Grid-dependency tests have been performed to verify that, as the grid resolution gets finer and finer, the simulation converges toward an asymptotic solution assumed here as the simulation with the following resolution: $\Delta x = \frac{1}{8}D$; $\Delta y = \frac{1}{17}D$; $\Delta z = \frac{1}{9}D$ (i.e. Figure 23 & Figure 24). In addition, these tests identify minimal grid resolutions that will render the turbine representation results relatively insensitive to the resolution and so grid independent. Additionally, not meeting those criteria would reveal inconsistency in the numerical implementation itself. Horizontal and vertical resolution tests have been conducted independently. In the ROMS model, changing the number of sigma levels implies re-tuning several input parameters, such as the bottom roughness and/or the minimum value of specific TKE in order to fit with the initial conditions imposed by the reference experiment (Figure 22). This imposed re-setting phase, although quite time consuming, is required in order to match the observed input conditions. Centre line velocity deficits are presented for expediency sake as these results have been confirmed to be representative of those observed by examining vertical profiles and horizontal transects.
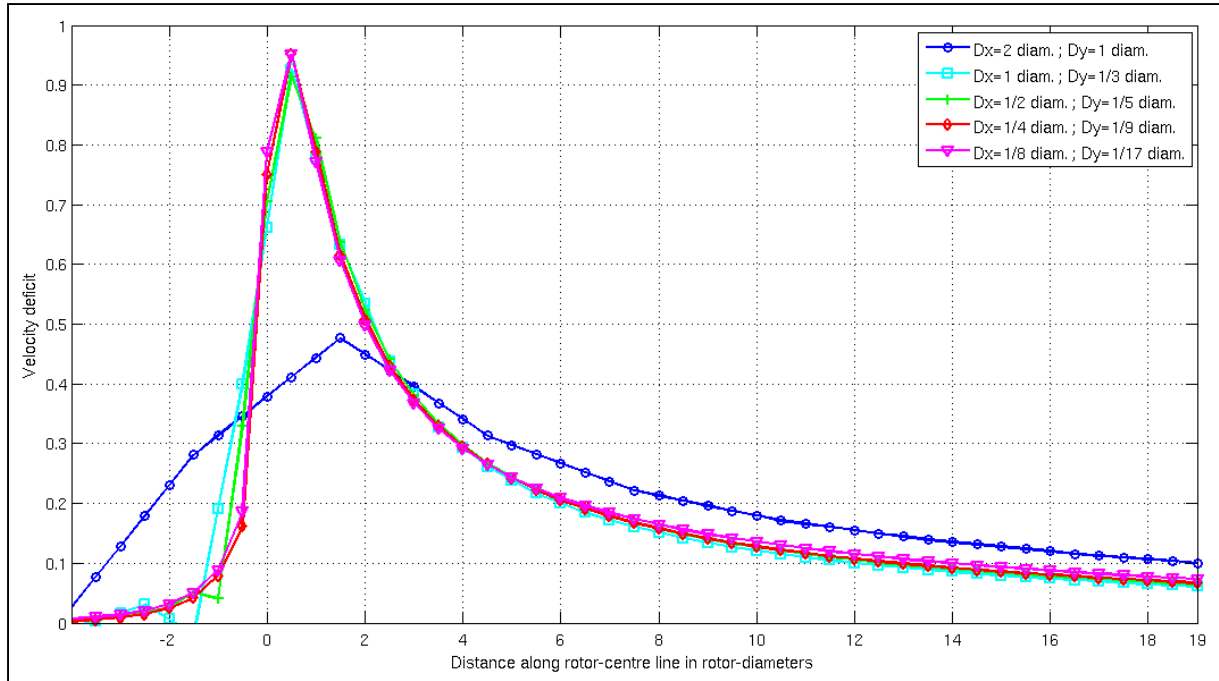
Figure 23: Velocity deficits along centre-Line – Horizontal-resolution dependency test. Each marked line is linked to a different horizontal grid resolution for the same simulation (blue to red correspond to coarse to fine resolution). Notice that all solutions converge toward an asymptotic solution.

Figure 23 gives results of velocity deficits where Δx and Δy vary simultaneously. Originally the intention was to keep the same ratio $\frac{\Delta y}{\Delta x}$ (i.e. $\frac{1}{2}$) as it appeared to be a reasonable criterion for grid generation. However, experience has shown the implementation gives better results for odd numbers of lateral cells. Using an even numbers leads to averaging of the rotor centre deficit peak and thus a misrepresentation of the centre-line wake decay. Consequently, the horizontal spacing ratio has been kept as constant as possible in the light of the odd number requirement on lateral cells. Figure 23 clearly shows that simulations converge toward an asymptotical solution as the grid resolution is refined. One can also observe that after a resolution of $\Delta x = \frac{1}{4}D$; $\Delta y = \frac{1}{9}D$ (red line with diamonds in Figure 23) the difference in wake decay on the simulation is almost imperceptible. As for the minimal resolution, in comparison with the error level that can be expected from the code (i.e. Section 5.2), a resolution of $\Delta x = 1D$; $\Delta y = \frac{1}{3}D$ (light-blue line with squares in Figure 23) and finer would be optimum since its deviation with the asymptotical value is less than 5%_{Nrmse}. Above this limit, coarser resolution leads to information loss and results in an unsatisfactory deviation with

the asymptotical value as, for instance, a resolution of $\Delta x = 2D$; $\Delta y = 1D$ leads to a deviation of 15%$_{Nrmse}$ with the optimal solution (blue line with circles in Figure 23).
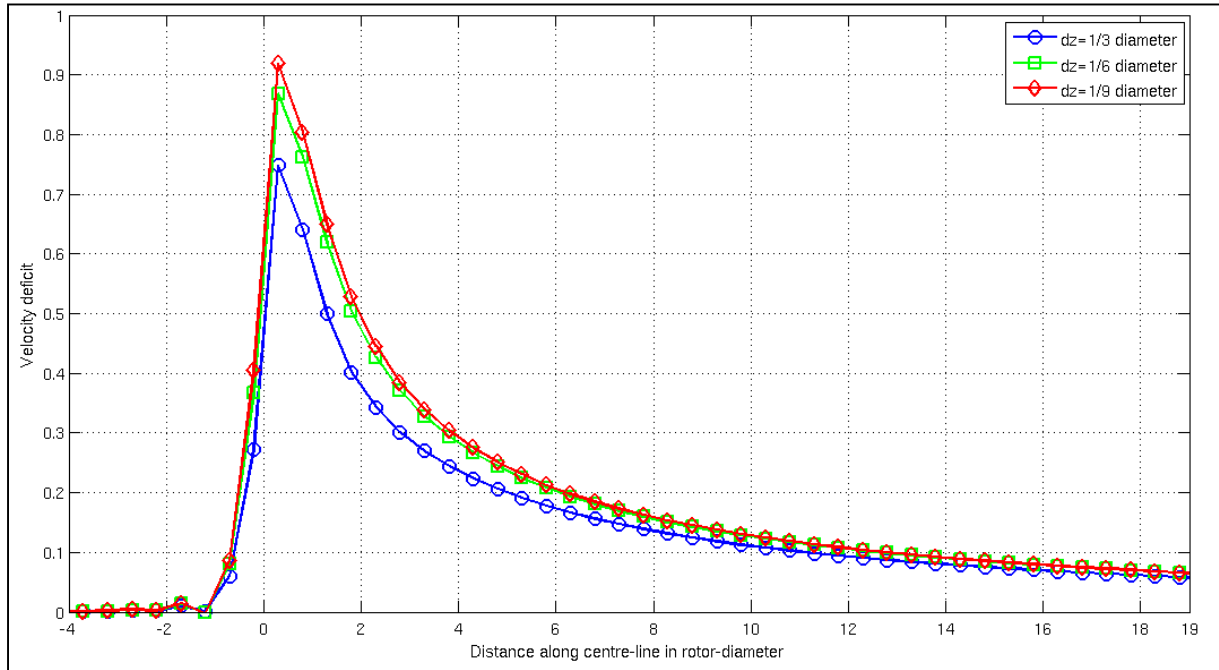
*Figure 24: Velocity deficits along centre-line – Vertical-resolution dependency test. Each marked line is linked to a different vertical grid resolution of the same simulation (blue to red correspond to coarse to fine resolution) and they all converge toward an asymptotic solution.*

In the same manner as Figure 23, Figure 24 shows results of velocity deficits but, in this case, for varying Δz. As can be determined by the discussion in the previous paragraph, the results presented in this section have been performed with a horizontal resolution of $\Delta x = \frac{1}{8}D$; $\Delta y = \frac{1}{17}D$. Owing to the practical reasons of re-setting stated previously, the figure does not display as many cases as Figure 23. Concerning the minimal resolution, an acceptable simulation (<5%$_{Nrmse}$) is reached with a $\Delta z = \frac{1}{6}D$ vertical-level resolution. It is worth noting that, in coastal applications where tidal turbines are likely to be sited, vertical resolution is unlikely to be a limiting feature. Indeed for a 3-D shallow-water numerical simulation, the number of vertical levels required to accurately catch vertical hydrodynamics would generally lead to a Δz finer than $\frac{1}{6}D$.

Spatial resolution in rotor-diameters			r^2	$\%_{Nrmse}$
Δx	Δy	Δz		
2	1	1/9	0.67	11.9
1	1/3	1/9	0.92	4.1
1/2	1/5	1/9	0.95	2.8
1/4	1/9	1/9	0.98	1.6
1/8	1/17	1/9	Reference case for horizontal grid dependency testing	
1/8	1/17	1/3	0.79	7.5
1/8	1/17	1/6	0.89	4.5
1/8	1/17	1/9	Reference case for vertical grid dependency testing	

Table 1: Recap chart of r^2 $\%_{Nrmse}$ for grid dependency testing

5.3.2. Time resolution dependency

Time convergence tests are used to investigate the time dependency of a numerical model. If the model is time independent then, no matter the time step, a model starting with the same initial solution should convergence toward a stable solution within the same period of time. In order to perform this test, the same simulation features described in Section 5.2 are used and the grid resolution is set to Δx=0.05m (1/2 rotor-diameter), Δy≈0.02m (1/5 rotor-diameter), Δz≈0.005m (1/20 rotor-diameter). The simulation is then ran five times with a different time step each time, namely Δt=(0.0005 s, 0.001 s, 0.005 s, 0.01 s, 0.05 s) whose related Courant numbers C_r respectively are C_r=(1/48, 1/24, 1/12, 1/6). Figure 8 represents the outcome of this test, namely the time convergence of velocity deficit of a point situated in the near wake, at the hub height, for simulations with different time step.
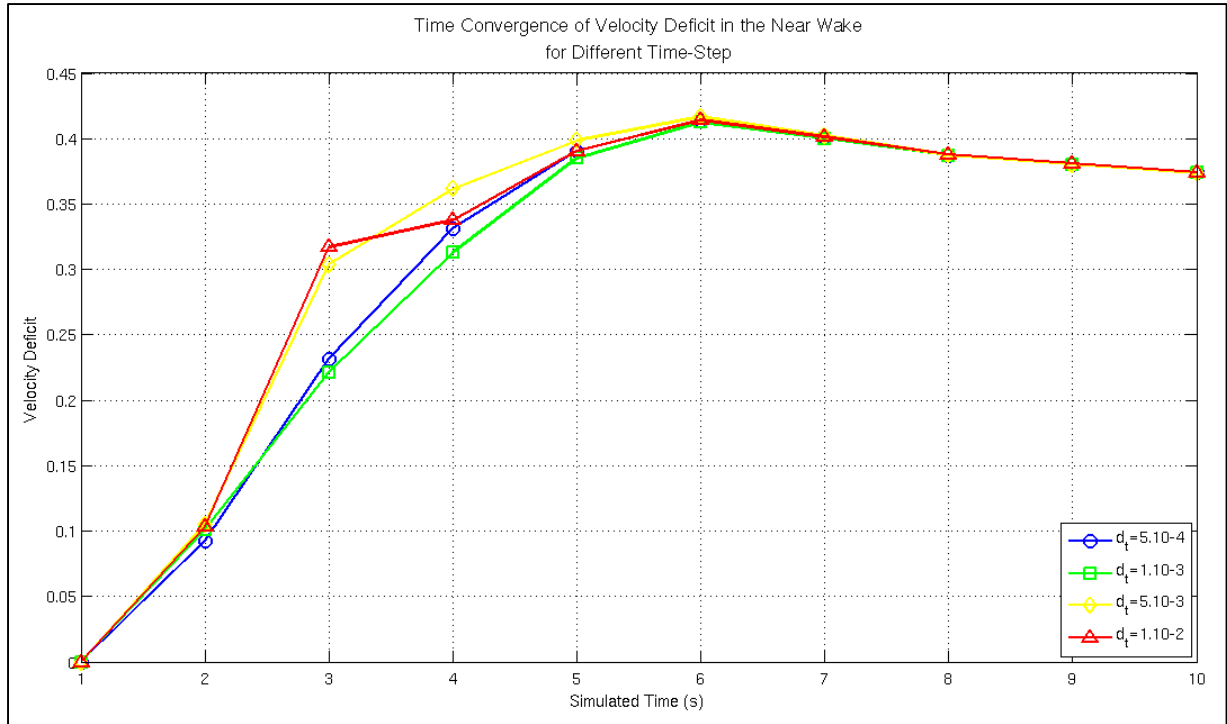
Figure 25: Flow Velocity in the Wake versus Simulated Time – Time Convergence Test

In the same way as the resolution dependency tests, one can observe that the velocity deficit in the wake, and by extension the wake recovery itself, converges towards the same value whatever the time-step use. This result convergence proves that the TCT representation implemented in ROMS is also independent from the time resolution and that the implementation of the TCT representation is consistent with the resolution scheme used in ROMS. Concerning the time-step limit, it seems hazardous to draw any conclusion since the time of convergence directly depends on the initial solution provided to kick-start the simulation. In this case, the closer the initial solution is to the stable solution, the shorter the convergence time gets. However, it is clear that the perturbation brought by the TCT module does not jeopardize the code stability. For the same reason, it is impossible to determine for which maximum time-step value the final result would drift away since the first step of computation crashes for a value greater than 0.01s. Theoretically and by having the closest initial solution to the converged solution, the time step shall reach 0.03s (i.e. $C_r = 0.5$), that is the upper limit of the CFL (Courant-Friedrichs-Lewy) criterion in our case (Haidvogel & Beckmann, 1999).

5.3.3. Validation against experimental data – Momentum and turbulence behaviours

Under the model development discussed in Section 4.2 and 4.3, the potential free coefficients (i.e. C_D, C_d, C_p, C_ψ) have been assigned the values recommended in the published literature hence, the only parameter that needs empirical calibration is the eddy viscosity. In the present case, the eddy viscosity is calibrated against the horizontal expansion of the turbine wake and far-wake vertical profiles of TKE provided by Harrison *et al.* 2010 (Figure 26).
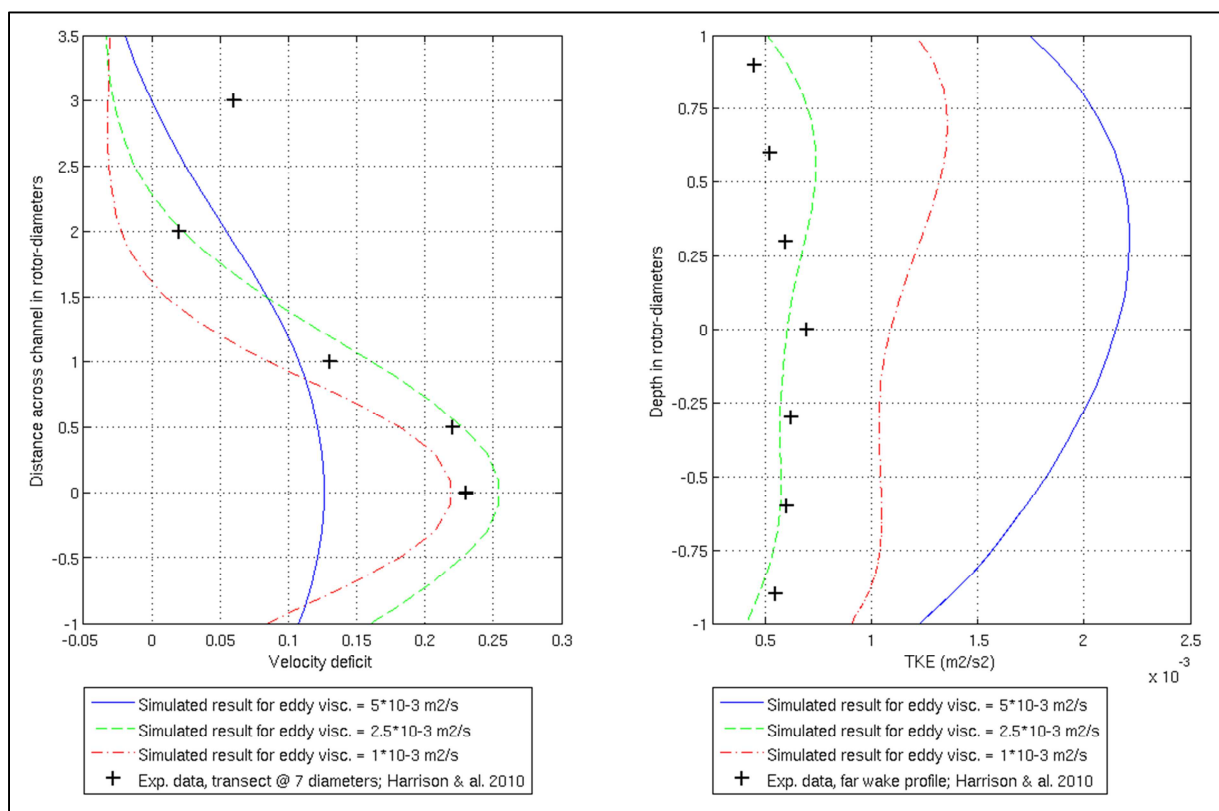
Figure 26: Eddy viscosity calibration figure showing horizontal transects of velocity deficits (left) & vertical profiles of TKE (right) at a distance of seven diameters downstream from the device. The experimental far-wake horizontal velocity and vertical TKE (black crosses) are used as benchmark for the eddy viscosity calibration; each type of lines (blue solid, green dashed and red dotted-dashed) represent simulated results of different eddy-viscosity values for the corresponding experimental data.

The left hand graph of Figure 26 shows horizontal transects of velocity deficit taken at seven diameters downstream of the device for various eddy viscosity values as well as the corresponding experimental data points. Predictably, increasing the eddy viscosity value used in the simulation

leads to an increase in the lateral spread of the wake. The right hand graph of Figure 26 shows vertical profiles of TKE taken at 15 diameters downstream of the device for various eddy viscosity values as well as the corresponding experimental profile. Noticeably, increasing the eddy viscosity value used in the simulation leads to a non-linear variation of TKE, in other words, a non-linear variation of far wake turbulence level. An eddy viscosity of $2.5 * 10^{-3} \mathrm{m}^2 . \mathrm{s}^{-1}$ appears to give, in terms of horizontal wake expansion and far wake turbulence level, the optimum match with the experimental data. Nonetheless, there are some differences towards the channel wall boundaries which are thoroughly discussed further in this section.

These results give confidence in the calibration of the horizontal momentum dissipation in the simulation and the aptitude of the method for accurately simulating the flow perturbation induced by the device. The case with the deployed devices can now be investigated. Figure 27, Figure 28 and Figure 29 illustrate comparison of the velocity deficit between the reference flume-scale model and its equivalent numerical simulation obtained by the present TCT representation method. Figure 27 shows velocity deficits along the centre-line for a case where only the thrust force is considered (dashed line), a case where both thrust force and turbulence correction are included (solid line) and the experimental data (crosses).
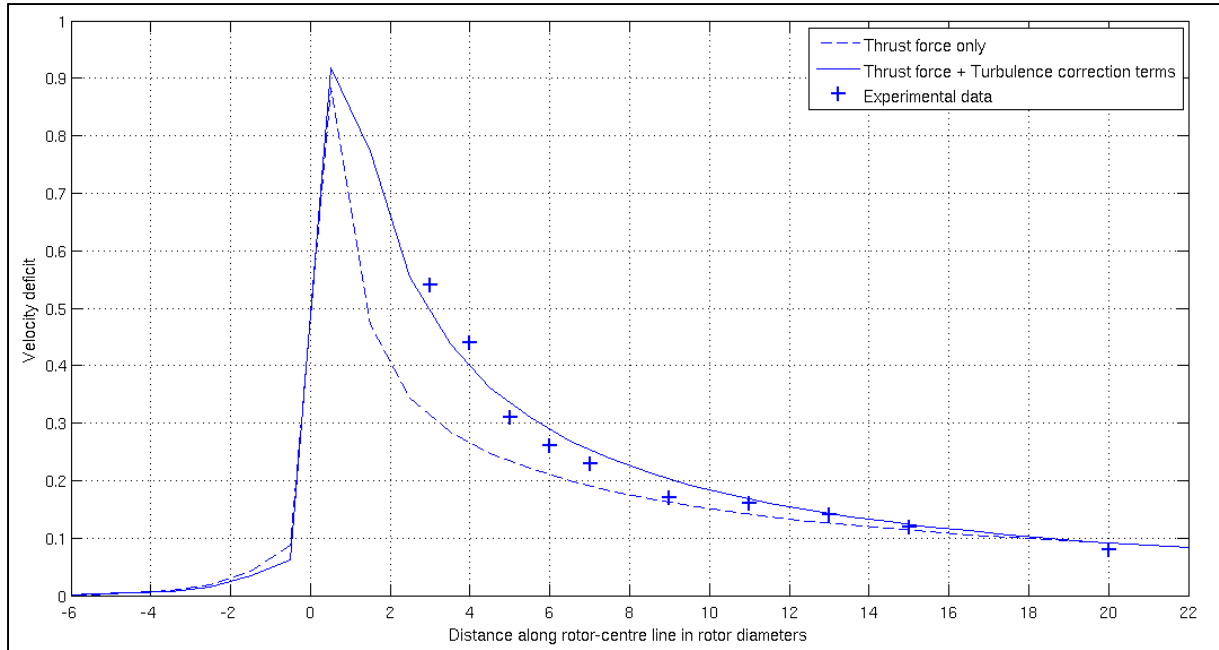
Figure 27: Plot of velocity deficits along centre-line demonstrating the effect of including turbulence correction terms. The experimental data is represented by the crosses. The corresponding simulation results which utilizes only the thrust force is shown with the dashed line and the full simulation accounting for both the thrust force and turbulence perturbations is presented with the solid line.

Accounting for the device-induced turbulence components in the numerical TCT representation appears to be necessary in large-scale simulations in which sub-scale turbulence phenomena are not fully and/or explicitly computed. Indeed Figure 27 illustrates the fact that, in large-scale models, only accounting for the momentum perturbation leads to a poor assessment of the wake recovery and that one way to reproduce accurately both the near and far wake recovery is to parameterize the non-linear turbulence perturbations generated by the near-wake turbulence-disequilibrium. By doing so, the match of velocity deficits along the rotor-centre lines between simulated and experimental data reaches a correlation coefficient of $r^2 = 0.92$ and a normalized root mean square error percentage ($\%_{Nrmse}$) of 5.8%.

Figure 28 displays the simulated horizontal transects of velocity deficit taken along a median plane at different locations downstream of the device and the corresponding experimental transects upon which a comparison can be made. There is a strong correlation between the simulated transects and the experimental data ($r^2 = 0.88$) although the highest disagreement occurs at the lateral extremity of the study area. The deviation of magnitude between simulated and experimental

data does not reach the level of confidence expected ($\%_{Nrmse} = 12.0\%$) but the reduced discrepancy ignoring the points closest to the wall results in a value of 9.4%.
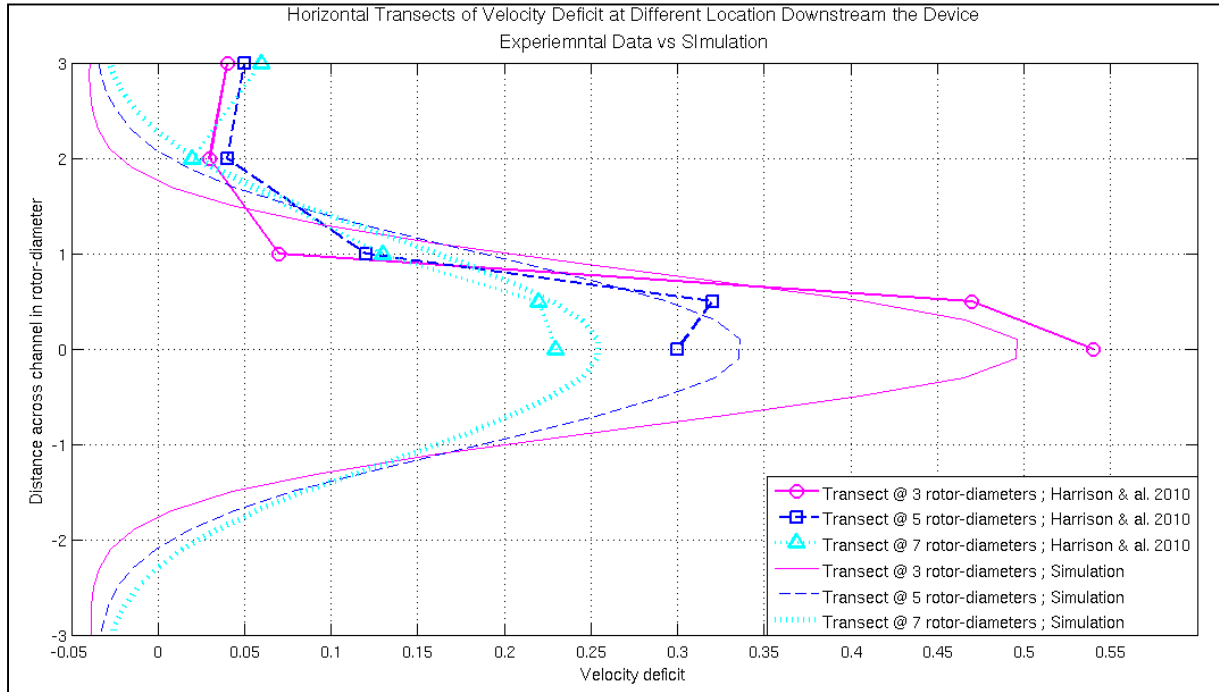
Figure 28: Horizontal transects of velocity deficits taken at different locations downstream to the device – Experimental data versus simulated results. Experimental transects (marked lines) are used as benchmarks to estimate the accuracy of their simulated equivalents (lines of matching colors and types).

This level of error can be attributed to two reasons. First the experimental data base being quite sparse (15 points) and spatially narrow (from 0D to 3D), any deviation from the data has high weight. More importantly however is the obvious disagreement on the horizontal flow recovery of the outer-disc region. The simulation shows a slight acceleration of the flow for the region greater than 2 diameters away from the disc centre whereas the experiment data shows an apparent deceleration. While the source of this discrepancy is unknown, mass conservation requires an acceleration in part of the unblocked gaps in a partially blocked channel as observed in the simulations. The free slip condition imposed on the side walls of the simulation may lead to an improper allocation of this region of acceleration to the sidewall region.

Figure 29 displays vertical profiles of velocity deficit taken along a median plane at different locations downstream of the device for both simulation and experimental data. Comparison has

been made between the simulation profiles and experimental data. In the same manner as the horizontal transects, a strong correlation between the simulation and the experiment ($r^2 = 0.81$) is evident and the deviation of magnitude ($\%_{\mathrm{Nrmse}} = 8.1\%$) again does not quite meet the optimum level of confidence obtained for the initial case (i.e. §3.3.) although omission of the data points nearest the bottom boundary reduces this number to 6.8%.
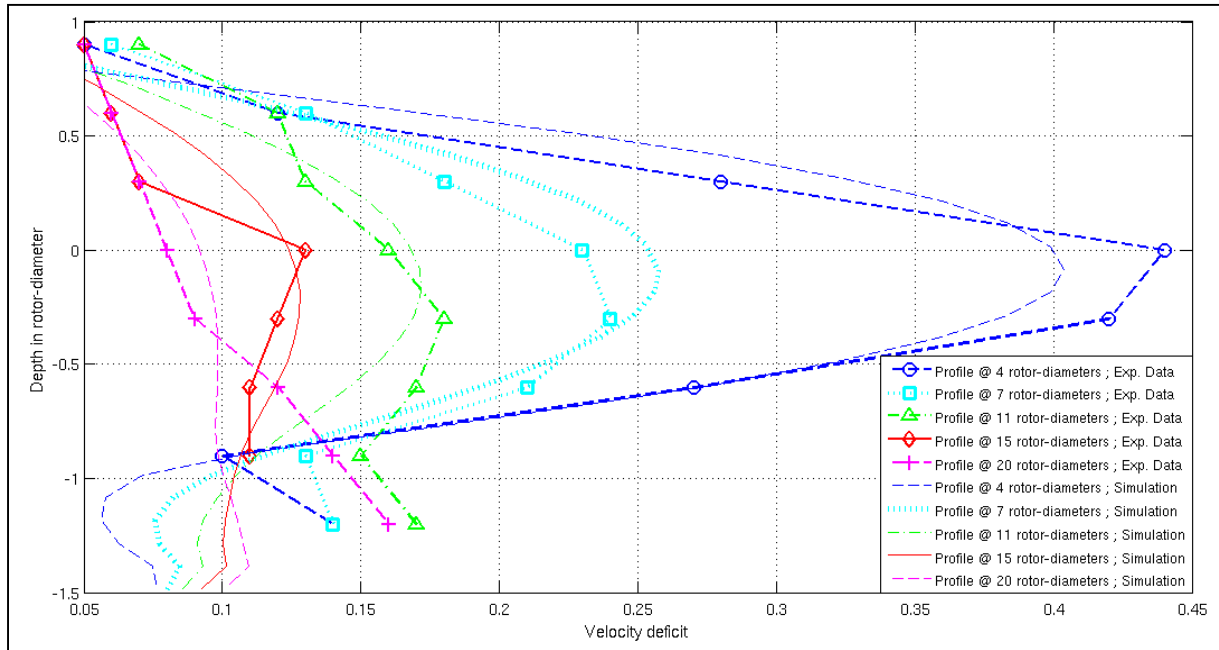

Figure 29: Vertical profiles of velocity deficits taken at different locations downstream to the device – experimental data versus simulated results. Experimental profiles (marked lines) are used as benchmarks to estimate the accuracy of their simulated equivalents (lines of matching colors and types).

The reasons mentioned in the previous paragraph to justify the discrepancies of the horizontal flow behaviour could be also applied here, yet an additional explanation is worth discussion. At the current stage of development, the TCT module structure relies on the ROMS built-in "body force" implementation. Application of this option requires an a-priori definition of the thickness of the bottom and upper mixed layers within which the boundary layers and related mixing processes will be restrained.

One of the advantages of the present method and probably a unique feature within the existing meso-scale TCT models is the ability to simulate the turbulence perturbations induced by the devices on the flow. Self-evidently, the model does not explicitly resolve the sub-scale turbulence

dynamics but does account for it, and it is important to understand the level of confidence in the results. Figure 30 and Figure 32 provide the required elements to answer this question by illustrating comparison of the turbulence features between the reference flume-scale model and its equivalent numerical simulation. It is worth noticing that the experimental values of TKE displayed in Figure Figure 30 and Figure 32 have been inferred from the turbulence intensity measurements (Harrison et al., 2009) performed during the referenced flume test (i.e. Section 5.2, Eq. (96)). Figure 30 displays comparison of simulated and experimental vertical profiles of TKE taken along a median plane at different locations downstream of the device.
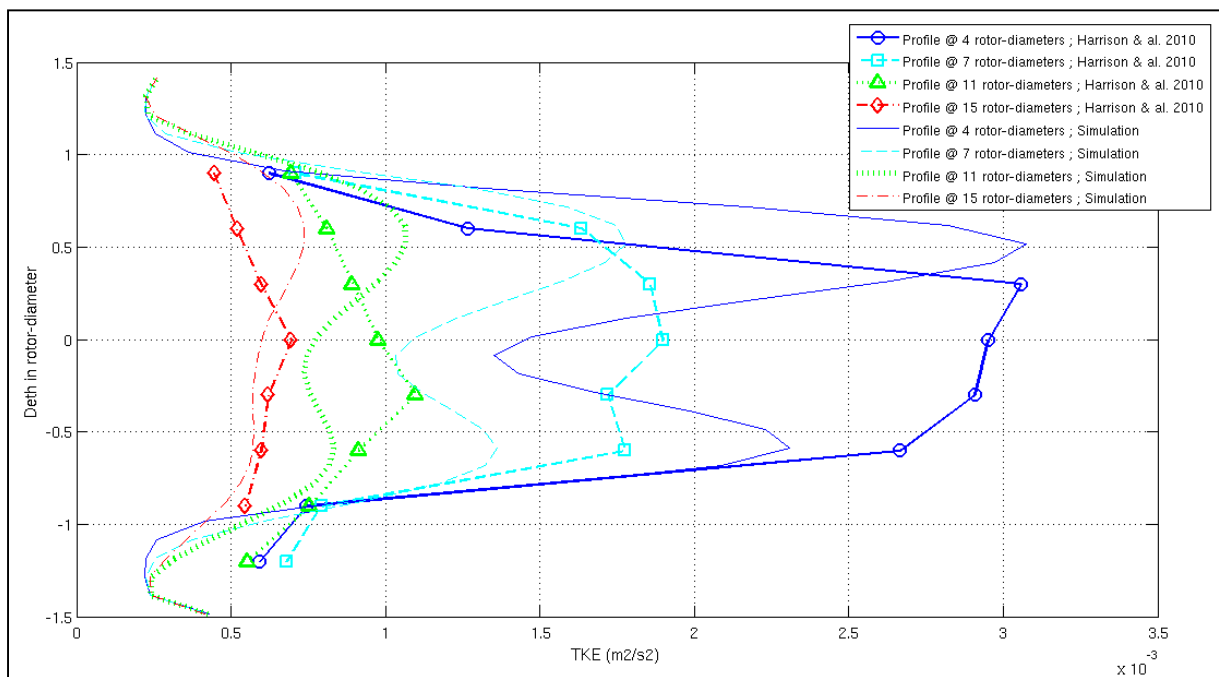
*Figure 30: Vertical profiles of TKE at different locations downstream of the device – Experimental data versus simulated results. Experimental profiles (marked lines) are used as benchmarks to estimate the accuracy of their simulated equivalents (lines of matching colour and type).*

The following table gathers correlation coefficients and error levels of the vertical profiles displayed on Figure 30. This table depicts in details the matching in vertical turbulence behaviour between experiment and simulation.

5.3. Results – Standalone Device

Location along channel	4 diameters	7 diameters	11 diameters	15 diameters
Correlation coef., r	0.62	0.74	0.53	-0.12
Error level $\%_{Nrmse}$	75.3	35.9	16.2	9.7

Table 2: Correlation coefficients and error levels for vertical profiles of TKE taken at different locations downstream of the device

The vertical turbulent behaviour of the downstream perturbed flow generally appears to have a low correlation especially at 15 diameters downstream. The latter seems however normal since, in the far wake, turbulence levels are so low as to be indistinguishable from noise and thus devoid of trend to be matched with. For the far wake profile, the important aspect is fitting with the experimental TKE magnitude which the present model achieved satisfactorily with regard to the optimum TKE error level (i.e. Section 5.2). Interestingly, the closer to the device hub the profiles are, the higher error they get. Looking closely at the data throughout the channel, there is noticeably less accurate match between the simulated results and physical experiments in the lower layer and in the close vicinity of the hub. However, the simulation does succeed in reproducing the vertical asymmetry of the TKE profile. This feature comes from the distinct nature of the top and bottom boundaries. The bottom boundary is a solid boundary characterized by a roughness height whereas the upper boundary is a fluctuating free-surface. The different natures of the top and bottom boundaries generate an asymmetrical velocity gradient throughout the depth, in spite of the vertical symmetry of the channel/turbine set-up, and therefore lead to a vertical asymmetry in the TKE profile. However, this vertical asymmetry appears to be amplified in the simulation especially in the lower boundary where TKE levels are under predicted. Potentially this could be due to the differences in the bottom boundary layer behaviour alluded in the previous paragraph.

The origin of the asymmetry discrepancy between the simulated and experimental TKE profiles as well as the double maxima observed only in the simulations is not fully understood. It is however worth noticing that the Reynolds stress results from Myers and Bahaj (2010) (i.e. Figure 31) do replicate the double peaked structure with amplified vertical asymmetry behavior seen in the

simulated TKE levels. This suggests that the simulations are properly reproducing the coherent stress generating turbulence arising from vortex shedding around the porous disk and that discrepancies arise from the small scale "grid" generated incoherent turbulence from the center of the porous disk. Thus it can be argued that the double peaked structure observed in the simulation is closer to true turbine behaviour, the reproduction of which is the ultimate goal of the model development.
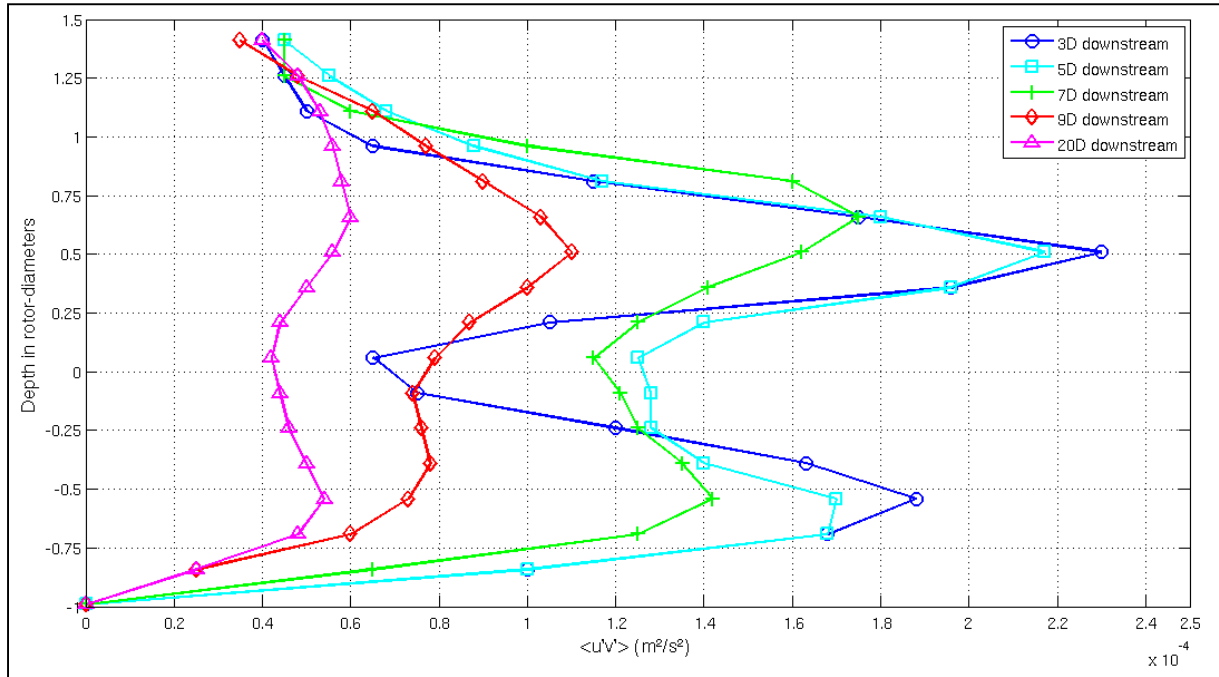
Figure 31: Vertical profiles of Reynolds stress at different locations downstream of the device – Experimental data from Myers and Bahaj, (2010).

Figure 32 displays comparison of the simulated and experimental horizontal transects of TKE taken on a mid-depth plane (Figure 21) at different locations downstream the device. The simulated TKE wakes are narrower than in the experiments, leading to a significant deviation ($\%_{\mathrm{Nrmse}} = 70.5\%$) yet the correlation with the experiment is satisfactory ($r^2 = 0.67$). The simulated peak magnitudes are lower than the experimental measurements, but this is likely to be because they are at the centre of the turbine and thus lie at the low point between the two peaks observed in Figure 30. The horizontal transects taken in Figure 32 are located right in the area where turbines and porous disks have fundamental difference in terms of "turbulence short-circuiting", and so a perfect match between experimental and simulated results cannot be expected.
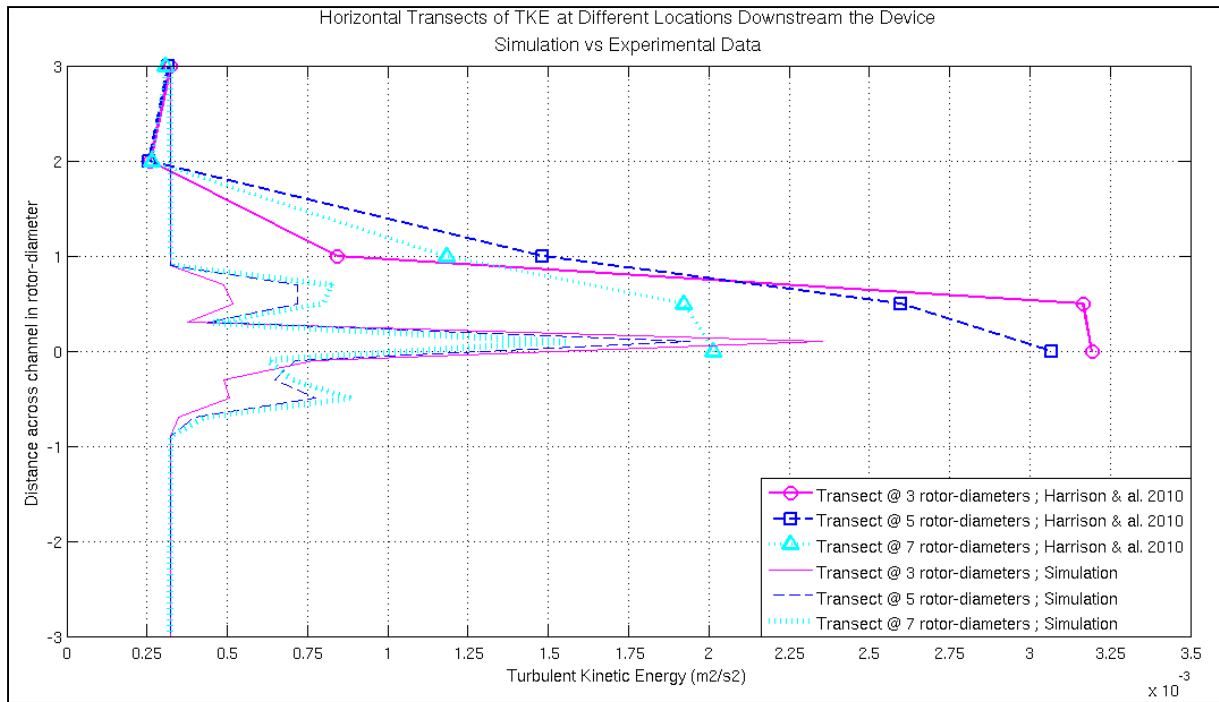
Figure 32: Horizontal transects of TKE at different locations downstream of the device – Experimental data versus simulated results. Experimental profiles (marked lines) are used as benchmarks to estimate the accuracy of their simulated equivalents (lines of matching colours and types).

Much if not all of the discrepancy in the lateral distribution of TKE is no doubt due to the implicit assumption in ROMS that TKE generation is derived from vertical shear whereas the axisymmetric nature of tidal turbines certainly suggests that lateral shear is equally important particularly on the mid-plane reproduced in Figure 32. This level of discrepancy in the lateral extent of turbulence production is probably an unavoidable consequence of the splitting between horizontal and vertical mixing present in ROMS. It is worth noting however that the lateral wake structure has been well represented in the simulations (Figure 28) and that the level of agreement observed in TKE prediction has to be put into perspective with the optimum level of confidence that can be expected for such a quantity (i.e. Section 5.2).

5.3.4. Validation against experimental data – C_t sensitivity

Once the model has been calibrated for a certain type of turbine and flow features, in this case a certain thrust coefficient, C_t , it should be able to compute with precision the flow perturbations associated with turbines of different C_t. In the same manner, Myers & Bahaj (2010) used the Chilworth flume set as described in Section 5.2 but used discs of various porosities and consequently

various C_t, that is $C_t = 0.61; 0.86; 0.94$ (Myers & Bahaj, 2010). Reproducing these scenarios with the proposed model and comparing their results with experimental data permit to evaluate both the theoretical consistency of the TCT representation and the numerical consistency of its implementation method in the ocean circulation model. Using the same numerical features and resolutions as described in Section 5.2, simulated results are obtained and compared with their experimental equivalents in Figure 33.
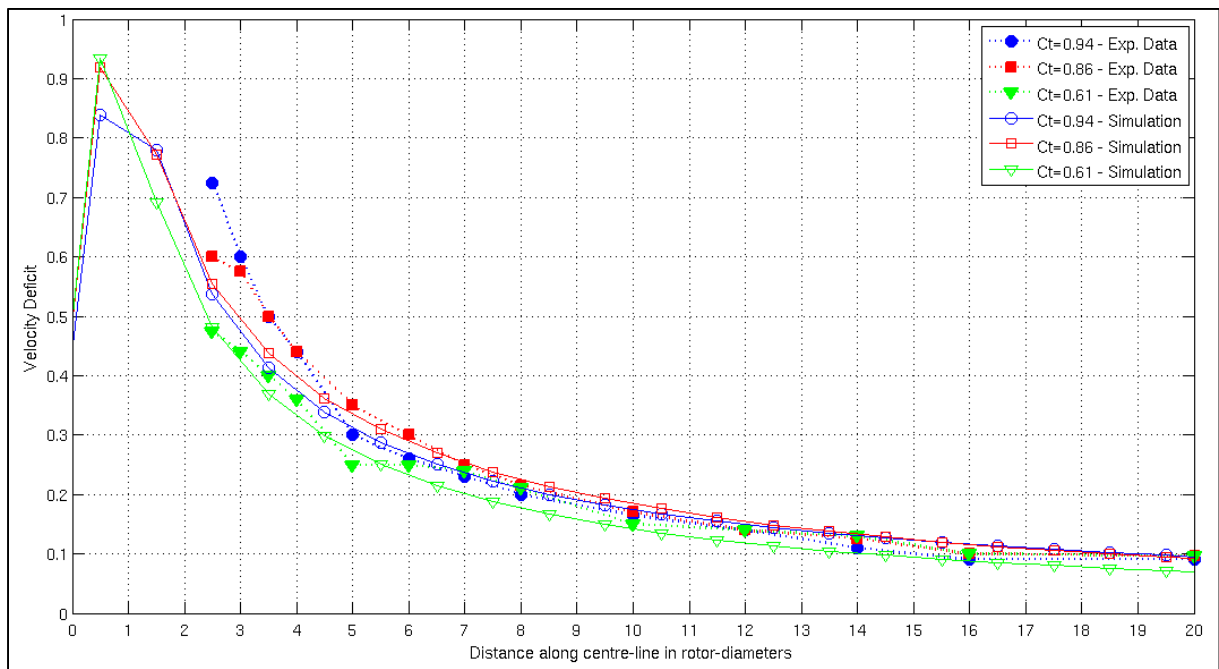
Figure 33: Comparison between simulated (solid lines) and experimental (dashed lines) velocity deficits along centre-line for various values of thrust coefficients. Mashing line types correspond to matching thrust coefficient.

Table 3 gathers correlation coefficients and error levels of velocity deficits along the centre-line for various values of thrust coefficients:

Thrust coefficient C_t	Correlation coefficient r^2	Error level $\%_{Nrmse}$
0.94	0.96	9.8
0.86	0.98	5.8
0.61	0.98	4.5

Table 3: Correlation coefficients and error levels for three cases of various thrust coefficients (0.61, 0.86, 0.94)

In general the correlation between experiments and simulations is high and the error level between them is satisfying ($\%_{Nrmse} = 6.7\%$ in average). The error level decreases with the thrust coefficient, however. Most of the discrepancies are located in the near wake, namely up to 5 diameters downstream of the device.

As the thrust coefficient increases, the near wake becomes turbulent and as the near wake becomes turbulent and complex, the discrepancies in turbulence behaviour between porous discs and the present TCT representation becomes obvious. Accordingly, one can observe in the near wake the almost perfect match of wake decay for $C_t = 0.61$ becoming less and less close as C_t increases. Nonetheless, after 5 diameters downstream of the device, the simulation reproduces with a great accuracy the experimental wake recovery. Especially the non-intuitive phenomenon that the wake associated with $C_t = 0.94$ recovers faster than the one associated with $C_t = 0.86$. Once again, the accuracy and the relevancy of the proposed TCT representation are demonstrated.

5.4. Discussion – Standalone device

The present method for representing TCT within an ocean circulation type model capable of performing regional scale simulations permits the TCT influence on the hydrodynamics to be modelled. The present method is proven to be grid convergent, both spatially (i.e. Section 5.3.1) and temporally (i.e. Section 5.3.2), and grid convergence tests have been used to identify the minimum grid spacing requirements. It is also demonstrated to reproduce the results of physical experiments with a single turbine in a channel to a good level of accuracy (i.e. Section 5.3.3) within short period of computational time. Moreover in terms of turbine induced momentum and turbulence behaviour, such level of detail has not been reached with such large scale 3-D model before. The proposed tool has also proved its ability to manage different turbine features, namely through various C_t, without having the need for further calibrations of the so-introduced parameters (i.e. Section 5.3.4).

In addition, the importance of sub-grid scale turbulence in the TCT forcing parameterization especially regarding both momentum flow recovery and energy balance has been highlighted. Although empirical parameterization of the drag coefficient could result in simulated wake recovery

similar to observation, it would misrepresent the energetic nature of the TCT perturbation and thus bias power yield assessments of any TCT array layout. In the same manner, the discrepancies noted in Figure 30 between simulated and experimental data as well as the mismatch of vertical shapes between the experimental profile from Figure 30 and the Reynolds stress profiles from Figure 31 suggest that the TCT-induced energy transfer may be misrepresented when the porous disc modelling approach is used. Nevertheless, although in the vicinity of the device the axisymmetric nature of tidal turbines certainly suggests that lateral and vertical shears are equally important, ROMS considers that TKE generation is only derived from vertical shear. This limiting assumption needs to be kept in mind during resource assessments.

The method developed here has two advantages in comparison with an empirically-enhanced thrust-coefficient parameterization. Firstly it does not require fastidious empirical fitting of the thrust coefficient. Such an empirical approach would entail deriving a new data set for any change in flow or device features. Secondly, by realistically accounting for the turbulence influence in the flow perturbation, the present TCT representation method is able to provide an assessment of the meso-scale turbulence behaviour induced by the device that is compulsory for TCT layout optimisation, whereas an empirically enhanced thrust coefficient method would completely ignore this feature. We emphasize that the entire set of parameters (i.e. C_t, C_1, C_2, C_3) was assigned values following recommendations given in published literature (Réthoré et al., 2009; Rados et al., 2009; Myers & Bahaj, 2010) and that only one user adjustable parameter (i.e. the eddy viscosity) has been used in the simulations presented here. Whether this result will hold in general must be determined following tests with other TCT devices.

To conclude, on the basis of comparisons with physical scale tests, a regional ocean modeling system (ROMS) has been successfully adapted to represent wake decay behind a marine current turbine in terms of both momentum and turbulence. Model alterations to achieve this required both the addition of momentum and turbulence correction terms to the model in order to provide a full account of the hydrodynamic effects induced by an idealized stream turbine in the near and far

fields. The model has been shown to be convergent and stable. Once the model has been properly set up and validated, model data comparisons utilizing the results of laboratory tests demonstrate the ability of the chosen implementation to adequately reproduce features of the turbine wake and its recovery.

Chapter 6. Turbine Wake Interactions

6.1. Introduction – Turbine Wake Interactions

Accounting for the TCT-induced turbulence phenomenon through GLS closure model corrections has been shown to be effective in compensating the sub-grid scale turbulence which is unresolved in ocean circulation models. It permits the use of computationally inexpensive techniques, such as the actuator disc theory, to simulate the wide range of TCT perturbation scales without losing the accuracy of both momentum and turbulence behaviours. After the design and optimization of a standalone TCT prototype, the next step for tidal energy development is towards deployment of multiple device arrays. TCT farms in which arrays of multiple turbines are deployed help to minimize the overall cost, by allowing for shared maintenance and grid connection cost and so maximize the power harvest of a particular site. Mastering turbine interactions will permit to use the beneficial effects on power yielding while limiting their harmful impacts on structure loading and large-scale hydrodynamics (Myers et al., 2011; Myers & Bahaj, 2012; Bai et al., 2009; Churchfield et al., 2011; Lee et al., 2009; Ingram et al., 2011).

In the current literature, the large majority of 3-D numerical investigations of TCT wake interactions have been performed with Computational Fluid Dynamics (CFD) models (Bai et al., 2009; Churchfield et al., 2011; Lee et al., 2009; Harrison et al., 2010; MacLeod et al., 2002) using either actuator disc or actuator line approaches (Burton et al., 2008). These high resolution models can give a very accurate picture of wake interactions occurring within TCT farms but can only be applied to simplified cases. Indeed, the computational power needed to run such models limits their use to

small spatial and temporal domains of simple bathymetries and geometries in which only basic forcing can be imposed. In realistic TCT farm deployment projects, it is imperative that the optimization layout tool accounts for the complex tidal flows and environment configurations where the devices will operate (Churchfield et al., 2011; Réthoré et al., 2009). Accordingly, the present method consists of integrating an innovative and promising TCT representation (Roc et al., 2012) within an existing 3-D ocean circulation model (Regional Ocean Modeling System, ROMS). The so-adapted numerical platform can potentially tackle any TCT layout in any tidal hydrodynamic system. However, prior to practical application, the relevancy of this TCT array optimization tool has to be validated. Ultimately a numerical tool for regional scale TCT array optimization has to prove its ability to simulate device interactions in a realistic environment in order to be considered as suitable for real-life applications. As this new field is still at an early stage, there is a lack so far of such power plants and real-life observational data and so experimental and analytical benchmark tests have to be used for compensate this.

In this section, the accuracy of the present TCT numerical representation in reproducing TCT interactions is investigated. Accordingly, two referenced physical scale model experiments illustrating device interaction features are used to perform comparison between experimental data and simulated results. From this comparison, the precision of the proposed numerical method to reproduce TCT interactions is estimated. The results from these two test series indicate that the proposed numerical tool for TCT arrays optimization can be considered suitable for realistic TCT layout.

6.2. Simulation Features and Benchmarks

In order to validate the capability of these proposed turbine modelling methods to simulate accurately wake interactions within TCT farm layouts, a model data comparison between physical scale model and numerical model results has been conducted. The physical experiments have been performed and published by Myers et al. (Myers & Bahaj, 2012; Myers et al., 2011) in the Chilworth flume at the University of Southampton. The flume experiment set-up is a rectangular channel with a

6.2. Simulation Features and Benchmarks

21000 mm long (L), 1350 mm wide (l) and 300 mm deep (h) working section in which turbines, represented by a 100 mm diameter (d) perforated disc with a porosity corresponding to C_t=0.9, are deployed. A constant, depth-averaged inflow of 0.26 m/s whose vertical profile closely matches a (1/7)th power law is imposed at the upstream boundary of the channel. The ambient turbulence intensity (Eq.(95) & (96)) of the flume fluctuates in the range of 6-8%. The first case consists of a first row of two discs whose centres are separated by 2.5 diameters and edges are 5 diameters away from the flume sides (Figure 35). For the second case, an additional third disc identical to the other two is positioned at a second row in the centre of the flume, 3 diameters downstream of the upstream pair (Figure 35). All of them are placed at mid-depth in the water column at a hub depth of 0.15 m.

The numerical grid used for the flume simulation has 420 grid cells in the stream wise direction (equivalent to $\Delta x = 0.05\text{m } (\frac{D}{2})$), 67 grid cells in the cross-stream direction (corresponding to $\Delta y \approx 0.02\text{m } (\frac{D}{5})$) and 30 vertical levels in the grid which are linearly distributed in sigma space in the vertical (equivalent to $\Delta z = 0.01\text{m } (\frac{D}{10})$). A constant, inflow is imposed at the upstream channel boundary and the free-surface elevation at the downstream boundary is held at 0 m. A free-surface radiation condition, 2D momentum Flather condition and 3D momentum radiation condition are applied on the upstream open boundary; a free-surface clamped condition, 2D momentum reduced-physics condition and 3D momentum radiation condition are used for the downstream open boundary (Carter & Merrifield, 2007); free-slip conditions are applied on the lateral walls. The model ran until the results indicated that a steady state had been achieved, namely when model averages of velocity, TKE and free surface elevation, taken at the device location, varied by less than 0.1% from one time step to the next. The time step used for the simulation meets CFL (Courant-Friedrichs-Lewy) criterion. It has been verified that using a shorter time step does not change the steady state solution (Roc et al., 2013). The simulations have been computed in parallel on 8 processors of 2.5 GHz clock-rate using Message Passing Interface (MPI) libraries. With this set-up, on average, it takes around 15 minutes (i.e. "real" time) for the simulations to reach a steady state.
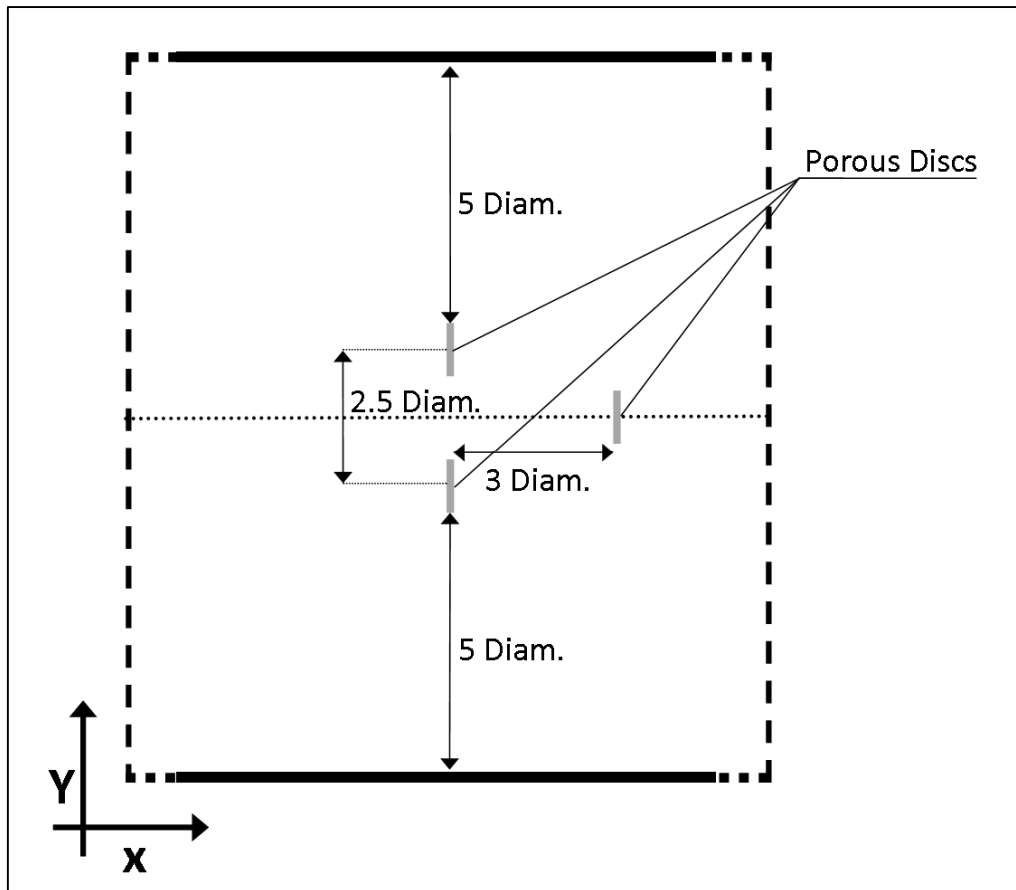
Figure 34: Channel section XY-plan of the experimental set-up with real proportion
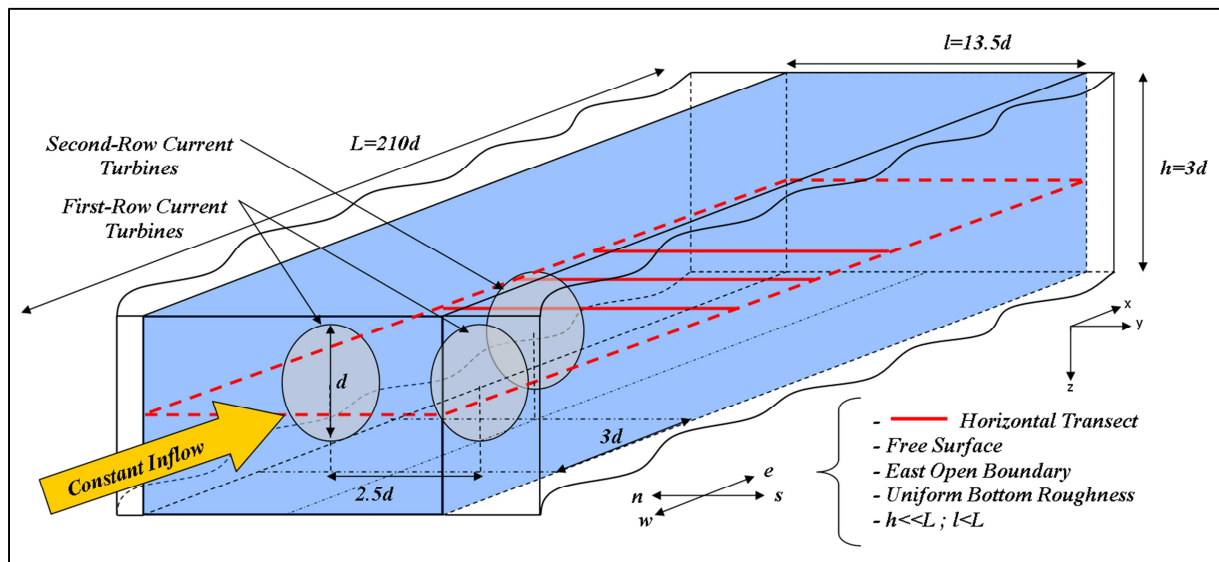

Figure 35: Idealized channel, multi-disc case - This conceptual diagram represents the multi-disc test geometry and dimensions as well as the locations where horizontal transects (red solid lines) have been taken.

The turbulence behaviour in the flow is characterised on three different quantities, the turbulence intensity (TI) (Eq.(95) & (96)) and the turbulent kinetic energy, TKE (or k). It is worth noting that the TI data from the experiment have been measured with a conventional Doppler velocimeter (Eq.(95)):

$$TI = \left(\frac{1}{3}(u'^2 + v'^2 + w'^2)\right)^{\frac{1}{2}} / (U^2 + V^2 + W^2)^{\frac{1}{2}} \tag{99}$$

whereas the simulated TIs derive from the simulated k and U (Eq.(96)). As reminder (i.e. Section 5.2) the optimum correlations and error levels which can be expected between an experiment performed in the Chilworth flume investigating the wake of a single turbine and the corresponding simulation computed via the proposed model are $r^2 = 0.77$ with an $error_{Nrmse} \cong 3.5\%$ for the velocity and $r^2 = 0.88$ with an $error_{Nrmse} \cong 10\%$ for TI.

6.3. Results – Turbine Wake Interactions

6.3.1. Wake Interactions – Wake Decay

In this part of the document, comparisons between experimental and simulated horizontal transects of velocity deficit taken at different locations downstream from the 2 disc front row are considered. In Figure 36 and Figure 37, the origin of the along channel distance is set at the location of the 2 disc front row. In the case of the 3 devices deployment, the origin of the second row is located 3 diameters downstream of the front row (i.e. Figure 35). Therefore, transects taken at 5 rotor-diameters downstream of the first row, are annotated on Figure 36 and Figure 37 "Transect @ 5 diam." although they are located 2 rotor-diameters downstream of the second row; likewise for the transects taken at 7 and 9 diameters downstream of the origin.

Figure 36: Horizontal transects for 2-devices cases – This graph permits the comparison between the experimental horizontal transects (marked lines) taken at different locations downstream of the channel with their simulated equivalents (lines of matching colours and types).
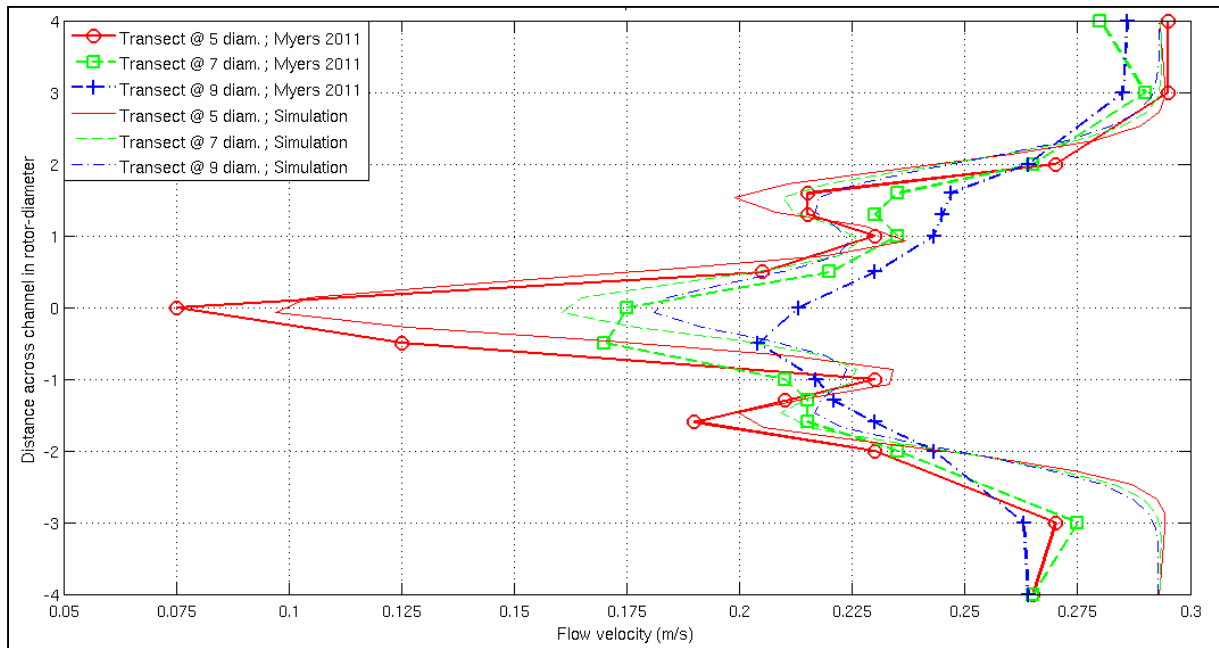
Figure 37: Horizontal transects for 3-devices cases – This graph permits the comparison between the experimental horizontal transects (marked lines) taken at different locations downstream of the channel with their simulated equivalents (lines of matching colours and types).

Generaly in both 2 and 3 device cases, experimental data and simulated results show a satisfactory correlation (average r in the 2 device scenario = 0.91 ; average r in the 3 device scenario = 0.9). In

94

terms of error, in both cases, simulations present an accurate match with the experimental data (average error$_{Nrmse}$ in 2devices scenario = 6.1% ; average error$_{Nrmse}$ in 3 devices scenario = 5.7%). Additionally, one can notice that the closer to the devices, the better correlation coefficients and error levels (Table 4). In general, the numerical predictions succeed in reproducing shapes and magnitudes of the wake decay along the channel. The model also reproduces the inter-space accelerations occurring in the lateral gaps between the devices. Eventually, in the light of the optimum uncertainty values (i.e. Section 5.2), the match between experiments and simulations can be considered as satisfactory. Nonetheless, obvious discrepancies persist and are worth being examined.

The first discrepancies come from the inability of the numerical method to reproduce the lateral asymmetry present in the experimental data. However, considering the geometrical features of the experimental set-up (Figure 35), this asymmetry should not exist or, if related to wake meandering, should have been smoothed by the time averaging routinely performed on such data acquisition. Besides, the differences in velocity deficit at the lateral ends in both cases seem to indicate a lateral anisotropy of the flume features; anisotropy not taken into account in the simulation parameterization. These considerations tend to minimize the actual error levels carried by the simulation and also bring more confidence to the simulated results.

		r	rmse	Error$_{Nrmse}$ (%)
5 diameters	2 discs	0.966	0.0128	4.5
	3 discs	0.938	0.0202	4
7 diameters	2 discs	0.898	0.0174	6.9
	3 discs	0.9	0.0170	6.25
9 diameters	2 discs	0.879	0.019	7
	3 discs	0.87	0.0209	6.8

Table 4: Statistical results of correlation and error – Simution vs experimental data

The discrepancies also seem to increase with the distance downstream of the devices, indicating a difference in the far wake recovery between experiments and simulations. It appears that the wake recovery is shorter in the experiments than in the simulations. It has been observed by others that the higher the turbulence level, the shorter the wake recovery (Churchfield et al., 2011; MacLeod et

al., 2002; Baker et al., 1985). Knowing that the ambient turbulence intensity fluctuates between 6% and 8% throughout the channel, one can suppose that the numerical homogenous ambient turbulence level initially imposed in the simulation should be higher or vary as a function of the distance along the channel. In the simulations, the ambient turbulence intensity before device deployment has been set to 6.5% throughout the channel. In the light of the previous analysis, one can confirm that the presented TCT representation method simulates wake interactions within device arrays to reasonable accuracy.

6.3.2.   Wake Interactions – Inter-array Wake Properties

Myers *et al.* (2011) used the 2 disc experiment described in Section 6.2 to investigate and characterize the inter-array wake properties (Myers et al., 2011). For this investigation, they measured the flow velocity as well as the turbulence intensity (Eq.(95)) of the flow along two mid-depth lines: the centre line and a parallel line offset by half a rotor-diameter in the *y*-direction from the centre line, referred to as the offset line (Figure 38).
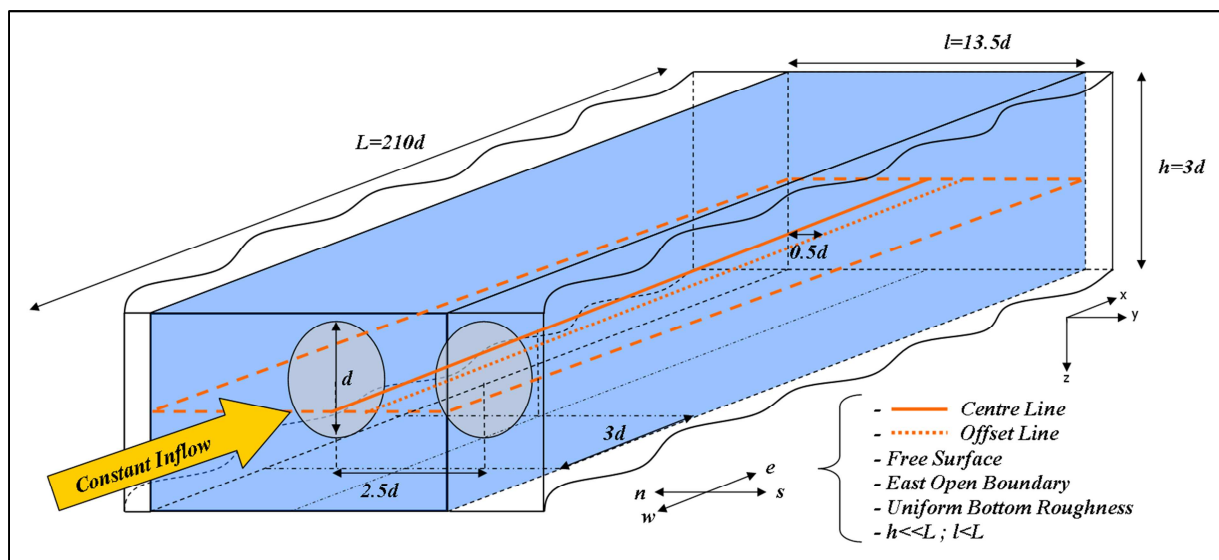
*Figure 38: Idealized channel, 2-disc case - This conceptual diagram represents the 2-disc test geometry and dimensions as well as the locations where centre and offset lines (orange solid and dotted lines) have been taken.*

In this section, comparisons between these experimental measurements and their simulated equivalents (Figure 39 & Figure 40) are studied. Figure 39 displays experiment and simulated flow

velocity along centre and offset lines. Along the former, the matching between the experiment and simulated values reaches the values of $r^2 = 0.81$ and $error_{Nrmse} = 3.6\%$; along the latter, the matching between the experiment and simulated values reaches the values of $r^2 = 0.92$ and $error_{Nrmse} = 2.9\%$. Although the statistical values are similar to those achieved in Section 5.2 and thus validate the accuracy of the simulation, one can observe differences between experiment and simulated wake recoveries along both lines.
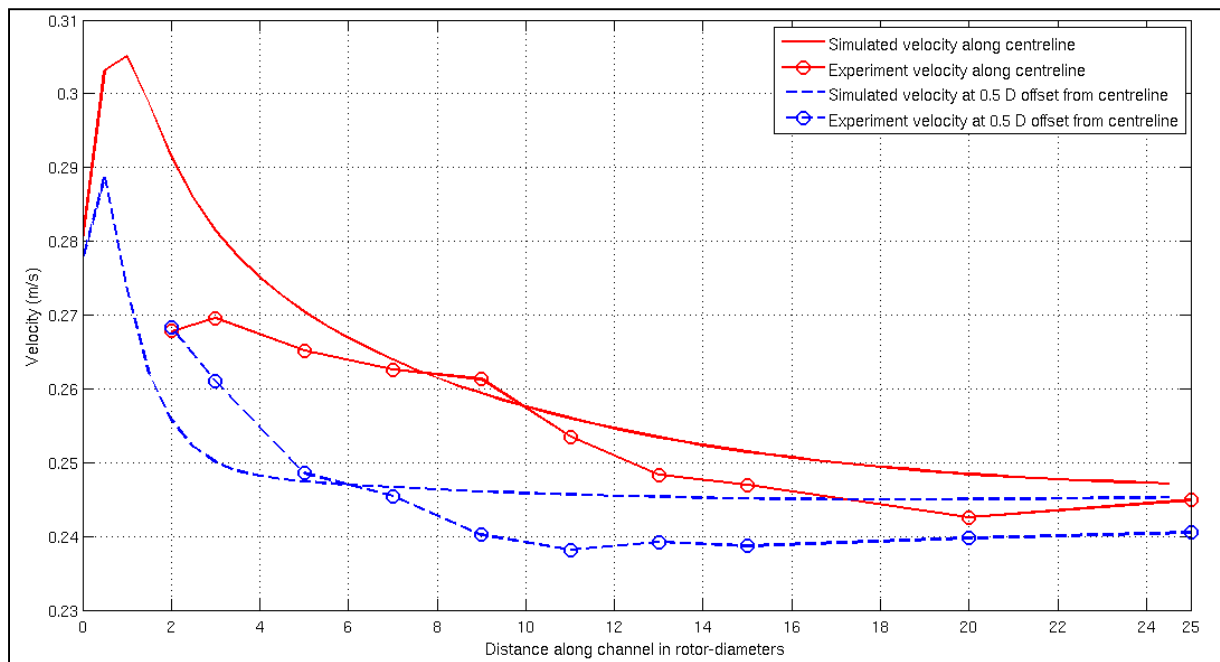
Figure 39: Flow velocities along centre line and offset line, 2-disc case – The graphs permits the comparison between experiment (marked lines) and simulation (unmarked lines) velocities along the centre line (solid lines) and the offset line (dashed lines).

Figure 40 displays experiment and simulated flow TIs along the centre and offset lines. Along the former, the matching between the experiment and simulated values reaches the values of $r^2 = 0.74$ and $error_{Nrmse} = 12.3\%$; along the latter, the matching between the experiment and simulated values reaches the values of $r^2 = 0.66$ and $error_{Nrmse} = 14.5\%$. The statistical values, more especially the error values, suggest a non-negligible level of uncertainty on the simulated values although they are not far from the optimum values of uncertainty mentioned in Section 5.2. Additionally, the evolution of the TIs along the channel seems significantly different in both experiment and simulation.
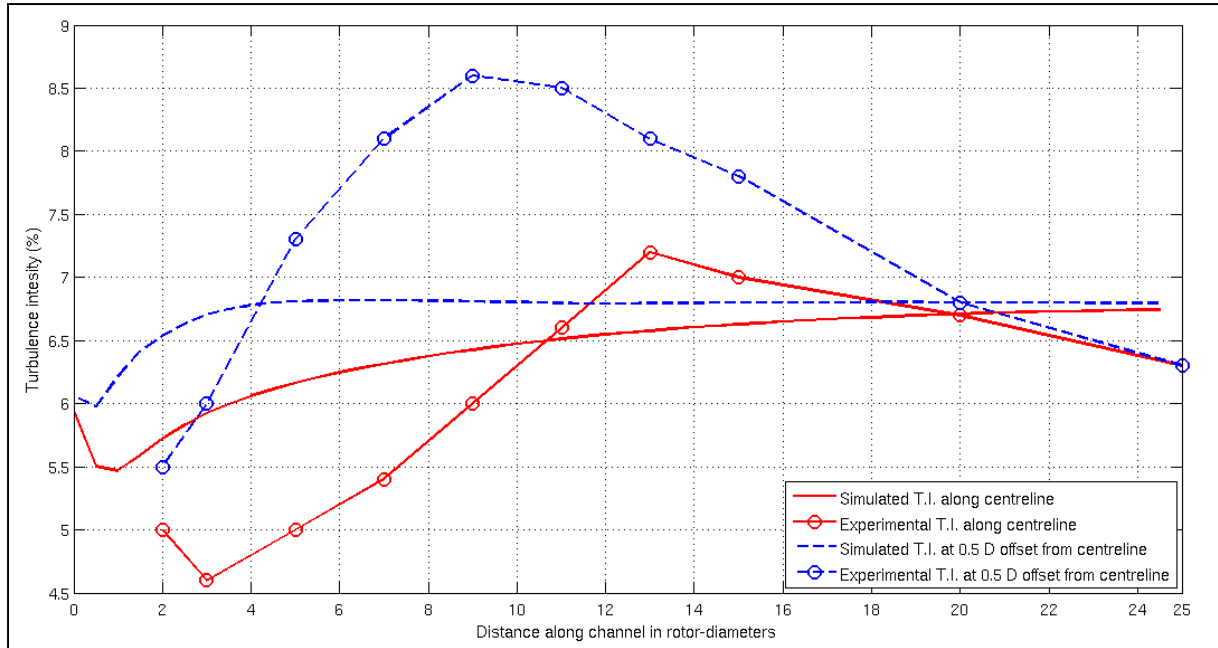
*Figure 40: Turbulence intensity along centre line and offset line, 2-disc case – The graphs permits the comparison between experiment (marked lines) and simulation (unmarked lines) turbulence intensities along the centre line (solid lines) and the offset line (dashed lines).*

In Figure 39, between 0 and 10 diameters along the centre line, the experimental velocity decay rate is lower than that simulated, and this coincides with lower experimental TI than that calculated by numerical simulation (Figure 40). On the contrary, between 10 and 20 diameters along the centre line, the experimental velocity decay rate is higher than simulated the one (Figure 39) and coincides with higher experimental TI than the simulated one (Figure 40). The same discrepency is observed along the offset line except that the changing point of wake decay rate is located at 4 diameters downstream of the front row instead of 10 diameters for the centre line values (i.e. Figure 39 & Figure 40). These observations are similar to the CFD results of Churchfield et al (2011) which show that the persistence and intensity of the rotor wake reduces as ambient turbulence levels increase and vice versa (Churchfield et al., 2011; MacLeod et al., 2002; Baker et al., 1985). Even though this phenomenon does not explain the origin of the discrepancies between experiment and simulation inter-device features, it shows the coherence of the discrepancies observed between experimental and simulated results. Moreover, discrepancies in TI are amplified by the disagreement

98

in terms of velocities between the experiment and the simulation and therefore do not illustrate with exactness the capacity of the method for reproducing device induced turbulences.

Several explanations can be suggested to understand the discrepancies in TI. Firstly, one of the few limitations of the present modelling platform is the fact that, although the hydrodynamics is fully 3-dimensional in the vicinity of the rotor, the present model does not account for the horizontal shear in the TKE production. Horizontal shear is merged into the eddy viscosity parameterization and consequently does not affect the turbine-induced TKE and TI (Eq. (16), (17), (18) & (19)). At this stage of development, this feature is unavoidable and is caused by the splitting between horizontal and vertical mixing present in ROMS kernel (Roc et al., 2013). Unfortunately this design limitation is imposed by ROMS implementation and is necessary for reducing computational cost. The second explanation for the discrepancies in TI might be linked to the difference in the means to obtain TI values in both experiment and simulation. As mentioned in Section 5.2, the experimental values of TIs were measured with a conventional Doppler velocimeter (Eq.(95)) whereas the simulated TIs derive from the simulated k and U (Eq.(96)). Typically, the experimental equipment integrates a wide range of velocity fluctuations as components of the turbulence activity, whereas the turbulence closure model used in the numerical approach sets an artificial threshold below which velocity fluctuations are considered as turbulence. Moreover, (Myers et al., 2011) Myers stresses that higher order flow effects as well as turbulent structures in tidal currents cannot be accurately defined using conventional Doppler profilers. Nonetheless, in the light of the optimum uncertainty values (i.e. Section 5.2), the agreement between experiments and simulations is reasonable.

6.4. Discussion – Turbine Wake Interactions

The present method for representing TCT within an ocean circulation type model capable of performing regional scale simulations is demonstrated here for modelling of TCT wake interactions. Two physical scale experiments are numerically reproduced on the present platform. The first experiment consists of a single row of two devices deployed across a rectangular channel. The second consists of a two-row layout of three devices where the front row is composed of two devices

and a single device downstream. The location of the downstream device has been deliberately positioned at the mid-point between the two upstream devices in order to exploit the flow acceleration occurring in this area. The proposed model succeeds in reproducing the inter-device flow increase of the 2-device case (i.e. Figure 39) and the wake interactions in both 2 and 3 device cases (i.e. Figure 36 & Figure 37). Laterally as well as in the main flow direction, the match between experimental and simulated flow velocities shows satisfactory results (i.e. Figure 36 and Figure 37); on average[4] the correlation coefficient reaches $r^2 = 0.85$ and the error level reaches $error_{Nrmse} = 4.6\%$. Surprisingly, in the light of these results and despite the fact that ROMS does not explicitly account for the horizontal shear induced by the presence of the devices in the TKE dynamics, inter-device momentum behaviour seems to be simulated to a reasonable degree of accuracy by the present approach.

While inter-device momentum aspects do not seem to suffer from the ROMS horizontal/vertical mixing splitting described in Section 3.1, inter-device turbulence aspects perform poorly in comparison ($r^2 = 0.74$ and $error_{Nrmse} = 12.3\%$). Consequently, this level of error in prediction of the turbulence behaviour will have to be kept in mind when using the present platform to assess TI and/or turbulence induced loading within TCT farm. Yet, this level of discrepancy has to be put in perspective with the optimum correlation level that can be expected from turbulence quantity comparisons between simulated results and results recorded in the Chilworth flume (i.e. Section 5.2). The proposed TCT representation method has proved its ability to simulate with reasonable accuracy TCT wake interactions over the scale of interest required for TCT layout optimisation.

---

[4] Based on the average values of correlation coefficients and error levels obtained for Figure 36, Figure 37 and Figure 39.

Chapter 7. Power Assessment - Quantifying Layout Effects

7.1. Quantifying the Power Capture

Traditionally turbine-array power-assessment strategy follows the following sequence: first the power available in the unperturbed flow is estimated, then the amount of power captured by the device is quantified and finally the latter is multiplied by the number of devices present in the layout or the sum of the rotor surface is determined (Bryden & Couch, 2007; Garrett & Cummins, 2005; Pham & Martin, 2009). In order to have a more precise picture of the power capture of a TCT farm, wake turbine interactions have recently been taken into account in the power assessment strategy (Li & Calisal, 2010; Ahmadian & Falconer, 2012). This generally consists in applying coefficients depending on the turbine locations within the farm, instead of coarsely multiplying the power capture of a standalone device by the number of devices composing the farm. Unfortunately, most of the turbine interaction relationships are based on empirical approaches with limiting assumptions leading to non-negligible deviation from realistic scenarios (Li & Calisal, 2010).

Using the model proposed here, one can investigate wake interactions with precision and test numerous farm layouts in a reasonable time. As a result, in the case of a unidirectional flow, the optimum layout can be found by placing rows of TCTs depending on the upstream array effects in the same manner as was used to determine the second row of the 3 disc case from the results of the 2 disc case (i.e. Section 6.3.1 & 6.3.2). Nonetheless, this implies that a new power assessment strategy

should be developed since the available power is different from one row to another. In other words, each array deployment will change the flow characteristics, as well as the power in the flow available to the next row downstream. In this section, the 2 and 3 disc cases described in Chapter 6 are used as basis for investigating an appropriate power assessment strategy.

7.2. Power Capture Assessment Strategy

By definition, the power captured by a TCT deployed in a flow corresponds to the flow rate through the disc multiplied by the pressure drop across the disc (Bai et al., 2009):

$$Power\ Capture\ = A_d U_d (p_d^+ - p_d^-) \equiv [\text{Watt}] \tag{100}$$

Although Eq. (110) does not account for any mechanical loss nor device yield, it gives a direct and accurate estimate of the power extracted by a TCT. According to the momentum theory (i.e. Eq. (40)), the expression of thrust force (i.e. Eq. (41)) and the definition of the induction factor (i.e. $a = \frac{U_\infty - U_d}{U_\infty}$), the pressure drop across the disc can be expressed as follows:

$$(p_d^+ - p_d^-) = 2\rho U_d (U_\infty - U_d) \tag{101}$$

Consequently, the power capture (i.e. Eq. (100)) can be rewritten as follows:

$$Power\ Capture = 2\rho A_d U_d{}^2 (U_\infty - U_d) \tag{102}$$

This formulation of the power capture is very interesting in our case since, contrary to most existing methods for TCT representation, the present method gives a direct and accurate estimate of the flow velocity passing through the rotor disc, U_d. However, what needs to be carefully defined is the meaning of U_∞ within a multi-array device-layout. U_∞ is defined as the unperturbed flow velocity and/or the flow velocity far upstream of a given device which, in the case of a standalone device system, amounts to the same thing. In a multi-device system, defining U_∞ turns out to be more complex.

7.3. Power Assessment and Wake Perturbations

We first consider the 2-disc case described in Chapter 5. Here, determining the value of U_∞ required to assess the power capture for each deployed device is achieved by measuring, at the

deployment locations of both devices, the flow velocity in the channel without the devices present.

This straightforward protocol leads to the following results:

	Turbine n°1	Turbine n°2
U_∞ (m. s^{-1})	0.27	0.27
U_d (m. s^{-1})	0.053	0.053
Power Capture (W)	0.013	0.013

Table 5: Power capture assessment – 2 disc case

Now considering the 3-disc case, there are two alternative approaches to determining the value of U_∞ required for the power capture assessment of the third disc located downstream of the 2 disc row (Figure 35).). Using the definition of U_∞ as the unperturbed flow velocity, then U_∞ for the third disc would be the same as for the front row discs (i.e. according the simulated results from the 2-disc case, $U_\infty = 0.27$ m. s^{-1}). However, one can consider that the true flow power available for the third disc is that at its intended location in the wake of the 2 upstream devices. Using this approach, from the 2 disc case simulation, the U_∞ equals to 0.28 m. s^{-1} (i.e. Simulated velocity along the centre-line at 3 diameters downstream of the first row). These different approaches result in different power capture assessment and thus different strategies layout optimization.

|	Turbine n°1	Turbine n°2	Turbine n°3	
			unperturbed flow	*wake perturbed flow*
U_∞ (m. s^{-1})	0.27	0.27	0.27	0.28
U_d (m. s^{-1})	0.053	0.053	0.055	0.055
Power Capture (W)	0.013	0.013	0.013	0.014

Table 6: Power capture assessment – 3 disc case

The implications of using these different approaches for determining U_∞ are shown in Table 6. By considering U_∞ as unperturbed flow, the increase in power capture between the front and

downstream devices reaches 5.5% whereas, by considering U_∞ as a wake perturbed flow, the increase is 11%. In other words, the increase in power capture due to the present layout optimization can be misrepresented by a factor of two if upstream wake perturbations are not accounted in the power assessment strategy.

7.4. Next Generation TCT Array – Device Layout Strategy

In the light of power capture assessments discussed in Chapter 7, accounting for upstream TCT interactions appears to be compulsory in order to find out optimum layout of the next row downstream. The proposed numerical tool provides highly interesting insight for answering this issue and developing a device layout strategy. Let's consider the 3 disc case (i.e. Figure 35) and let's imagine that a third row of device were to be deployed somewhere downstream of the second one. The question being "where would be the optimum places in this one directional flow for siting devices?". The currently admitted answer to this question would be to deploy a row with a similar lateral device-spacing as the front row somewhere downstream the second row device (Myers & Bahaj, 2012). Thanks to the proposed model and a row-by-row deployment approach this latter assumption shall be verified.

Figure 41 displays flow velocities, over a XY plane taken at the hub height, resulting from the three devices interactions. According to the colour-scale and knowing that the unperturbed flow velocity is 0.26 m/s, dark red areas represent areas of interests in terms of power capture since they are subject to flow increase. The dark red zone hemmed in by the three devices cannot be considered as a potential site of deployment for another TCT though. It would mask the second row device and annihilate the acceleration benefit occurring in the front row inter-space.

Figure 41: Colour-map of flow velocity (m/s) – XY mid-depth plane

Another parameter necessary to consider in layout deployment strategy is the enhanced flow turbulence intensity generated by the upstream TCT rows. Above a TI of 14%, standard TCT design components have to be adapted to the turbulent flow induced fatigue loading the turbine blades and structure (McCann, 2007). For this case, assume that the devices available for deployment cannot be different in design. Figure 42 displays TI resulting from the three devices interactions, in the wake of the second row, over a XY plane taken at the hub height.
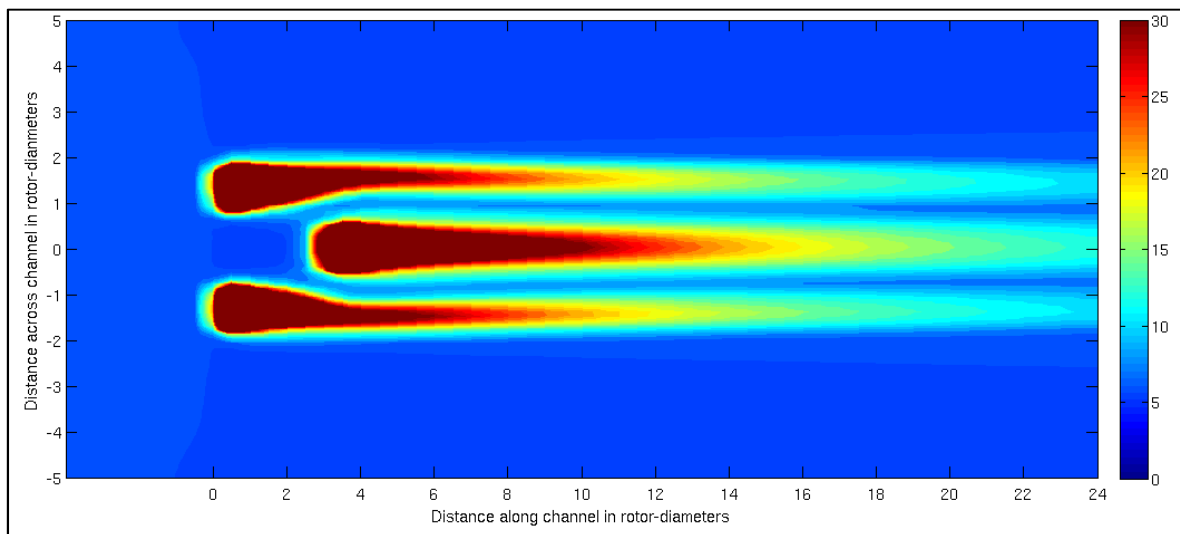

Figure 42: Colour-map of TI (%) – XY mid-depth plane

Figure 43 over-plots velocity contours normalised by the initial free-stream velocity (in %) and the areas where the TI is greater than 14% (green areas). Considering McCann's study and the currently admitted deployment strategy, the next row of devices laterally aligned with the 2 front row devices could be potentially deployed anywhere from 18 diameters downstream onwards. However it seems more optimal in terms of device spacing and available flow speed to deploy the next row devices at 4 diameters downstream, anywhere at least 3 diameters laterally away from the centre-line. This goes against the currently admitted deployment strategy which consists in laterally aligning the third row with lateral positions of the front row devices somewhere downstream the second row device. Ultimately in order to confirm the relevancy of third row positioning, the upstream and downstream influences due to the presence of the third row must be simulated and assessed. A smart positioning of the third row could potentially redirect the downstream flow surges and thus extend the potential deployment area for the next rows. Moreover, in terms of power production, it might be worth considering increasing the number of devices constituting the first two rows instead of deploying a third row of devices. In any case, these scenarios are hardly to be resolved a-priori and thus need to be computed and to account for site specificities before being assume as the optimum layout solution.

Figure 43: Combined colour-map of TI and normalised flow velocity contours (in %) – XY mid-depth plane. green areas correspond to TI>14% and flow velocity contours are normalised by the initial free-stream velocity.

The same kind of positioning optimization could be made vertically. However, in this peculiar case, the high blockage ratio does not allow much variation on the vertical placement of the device. The blockage ratio is defined as the ratio between the size of the rotor and the total depth and reaches in this case 1/3. Additionally, it is worth noting that the third row of any given layout is bound to experience negative effects related to upstream wake interactions and that most of the potential deployment sites are narrow. Consequently, the choice in the distance downstream of the upstream second row is more likely to be driven by a cost/benefit approach (Myers & Bahaj, 2012).

7.5. Discussion - Quantifying Layout Effects

The present method for representing TCT within an ocean circulation type model capable of performing regional scale simulations is demonstrated here for modelling of TCT wake interactions. Two physical scale experiments are numerically reproduced on the present platform. The first experiment consists of a single row of two devices deployed across a rectangular channel. The second consists of a two-row layout of three devices where the front row is composed of two devices

and a single device downstream. The location of the downstream device has been deliberately positioned at the mid-point between the two upstream devices in order to exploit the flow acceleration occurring in this area. The proposed model succeeds in reproducing wake interactions and inter-device flow acceleration in both cases. Laterally as well as in the main flow direction, the match between experimental and simulated flow velocities shows satisfactory results; on average[5] the correlation coefficient reaches $r^2 = 0.85$ and the error level reaches $error_{Nrmse} = 4.6\%$. Surprisingly, in the light of these results and despite the fact that ROMS does not explicitly account for the horizontal shear induced by the presence of the devices in the TKE dynamics, inter-device momentum behaviour seems to be simulated to a reasonable degree of accuracy by the present approach.

While inter-device momentum aspects do not seem to suffer from the ROMS horizontal/vertical mixing splitting described in Section 3.1, inter-device turbulence aspects perform poorly in comparison ($r^2 = 0.74$ and $error_{Nrmse} = 12.3\%$). Consequently, this level of error in prediction of the turbulence behaviour will have to be kept in mind when using the present platform to assess TI and/or turbulence induced loading within TCT farm. Yet, this level of discrepancy has to be put in perspective with the optimum correlation level that can be expected from turbulence quantity comparisons between simulated results and results recorded in the Chilworth flume (i.e. Section 5.2). The proposed TCT representation method has proved its ability to simulate with reasonable accuracy TCT wake interactions over the scale of interest required for TCT layout optimization.

This section also highlights alternative methods for device power assessment when considering TCT farm layout optimization. Although mechanical losses and actual electrical power yield are not included in the present investigation, a formula for the potential power capture per TCT has been developed that uses velocity features predicted by the proposed numerical tool (Eq. (115)). This power assessment approach raised the issue of layout optimization strategy based on power

---

[5] Based on the average values of correlation coefficients and error levels obtained for Figure 36, Figure 37 and Figure 39.

capture maximisation and revealed that simulation of each upstream row is necessary in order to appreciate the impacts on downstream rows. Additionally, other vectors of power capture optimization, such as blade and rotation controls, have been omitted here, but should be considered as part of a full row by row optimization strategy. In this way, depending on the momentum and turbulence characteristics of the upstream row perturbations, design features such as pitch angle, blade shape and electrical control could be tuned to enhance power capture and reduce array layout expanse.

Chapter 8. Scaling Characteristics

8.1. Introduction - Scale Applicability

In Chapter 5, the present TCT platform has been shown to have a numerically consistent implementation structure and to be able to accurately reproduce hydrodynamic perturbations induced by a standalone device. Test series, presented in Chapter 6, investigated and proved the ability of the proposed numerical tool to simulate precisely wake interactions within different TCT layout deployments at laboratory scale. Ultimately a numerical tool for regional scale TCT array optimization has to prove its ability to simulate TCT farm perturbations at realistic environment scale in order to be considered as suitable for real-life applications, based on real sea observations. However, as we mentioned previously, in the absence so far of such power plants, in-situ observational information are lacking. To compensate for this, an analytical benchmark test has to be used.

Accordingly, in this section, the accuracy of the present numerical tool for TCT arrays optimization in reproducing TCT real-scale wake decay has been investigated thanks to an analytical exercise of up-scaling. By comparing referenced dimensionless quantities from physical scale experiment with their corresponding real-scale simulation, one can a-priori assess the accuracy of the present model in dealing with real-flow forcing and perturbations. The results from this test indicate that the proposed numerical tool for TCT arrays optimization can be considered suitable for realistic applications.

8.2. Analytic Benchmarking and Simulation Features

In order to validate the applicability of the proposed turbine modelling method to realistic flows and configurations, the numerical TCT representation method has been applied to a simplified case having the same flow features as the laboratory tests described in (Myers & Bahaj, 2010; Roc et al., 2013) but at scales which are representative of a full scale realistic case (Thyng & Riley, 2010). In this way, the ability of the adapted code to provide reasonable results will be taken as an indication that the approach proposed is valid for full scale simulations. To do so, the flume-experiment characteristics, including dimensions, forcing and flow features have been scaled-up according to Froude scaling.

$$Fr = \frac{\|\vec{v}\|}{\sqrt{gd}} \qquad (103)$$

Here, g corresponds to the acceleration due to gravity and v to the kinematic viscosity of water. The aim is to up-scale the depth averaged velocity from 0.33m/s to 2.5m/s. Accordingly, the dimensions of the channel and the turbine have been resized by using the Froude number, Fr (Eq. (103)).

	Channel features				Turbine feature
	Length (m)	Width (m)	Depth (m)	Flow velocity (m.s^{-1})	Rotor-diameter (m)
Flume-scale	21	1.35	0.3	0.33	0.1
Full-scale	1205.2	77.5	17.2	2.5	5.7

Table 7: Channel and turbine features of both flume and full scale simulations

In physical modelling, it is well-known that Froude and Reynolds scaling cannot be satisfied simultaneously.

$$Re_{num} = \frac{\|\vec{v}\|L}{v_{eddy}} \qquad (104)$$

Here, L corresponds to a characteristic length of the system and v_{eddy} to the eddy viscosity. Nonetheless, in numerical modelling there is no such limitation and the "numerical Reynolds number" Re_{num} (Eq. (115)) can be used to up-scale the eddy viscosity v_{eddy} and therefore partially

account for the turbulent regime discrepancy between the models. Numerical features applied to both flume-scale and up-scaled simulations are exactly the same as those used in the wake interaction investigation simulations (i.e. § 3.1.) but the bottom roughness has been set to zero. However in the present set up, in contrast to the wake interaction investigation simulations, only one device is deployed.

Based on Froude scaling, it is expected that dimensionless momentum-based quantities will exhibit similar results to those observed in the flume-scale experiments (Figure 44). This former statement is the cornerstone of scale modelling theory. In this manner, velocity deficit should have the same order of magnitude, both in the flume-scale simulation and the related real-scale simulation. However, knowing that the Reynolds scaling cannot be achieved, one should expect different turbulent regimes between the flume-scale and the full scale simulations. Consequently, discrepancies in terms of wake decay rate between the two simulations should be observed (Churchfield et al., 2011; MacLeod et al., 2002; Baker et al., 1985). The predictions of velocity deficit, $U_{deficit}$, are used to compare the model scale flume with the full scale realistic cases, this $U_{deficit}$ has been chosen in order to verify the dimensional consistency and relevancy the momentum behaviour induced and computed by the device representation method. For the sake of clarity, only velocity deficits along the rotor centre-line (Figure 44) will be shown in the present document.

8.3. Up-Scaling Results

Despite the clear similarities and high correlation values (r= 0.998 ; error$_{Nrmse}$=4.5%) between the simulated flume-scale and real-scale velocity deficits along the rotor centre-line (Figure 44), differences between the two curves are visible. Along the centre-line, from upstream of the disc location to half a diameter downstream of it as well as beyond seventeen diameters downstream, both flume and full scale velocity deficits match perfectly. This shows that, from a dimensionless aspect, inflow, far-wake recovery and turbine-induced momentum sink are identical in both flume and full scale simulations. The discrepancy lies in the wake recovery between half a diameter and ten

diameters downstream of the device. The wake recovery in this area is known to be strongly linked with mixing phenomena and ambient turbulence levels (Burton et al., 2008).
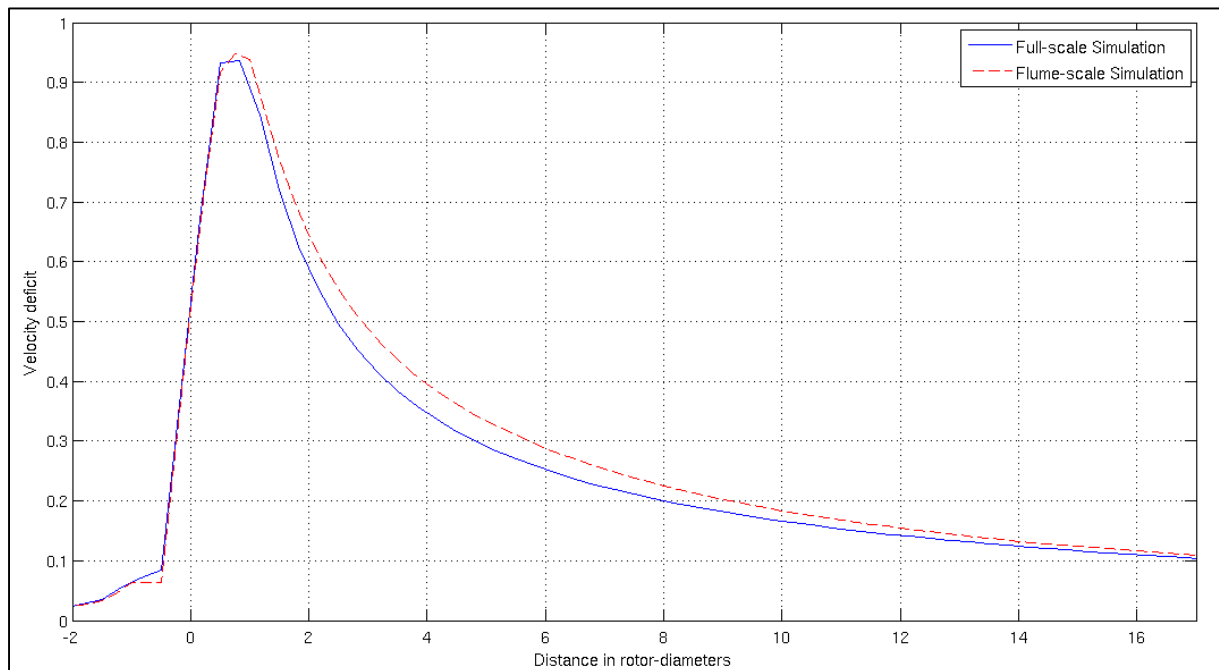

Figure 44: Velocity deficits along rotor-centre line, "Up-scale" case – The graphs permits the comparison between the simulated flume-scale (red solid line) and up-scale (blue marked solid line) dimensionless velocity deficits along the rotor-centre line.

8.4. Discussion - Scale Applicability

As predicted in Section 8.2, the discrepancy is significant only for the wake recovery rate. In fact, Froude scaling permits an equivalent momentum flow-regime between two models of different sizes, but does not maintain the same turbulent flow-regime in spite of the partially eddy viscosity compensation. As previously mentioned, it has been shown that the higher the turbulence intensity, the faster the wake recovery (Churchfield et al., 2011; MacLeod et al., 2002; Baker et al., 1985). In the present case, the Reynolds number related to the flume Re_{flume} is less than the Reynolds number related to the up-scaled flume $Re_{up-scale}$, in other words a more turbulent regime exists in the "up-scale" case. Accordingly, one can observe in Figure 44 that the wake recovery is slower in the flume-scale case and that the order of magnitude in peak of momentum deficit, occurring at the location of the device rotor, has been conserved during the up-scaling. These results are in

accordance with the theoretical predictions and therefore suggest that the method is applicable whatever the dimensions of the problem.

Chapter 9. Test Case Application – TCT Array Deployment in the Puget Sound

9.1. The Puget Sound - a Promising Site for Commercial Scale TCT Array Deployment

A model for simulating TCT has been developed. The implementation used to inject it into ROMS model platform has successfully passed standards numerical consistency tests (i.e. Section 5.3.1 & 5.3.2). By satisfactorily reproducing experimental results, it has proven its ability to simulate turbine induced hydrodynamics and wake device interactions (i.e. Section 5.3 & 0). Finally, thanks to a theoretical up-scaling test (i.e. Section 5.3.3), the modelling technique is shown to be applicable whatever the hydrodynamic system dimensions being tackled (i.e. Section 8.3). Therefore this numerical platform is in a form such that its next logical development step is to apply to a realistic TCT farm deployment scenario. This section describes such an application and demonstrates how the present numerical tool can be used for power and environmental impact assessments as well as proposing a method in which the model can be utilised for array optimization. This task has been performed in collaboration with researchers at the University of Washington (UW) and particularly with Dr. K. M. Thyng. The UW team conducted extended studies on a promising site for commercial

9.1. The Puget Sound - a Promising Site for Commercial Scale TCT Array Deployment

scale TCT array deployment, namely Admiralty Inlet, main entrance for Puget Sound (i.e. Figure 45). Applying the modelling technique to this well-studied site provide an advantageous opportunity for collaboration. The high potential of this area comes from its peculiar bathymetric and hydrodynamic features as well as its location. Indeed, the Puget Sound of western Washington State is a deep, fjord-like estuary of high-speed tidal currents (up to 2.5 m/s) with several large cities, including Seattle and Tacoma, on its shoreline (i.e. Figure 45) (Thyng & Riley, 2010). Its proximity to a large population allows short transmission lines. The Sound supports about 3.5 million people[6], a much higher population density than in the eastern half of the state, where much of the existing (conventional hydroelectric and wind) electricity is produced (Thyng & Riley, 2010).
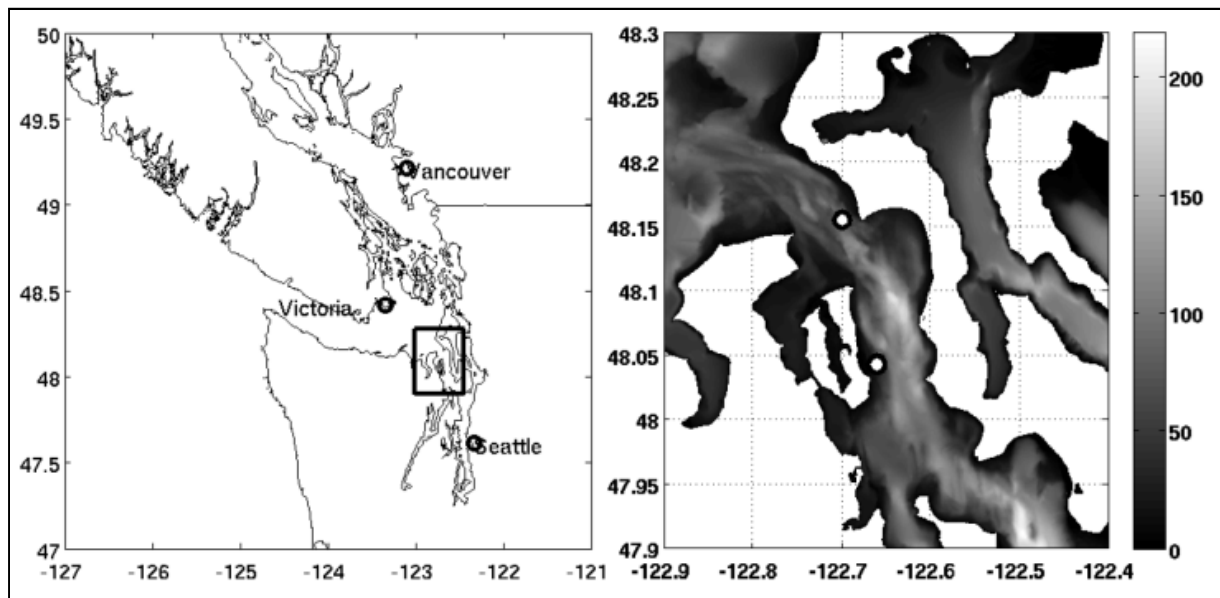
Figure 45: Coastline map of north-western Washington State, part of Vancouver Island and Vancouver, B.C. The black box in the Puget Sound shows the area of interest, Admiralty Inlet, which is plotted on the right with shading representing bathymetry. Lighter grey represents deeper water and two white circles show the approximate location of two pilot tidal hydrokinetic turbine projects currently being pursued. After (Thyng & Riley, 2010)

The site resource evaluation reported in Thyng & Riley (2010) has been performed as suggested by the European Marine Energy Centre (EMEC). Determining the influence of the bathymetric and coastline features on the utility of any given location in Admiralty Inlet for TCTs is necessary to know before placing a significant number of turbines. It is desirable to quantify, through

---

[1]   [6] City of Seattle (2010). The greater Seattle datasheet [Online]. Available: http://www.seattle.gov/oir/datasheet/demographics.htm

standardised metrics, what flow conditions create the "best" turbine site a priori (Thyng & Riley, 2010). The potential of Admiralty Inlet has been assessed by a series of metrics in order to identify the best location for TCT farm deployment. The European Marine Energy Centre (EMEC) proposed that vertical shear, turbulent eddy intensity, asymmetry of currents on ebb versus flood, peak sustained velocities, velocity distribution and mean kinetic power density be measured over a tidal cycle (Legrand, 2009) in order to evaluate scientifically and consistently potential tidal hydrokinetic energy sites. Analysis of Acoustic Doppler Current Profiler (ADCP) data from Admiralty Inlet in terms of turbine siting metrics (Polagye et al., 2007; Previsic et al., 2008; Gooch et al., 2009) were performed prior to Thyng & Riley's study. In this section, the focus is put on two of these metrics: kinetic power density and asymmetry of flow. The primary prerequisite for any TCT farm site is sufficient currents to produce a viable amount of power. Mean kinetic power density allows the quantification of the latter and is calculated as followed:

$$\Upsilon(t) = \frac{1}{2}\rho\|\overrightarrow{v_H}\|^3 \tag{105}$$

Where ρ is the depth-averaged density at the location and $\|\overrightarrow{v_H}\|$ is the speed calculated from the east-west (u) and north-south (v) velocities, such that $\|\overrightarrow{v_H}\| = \sqrt{u^2 + v^2}$. The mean kinetic power density is then found by averaging kinetic power density over one tidal cycle:

$$\Upsilon_T = \frac{1}{T}\int \Upsilon(t)dt \tag{106}$$

where T is the period of one tidal cycle. Bedard et al. (2006) suggested that the threshold for economic viability is a kinetic power density higher than 1 kW/m² (Bedard et al., 2006).

Bidirectionality, the "spread" of directions on each flood and ebb, and the strength of power generation on ebb versus flood tides are three usual quantities allowing the characterisation of flow asymmetry. The bidirectionality of tidal flow at an (x,y) point consists in the difference of mean direction between ebb and flood tides. The asymmetry parameter can then be calculated as (Gooch et al., 2009):

$$\Delta\theta = |\theta_{ebb} - \theta_{flood} - 180°| \tag{107}$$

According to this definition, $\Delta\theta = 0$ corresponds to a perfectly bidirectional flow. Spread in Tide Direction, which is closely linked to the bidirectionality parameter $\Delta\theta$ is a measure of the spread in direction at each point. After calculating the mean angle for each (x,y) point on ebb and flood, we can also calculate the standard deviation of that mean angle, θ_{ebb} and θ_{flood}, giving us another measure of bidirectionality throughout a tidal semi-cycle.
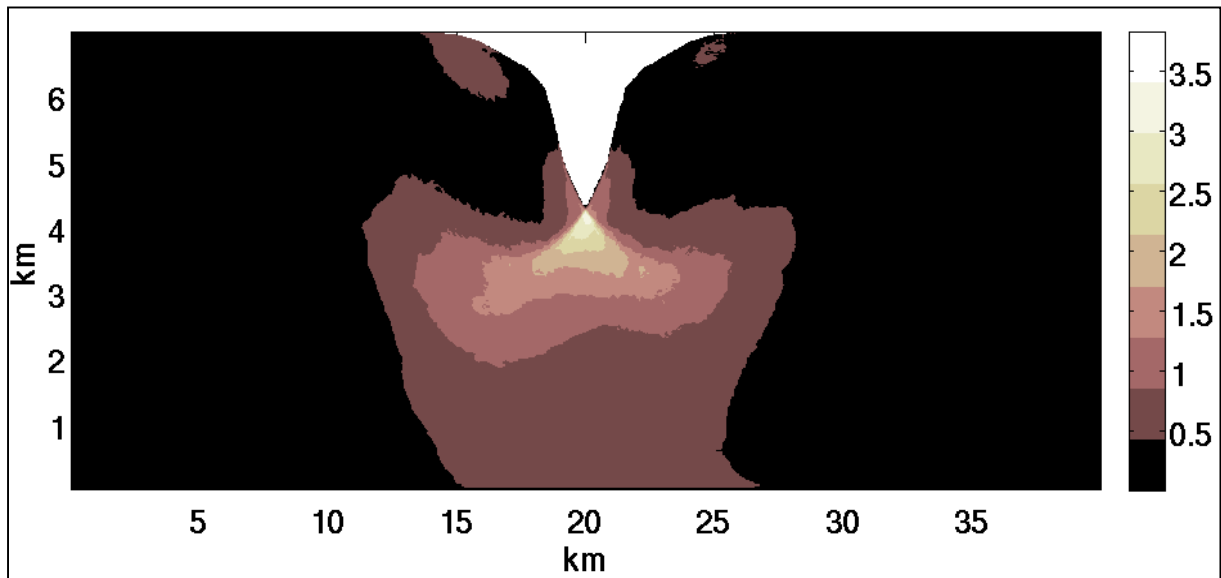
*Figure 46: Top-down view contours of the mean kinetic power density Y_T (kW/m²), at a hub height of 50 meters above the seabed. The headland is shown in white and x and y axes are in meters. AfterThyng (2012)*
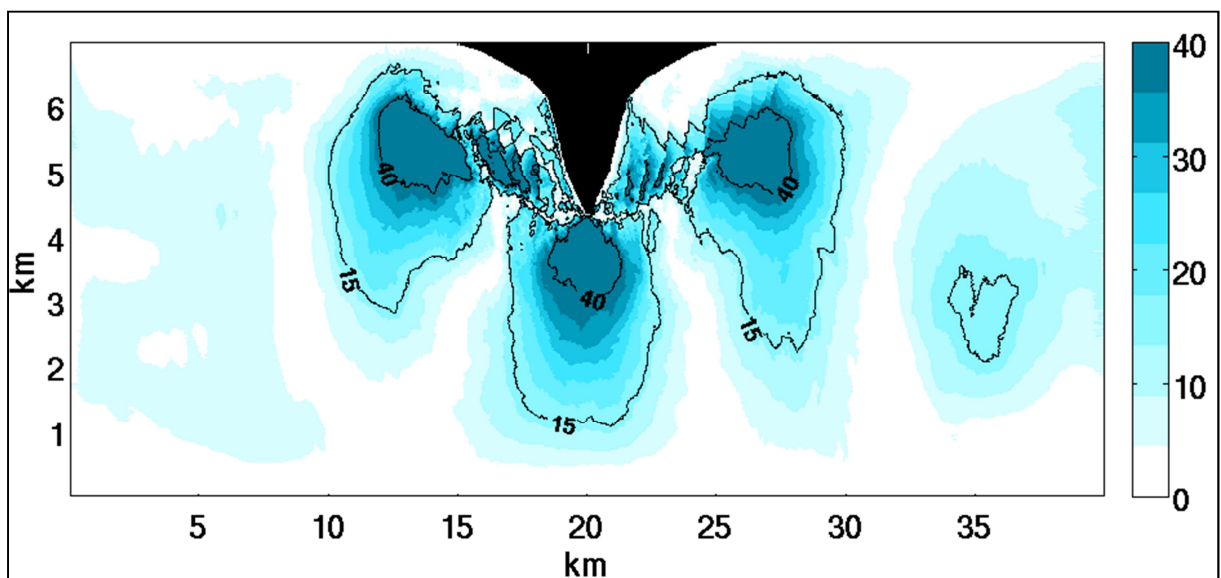

Figure 47: Top-down view contours of the bidirectionality parameter Δθ (degrees), at a hub height of 50 meters above the seabed. The headland is shown in black and x and y axes are in meters. After Thyng (2012)

9.1. The Puget Sound - a Promising Site for Commercial Scale TCT Array Deployment

Thanks to analysis of the initial case without turbines (Thyng & Riley, 2010; Roc et al., 2012), one can find that the area of highest mean kinetic power density, Υ_T, and therefore of highest potential power-generation, is off the tip of the headland centred around the coordinates $(x: 20\ km, y: 4\ km)$ (up to $\Upsilon_T = 4\ kW.m^{-2}$, i.e. Figure 46). This local increase in power density is mostly due to the amplification of speed due to the presence of the headland. Accordingly and despite the fact that the currents in this area are not particularly bidirectional ($\Delta\theta \cong 40$), the proposed TCT farm test case will be deployed in this location on account of the peak kinetic power density considerations (Thyng & Riley, 2010). However, as has already been discussed, comprehensive device optimization of device is based not only on a thorough understanding of pre-deployment flow conditions but also on an accurate assessment of the post-deployment impacts and power harvesting characteristics. Investigations on the power harvesting have been conducted in the frame of the present thesis and are reported here. Environmental impact assessments have been performed by the UW collaborators and are reported in the Appendix C of Dr. Thyng's doctoral dissertation (i.e. "Numerical Simulation of Admiralty Inlet, WA, with Tidal Hydrokinetic Turbine Siting Application" (2012)).

9.2. The Puget Sound - Simulation Features and Benchmarks

In the study reported here, Admiralty Inlet has been represented as a symmetric headland with a flat-bottomed rectangular channel. This idealized case permits the effects due to the headland to be isolated from the effects of complex bathymetry and thus a better understanding of the interaction between the TCT farm and the vortices occurring at the tip of the headland to be reached. The vortex propagation has been shown to be the most significant hydrodynamic element of this tidal flow (Thyng, 2012; Polagye, 2009). The headland model domain has a length of 40 km, a width of 7 km and possesses a 100 meter deep flat bathymetry. It is worth noting that the depth of the domain has been enhanced in comparison with the real Puget Sound depth for numerical purposes. The headland is symmetric and extends just over 2 km into the channel (Figure 48, a)).

Since the turbine model requires one grid cell in thickness and three grid cells across (i.e. as determined in Section 5.3.1) and knowing that each simulated turbine has a diameter of 30 meters, the resolution employed for these simulations is 30 meters in the x-direction and 10 meters in the y-direction with 20 vertical layers.
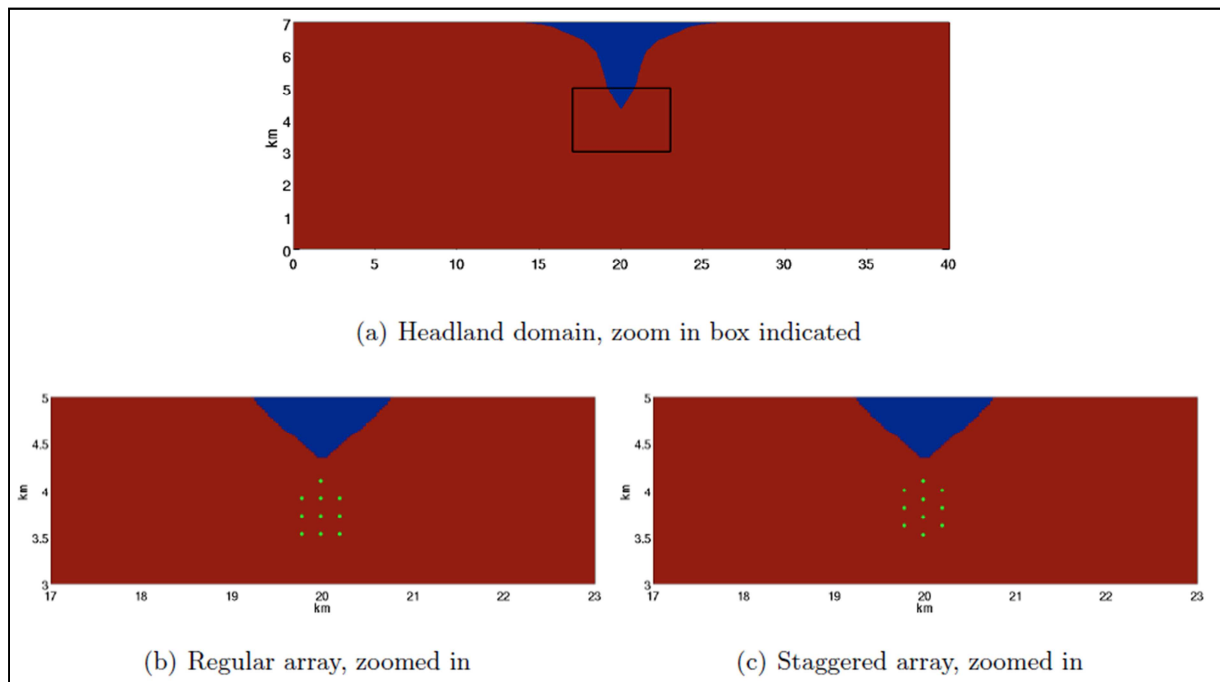
Figure 48: Simplified headland domain (a) and zoomed-in views of the regular and staggered array layout (b & c). Green dots represent the TCT location. After (Thyng, 2012)

The limits of the numerical domain are composed of two open boundaries at the west and east ends of the channel and two walls at the north and south ends. The boundary condition imposed on the walls is "no-slip" (i.e. Section 3.1). At the open boundaries, the free surface elevation is imposed via ROMS open boundary forcing methods of Chapman (1985). A semi-diurnal M2 tide of 4 meter tidal amplitude is applied on both open boundaries. The u-velocity components are forced using ROMS open boundary forcing methods of Flather. Additionally, the initial densities at the east and west open boundaries are enforced and outward-moving baroclinic momentum is radiated out of the system. The phase difference between each boundary is approximated accordingly with the shallow water wave speed $\left(\sqrt{gH}\right)$, channel length (L), and frequency of forcing (ω) (Thyng, 2012). That is

$$\phi = \frac{L\omega}{\sqrt{gH}} = 0.38 \text{ radians} \tag{108}$$

where $\omega = 1.4 \times 10^{-4} \text{ s}^{-1}$ and H is the channel depth. The density field at the open boundaries is set using a linear stratification from 1023 kg. m^{-3} at the surface to 1025 kg. m^{-3} at the bottom, giving a buoyancy frequency of $N = 0.01 \text{ s}^{-1}$. The bottom roughness is parameterised by ROMS quadratic bottom friction expression (i.e. Section 3.1) whose dimensionless friction parameter $C_D = 3 \times 10^{-3}$. The Coriolis force is included and the $k - \omega$ turbulence closure scheme is used (i.e. Section 3.1). The model was run for two tidal cycles for each case. The first tidal cycle is considered ramp-up and the second tidal cycle is considered as suitable for analysis as ebb and flood flows are almost symmetrical. Simulation outputs were recorded every 15 minutes (i.e. simulated time), that is 96 output files. The models have been ran in parallel via Message Passing Interface (MPI) libraries on a 24 2.50Ghz-core cluster[7], each simulation took approximately 2 weeks to compute depending on the cluster activity. This quite large computational time could be decreased by using grid optimization techniques, such as curvilinear coordinates or nested grid. The bathymetric grid, boundary and forcing conditions were developed by our University of Washington collaborators whereas the turbine farm modelling was performed as part of the current effort.

As an example of the type of issue which could be examined by this technique, it was decided to study two different TCT layouts, both composed of 10 turbines (i.e. Figure 48, b) & c)). Turbines are similar in design, they all have a 33 diameter rotor, a thrust coefficient $Ct = 0.86$, they are all fixed with their rotor axis aligned East and West directions and they work in both East-West and West-East directions but cannot yaw. The fact that the turbines cannot yaw in a flow region where the bidirectionality reaches 40° means that the power capture will not be optimum. The fixed orientation of the device however is inherent at this stage of the numerical platform development but will be improved in the next stage of its development and is also a feature of many tidal turbines.

---

[7] Fotcluster2, high performance computer of the University of Plymouth. Web link: http://www.plymouth.ac.uk/pages/view.asp?page=33936

 Future stages of model development will permit any turbine alignment. Considering this, the flow bidirectionality and domain symmetry, a East-west hub orientation seems the most appropriate to optimize the power capture of fixed TCT. The blockage ratio being quite high $\left(i.e. \ \frac{Rotor \ Diameter}{Water \ column \ height} = \frac{1}{3}\right)$, turbine hubs are situated at mid-depth, at 50 m deep, in order to avoid bottom and surface turbulences and loadings. The first layout is referred as "regular" and the second layout is referred to as "staggered". They are both composed of 10 devices and their geometrical configurations as well as localisations of deployment are illustrated in Figure 49 and Figure 48. Here the array layouts have been chosen a-priori and without performing row-by-row simulations, as suggested in Section 7.4, and therefore without considering the potential flow accelerations or turbulence intensity increases which could be induced by the wake interactions within the farm. The distances between each device within the farm have been chosen to maintain a minimum spacing of 6 rotor-diameters between them and thus none of the turbines would be sitting in the near wake of an upstream device (Figure 49).
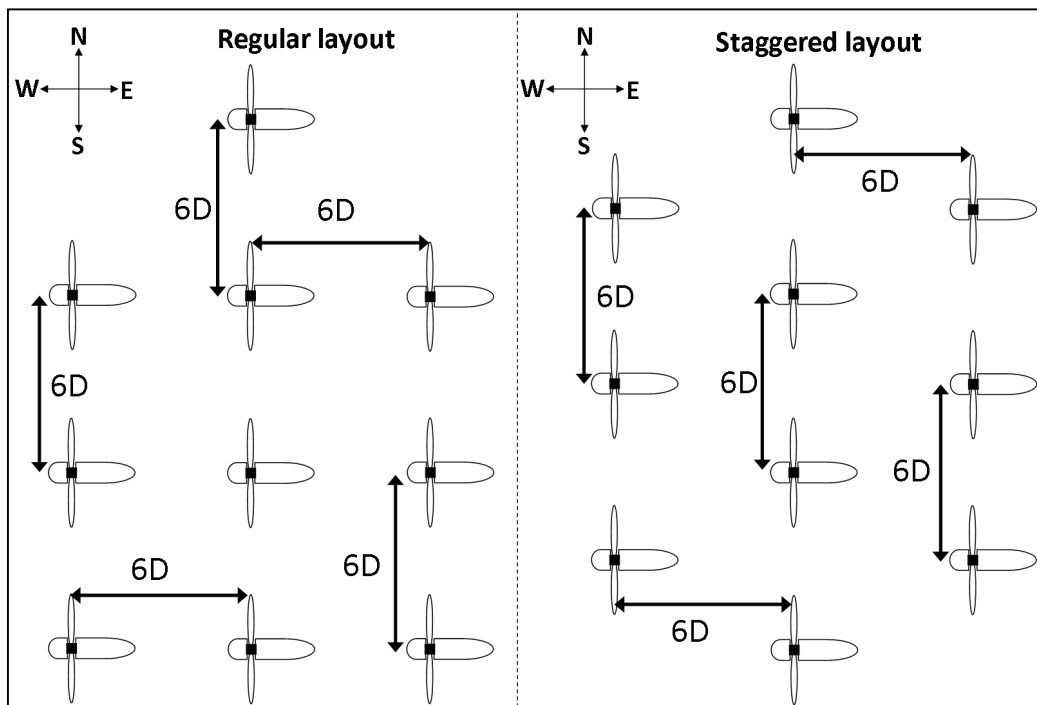

Figure 49: Turbine array layouts, geometrical configuration and device spacing – Regular (left hand side) and staggered (right hand side) layouts

9.3. The Puget Sound - Results

Two different approaches are considered to assess the power capture of the different TCT farm layouts. The first one is based on Eq. (102). Unlike the simulations presented in Chapter 6, the present simulations are subjected to time varying forcing. Therefore, the following adaptation of Eq. (102) must be made to obtain the power captured by each turbine within the farm:

$$Mean\ power\ of\ one\ turbine = \frac{1}{T} \sum_t^n 2\rho A_d U_{d_t}^2 (U_{\infty_t} - U_{d_t}) \times \Delta t \tag{109}$$

where T is a full tidal cycle (i.e. 43200 seconds), Δt the time step between each output (i.e. 900 seconds), $n = 50$ and corresponds the time-step index, U_∞ the u-velocity component of the unperturbed flow simulations at the appropriate disc location and U_{d_t} is the u-velocity component from the simulations including the turbine at the same disc location for a given time index. By extension, in the case of a 10 device farm, the overall power capture of the farm is determined by the following formula:

$$Power\ of\ the\ farm = \frac{1}{T} \sum_N^{10} \sum_t^n 2\rho A_d U_{d_{N,t}}^2 (U_{\infty_{N,t}} - U_{d_{N,t}}) \times \Delta t \tag{110}$$

here N is the index related to each turbine composing the farm, U_{∞_N} the u-velocity component of the unperturbed flow right at the disc location of the Nth turbine and $U_{d_{N,t}}$ is the u-velocity component right at the disc location of the Nth turbine for a given time index t. A second approach based on simple energetic considerations is also performed. The base statement is that the power available for the devices equals to the amount of kinetic energy present in the flow without devices over a tidal cycle period:

$$Available\ Power = \sum_t^n \sum_{i,j,k} \frac{1}{2} \rho \left\| \overrightarrow{v_\infty}_{t,i,j,k} \right\|^2 \times \Delta V_{i,j,k} \times \Delta t \tag{111}$$

where i, j, k correspond respectively to the numerical index along x, y and z directions, $\left\| \overrightarrow{v_\infty}_{t,i,j,k} \right\|$ is the unperturbed flow velocity norm and $\Delta V_{i,j,k}$ represents the control volume of the $(i, j, k)^{th}$ cell composing the numerical mesh. In the same manner, by computing the amount of kinetic energy

present in the flow with devices over a tidal cycle period, one can estimate the remaining power of

the so-exploited tidal flow:

$$Remaining\ Power = \sum_{t}^{n} \sum_{i,j,k} \frac{1}{2} \rho \left\| \vec{v}_{t,i,j,k} \right\|^{2} \times \Delta V_{i,j,k} \times \Delta t \tag{112}$$

where $\left\| \vec{v}_{t,i,j,k} \right\|$ is the flow velocity norm of the studied case. Therefore the amount of power

dissipated by the present of the TCT farm can be assessed through the following expression:

$$Power\ Capture = Available\ Power - Remaining\ Power \tag{113}$$

These local (I.e. Eq. (110)) and global (i.e. Eq. (113)) approaches permit a complementary

investigation of the power extraction induced by the two-considered TCT farm layouts on the tidal

system.

For most of the tidal cycle but the turns of tide, in the case of the staggered layout the devices'

wakes are overlapping whereas in the case of the regular layout devices' wake surge into the device

inter-space without overlapping over the next row. This counter intuitive phenomenon is due to the

flow bidirectionality induced by the headland geometry. This observation tends to suggest that the

regular layout farm should have extracted more energy out of the tidal flow than the staggered

layout farm. Interestingly, the outcomes of the local approach for power extraction reveal that, the

energy extraction difference between the both layouts appears as negligible. whereas the global

approach for power extraction (i.e. Eq. (113)) tends to confirm the latter hypothesis. Indeed, by

applying the local approach for power extraction over a full tidal cycle, the regular layout farm seems

to extract 6.008 MWatts while the staggered layout farm extracts 6.051 MWatts, but by considering

the energy budget over the entire domain and over a full tidal cycle, the power extraction

assessment for the regular layout farm equals7.5348 MWattsand 6.1845 MWatts for the staggered

layout farm. Consequently, the global approach reaveals a 18% difference in terms of power capture

between the two farm layouts and thus confirms the hypothesis made on the wake over-lapping

obserations. In the light of Section 7.4, one could also venture that this local approach excludes

potential flow acceleration within the farm and thus underestimates the real power extraction.

On Figure 51, on can observe that the overall farm-induced turbulence perturbations do not differ much between the both layouts either in magnitude or spatial spreading. In addition, by performing a TKE budget over the entire domain for the two layout cases (i.e. Eq. (114)) and subtracting them, the so-obtained difference in TKE is a thousand times smaller, and therefore negligible, than the difference in power extraction between the same cases.

$$TKE\ Budget = \sum_{t}^{n} \sum_{i,j,k} \rho \times k_{t,i,j,k} \times \Delta V_{i,j,k} \times \Delta t \tag{114}$$

Consequently, we can approximate that all of the 18% of power extraction difference between the two farm layouts is due to actual power capture improvement rather than an increase in turbulent dissipation. Additionally, Figure 51 shows that, for the staggered layout, the turbulence intensities are higher in front of the turbines located in the farm's wake than they are for the regular layout. Accordingly, one could expect more turbulence-related loading on the turbine blades and structures for the staggered layout than for the regular layout. Interestingly the "regular" layout appears regular from an East-West direction consideration but appears as staggered from a wake consideration due to the bidirectionality of the flow and vice-versa for the "staggered" array layout. To conclude, although a-priori staggered layouts tend to be more adequate for tidal flows in straight channels, the previous section showed that the optimum farm layout cannot be found on a-priori considerations but solely by accounting for site-specificities, namely flow bidirectionality and farm-induced turbulences in this case.
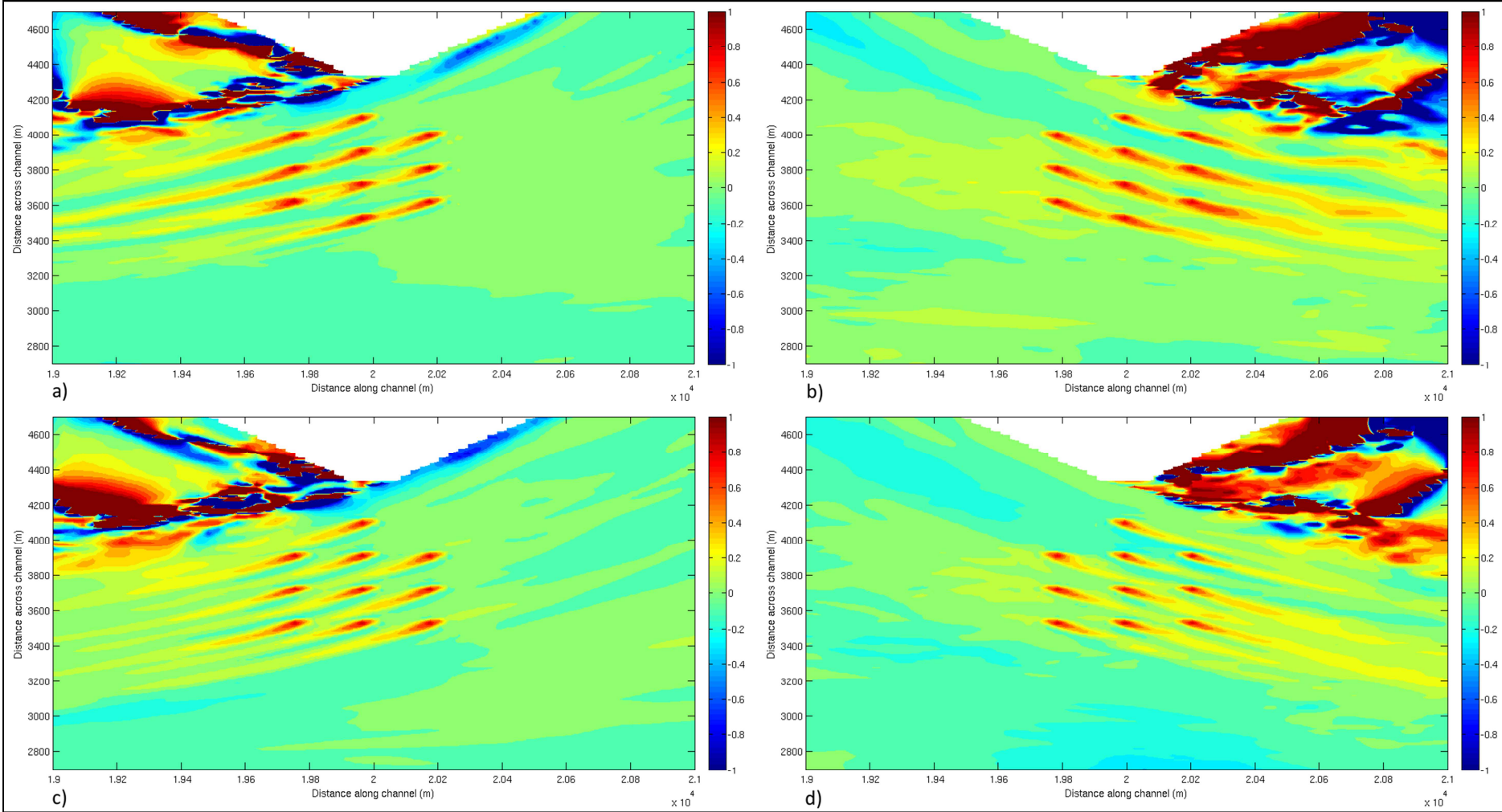
Figure 50: Colour-map of velocity deficit for staggered (i.e. a) & b)) and regular (i.e. c) & d)) farm layouts at the peak speeds of both ebb (i.e. b) & d)) and flow (i.e. a) & c))

126
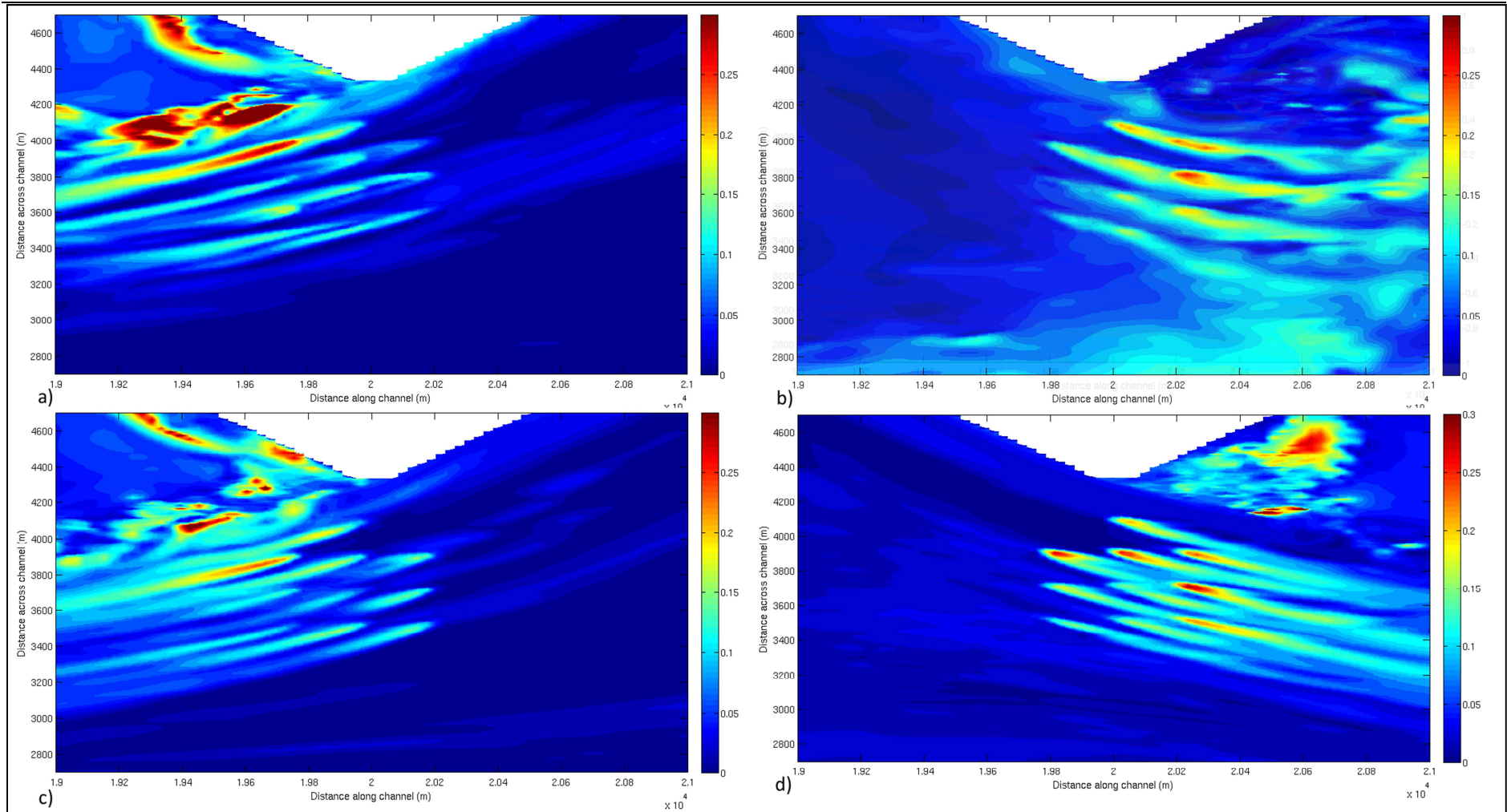
Figure 51: Colour-map of TI for staggered (i.e. a) & b)) and regular (i.e. c) & d)) farm layouts at the peak speeds of both ebb (i.e. b) & d)) and flow (i.e. a) & c))

Based on the previous simulation results, a rule of thumb for assessing the power capture might be worked out. Knowing the power capture of the entire farm thanks to the global approach (i.e. Eq. (113)), one could postulate that this quantity can be expressed as a function of the velocities (i.e. $U_{u.d.}$, $u.d.$ standing for "upstream distance") taken at a similar distance upstream of each turbine composing the farm (Eq. (115)).

$$Power\ capture\ of\ the\ farm = \frac{1}{T} \sum_{N}^{10} \sum_{t}^{n} \frac{1}{2} \rho A_d U_{u.d.N,t}{}^3 \times \Delta t \qquad (115)$$

If such rule of thumb exists and could be applied to any kind of array layout, the power capture assessment would be heavily simplified. In order to find the upstream distance, velocities at different distance upstream of each device constituting the regular layout farm have been recorded over a full tidal cycle. These velocities have been then applied to Eq. (115). The power extraction estimations so-obtained are then normalised by the power extraction estimation obtained via the global approach (i.e. Eq. (113)), namely 7.5348 MWatts, and then display against the distance upstream of the devices (Figure 52).
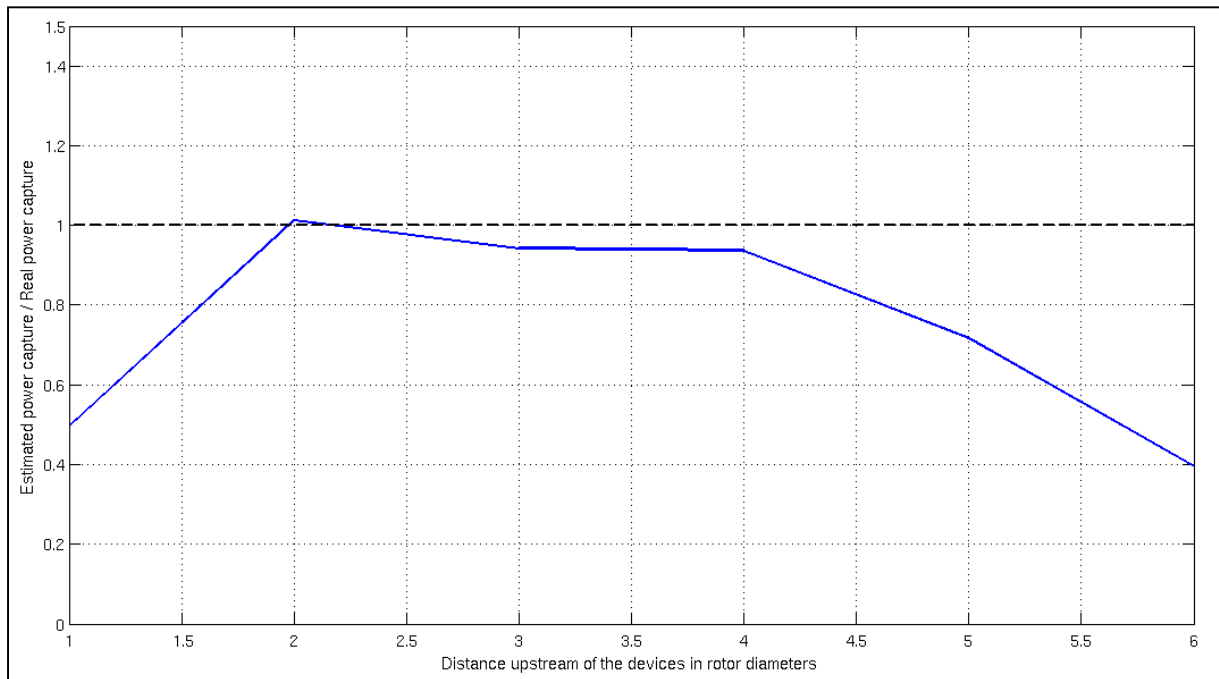
Figure 52: Normalised power extraction versus distance upstream of the devices – The dashed line represents the aimed value and the solid line represents the estimations from the regular array layout simulation

On Figure 52, the dashed line representing the aimed value of power capture obtained via the global approach (i.e. Eq. (113)) meets the solid line representing the estimated power capture obtained via Eq. (115) at 2 diameters upstream of the device. One could therefore postulate that by applying the velocities at 2 diameters upstream of each device to Eq. (115) would give an accurate estimation of the real power capture. To validate this hypothesis, we apply this rule of thumb to the staggered layout case and compare this power capture estimation to the estimation obtained thanks to the global approach (i.e. Eq. (113)) for the same case. Unfortunately, by doing so, the power capture estimation is 26% lower than the estimation obtained via the global approach (i.e. Eq. (113)) for the staggered layout case. This observation tends to show that, as the optimum farm layout, precise power capture assessments of TCT arrays cannot be made on a-priori considerations but solely by accounting for site flow-specificities.

9.4. The Puget Sound - Discussion

In this section, several power assessment methodologies have been used and compared in order to calculate the power capture of two different layouts of 10 device arrays. The first assessment method is based on the flow velocity passing at the position of each device for each time step (i.e. Eq. (110), also called "local approach" in this document), the second one consists in estimating the amount of power dissipated by the present of the over an entire tidal cycle (i.e. Eq. (113) also called "global approach" in thi document) and the third on is a function of the velocities taken at a similar distance upstream of each turbine composing the array (Eq. (115)). In the present case, result comparison has demonstrated the global approach to be more relevant above the two other methodologies. Nonetheless, the global approach can be considered as unbiased only when the open boundaries of the simulation are not directly subject to the blockage effects, such as flow increase, caused by the presence of TCT arrays. Therefore, simulation domains have to be sufficiently larger than the TCT footprint in order to safely apply this methodology.

Similarly to Chapter 7, emphasis has been placed on using the appropriate approach for power assessment as well as the necessity to account for site specificities in the optimization process. Under

this focus, an 18% increase in power capture achieved through farm layout optimization based on the flow bidirectionality. Allowing for device yawing and blade design adaptation and control could also no doubt improve this number and will certainly be implemented in future versions of the model. Furthermore, according to Bryden & Couch (2004) natural flows intrinsically possess both potential and kinetic energy and the energy extraction is partly balanced between these two components. Consequently, integrating the potential energy variations and transfers in the power capture assessment approach might have to be considered and raises the question of the relevance of assessing the potential of a site only on kinetic considerations (Salter, 2009).

The power output assessment could be even more realistic by taking into account "cut-in speed" and "rated power speed". The cut-in speed is the flow velocity below which the turbine's electrical system cuts out and turbine's rotor hence stays still. On the other hand, the rated power is the maximum power that a turbine can produce. This maximum of power production coincides with a threshold flow velocity above which pitch-control mechanism reduces angle of attack of the blades and thus maintains a power output close to the rated power (Fraenkel, 2007). This threshold aids in avoiding failure and dismantling of the turbine structure and blades due to extreme loadings (Fraenkel, 2007). For the sake of the illustration, let's consider that the turbines studied here have the same features as Seagen turbines. In that case, cut-in speed equals to 0.7 m/s and the rated power speed equals to 2.3 m/s. Along with a more realistic speed-control of the device power production, an estimate of electrical and mechanical losses involved in the process would ameliorate the power extraction assessment.

Chapter 10. Conclusions

The main contribution of this research is that a numerical method for representing TCT hydrodynamic perturbations within large-scale ocean circulation models has been developed, described in detail and demonstrated. This innovative method accounts for the momentum capture as well as the turbulence balance perturbations caused by discrete TCT devices on flow hydrodynamics. Accordingly, over the area swept by the turbine blades, the momentum sink is generated through an additional body force as explained in Section 4.2. The turbulence balance perturbations are parameterised through a source term of TKE production accounting for the vortices shed by the blades, a sink term of TKE accounting for the short circuiting of the turbulence cascade and finally an extra term in the turbulent length scale transport equation permitting the computation of the so-induced length-scale transfer from large to small-scale turbulence. Such an approach permits the momentum theory limitations and sub-grid scale effects related to the turbine turbulence in coarse resolution ocean circulation models to be compensated for. Consequently, realistic wake decays and turbulence fields can be achieved with the numerical method with numerical grid resolutions larger than the turbine turbulence length scale.

This TCT representation has been implemented into ROMS, a widely used ocean circulation model that is described in detail in Section 3.1. The implementation scheme used for this method is proven to be grid and time independent up to a certain extent and grid dependency tests have shown that the so-adapted model gives almost identical results for any step resolution finer than $(\Delta x = 1D, \Delta y = \frac{1}{3}D, \Delta z = \frac{1}{6}D)$. Although already relatively coarse, these grid resolution limitations

could be improved in future work by the use of a further adapted and sophisticated discretization scheme for the TCT perturbation term implementation and the use of nested grids. As for the time dependency test, it shows same time of convergence for any time step finer than 0.01s. Above this limit the simulation simply crashes. However, according the CFL (Courant-Friedrichs-Lewy) criterion, the time step resolution could theoretically reach 0.03s in this test case described in Section 5.3.2. This time resolution limitation is due to numerical fluctuations in the first iterations, themselves generated by the discrepancies between initial conditions and the converged solutions. This could be improved by starting the simulation with an initial solution closer to the final solution. Nonetheless, despite these temporal and spatial resolution limitations, on an 8 core workstation, the 840000 cell simulation takes only 15 minutes to converge towards a final steady solution. On top of the previously mentioned discretisation and computational grid improvements, implementation optimizations. For instance applying a bolean mask matrix permitting the geo-localisation of every devices on the domain grid instead of recursive "if" loops as used in the code reproduced in Appendices A & B could drastically reduce this computational time.

Like most of the models of this kind, ROMS relies on hydrostatic and shallow-water assumptions. The hydrostatic assumption implies that the pressure variations are solely due to the free-surface elevation. However, non-hydrostatic pressure variations are expected as the flow bulks on the front face of TCT rotors. This phenomenon has been studied in Polagye's Thesis (Polagye, 2009) and non-hydrostatic pressure due to the presence of a turbine in a flow is shown to have limited impact on the overall pressure field, is only localised in front of the turbine and thus will not interfere with the hydrodynamics downstream of the device. The shallow water assumption influences the vertical/horizontal mixing splitting in this model. Accordingly, the vertical mixing is driven by the turbulence closure model whereas the horizontal mixing is parameterised through an eddy viscosity. Although this splitting is valid in most ocean circulation situations and has the advantage of drastically decreasing the computational time, it leads to a misrepresentation of the TKE production by horizontal shear at the lateral edges of a TCT as shown in Section 5.3.3. Adding a

local term of TKE production by horizontal shear over the disc rotor or, using symmetry, imposing the same TKE levels at the lateral edges as the TKE level computed at the vertical edges of the disc might compensate for this generic model limitation.

Despite these model limitations this method has proved to reproduce with satisfying accuracy momentum and turbulence behaviours for both a single and an array of experimental porous discs of various thrust coefficients and to be applicable at any given scale (averaged value over all the conducted tests: $r^2 = 0.76$ with an $error_{Nrmse} \cong 12.0\%$). However, the calibration of the eddy viscosity cannot still be done under a-priori grounds. Although a theoretical upper limit exists (i.e. Eq. (68)), the calibration of the eddy viscosity has to be done against empirical considerations or measurements as described in Section 5.3.3. In addition, the set of turbulence correction parameters may vary for specific blade designs. In the cases studied for this research project, only standard designs have been examined and thus only the referenced set of parameters have been used. An extended comparison test series with CFD simulations would provide greater insight to develop empirical rules for turbulence parameter calibration. Eventually, in order to extend the range of applications of the modelling technique, further numerical development is needed to enable the device to yaw and have realistic blade pitch control.

Thanks to its low computational consumption and its satisfying precision, this method is found to be highly suitable for regional-scale simulation of tidal flows with complex bathymetry and forcing. Accordingly, the numerical platform, a product of the alliance between ROMS and the present method, permits realistic impact and power assessments of TCT array deployments, such as that presented in Chapter 9. Moreover, this numerical platform allows future developments in order to investigate further impacts. For instance, ROMS can be coupled with codes accounting for wave forcing (SWAN), atmospheric forcing (WRF) or sediment transport (Warner et al., 2010), and thus open a boundless range of assessment options. More especially, this modelling platform opens a new range of insight for TCT array power assessments, both local and global. Accordingly, a reflection on the relevancy of this method to identification of power assessment and layout optimization

strategies has been initiated through this work. Furthermore, by simplifying case studies and coupling the numerical model with siting-optimization routines based on device performance and cost/benefit benchmarks, the so-adapted platform could also be used as a TCT array optimizer. Potentially, thanks to the TCT representation method developed for this research project, a unique numerical platform for optimizing TCT array layout could be achieved. Such a tool would be highly beneficial to the marine renewable energy industry and the compulsory step forward towards commercial-scale deployments of TCT arrays around the world.

Appendix A: ROMS Modifications for Validation Case – Momentum Term

This appendix displays the "rhs3d.F" ROMS file usually located in ROMS/Nonlinear/ architecture. It has been adapted to account for the additional body force $\overrightarrow{F'_{i,j,k}}$ (i.e. Section 4.3) related to the rotor disc force retarding the flow. The following modifications are highlighted in red, work for ROMS version 392 and may need adaptions if newer versions of the software are used.

```
#include "cppdefs.h"
      MODULE rhs3d_mod
#if defined NONLINEAR && defined SOLVE3D
!
!svn $Id: rhs3d.F 294 2009-01-09 21:37:26Z arango $
!=======================================================================
!  Copyright (c) 2002-2009 The ROMS/TOMS Group                        !
!    Licensed under a MIT/X style license                             !
!    See License_ROMS.txt                            Hernan G. Arango  !
!========================================= Alexander F. Shchepetkin ===
!                                                                     !
!  This subroutine evaluates right-hand-side terms for 3D momentum    !
!  and tracers equations.                                             !
!                                                                     !
!=======================================================================
!
      implicit none

      PRIVATE
      PUBLIC  :: rhs3d

      CONTAINS
!
!***********************************************************************
```

```
      SUBROUTINE rhs3d (ng, tile)
!***********************************************************************
!
      USE mod_param
# ifdef CLIMATOLOGY
      USE mod_clima
# endif
      USE mod_coupling
# if defined DIAGNOSTICS_TS || defined DIAGNOSTICS_UV
      USE mod_diags
# endif
      USE mod_forces
      USE mod_grid
# ifdef NEARSHORE_MELLOR
      USE mod_mixing
# endif
# if defined ASSIMILATION || defined NUDGING
      USE mod_obs
# endif
      USE mod_ocean
      USE mod_stepping
!
      USE pre_step3d_mod, ONLY : pre_step3d
      USE prsgrd_mod, ONLY : prsgrd
# ifndef TS_FIXED
#  ifdef TS_DIF2
      USE t3dmix_mod, ONLY : t3dmix2
#  endif
#  ifdef TS_DIF4
      USE t3dmix_mod, ONLY : t3dmix4
#  endif
# endif
# ifdef UV_VIS2
      USE uv3dmix_mod, ONLY : uv3dmix2
# endif
# ifdef UV_VIS4
      USE uv3dmix_mod, ONLY : uv3dmix4
# endif
!
!  Imported variable declarations.
!
      integer, intent(in) :: ng, tile
!
!  Local variable declarations.
!
# include "tile.h"
!
!-----------------------------------------------------------------------
!  Initialize computations for new time step of the 3D primitive
!  variables.
!-----------------------------------------------------------------------
!
      CALL pre_step3d (ng, tile)
!
!-----------------------------------------------------------------------
!  Compute baroclinic pressure gradient.
```

```
!-----------------------------------------------------------------------
!
      CALL prsgrd (ng, tile)
# ifndef TS_FIXED
#  ifdef TS_DIF2
!
!-----------------------------------------------------------------------
!  Compute horizontal harmonic mixing of tracer type variables.
!-----------------------------------------------------------------------
!
      CALL t3dmix2 (ng, tile)
#  endif
#  ifdef TS_DIF4
!
!-----------------------------------------------------------------------
!  Compute horizontal biharmonic mixing of tracer type variables.
!-----------------------------------------------------------------------
!
      CALL t3dmix4 (ng, tile)
#  endif
# endif
!
!-----------------------------------------------------------------------
!  Compute right-hand-side terms for the 3D momentum equations.
!-----------------------------------------------------------------------
!
# ifdef PROFILE
      CALL wclock_on (ng, iNLM, 21)
# endif
      CALL rhs3d_tile (ng, tile,                                        &
     &                 LBi, UBi, LBj, UBj,                              &
     &                 IminS, ImaxS, JminS, JmaxS,                      &
     &                 nrhs(ng),                                        &
     &                 GRID(ng) % Hz,                                   &
     &                 GRID(ng) % Huon,                                 &
     &                 GRID(ng) % Hvom,                                 &
# if defined CURVGRID && defined UV_ADV
     &                 GRID(ng) % dmde,                                 &
     &                 GRID(ng) % dndx,                                 &
# endif
     &                 GRID(ng) % fomn,                                 &
     &                 GRID(ng) % om_u,                                 &
     &                 GRID(ng) % om_v,                                 &
     &                 GRID(ng) % om_r,                                 &
     &                 GRID(ng) % on_u,                                 &
     &                 GRID(ng) % on_v,                                 &
     &                 GRID(ng) % pm,                                   &
     &                 GRID(ng) % pn,                                   &
     &                 GRID(ng) % z_r,                                  &
     &                 GRID(ng) % z_w,                                  &
     &                 GRID(ng) % xu,                                   &
     &                 GRID(ng) % yu,                                   &
     &                 FORCES(ng) % bustr,                              &
     &                 FORCES(ng) % bvstr,                              &
     &                 FORCES(ng) % sustr,                              &
     &                 FORCES(ng) % svstr,                              &
```

```
# ifdef M3CLM_NUDGING
     &                     CLIMA(ng) % M3nudgcof,                    &
     &                     CLIMA(ng) % uclm,                         &
     &                     CLIMA(ng) % vclm,                         &
# endif
# if defined NUDGING_UVsur || defined NUDGING_UV
     &                     OBS(ng) % EobsUV,                         &
     &                     OBS(ng) % Uobs,                           &
     &                     OBS(ng) % Vobs,                           &
# endif
     &                     OCEAN(ng) % u,                            &
     &                     OCEAN(ng) % v,                            &
     &                     OCEAN(ng) % W,                            &
# ifndef SET_ZETA
     &                     COUPLING(ng) % Zt_avg1,                   &
# endif
# ifdef NEARSHORE_MELLOR
     &                     OCEAN(ng) % u_stokes,                     &
     &                     OCEAN(ng) % v_stokes,                     &
     &                     OCEAN(ng) % rulag3d,                      &
     &                     OCEAN(ng) % rvlag3d,                      &
     &                     MIXING(ng) % rustr3d,                     &
     &                     MIXING(ng) % rvstr3d,                     &
# endif
     &                     COUPLING(ng) % rufrc,                     &
     &                     COUPLING(ng) % rvfrc,                     &
# ifdef DIAGNOSTICS_UV
     &                     DIAGS(ng) % DiaRUfrc,                     &
     &                     DIAGS(ng) % DiaRVfrc,                     &
     &                     DIAGS(ng) % DiaRU,                        &
     &                     DIAGS(ng) % DiaRV,                        &
# endif
     &                     OCEAN(ng) % ru,                           &
# ifdef SET_ZETA
     &                     OCEAN(ng) % rv)
# else
     &                     OCEAN(ng) % rv,                           &
     &                     OCEAN(ng) % zeta)
# endif
# ifdef PROFILE
      CALL wclock_off (ng, iNLM, 21)
# endif
# ifdef UV_VIS2
!
!-----------------------------------------------------------------------
!  Compute horizontal, harmonic mixing of momentum.
!-----------------------------------------------------------------------
!
      CALL uv3dmix2 (ng, tile)
# endif
# ifdef UV_VIS4
!
!-----------------------------------------------------------------------
!  Compute horizontal, biharmonic mixing of momentum.
!-----------------------------------------------------------------------
!
```

```
      CALL uv3dmix4 (ng, tile)
# endif
      RETURN
      END SUBROUTINE rhs3d
!
!***********************************************************************
      SUBROUTINE rhs3d_tile (ng, tile,                              &
     &                       LBi, UBi, LBj, UBj,                    &
     &                       IminS, ImaxS, JminS, JmaxS,            &
     &                       nrhs,                                  &
     &                       Hz, Huon, Hvom,                        &
# if defined CURVGRID && defined UV_ADV
     &                       dmde, dndx,                            &
# endif
     &                       fomn,                                  &
     &                       om_u, om_v, om_r, on_u, on_v, pm, pn,  &
     &                       z_w, z_r, xu, yu,                      &
     &                       bustr, bvstr,                          &
     &                       sustr, svstr,                          &
# ifdef M3CLM_NUDGING
     &                       M3nudgcof, uclm, vclm,                 &
# endif
# if defined NUDGING_UVsur || defined NUDGING_UV
     &                       EobsUV, Uobs, Vobs,                    &
# endif
     &                       u, v, W,                               &
# ifndef SET_ZETA
     &                       Zt_avg1,                               &
# endif
# ifdef NEARSHORE_MELLOR
     &                       u_stokes, v_stokes,                    &
     &                       rulag3d, rvlag3d,                      &
     &                       rustr3d, rvstr3d,                      &
# endif
     &                       rufrc, rvfrc,                          &
# ifdef DIAGNOSTICS_UV
     &                       DiaRUfrc, DiaRVfrc,                    &
     &                       DiaRU, DiaRV,                          &
# endif
# ifdef SET_ZETA
     &                       ru, rv)
# else
     &                       ru, rv,                                &
     &                       zeta)
# endif
!***********************************************************************
!
      USE mod_param
      USE mod_scalars

# ifndef SET_ZETA
#  if defined EW_PERIODIC || defined NS_PERIODIC
!
      USE exchange_2d_mod, ONLY : exchange_r2d_tile
#  endif
#  ifdef DISTRIBUTE
```

```
        USE mp_exchange_mod, ONLY : mp_exchange2d
#  endif
# endif
!
!  Imported variable declarations.
!
      integer, intent(in) :: ng, tile
      integer, intent(in) :: LBi, UBi, LBj, UBj
      integer, intent(in) :: IminS, ImaxS, JminS, JmaxS
      integer, intent(in) :: nrhs
!
# ifdef ASSUMED_SHAPE
      real(r8), intent(in) :: Hz(LBi:,LBj:,:)
      real(r8), intent(in) :: Huon(LBi:,LBj:,:)
      real(r8), intent(in) :: Hvom(LBi:,LBj:,:)
#  if defined CURVGRID && defined UV_ADV
      real(r8), intent(in) :: dmde(LBi:,LBj:)
      real(r8), intent(in) :: dndx(LBi:,LBj:)
#  endif
      real(r8), intent(in) :: fomn(LBi:,LBj:)
      real(r8), intent(in) :: om_u(LBi:,LBj:)
      real(r8), intent(in) :: om_v(LBi:,LBj:)
      real(r8), intent(in) :: om_r(LBi:,LBj:)
      real(r8), intent(in) :: on_u(LBi:,LBj:)
      real(r8), intent(in) :: on_v(LBi:,LBj:)

      real(r8), intent(in) :: z_w(LBi:,LBj:,0:)
      real(r8), intent(in) :: z_r(LBi:,LBj:,0:)
      real(r8), intent(in) :: xu(LBi:,LBj:)
      real(r8), intent(in) :: yu(LBi:,LBj:)

      real(r8), intent(in) :: pm(LBi:,LBj:)
      real(r8), intent(in) :: pn(LBi:,LBj:)
      real(r8), intent(in) :: bustr(LBi:,LBj:)
      real(r8), intent(in) :: bvstr(LBi:,LBj:)
      real(r8), intent(in) :: sustr(LBi:,LBj:)
      real(r8), intent(in) :: svstr(LBi:,LBj:)
#  ifdef M3CLM_NUDGING
      real(r8), intent(in) :: M3nudgcof(LBi:,LBj:)
      real(r8), intent(in) :: uclm(LBi:,LBj:,:)
      real(r8), intent(in) :: vclm(LBi:,LBj:,:)
#  endif
#  if defined NUDGING_UVsur || defined NUDGING_UV
      real(r8), intent(in) :: EobsUV(LBi:,LBj:,:)
      real(r8), intent(in) :: Uobs(LBi:,LBj:,:)
      real(r8), intent(in) :: Vobs(LBi:,LBj:,:)
#  endif
      real(r8), intent(in) :: u(LBi:,LBj:,:,:)
      real(r8), intent(in) :: v(LBi:,LBj:,:,:)
      real(r8), intent(in) :: W(LBi:,LBj:,0:)
#  ifndef SET_ZETA
      real(r8), intent(in) :: Zt_avg1(LBi:,LBj:)
#  endif
#  ifdef NEARSHORE_MELLOR
      real(r8), intent(in) :: u_stokes(LBi:,LBj:,:)
      real(r8), intent(in) :: v_stokes(LBi:,LBj:,:)
```

```
      real(r8), intent(in) :: rulag3d(LBi:,LBj:,:)
      real(r8), intent(in) :: rvlag3d(LBi:,LBj:,:)
      real(r8), intent(in) :: rustr3d(LBi:,LBj:,:)
      real(r8), intent(in) :: rvstr3d(LBi:,LBj:,:)
#  endif
      real(r8), intent(inout) :: ru(LBi:,LBj:,0:,:)
      real(r8), intent(inout) :: rv(LBi:,LBj:,0:,:)
#  ifdef DIAGNOSTICS_UV
      real(r8), intent(inout) :: DiaRUfrc(LBi:,LBj:,:,:)
      real(r8), intent(inout) :: DiaRVfrc(LBi:,LBj:,:,:)
      real(r8), intent(inout) :: DiaRU(LBi:,LBj:,:,:,:)
      real(r8), intent(inout) :: DiaRV(LBi:,LBj:,:,:,:)
#  endif

      real(r8), intent(out) :: rufrc(LBi:,LBj:)
      real(r8), intent(out) :: rvfrc(LBi:,LBj:)
#  ifndef SET_ZETA
      real(r8), intent(out) :: zeta(LBi:,LBj:,:)
#  endif
#  else
      real(r8), intent(in) :: Hz(LBi:UBi,LBj:UBj,N(ng))
      real(r8), intent(in) :: Huon(LBi:UBi,LBj:UBj,N(ng))
      real(r8), intent(in) :: Hvom(LBi:UBi,LBj:UBj,N(ng))
#  if defined CURVGRID && defined UV_ADV
      real(r8), intent(in) :: dmde(LBi:UBi,LBj:UBj)
      real(r8), intent(in) :: dndx(LBi:UBi,LBj:UBj)
#  endif
      real(r8), intent(in) :: fomn(LBi:UBi,LBj:UBj)
      real(r8), intent(in) :: om_u(LBi:UBi,LBj:UBj)
      real(r8), intent(in) :: om_v(LBi:UBi,LBj:UBj)
      real(r8), intent(in) :: om_r(LBi:UBi,LBj:UBj)
      real(r8), intent(in) :: on_u(LBi:UBi,LBj:UBj)
      real(r8), intent(in) :: on_v(LBi:UBi,LBj:UBj)

      real(r8), intent(in) :: z_w(LBi:UBi,LBj:UBj,0:N(ng))
      real(r8), intent(in) :: z_r(LBi:UBi,LBj:UBj,0:N(ng))
      real(r8), intent(in) :: xu(LBi:UBi,LBj:UBj)
      real(r8), intent(in) :: yu(LBi:UBi,LBj:UBj)

      real(r8), intent(in) :: pm(LBi:UBi,LBj:UBj)
      real(r8), intent(in) :: pn(LBi:UBi,LBj:UBj)
      real(r8), intent(in) :: bustr(LBi:UBi,LBj:UBj)
      real(r8), intent(in) :: bvstr(LBi:UBi,LBj:UBj)
      real(r8), intent(in) :: sustr(LBi:UBi,LBj:UBj)
      real(r8), intent(in) :: svstr(LBi:UBi,LBj:UBj)
#  ifdef M3CLM_NUDGING
      real(r8), intent(in) :: M3nudgcof(LBi:UBi,LBj:UBj)
      real(r8), intent(in) :: uclm(LBi:UBi,LBj:UBj,N(ng))
      real(r8), intent(in) :: vclm(LBi:UBi,LBj:UBj,N(ng))
#  endif
#  if defined NUDGING_UVsur || defined NUDGING_UV
      real(r8), intent(in) :: EobsUV(LBi:UBi,LBj:UBj,N(ng))
      real(r8), intent(in) :: Uobs(LBi:UBi,LBj:UBj,N(ng))
      real(r8), intent(in) :: Vobs(LBi:UBi,LBj:UBj,N(ng))
#  endif
      real(r8), intent(in) :: u(LBi:UBi,LBj:UBj,N(ng),2)
```

```
      real(r8), intent(in) :: v(LBi:UBi,LBj:UBj,N(ng),2)
      real(r8), intent(in) :: W(LBi:UBi,LBj:UBj,0:N(ng))
#  ifndef SET_ZETA
      real(r8), intent(in) :: Zt_avg1(LBi:UBi,LBj:UBj)
#  endif
#  ifdef NEARSHORE_MELLOR
      real(r8), intent(in) :: u_stokes(LBi:UBi,LBj:UBj,N(ng))
      real(r8), intent(in) :: v_stokes(LBi:UBi,LBj:UBj,N(ng))
      real(r8), intent(in) :: rulag3d(LBi:UBi,LBj:UBj,N(ng))
      real(r8), intent(in) :: rvlag3d(LBi:UBi,LBj:UBj,N(ng))
      real(r8), intent(in) :: rustr3d(LBi:UBi,LBj:UBj,N(ng))
      real(r8), intent(in) :: rvstr3d(LBi:UBi,LBj:UBj,N(ng))
#  endif
      real(r8), intent(inout) :: ru(LBi:UBi,LBj:UBj,0:N(ng),2)
      real(r8), intent(inout) :: rv(LBi:UBi,LBj:UBj,0:N(ng),2)
#  ifdef DIAGNOSTICS_UV
      real(r8), intent(inout) :: DiaRUfrc(LBi:UBi,LBj:UBj,3,NDM2d-1)
      real(r8), intent(inout) :: DiaRVfrc(LBi:UBi,LBj:UBj,3,NDM2d-1)
      real(r8), intent(inout) :: DiaRU(LBi:UBi,LBj:UBj,N(ng),2,NDrhs)
      real(r8), intent(inout) :: DiaRV(LBi:UBi,LBj:UBj,N(ng),2,NDrhs)
#  endif

      real(r8), intent(out) :: rufrc(LBi:UBi,LBj:UBj)
      real(r8), intent(out) :: rvfrc(LBi:UBi,LBj:UBj)
#  ifndef SET_ZETA
      real(r8), intent(out) :: zeta(LBi:UBi,LBj:UBj,3)
#  endif
# endif
!
!  Local variable declarations.
!
# ifdef DISTRIBUTE
#  ifdef EW_PERIODIC
      logical :: EWperiodic=.TRUE.
#  else
      logical :: EWperiodic=.FALSE.
#  endif
#  ifdef NS_PERIODIC
      logical :: NSperiodic=.TRUE.
#  else
      logical :: NSperiodic=.FALSE.
#  endif
# endif
      integer :: i, j, k

      real(r8) :: cff, cff1, cff2, cff3, coef1, coef2

      real(r8) :: cx, kcff, width, diam, surf, zturb, xturb, yturb

      logical :: T1, T2, T3, T4

      real(r8), dimension(IminS:ImaxS,0:N(ng)) :: CF
      real(r8), dimension(IminS:ImaxS,0:N(ng)) :: DC
      real(r8), dimension(IminS:ImaxS,0:N(ng)) :: FC

      real(r8), dimension(IminS:ImaxS,JminS:JmaxS) :: Huee
```

```fortran
      real(r8), dimension(IminS:ImaxS,JminS:JmaxS) :: Huxx
      real(r8), dimension(IminS:ImaxS,JminS:JmaxS) :: Hvee
      real(r8), dimension(IminS:ImaxS,JminS:JmaxS) :: Hvxx
      real(r8), dimension(IminS:ImaxS,JminS:JmaxS) :: UFx
      real(r8), dimension(IminS:ImaxS,JminS:JmaxS) :: UFe
      real(r8), dimension(IminS:ImaxS,JminS:JmaxS) :: Uwrk
      real(r8), dimension(IminS:ImaxS,JminS:JmaxS) :: VFx
      real(r8), dimension(IminS:ImaxS,JminS:JmaxS) :: VFe
      real(r8), dimension(IminS:ImaxS,JminS:JmaxS) :: Vwrk
      real(r8), dimension(IminS:ImaxS,JminS:JmaxS) :: uee
      real(r8), dimension(IminS:ImaxS,JminS:JmaxS) :: uxx
      real(r8), dimension(IminS:ImaxS,JminS:JmaxS) :: vee
      real(r8), dimension(IminS:ImaxS,JminS:JmaxS) :: vxx
      real(r8), dimension(IminS:ImaxS,JminS:JmaxS) :: wrk

      real(r8), dimension(IminS:ImaxS,JminS:JmaxS) :: mustr
      real(r8), dimension(IminS:ImaxS,JminS:JmaxS) :: mvstr

# include "set_bounds.h"

# ifdef BODYFORCE
!
!-----------------------------------------------------------------------
!  Apply surface stress as a bodyforce: determine the thickness (m)
!  of the surface layer; then add in surface stress as a bodyfoce.
!-----------------------------------------------------------------------
!
#  ifdef DIAGNOSTICS_UV
      DO k=1,N(ng)
        DO j=Jstr,Jend
          DO i=Istr,Iend
            DiaRU(i,j,k,M3vvis)=0.0_r8
            DiaRV(i,j,k,M3vvis)=0.0_r8
          END DO
        END DO
      END DO
      DO j=Jstr,Jend
        DO i=IstrU,Iend
          DiaRUfrc(i,j,3,M2sstr)=0.0_r8
          DiaRUfrc(i,j,3,M2bstr)=0.0_r8
        END DO
      END DO
      DO j=JstrV,Jend
        DO i=Istr,Iend
          DiaRVfrc(i,j,3,M2sstr)=0.0_r8
          DiaRVfrc(i,j,3,M2bstr)=0.0_r8
        END DO
      END DO
#  endif
      DO j=JstrV-1,Jend
        DO i=IstrU-1,Iend
          wrk(i,j)=0.0_r8
        END DO
      END DO
      DO k=N(ng),levsfrc(ng),-1
        DO j=JstrV-1,Jend
```

143

```
              DO i=IstrU-1,Iend
                wrk(i,j)=wrk(i,j)+Hz(i,j,k)
              END DO
            END DO
          END DO
        DO j=Jstr,Jend
          DO i=IstrU,Iend
            cff=0.25_r8*(pm(i-1,j)+pm(i,j))*                    &
     &                  (pn(i-1,j)+pn(i,j))
            cff1=1.0_r8/(cff*(wrk(i-1,j)+wrk(i,j)))
            Uwrk(i,j)=sustr(i,j)*cff1
          END DO
        END DO
        DO j=JstrV,Jend
          DO i=Istr,Iend
            cff=0.25*(pm(i,j-1)+pm(i,j))*                       &
     &              (pn(i,j-1)+pn(i,j))
            cff1=1.0_r8/(cff*(wrk(i,j-1)+wrk(i,j)))
            Vwrk(i,j)=svstr(i,j)*cff1
          END DO
        END DO
        DO k=levsfrc(ng),N(ng)
          DO j=Jstr,Jend
            DO i=IstrU,Iend
              cff=Uwrk(i,j)*(Hz(i  ,j,k)+                       &
     &                       Hz(i-1,j,k))
              ru(i,j,k,nrhs)=ru(i,j,k,nrhs)+cff
#  ifdef DIAGNOSTICS_UV
              DiaRU(i,j,k,nrhs,M3vvis)=DiaRU(i,j,k,nrhs,M3vvis)+cff
              DiaRUfrc(i,j,3,M2sstr)=DiaRUfrc(i,j,3,M2sstr)+cff
#  endif
            END DO
          END DO
          DO j=JstrV,Jend
            DO i=Istr,Iend
              cff=Vwrk(i,j)*(Hz(i,j  ,k)+                       &
     &                       Hz(i,j-1,k))
              rv(i,j,k,nrhs)=rv(i,j,k,nrhs)+cff
#  ifdef DIAGNOSTICS_UV
              DiaRV(i,j,k,nrhs,M3vvis)=DiaRV(i,j,k,nrhs,M3vvis)+cff
              DiaRVfrc(i,j,3,M2sstr)=DiaRVfrc(i,j,3,M2sstr)+cff
#  endif
            END DO
          END DO
        END DO
!
!  Apply bottom stress as a bodyforce: determine the thickness (m)
!  of the bottom layer; then add in bottom stress as a bodyfoce.
!
      DO j=JstrV-1,Jend
        DO i=IstrU-1,Iend
          wrk(i,j)=0.0_r8
        END DO
      END DO
      DO k=1,levbfrc(ng)
        DO j=JstrV-1,Jend
```

```
                DO i=IstrU-1,Iend
                  wrk(i,j)=wrk(i,j)+Hz(i,j,k)
                END DO
              END DO
            END DO
            DO j=Jstr,Jend
              DO i=IstrU,Iend
                cff=0.25_r8*(pm (i-1,j)+pm (i,j))*                          &
     &                     (pn (i-1,j)+pn (i,j))
                cff1=1.0_r8/(cff*(wrk(i-1,j)+wrk(i,j)))
                Uwrk(i,j)=bustr(i,j)*cff1
              END DO
            END DO
            DO j=JstrV,Jend
              DO i=Istr,Iend
                cff=0.25_r8*(pm (i,j-1)+pm (i,j))*                          &
     &                     (pn (i,j-1)+pn (i,j))
                cff1=1.0_r8/(cff*(wrk(i,j-1)+wrk(i,j)))
                Vwrk(i,j)=bvstr(i,j)*cff1
              END DO
            END DO
            DO k=1,levbfrc(ng)
              DO j=Jstr,Jend
                DO i=IstrU,Iend
                  cff=Uwrk(i,j)*(Hz(i  ,j,k)+                               &
     &                          Hz(i-1,j,k))
                  ru(i,j,k,nrhs)=ru(i,j,k,nrhs)-cff
#  ifdef DIAGNOSTICS_UV
                  DiaRU(i,j,k,nrhs,M3vvis)=DiaRU(i,j,k,nrhs,M3vvis)-cff
                  DiaRUfrc(i,j,3,M2bstr)=DiaRUfrc(i,j,3,M2bstr)-cff
#  endif
                END DO
              END DO
              DO j=JstrV,Jend
                DO i=Istr,Iend
                  cff=Vwrk(i,j)*(Hz(i,j  ,k)+                               &
     &                          Hz(i,j-1,k))
                  rv(i,j,k,nrhs)=rv(i,j,k,nrhs)-cff
#  ifdef DIAGNOSTICS_UV
                  DiaRV(i,j,k,nrhs,M3vvis)=DiaRV(i,j,k,nrhs,M3vvis)-cff
                  DiaRVfrc(i,j,3,M2bstr)=DiaRVfrc(i,j,3,M2bstr)-cff
#  endif
                END DO
              END DO
            END DO
!
!  Apply mid-depth stress as a bodyforce: determine the thickness (m)
!  of the mid-depth layer; then add in mid-depth stress as a bodyfoce.
!
      DO j=JstrV-1,Jend
        DO i=IstrU-1,Iend
          wrk(i,j)=0.0_r8
        END DO
      END DO
!Start K-LOOP
      DO k=levbfrc(ng)+1,levsfrc(ng)-1
```

```
        DO j=Jstr,Jend
          DO i=IstrU,Iend
!turbine features
          diam=0.1_r8
          zturb=-0.15_r8
          xturb=4.05_r8
          yturb=0.65_r8
          cx=1.82_r8 !=4*(1-root(1-Ct))/(1+root(1-Ct))
          width=0.001_r8 !Chord*sin(pitch angle)=Turbine apparent thickness
          kcff=1000.0_r8 !Anomaly density correction
!Turbine localisation
          coef1=MAX(0.5_r8*diam,Hz(i,j,k))
          coef2=MAX(0.5_r8*diam,on_v(i,j))

            T1=(z_r(i,j,k).GT.(zturb-coef1)).AND.                    &
     &         (z_r(i,j,k).LT.(zturb+coef1))
            T2=(yu(i,j).GE.(yturb-coef2)).AND.                       &
     &         (yu(i,j).LE.(yturb+coef2))
            T3=(xu(i,j).GT.(xturb-om_r(i,j))).AND.(xu(i,j).LT.xturb)
            T4=(xu(i,j).GT.xturb).AND.(xu(i,j).LT.(xturb+om_r(i,j)))

            IF (T1.AND.T2) THEN
              IF (T3) THEN

!Pressure drop in term of stress in u-direction, BODYFORCE formulation imposes
such a formulation
!For versatility sake, turbine is located at the rho point therefore a split
implementation between
!the surrounding u points is needed.

!u point downstream the aimed rho point
          surf=0.25_r8*(Hz(i-1,j,k)+Hz(i,j,k))*(on_v(i-1,j)+on_v(i,j))
!          cff1=u(i,j,k,nrhs)
          cff1=0.5_r8*(u(i,j,k,nrhs)+u(i+1,j,k,nrhs))
          cff2=(cff1**2.0_r8)**0.5_r8
          cff3=cff1*cff2
!          cff3=u(i,j,k,nrhs)**2.0_r8
          Uwrk(i,j)=0.25_r8*kcff*cx*(width/om_u(i,j))*surf*cff3
          ru(i,j,k,nrhs)=ru(i,j,k,nrhs)-Uwrk(i,j)
            ELSEIF (T4) THEN
!u point upstream the aimed rho point
          surf=0.25_r8*(Hz(i-1,j,k)+Hz(i,j,k))*(on_v(i-1,j)+on_v(i,j))
!          cff1=u(i,j,k,nrhs)
          cff1=0.5_r8*(u(i-1,j,k,nrhs)+u(i,j,k,nrhs))
          cff2=(cff1**2.0_r8)**0.5_r8
          cff3=cff1*cff2
!          cff3=u(i,j,k,nrhs)**2.0_r8
          Uwrk(i,j)=0.25_r8*kcff*cx*(width/om_u(i-1,j))*surf*cff3
          ru(i,j,k,nrhs)=ru(i,j,k,nrhs)-Uwrk(i,j)
#  ifdef DIAGNOSTICS_UV
          DiaRU(i,j,k,nrhs,M3vvis)=DiaRU(i,j,k,nrhs,M3vvis)-Uwrk(i,j)
          DiaRUfrc(i,j,3,M2bstr)=DiaRUfrc(i,j,3,M2bstr)-Uwrk(i,j)
#  endif
            ELSE
          ru(i,j,k,nrhs)=ru(i,j,k,nrhs)
              ENDIF
```

```
         ELSE
      ru(i,j,k,nrhs)=ru(i,j,k,nrhs)
         END IF
       END DO
     END DO
   END DO
   K_LOOP : DO k=1,N(ng)
```

```
# if defined UV_COR || (defined CURVGRID && defined UV_ADV)
!
!--------------------------------------------------------------------
!  Add in Coriolis and curvilinear transformation terms, if any.
!--------------------------------------------------------------------
...
```
…and the rest of the file stays unchanged.

Appendix B: ROMS Modifications for

Validation Case – Turbulence Terms

This appendix displays the "gls_corstep.F" ROMS file usually located in ROMS/Nonlinear/ architecture. It has been adapted to account for turbulence correction terms $\left(S_{p_{i,j,k}}, S_{d_{i,j,k}}, S_{\psi_{i,j,k}}\right)$ (i.e. Section 4.2) related to the rotor disc turbulence perturbations. The following modifications are highlighte in red, work for ROMS version 392 and may need adaptions if newer versions of the software are used.

```
#include "cppdefs.h"
      MODULE gls_corstep_mod
#if defined NONLINEAR && defined GLS_MIXING && defined SOLVE3D
!
!svn $Id: gls_corstep.F 294 2009-01-09 21:37:26Z arango $
!=======================================================================
!  Copyright (c) 2002-2009 The ROMS/TOMS Group                        !
!    Licensed under a MIT/X style license          Hernan G. Arango   !
!    See License_ROMS.txt                     Alexander F. Shchepetkin !
!==================================================== John C. Warner ===
!                                                                     !
!  This routine perfoms the corrector step for turbulent kinetic      !
!  energy and generic length scale prognostic variables, tke and      !
!  gls.                                                               !
!                                                                     !
!  References:                                                        !
!                                                                     !
!  Umlauf, L. and H. Burchard, 2001:  A generic length-scale         !
!    Equation for geophysical turbulence models.                     !
!                                                                     !
!=======================================================================
!
      implicit none

      PRIVATE
      PUBLIC  :: gls_corstep

      CONTAINS
```

10. Conclusions

```
!
!***********************************************************************
      SUBROUTINE gls_corstep (ng, tile)
!***********************************************************************
!
      USE mod_param
      USE mod_forces
      USE mod_grid
      USE mod_mixing
      USE mod_ocean
      USE mod_stepping
!
!  Imported variable declarations.
!
      integer, intent(in) :: ng, tile
!
!  Local variable declarations.
!
# include "tile.h"
!
# ifdef PROFILE
      CALL wclock_on (ng, iNLM, 19)
# endif
      CALL gls_corstep_tile (ng, tile,                            &
     &                       LBi, UBi, LBj, UBj,                  &
     &                       IminS, ImaxS, JminS, JmaxS,          &
     &                       nstp(ng), nnew(ng),                  &
# ifdef MASKING
     &                       GRID(ng) % umask,                    &
     &                       GRID(ng) % vmask,                    &
# endif
     &                       GRID(ng) % Huon,                     &
     &                       GRID(ng) % Hvom,                     &
     &                       GRID(ng) % Hz,                       &
     &                       GRID(ng) % om_r,                     &
     &                       GRID(ng) % pm,                       &
     &                       GRID(ng) % pn,                       &
     &                       GRID(ng) % z_w,                      &
     &                       GRID(ng) % z_r,                      &
     &                       GRID(ng) % xr,                       &
     &                       GRID(ng) % yr,                       &
     &                       OCEAN(ng) % u,                       &
     &                       OCEAN(ng) % v,                       &
     &                       OCEAN(ng) % W,                       &
     &                       FORCES(ng) % bustr,                  &
     &                       FORCES(ng) % bvstr,                  &
     &                       FORCES(ng) % sustr,                  &
     &                       FORCES(ng) % svstr,                  &
# ifdef ZOS_HSIG
     &                       FORCES(ng) % Hwave,                  &
# endif
# ifdef TKE_WAVEDISS
     &                       FORCES(ng) % Wave_dissip,            &
# endif
     &                       MIXING(ng) % Akt,                    &
     &                       MIXING(ng) % Akv,                    &
```

```
      &                                MIXING(ng) % bvf,                        &
      &                                MIXING(ng) % Akk,                        &
      &                                MIXING(ng) % Akp,                        &
      &                                MIXING(ng) % Lscale,                     &
      &                                MIXING(ng) % gls,                        &
      &                                MIXING(ng) % tke)
# ifdef PROFILE
      CALL wclock_off (ng, iNLM, 19)
# endif
      RETURN
      END SUBROUTINE gls_corstep
!
!***********************************************************************
      SUBROUTINE gls_corstep_tile (ng, tile,                            &
      &                                LBi, UBi, LBj, UBj,              &
      &                                IminS, ImaxS, JminS, JmaxS,      &
      &                                nstp, nnew,                      &
# ifdef MASKING
      &                                umask, vmask,                    &
# endif
      &                                Huon, Hvom, Hz, om_r, pm,        &
      &                                pn, z_r, z_w,                    &
      &                                xr, yr,                          &
      &                                u, v, W,                         &
      &                                bustr, bvstr, sustr, svstr,      &
# ifdef ZOS_HSIG
      &                                Hwave,                           &
# endif
# ifdef TKE_WAVEDISS
      &                                Wave_dissip,                     &
# endif
      &                                Akt, Akv, bvf,                   &
      &                                Akk, Akp, Lscale, gls, tke)
!***********************************************************************
!
      USE mod_param
      USE mod_scalars
!
# if defined EW_PERIODIC || defined NS_PERIODIC
      USE exchange_3d_mod, ONLY : exchange_w3d_tile
# endif
# ifdef DISTRIBUTE
      USE mp_exchange_mod, ONLY : mp_exchange3d, mp_exchange4d
# endif
      USE tkebc_mod, ONLY : tkebc_tile
!
!  Imported variable declarations.
!
      integer, intent(in) :: ng, tile
      integer, intent(in) :: LBi, UBi, LBj, UBj
      integer, intent(in) :: IminS, ImaxS, JminS, JmaxS
      integer, intent(in) :: nstp, nnew
!
# ifdef ASSUMED_SHAPE
#  ifdef MASKING
      real(r8), intent(in) :: umask(LBi:,LBj:)
```

```
          real(r8), intent(in) :: vmask(LBi:,LBj:)
#   endif
          real(r8), intent(in) :: Huon(LBi:,LBj:,:)
          real(r8), intent(in) :: Hvom(LBi:,LBj:,:)
          real(r8), intent(in) :: Hz(LBi:,LBj:,:)
          real(r8), intent(in) :: om_r(LBi:,LBj:)
          real(r8), intent(in) :: pm(LBi:,LBj:)
          real(r8), intent(in) :: pn(LBi:,LBj:)
          real(r8), intent(in) :: z_r(LBi:,LBj:,:)
          real(r8), intent(in) :: z_w(LBi:,LBj:,0:)
          real(r8), intent(in) :: xr(LBi:,LBj:)
          real(r8), intent(in) :: yr(LBi:,LBj:)
          real(r8), intent(in) :: u(LBi:,LBj:,:,:)
          real(r8), intent(in) :: v(LBi:,LBj:,:,:)
          real(r8), intent(in) :: W(LBi:,LBj:,0:)
          real(r8), intent(in) :: bustr(LBi:,LBj:)
          real(r8), intent(in) :: bvstr(LBi:,LBj:)
          real(r8), intent(in) :: sustr(LBi:,LBj:)
          real(r8), intent(in) :: svstr(LBi:,LBj:)
#   ifdef ZOS_HSIG
          real(r8), intent(in) :: Hwave(LBi:,LBj:)
#   endif
#   ifdef TKE_WAVEDISS
          real(r8), intent(in) :: Wave_dissip(LBi:,LBj:)
#   endif
          real(r8), intent(in) :: bvf(LBi:,LBj:,0:)

          real(r8), intent(inout) :: Akt(LBi:,LBj:,0:,:)
          real(r8), intent(inout) :: Akv(LBi:,LBj:,0:)
          real(r8), intent(inout) :: Akk(LBi:,LBj:,0:)
          real(r8), intent(inout) :: Akp(LBi:,LBj:,0:)
          real(r8), intent(inout) :: Lscale(LBi:,LBj:,0:)
          real(r8), intent(inout) :: gls(LBi:,LBj:,0:,:)
          real(r8), intent(inout) :: tke(LBi:,LBj:,0:,:)
# else
#   ifdef MASKING
          real(r8), intent(in) :: umask(LBi:UBi,LBj:UBj)
          real(r8), intent(in) :: vmask(LBi:UBi,LBj:UBj)
#   endif
          real(r8), intent(in) :: Huon(LBi:UBi,LBj:UBj,N(ng))
          real(r8), intent(in) :: Hvom(LBi:UBi,LBj:UBj,N(ng))
          real(r8), intent(in) :: Hz(LBi:UBi,LBj:UBj,N(ng))
          real(r8), intent(in) :: om_r(LBi:UBi,LBj:UBj)
          real(r8), intent(in) :: pm(LBi:UBi,LBj:UBj)
          real(r8), intent(in) :: pn(LBi:UBi,LBj:UBj)
          real(r8), intent(in) :: z_w(LBi:UBi,LBj:UBj,0:N(ng))
          real(r8), intent(in) :: z_r(LBi:UBi,LBj:UBj,N(ng))
          real(r8), intent(in) :: xr(LBi:UBi,LBj:UBj)
          real(r8), intent(in) :: yr(LBi:UBi,LBj:UBj)
          real(r8), intent(in) :: u(LBi:UBi,LBj:UBj,N(ng),2)
          real(r8), intent(in) :: v(LBi:UBi,LBj:UBj,N(ng),2)
          real(r8), intent(in) :: W(LBi:UBi,LBj:UBj,0:N(ng))
          real(r8), intent(in) :: bustr(LBi:UBi,LBj:UBj)
          real(r8), intent(in) :: bvstr(LBi:UBi,LBj:UBj)
          real(r8), intent(in) :: sustr(LBi:UBi,LBj:UBj)
          real(r8), intent(in) :: svstr(LBi:UBi,LBj:UBj)
```

```
#  if defined ZOS_HSIG
      real(r8), intent(in) :: Hwave(LBi:UBi,LBj:UBj)
#  endif
#  ifdef TKE_WAVEDISS
      real(r8), intent(in) :: Wave_dissip(LBi:UBi,LBj:UBj)
#  endif
      real(r8), intent(in) :: bvf(LBi:UBi,LBj:UBj,0:N(ng))

      real(r8), intent(inout) :: Akt(LBi:UBi,LBj:UBj,0:N(ng),NAT)
      real(r8), intent(inout) :: Akv(LBi:UBi,LBj:UBj,0:N(ng))
      real(r8), intent(inout) :: Akk(LBi:UBi,LBj:UBj,0:N(ng))
      real(r8), intent(inout) :: Akp(LBi:UBi,LBj:UBj,0:N(ng))
      real(r8), intent(inout) :: Lscale(LBi:UBi,LBj:UBj,0:N(ng))
      real(r8), intent(inout) :: gls(LBi:UBi,LBj:UBj,0:N(ng),3)
      real(r8), intent(inout) :: tke(LBi:UBi,LBj:UBj,0:N(ng),3)
#  endif
!
!  Local variable declarations.
!
      logical :: Lmy25
#  ifdef DISTRIBUTE
#   ifdef EW_PERIODIC
      logical :: EWperiodic=.TRUE.
#   else
      logical :: EWperiodic=.FALSE.
#   endif
#   ifdef NS_PERIODIC
      logical :: NSperiodic=.TRUE.
#   else
      logical :: NSperiodic=.FALSE.
#   endif
#  endif
      integer :: i, itrc, j, k

      real(r8), parameter :: Gadv = 1.0_r8/3.0_r8
      real(r8), parameter :: eps = 1.0E-10_r8
      real(r8) :: Zos_min, Zob_min


      real(r8) :: Gh, Gm, Kprod, Ls_unlmt, Ls_lmt, Pprod, Sh, Sm
      real(r8) :: cff, cff1, cff2, cff3
! Turbulence correction parameters
      real(r8) :: coef1, coef2, coef3, coef4, coef5, coef6, kcff
      real(r8) :: diam, zturb, xturb, yturb
      real(r8) :: T_k, T_gls, c_p, c_d, cpx, c_gls
      real(r8) :: wi, we
      logical :: T1, T2, T3, T4
!
      real(r8) :: cmu_fac1, cmu_fac2, cmu_fac3, cmu_fac4
      real(r8) :: gls_c3, gls_exp1, gls_fac1, gls_fac2, gls_fac3
      real(r8) :: gls_fac4, gls_fac5, gls_fac6, ql, sqrt2, strat2
      real(r8) :: tke_exp1, tke_exp2, tke_exp3, tke_exp4, wall_fac
      real(r8) :: gls_d, gls_sigp_cb, ogls_sigp, sig_eff
      real(r8) :: L_sft
#  if defined CRAIG_BANNER || defined TKE_WAVEDISS
```

```
          real(r8) :: cb_wallE
# endif

      real(r8), dimension(IminS:ImaxS) :: tke_fluxt
      real(r8), dimension(IminS:ImaxS) :: tke_fluxb
      real(r8), dimension(IminS:ImaxS) :: gls_fluxt
      real(r8), dimension(IminS:ImaxS) :: gls_fluxb
      real(r8), dimension(IminS:ImaxS) :: Zos_eff

      real(r8), dimension(IminS:ImaxS,0:N(ng)) :: BCK
      real(r8), dimension(IminS:ImaxS,0:N(ng)) :: BCP
      real(r8), dimension(IminS:ImaxS,0:N(ng)) :: CF
      real(r8), dimension(IminS:ImaxS,0:N(ng)) :: FCK
      real(r8), dimension(IminS:ImaxS,0:N(ng)) :: FCP
      real(r8), dimension(IminS:ImaxS,0:N(ng)) :: dU
      real(r8), dimension(IminS:ImaxS,0:N(ng)) :: dV

      real(r8), dimension(IminS:ImaxS,JminS:JmaxS,0:N(ng)) :: shear2
      real(r8), dimension(IminS:ImaxS,JminS:JmaxS,0:N(ng)) :: buoy2

      real(r8), dimension(IminS:ImaxS,JminS:JmaxS) :: FEK
      real(r8), dimension(IminS:ImaxS,JminS:JmaxS) :: FEP
      real(r8), dimension(IminS:ImaxS,JminS:JmaxS) :: FXK
      real(r8), dimension(IminS:ImaxS,JminS:JmaxS) :: FXP
      real(r8), dimension(IminS:ImaxS,JminS:JmaxS) :: curvK
      real(r8), dimension(IminS:ImaxS,JminS:JmaxS) :: curvP
      real(r8), dimension(IminS:ImaxS,JminS:JmaxS) :: gradK
      real(r8), dimension(IminS:ImaxS,JminS:JmaxS) :: gradP

# include "set_bounds.h"
!
!-----------------------------------------------------------------------
!  Compute several constants.
!-----------------------------------------------------------------------
!
      Zos_min=MAX(Zos(ng),0.0001_r8)
      Zob_min=MAX(Zob(ng),0.0001_r8)
!
      Lmy25=.FALSE.
      IF ((gls_p(ng).eq.0.0_r8).and.                                &
     &    (gls_n(ng).eq.1.0_r8).and.                                &
     &    (gls_m(ng).eq.1.0_r8)) THEN
        Lmy25=.TRUE.
      END IF

# if defined CRAIG_BANNER || defined TKE_WAVEDISS
      IF (Lmy25) THEN
!!      cb_wallE=1.0_r8+gls_E2
        cb_wallE=1.25_r8
      ELSE
        cb_wallE=1.0_r8
      END IF
      L_sft=vonKar
      cff1=sqrt(1.5_r8*gls_sigk(ng))*gls_cmu0(ng)/L_sft
      gls_sigp_cb=L_sft**2/(gls_cmu0(ng)**2*gls_c2(ng)*cb_wallE)*    &
     &            (gls_n(ng)**2-                                     &
```

153

```
      &                cff1*gls_n(ng)/3.0_r8*(4.0_r8*gls_m(ng)+1.0_r8)+     &
      &                cff1**2*gls_m(ng)/9.0_r8*(2.0_r8+4.0_r8*gls_m(ng)))
# else
       L_sft=vonKar
       gls_sigp_cb=gls_sigp(ng)
# endif
       ogls_sigp=1.0_r8/gls_sigp_cb
!
       sqrt2=SQRT(2.0_r8)
       cmu_fac1=gls_cmu0(ng)**(-gls_p(ng)/gls_n(ng))
       cmu_fac2=gls_cmu0(ng)**(3.0_r8+gls_p(ng)/gls_n(ng))
       cmu_fac3=1.0_r8/gls_cmu0(ng)**2.0_r8
       cmu_fac4=(1.5_r8*gls_sigk(ng))**(1.0_r8/3.0_r8)/               &
      &         (gls_cmu0(ng)**(4.0_r8/3.0_r8))
       gls_fac1=gls_n(ng)*gls_cmu0(ng)**(gls_p(ng)+1.0_r8)
       gls_fac2=gls_cmu0(ng)**(gls_p(ng))*gls_n(ng)*                  &
      &         vonKar**(gls_n(ng))
       gls_fac3=gls_cmu0(ng)**(gls_p(ng))*gls_n(ng)
       gls_fac4=gls_cmu0(ng)**(gls_p(ng))*                           &
      &         (vonKar*Zob_min)**(gls_n(ng))
       gls_fac5=0.56_r8**(0.5_r8*gls_n(ng))*gls_cmu0(ng)**gls_p(ng)
       gls_fac6=8.0_r8/gls_cmu0(ng)**6.0_r8
!
       gls_exp1=1.0_r8/gls_n(ng)
       tke_exp1=gls_m(ng)/gls_n(ng)
       tke_exp2=0.5_r8+gls_m(ng)/gls_n(ng)
       tke_exp3=0.5_r8+gls_m(ng)
       tke_exp4=gls_m(ng)+0.5_r8*gls_n(ng)
!
!-----------------------------------------------------------------------
!  Compute vertical velocity shear at W-points.
!-----------------------------------------------------------------------
!
# define I_RANGE MAX(1,Istr-1),MIN(Iend+1,Lm(ng))
# define J_RANGE MAX(1,Jstr-1),MIN(Jend+1,Mm(ng))
# ifdef SPLINES
       DO j=J_RANGE
         DO i=I_RANGE
           CF(i,0)=0.0_r8
           dU(i,0)=0.0_r8
           dV(i,0)=0.0_r8
         END DO
         DO k=1,N(ng)-1
           DO i=I_RANGE
             cff=1.0_r8/(2.0_r8*Hz(i,j,k+1)+                          &
      &                  Hz(i,j,k)*(2.0_r8-CF(i,k-1)))
             CF(i,k)=cff*Hz(i,j,k+1)
             dU(i,k)=cff*(3.0_r8*(u(i  ,j,k+1,nstp)-u(i,  j,k,nstp)+   &
      &                           u(i+1,j,k+1,nstp)-u(i+1,j,k,nstp))-  &
      &                   Hz(i,j,k)*dU(i,k-1))
             dV(i,k)=cff*(3.0_r8*(v(i,j  ,k+1,nstp)-v(i,j  ,k,nstp)+   &
      &                           v(i,j+1,k+1,nstp)-v(i,j+1,k,nstp))-  &
      &                   Hz(i,j,k)*dV(i,k-1))
           END DO
         END DO
         DO i=I_RANGE
```

```
              dU(i,N(ng))=0.0_r8
              dV(i,N(ng))=0.0_r8
            END DO
            DO k=N(ng)-1,1,-1
              DO i=I_RANGE
                dU(i,k)=dU(i,k)-CF(i,k)*dU(i,k+1)
                dV(i,k)=dV(i,k)-CF(i,k)*dV(i,k+1)
              END DO
            END DO
            DO k=1,N(ng)-1
              DO i=I_RANGE
                shear2(i,j,k)=dU(i,k)*dU(i,k)+dV(i,k)*dV(i,k)
              END DO
            END DO
          END DO
# else
        DO k=1,N(ng)-1
          DO j=J_RANGE
            DO i=I_RANGE
              cff=0.5_r8/(z_r(i,j,k+1)-z_r(i,j,k))
              shear2(i,j,k)=(cff*(u(i  ,j,k+1,nstp)-u(i  ,j,k,nstp)+      &
      &                             u(i+1,j,k+1,nstp)-u(i+1,j,k,nstp)))**2+ &
      &                     (cff*(v(i,j  ,k+1,nstp)-v(i,j  ,k,nstp)+      &
      &                             v(i,j+1,k+1,nstp)-v(i,j+1,k,nstp)))**2
            END DO
          END DO
        END DO
# endif
# undef I_RANGE
# undef J_RANGE
!
! Load Brunt-Vaisala frequency.
!
        DO k=1,N(ng)-1
          DO j=Jstr-1,Jend+1
            DO i=Istr-1,Iend+1
              buoy2(i,j,k)=bvf(i,j,k)
            END DO
          END DO
        END DO
# ifdef N2S2_HORAVG
!
!-----------------------------------------------------------------------
!  Smooth horizontally buoyancy and shear.  Use buoy2(:,:,0) and
!  shear2(:,:,0) as scratch utility array.
!-----------------------------------------------------------------------
!
        DO k=1,N(ng)-1
          IF (WESTERN_EDGE) THEN
            DO j=MAX(1,Jstr-1),MIN(Jend+1,Mm(ng))
              shear2(Istr-1,j,k)=shear2(Istr,j,k)
            END DO
          END IF
          IF (EASTERN_EDGE) THEN
            DO j=MAX(1,Jstr-1),MIN(Jend+1,Mm(ng))
              shear2(Iend+1,j,k)=shear2(Iend,j,k)
```

```
              END DO
            END IF
            IF (SOUTHERN_EDGE) THEN
              DO i=MAX(1,Istr-1),MIN(Iend+1,Lm(ng))
                shear2(i,Jstr-1,k)=shear2(i,Jstr,k)
              END DO
            END IF
            IF (NORTHERN_EDGE) THEN
              DO i=MAX(1,Istr-1),MIN(Iend+1,Lm(ng))
                shear2(i,Jend+1,k)=shear2(i,Jend,k)
              END DO
            END IF
            IF (SOUTH_WEST_CORNER) THEN
              shear2(Istr-1,Jstr-1,k)=shear2(Istr,Jstr,k)
            END IF
            IF (NORTH_WEST_CORNER) THEN
              shear2(Istr-1,Jend+1,k)=shear2(Istr,Jend,k)
            END IF
            IF (SOUTH_EAST_CORNER) THEN
              shear2(Iend+1,Jstr-1,k)=shear2(Iend,Jstr,k)
            END IF
            IF (NORTH_EAST_CORNER) THEN
              shear2(Iend+1,Jend+1,k)=shear2(Iend,Jend,k)
            END IF
!
!  Average horizontally.
!
            DO j=Jstr-1,Jend
              DO i=Istr-1,Iend
                buoy2(i,j,0)=0.25_r8*(buoy2(i,j  ,k)+buoy2(i+1,j  ,k)+       &
     &                                buoy2(i,j+1,k)+buoy2(i+1,j+1,k))
                shear2(i,j,0)=0.25_r8*(shear2(i,j  ,k)+shear2(i+1,j  ,k)+   &
     &                                 shear2(i,j+1,k)+shear2(i+1,j+1,k))
              END DO
            END DO
            DO j=Jstr,Jend
              DO i=Istr,Iend
                buoy2(i,j,k)=0.25_r8*(buoy2(i,j  ,0)+buoy2(i-1,j  ,0)+       &
     &                                buoy2(i,j-1,0)+buoy2(i-1,j-1,0))
                shear2(i,j,k)=0.25_r8*(shear2(i,j  ,0)+shear2(i-1,j  ,0)+   &
     &                                 shear2(i,j-1,0)+shear2(i-1,j-1,0))
              END DO
            END DO
          END DO
# endif
!
!-----------------------------------------------------------------------
!  Time-step advective terms.
!-----------------------------------------------------------------------
!
!  At entry, it is assumed that the turbulent kinetic energy fields
!  "tke" and "gls", at time level "nnew", are set to its values at
!  time level "nstp" multiplied by the grid box thicknesses Hz
!  (from old time step and at W-points).
!
        DO k=1,N(ng)-1
```

10. Conclusions

```
# ifdef K_C2ADVECTION
!
!  Second-order, centered differences advection.
!
        DO j=Jstr,Jend
          DO i=Istr,Iend+1
            cff=0.25_r8*(Huon(i,j,k)+Huon(i,j,k+1))
            FXK(i,j)=cff*(tke(i,j,k,3)+tke(i-1,j,k,3))
            FXP(i,j)=cff*(gls(i,j,k,3)+gls(i-1,j,k,3))
          END DO
        END DO
        DO j=Jstr,Jend+1
          DO i=Istr,Iend
            cff=0.25_r8*(Hvom(i,j,k)+Hvom(i,j,k+1))
            FEK(i,j)=cff*(tke(i,j,k,3)+tke(i,j-1,k,3))
            FEP(i,j)=cff*(gls(i,j,k,3)+gls(i,j-1,k,3))
          END DO
        END DO
# else
#  ifdef EW_PERIODIC
#   define I_RANGE Istr-1,Iend+2
#  else
#   define I_RANGE MAX(Istr-1,1),MIN(Iend+2,Lm(ng)+1)
#  endif
        DO j=Jstr,Jend
          DO i=I_RANGE
            gradK(i,j)=(tke(i,j,k,3)-tke(i-1,j,k,3))
#  ifdef MASKING
            gradK(i,j)=gradK(i,j)*umask(i,j)
#  endif
            gradP(i,j)=(gls(i,j,k,3)-gls(i-1,j,k,3))
#  ifdef MASKING
            gradP(i,j)=gradP(i,j)*umask(i,j)
#  endif
          END DO
        END DO
#  undef I_RANGE
#  ifndef EW_PERIODIC
        IF (WESTERN_EDGE) THEN
          DO j=Jstr,Jend
            gradK(Istr-1,j)=gradK(Istr,j)
            gradP(Istr-1,j)=gradP(Istr,j)
          END DO
        END IF
        IF (EASTERN_EDGE) THEN
          DO j=Jstr,Jend
            gradK(Iend+2,j)=gradK(Iend+1,j)
            gradP(Iend+2,j)=gradP(Iend+1,j)
          END DO
        END IF
#  endif
#  ifdef K_C4ADVECTION
!
!  Fourth-order, centered differences advection.
!
        cff1=1.0_r8/6.0_r8
```

```
      DO j=Jstr,Jend
        DO i=Istr,Iend+1
          cff=0.5_r8*(Huon(i,j,k)+Huon(i,j,k+1))
          FXK(i,j)=cff*0.5_r8*(tke(i-1,j,k,3)+tke(i,j,k,3)-      &
   &                          cff1*(gradK(i+1,j)-gradK(i-1,j)))
          FXP(i,j)=cff*0.5_r8*(gls(i-1,j,k,3)+gls(i,j,k,3)-      &
   &                          cff1*(gradP(i+1,j)-gradP(i-1,j)))
        END DO
      END DO
# else
!
! Third-order, upstream bias advection with velocity dependent
! hyperdiffusion.
!
      DO j=Jstr,Jend
        DO i=Istr-1,Iend+1
          curvK(i,j)=gradK(i+1,j)-gradK(i,j)
          curvP(i,j)=gradP(i+1,j)-gradP(i,j)
        END DO
      END DO
      DO j=Jstr,Jend
        DO i=Istr,Iend+1
          cff=0.5_r8*(Huon(i,j,k)+Huon(i,j,k+1))
          IF (cff.gt.0.0_r8) THEN
            cff1=curvK(i-1,j)
            cff2=curvP(i-1,j)
          ELSE
            cff1=curvK(i,j)
            cff2=curvP(i,j)
          END IF
          FXK(i,j)=cff*0.5_r8*(tke(i-1,j,k,3)+tke(i,j,k,3)-      &
   &                          Gadv*cff1)
          FXP(i,j)=cff*0.5_r8*(gls(i-1,j,k,3)+gls(i,j,k,3)-      &
   &                          Gadv*cff2)
        END DO
      END DO
# endif
# ifdef NS_PERIODIC
#  define J_RANGE Jstr-1,Jend+2
# else
#  define J_RANGE MAX(Jstr-1,1),MIN(Jend+2,Mm(ng)+1)
# endif
      DO j=J_RANGE
        DO i=Istr,Iend
          gradK(i,j)=(tke(i,j,k,3)-tke(i,j-1,k,3))
# ifdef MASKING
          gradK(i,j)=gradK(i,j)*vmask(i,j)
# endif
          gradP(i,j)=(gls(i,j,k,3)-gls(i,j-1,k,3))
# ifdef MASKING
          gradP(i,j)=gradP(i,j)*vmask(i,j)
# endif
        END DO
      END DO
# undef J_RANGE
# ifndef NS_PERIODIC
```

```
              IF (SOUTHERN_EDGE) THEN
                DO i=Istr,Iend
                  gradK(i,Jstr-1)=gradK(i,Jstr)
                  gradP(i,Jstr-1)=gradP(i,Jstr)
                END DO
              END IF
              IF (NORTHERN_EDGE) THEN
                DO i=Istr,Iend
                  gradK(i,Jend+2)=gradK(i,Jend+1)
                  gradP(i,Jend+2)=gradP(i,Jend+1)
                END DO
              END IF
#   endif
#   ifdef K_C4ADVECTION
              cff1=1.0_r8/6.0_r8
              DO j=Jstr,Jend+1
                DO i=Istr,Iend
                  cff=0.5_r8*(Hvom(i,j,k)+Hvom(i,j,k+1))
                  FEK(i,j)=cff*0.5_r8*(tke(i,j-1,k,3)+tke(i,j,k,3)-        &
    &                                  cff1*(gradK(i,j+1)-gradK(i,j-1)))
                  FEP(i,j)=cff*0.5_r8*(gls(i,j-1,k,3)+gls(i,j,k,3)-        &
    &                                  cff1*(gradP(i,j+1)-gradP(i,j-1)))
                END DO
              END DO
#   else
              DO j=Jstr-1,Jend+1
                DO i=Istr,Iend
                  curvK(i,j)=gradK(i,j+1)-gradK(i,j)
                  curvP(i,j)=gradP(i,j+1)-gradP(i,j)
                END DO
              END DO
              DO j=Jstr,Jend+1
                DO i=Istr,Iend
                  cff=0.5_r8*(Hvom(i,j,k)+Hvom(i,j,k+1))
                  IF (cff.gt.0.0_r8) THEN
                    cff1=curvK(i,j-1)
                    cff2=curvP(i,j-1)
                  ELSE
                    cff1=curvK(i,j)
                    cff2=curvP(i,j)
                  END IF
                  FEK(i,j)=cff*0.5_r8*(tke(i,j-1,k,3)+tke(i,j,k,3)-        &
    &                                  Gadv*cff1)
                  FEP(i,j)=cff*0.5_r8*(gls(i,j-1,k,3)+gls(i,j,k,3)-        &
    &                                  Gadv*cff2)
                END DO
              END DO
#   endif
#   endif
!
!  Time-step horizontal advection.
!
              DO j=Jstr,Jend
                DO i=Istr,Iend
                  cff=dt(ng)*pm(i,j)*pn(i,j)
                  tke(i,j,k,nnew)=tke(i,j,k,nnew)-                         &
```

```
     &                          cff*(FXK(i+1,j)-FXK(i,j)+                     &
     &                              FEK(i,j+1)-FEK(i,j))
           tke(i,j,k,nnew)=MAX(tke(i,j,k,nnew),gls_Kmin(ng))
           gls(i,j,k,nnew)=gls(i,j,k,nnew)-                                   &
     &                          cff*(FXP(i+1,j)-FXP(i,j)+                     &
     &                              FEP(i,j+1)-FEP(i,j))
           gls(i,j,k,nnew)=MAX(gls(i,j,k,nnew),gls_Pmin(ng))
         END DO
       END DO
     END DO
!
! Compute vertical advection.
!
     DO j=Jstr,Jend
# ifdef K_C2ADVECTION
       DO k=1,N(ng)
         DO i=Istr,Iend
           cff=0.25_r8*(W(i,j,k)+W(i,j,k-1))
           FCK(i,k)=cff*(tke(i,j,k,3)+tke(i,j,k-1,3))
           FCP(i,k)=cff*(gls(i,j,k,3)+gls(i,j,k-1,3))
         END DO
       END DO
# else
       cff1=7.0_r8/12.0_r8
       cff2=1.0_r8/12.0_r8
       DO k=2,N(ng)-1
         DO i=Istr,Iend
           cff=0.5*(W(i,j,k)+W(i,j,k-1))
           FCK(i,k)=cff*(cff1*(tke(i,j,k-1,3)+                                &
     &                         tke(i,j,k  ,3))-                               &
     &                   cff2*(tke(i,j,k-2,3)+                                &
     &                         tke(i,j,k+1,3)))
           FCP(i,k)=cff*(cff1*(gls(i,j,k-1,3)+                                &
     &                         gls(i,j,k  ,3))-                               &
     &                   cff2*(gls(i,j,k-2,3)+                                &
     &                         gls(i,j,k+1,3)))
         END DO
       END DO
       cff1=1.0_r8/3.0_r8
       cff2=5.0_r8/6.0_r8
       cff3=1.0_r8/6.0_r8
        DO i=Istr,Iend
         cff=0.5_r8*(W(i,j,0)+W(i,j,1))
         FCK(i,1)=cff*(cff1*tke(i,j,0,3)+                                     &
     &                 cff2*tke(i,j,1,3)-                                     &
     &                 cff3*tke(i,j,2,3))
         FCP(i,1)=cff*(cff1*gls(i,j,0,3)+                                     &
     &                 cff2*gls(i,j,1,3)-                                     &
     &                 cff3*gls(i,j,2,3))
         cff=0.5_r8*(W(i,j,N(ng))+W(i,j,N(ng)-1))
         FCK(i,N(ng))=cff*(cff1*tke(i,j,N(ng)  ,3)+                          &
     &                     cff2*tke(i,j,N(ng)-1,3)-                          &
     &                     cff3*tke(i,j,N(ng)-2,3))
         FCP(i,N(ng))=cff*(cff1*gls(i,j,N(ng)  ,3)+                          &
     &                     cff2*gls(i,j,N(ng)-1,3)-                          &
     &                     cff3*gls(i,j,N(ng)-2,3))
```

```
        END DO
# endif
!
!   Time-step vertical advection term.
!
        DO k=1,N(ng)-1
          DO i=Istr,Iend
            cff=dt(ng)*pm(i,j)*pn(i,j)
            tke(i,j,k,nnew)=tke(i,j,k,nnew)-                        &
     &                        cff*(FCK(i,k+1)-FCK(i,k))
            tke(i,j,k,nnew)=MAX(tke(i,j,k,nnew),gls_Kmin(ng))
            gls(i,j,k,nnew)=gls(i,j,k,nnew)-                        &
     &                        cff*(FCP(i,k+1)-FCP(i,k))
            gls(i,j,k,nnew)=MAX(gls(i,j,k,nnew),gls_Pmin(ng))
          END DO
        END DO
!
!-------------------------------------------------------------------
!   Compute vertical mixing, turbulent production, turbulent
!   dissipation terms and the turbulence correction term for turbine.
!-------------------------------------------------------------------
!
!   Set term for vertical mixing of turbulent fields.
!
        cff=-0.5_r8*dt(ng)
        DO i=Istr,Iend
          DO k=2,N(ng)-1
            FCK(i,k)=cff*(Akk(i,j,k)+Akk(i,j,k-1))/Hz(i,j,k)
            FCP(i,k)=cff*(Akp(i,j,k)+Akp(i,j,k-1))/Hz(i,j,k)
            CF(i,k)=0.0_r8
          END DO
          FCP(i,1)=0.0_r8
          FCP(i,N(ng))=0.0_r8
          FCK(i,1)=0.0_r8
          FCK(i,N(ng))=0.0_r8
        END DO
!
!   Compute production and dissipation terms.
!
        DO i=Istr,Iend
          DO k=1,N(ng)-1
!
!   Compute shear and bouyant production of turbulent energy (m3/s3)
!   at W-points (ignore small negative values of buoyancy).
!
            strat2=buoy2(i,j,k)
            IF (strat2.gt.0.0_r8) THEN
              gls_c3=gls_c3m(ng)
            ELSE
              gls_c3=gls_c3p(ng)
            END IF
            Kprod=shear2(i,j,k)*(Akv(i,j,k)-Akv_bak(ng))-          &
     &            strat2*(Akt(i,j,k,itemp)-Akt_bak(itemp,ng))
            Pprod=gls_c1(ng)*shear2(i,j,k)*(Akv(i,j,k)-Akv_bak(ng))-    &
     &            gls_c3*strat2*(Akt(i,j,k,itemp)-Akt_bak(itemp,ng))
!
```

```
!  If negative production terms, then add buoyancy to dissipation terms
!  (BCK and BCP) below, using "cff1" and "cff2" as the on/off switch.
!
            cff1=1.0_r8
            IF (Kprod.lt.0.0_r8) THEN
              Kprod=Kprod+strat2*(Akt(i,j,k,itemp)-Akt_bak(itemp,ng))
              cff1=0.0_r8
            END IF
            cff2=1.0_r8
            IF (Pprod.lt.0.0_r8) THEN
              Pprod=Pprod+gls_c3*strat2*(Akt(i,j,k,itemp)-           &
     &                                    Akt_bak(itemp,ng))
              cff2=0.0_r8
            END IF
!
!--------------------------------------------------------------------
!   Compute the turbulence correction term.
!--------------------------------------------------------------------
!

!Turbine features
          diam=0.1_r8
          zturb=-0.15_r8
          xturb=4.05_r8
          yturb=0.65_r8
          coef1=0.5_r8*diam

!turbine localisation (start IF LOOP)
          T1=(xr(i,j).GE.(xturb-(om_r(i,j)/2.0_r8))).AND.            &
     &        (xr(i,j).LE.(xturb+(om_r(i,j)/2.0_r8)))
          T2=(yr(i,j).GE.(yturb-(coef1))).AND.                       &
     &        (yr(i,j).LE.(yturb+(coef1)))
          T3=(z_w(i,j,k).GE.(zturb-coef1)).AND.                      &
     &        (z_w(i,j,k).LE.(zturb+coef1))

          IF (T2.AND.T3)  THEN

!   Tuning parameters
          kcff=1000.0_r8 !Density anomaly correction
          wi=0.001_r8 !Chord*sin(pitch angle)=turbine apparent width
          we=wi/(0.5_r8*(om_r(i-1,j)+om_r(i,j))) !volumic weight due to
numerical smearing
          cpx=0.322_r8 !=Ct*root(1-Ct)
          c_p=0.05_r8
          c_d=1.5_r8
          c_gls=4.0_r8

!correction term cf. Rados 2009
          IF (T1) THEN
          coef4=(gls_cmu0(ng)**3.0_r8)*((tke(i,j,k,nstp)**1.5_r8)/    &
     &          Lscale(i,j,k))
          coef2=(shear2(i,j,k)*(Akv(i,j,k)-Akv_bak(ng)))**2.0_r8
          T_gls=kcff*(c_gls*((cpx*we)**2.0_r8)*coef2)/coef4
!--------------------------------------------------------------------
          coef5=ABS(0.25_r8*(u(i,j,k,nstp)+u(i,j,k+1,nstp)           &
     &             + u(i,j+1,k,nstp)+u(i,j+1,k+1,nstp)))
```

```
                T_k=((cpx*we)/(0.5_r8*(om_r(i-1,j)+om_r(i,j))))               &
                    *((c_p*(coef5**3.0_r8))-(c_d*coef5*tke(i,j,k,nstp)))
            coef3=1.0_r8
                ELSE
            coef3=0.0_r8
                END IF
              ELSE
            coef3=0.0_r8
                END IF

!
!  Time-step shear and buoyancy production terms and the correction term.
!
                cff=0.5_r8*(Hz(i,j,k)+Hz(i,j,k+1))
                tke(i,j,k,nnew)=tke(i,j,k,nnew)+                              &
        &                    dt(ng)*cff*Kprod+                               &
!Turbine term
        &                        coef3*cff*dt(ng)*T_k

                gls(i,j,k,nnew)=gls(i,j,k,nnew)+                             &
        &                    (dt(ng)*cff*(Pprod+(coef3*T_gls))*             &
        &                gls(i,j,k,nstp)/MAX(tke(i,j,k,nstp),gls_Kmin(ng)))
!Turbine Terms
```

```
!
!  Compute dissipation of turbulent energy (m3/s3).
!
                wall_fac=1.0_r8
                IF (Lmy25) THEN
!
!  Parabolic wall function,  L = ds db / (ds + db).
!
!!              wall_fac=1.0_r8+gls_E2/(vonKar*vonKar)*                    &
!!   &                (gls(i,j,k,nstp)**( gls_exp1)*cmu_fac1*              &
!!   &                tke(i,j,k,nstp)**(-tke_exp1)*                        &
!!   &                (1.0_r8/(z_w(i,j,N(ng))-z_w(i,j,k))+                 &
!!   &                 1.0_r8/(z_w(i,j,k)-z_w(i,j,0))))**2
!!
!! Triangular wall function, L = min (ds, db).
!!
!!              wall_fac=1.0_r8+gls_E2/(vonKar*vonKar)*                    &
!!   &                (gls(i,j,k,nstp)**( gls_exp1)*cmu_fac1*              &
!!   &                tke(i,j,k,nstp)**(-tke_exp1)*                        &
!!   &                (1.0_r8/MIN((z_w(i,j,N(ng))-z_w(i,j,k)),            &
!!   &                            (z_w(i,j,k)-z_w(i,j,0)))))**2
!!
!! Linear wall function for , L = ds (=dist to surface).

!               wall_fac=1.0_r8+gls_E2/(vonKar*vonKar)*                   &
!    &                (gls(i,j,k,nstp)**( gls_exp1)*cmu_fac1*             &
!    &                tke(i,j,k,nstp)**(-tke_exp1)*                       &
!    &                (1.0_r8/ (z_w(i,j,N(ng))-z_w(i,j,k))))**2

!! Parabolic wall function + free surface correction
!
                wall_fac=1.0_r8+gls_E2/(vonKar*vonKar)*                   &
```

```
      &                        (gls(i,j,k,nstp)**( gls_exp1)*cmu_fac1*             &
      &                         tke(i,j,k,nstp)**(-tke_exp1)*                       &
      &                         (1.0_r8/ (z_w(i,j,k)-z_w(i,j,0))))**2+             &
      &                        0.25_r8/(vonKar*vonKar)*                            &
      &                        (gls(i,j,k,nstp)**( gls_exp1)*cmu_fac1*             &
      &                         tke(i,j,k,nstp)**(-tke_exp1)*                       &
      &                         (1.0_r8/ (z_w(i,j,N(ng))-z_w(i,j,k))))**2
              END IF
!
              BCK(i,k)=cff*(1.0_r8+dt(ng)*                                          &
      &                       gls(i,j,k,nstp)**(-gls_exp1)*cmu_fac2*               &
      &                       tke(i,j,k,nstp)**( tke_exp2)+                        &
      &                       dt(ng)*(1.0_r8-cff1)*strat2*                         &
      &                       (Akt(i,j,k,itemp)-Akt_bak(itemp,ng))/               &
      &                       tke(i,j,k,nstp))-                                     &
      &                       FCK(i,k)-FCK(i,k+1)
              BCP(i,k)=cff*(1.0_r8+dt(ng)*gls_c2(ng)*wall_fac*                     &
      &                       gls(i,j,k,nstp)**(-gls_exp1)*cmu_fac2*               &
      &                       tke(i,j,k,nstp)**( tke_exp2)+                        &
      &                       dt(ng)*(1.0_r8-cff2)*gls_c3*strat2*                  &
      &                       (Akt(i,j,k,itemp)-Akt_bak(itemp,ng))/               &
      &                       tke(i,j,k,nstp))-                                     &
      &                       FCP(i,k)-FCP(i,k+1)
            END DO
          END DO
!
!-----------------------------------------------------------------------
!  Time-step dissipation and vertical diffusion terms implicitly.
!-----------------------------------------------------------------------
...
```

…and the rest of the file stays unchanged.

List of References

Ahmadian, R., Falcone, R. & Bockelmann, . B., 2012. Far-field modelling of the hydro-environmental impact of tidal stream turbines. *Renewable Energy,* Volume 38, pp. 107-116.

Ahmadian, R. & Falconer, R. A., 2012. Assessment of array shape of tidal stream turbines on hydro-environmental impacts and power output. *Renewable Energy,* Volume 44, pp. 318-327.

Arakawa, A. & Lamb, V. R., 1977. Methods of computational physics. *Academic Press,* Volume 17, pp. 174-265.

Bai, L., Spence, R. R. G. & Dudziak, G., 2009. *Investigation of the Influence of Array Arrangement and Spacing on Tidal Energy Converter (TEC) Performance using a 3-Dimensional CFD Model.* Uppsala, EWTEC.

Baker, . R. W., Walker, S. N. & Katen, P. C., 1985. Wake measurements around operating wind turbines. *JournalofSolarEnergyEngineering,* Volume 107, p. 183–185.

Baker, R. W., Walker, S. N. & Katen, P. C., 1985. Wake Measurements around Operating Wind Turbines. *Journal of Solar Energy Engineering,* Volume 107, pp. 183-185.

Barltrop, N. et al., 2006. Wave-Current interactions in marine current turbines. *Proc. IMechE,* Volume 220, pp. 195-201.

Bedard, R. et al., 2006. *North America Tidal Instream Energy Conversion Technology Feasibility Study, Technical Report*.

Blunden, L. S. & Bahaj, A. S., 2007. Tidal Energy Resource Assessent for Tidal Stream Generators. *Proceedings of the Institution of Mechanical Engineers,* Volume 221(A2), pp. 137-146.

Blunden, L. S., Batten, W. M. J., Harrison, M. E. & Bahaj, A., 2009. *Comparison of boundary-layer and field models for simulation of flow through multiple-row tidal fences.* Uppsala, EWTEC.

Boone, J., 2004. *Secrets of the tide: tide and tidal current analysis and applications, storm surges and sea level trends.* Chichester: Horwood Publications.

Boussinesq, J., 1903. *Théorie analytique de la chaleur.* Paris: Gathier-Villars.

Bryden, I. G., Couch, S. I., Owen, A. & Melville, G., 2007. Tidal current resource assessment. *Journal of Power and Energy,* Volume 221(A2), pp. 125-135.

Bryden, I. G. & Couch, S. J., 2004. *ME1 - Marine Energy Extraction: Tidal Resource Analysis.* Denver, Renwable Energy, pp. 133-139.

Bryden, I. G. & Couch, S. J., 2007. How Much Energy Can Be Extracted from Moving Water with a Free Surface: A Question of Importance in the Fiel of Tidal Current Energy ?. *Renewable Energy,* Volume 32(11), pp. 1961-1966.

Bryden, I. G., Grinsted, T. & Melville, G. T., 2004. Assessing the potential of a simple tidal channel to deliver useful energy. *Applied Ocean Research,* Volume 26, pp. 198-204.

Bryden, I. G. & Melville, G., 2004. Choosing and Evaluating Sites for Tidal Current Development. *Journal of Power and Energy,* Volume 218, pp. 567-577.

Buhl, M. L., 2005. *A New EMpirical Relationship between Thrust Coefficient and Induction Factor for the Turbulent Windmill State*

Burton, T., Sharpe, D., Jenkins, N. & Bossayi, E., 2008. *Wind Energy Handbook.* John Wiley & Sons Ltd.

Canuto, V. M., Howard, A., Cheng, Y. & Dubivikov, M. S., 2001. Ocean turbulence I: one-point closure model. Momentum and heat vertical diffusivities. *Jouranl of Physical Oceanography,* Volume 31, pp. 1413-1426.

Carballo, R., Iglesias, G. & Castro, A., 2009. Numerical model evaluation of tidal stream energy resources in the Rı´a de Muros (NW Spain),. *Renewable Energy,* Volume 34, pp. 1517-1524.

Carter, G. S. & Merrifield, M. A., 2007. Open Boundary Conditions for Regional Tidal Simulations. *Ocena Modelling,* Volume 18, pp. 194-209.

Chapman, D. C., 1985. Numerical Treatment of Cross-Shelf Open Boundaries in a Barotropic Coastal Ocean Model. *Journal of Physical Oceanography,* Volume 15, pp. 1060-1075.

Chen & Kim, 1987. *Computation for turbulent flow using an extended closure model, NASA technical report*.

10. Conclusions

Chick, J. P., Bryden, I. G. & Couch, S. J., 2007. The Influence of energy extraction from open channel flow and its impact on tidal current energy system design. *International Jouranl of the Society for Underwater Technology,* Volume 27(2), pp. 49-56.

Churchfield, M. J., Li, Y. & Moriarty, P. J., 2011. *A Large-Eddy Simulation Study of Wake Propagation and Power Production in an Array of Tidal-Current Turbines.* Southampton, EWTEC.

Connel, J. R. & George, R. L., 1981. *The wake of the MOD-0A1 wind turbine at two rotor diameters downwind,* Battelle, Technical report.

Couch, S. & Bryden, I. G., 2004. The Impact of Energy Extraction on Tidal Flow Development. *Supergen Marine Marec Paper.*

Couch, S. J. & Bryden, I. G., 2006. Tidal Current Energy Extraction: Hydrodynamic Resource Characteristics. *Proc. IMechE,* Volume 220, pp. 185-194.

Daly, T., Myers, L. E. & Bahaj , A. S., 2010. *Experimental analysis of the local flow effects around single row tidal turbine arrays.* Bilbao, ICOE.

Defne, Z., Haas, K. A. & Fritz, H. M., 2011. Numerical modeling of tidal currents and the effects of power extraction on estuarine hydrodynamics along the Georgia coast, USA. *Renewable Energy,* Volume 36, pp. 3461-3471.

Draper, S., Houlsby, G. T., Oldfield, M. L. G. & Borthwick, A. G. L., 2009. *Modelling Tidal Energy Extraction in a Depth-Averaged Coastal Domain. EWTEC.*

Ekman, V. W., 1905. On the influence of the earth's rotation on ocean currents. *Ark. Mat. Astron. Fys.,* Volume 2(11), pp. 1-52.

Fettweis, M., Francken, F., Pison, V. & Van den Eynde, D., 2006. Suspended particulate matter dynamics and aggregate sizes in a high turbidity area. *Marine Geology,* Volume 235, pp. 63-74.

Fofonoff, N. P. & Millard, R. C., 1983. Algorithms for the computation of fundamental properties of seawater. *Unesco Technical Papers in Marine Sciences,* Volume 44, pp. 1-53.

Fraenkel, P., 2007. Marine current turbines: pioneering the development of marine kinetic energy converters. *Journal of Power and Energy,* 221(A).

Garrett, C. & Cummins, P., 2005. The power potential of tidal currents in channels. *Proc. of the Royal Society A-Mathematical Physical and Engineering Sciences,* Volume 461(2060), pp. 2563-2572.

Gooch, S., Thomson, J., Polagye, B. & Meggitt, D., 2009. Site characterization for tidal power. *Oceans,* pp. 26-29.

Gretton, G. I., Bruce, T. & Ingram, D. M., 2009. *Hydrodynamic modelling of a vertical axis tidal current turbine using CFD.* Uppsala, EWTEC.

Griffies, S. M. & Hallberg, R. W., 2000. Biharmonic friction with a Smagorinsky-like viscosity for use in large-scale eddy-permitting ocean models. *Monthly Weather,* Volume 8(2), pp. 2935-2946.

Haidvogel, D. B. & Beckmann, A., 1999. *Numerical Ocean Circulation Modeling.* s.l.:Imperial College Press.

Harrison, M. E., Batten, W. M. J. & Bahaj, A. S., 2010. *A blade element actuator disc approach applied to tidal stream turbines.* Seattle, OCEANS 2010.

Harrison, M. E., Batten, W. M. J., Myers, L. E. & Bahaj, A. S., 2009. *A Comparison between CFD SImulations and Experiments for Predicting the far Wake of Horizontal Axis Turbines.* Uppsala, EWTEC.

Ingram, D., Smith, G., Bittencourt-Ferreira, C. & Smith, H., 2011. *Protocols for the Equitable Assesment of Marine Energy Convertors,* Technical report, University of Edinburgh, School of Engineering.

Kadiri, M. et al., 2012. A review of the potential water quality impacts of tidal renewable energy systems. *Renewable and Sustainable Energy Reviews,* Volume 16, p. 329– 341.

Kantha, L. H. & Clayson, C. A., 1994. Numerical Models of Oceans and Oceanic Processes.. In: *International Geophysics Series.* San Diego: Academic Press, p. 940.

Karsten, R. H., McMillan, J. M., Lickley, M. J. & Haynes, R. D., 2008. Assessment of tidal current energy in the Minas Passage,Bay of Fundy. *Journal of Power and Energy,* Volume 222, pp. 493-507.

Kasmi, E. & Masson, C., 2008. An extend k-ε model for turbulent flow through horizontal-axis wind turbines. *J. of Wind Eng. & Ind. Aero.,* Volume 96, pp. 103-122.

Kawase, M. & Thyng, K. M., 2009. *A Three-dimensional Hydrodynamic Model of Inland Marine Waters of Washington State, United States, for Tidal Resource and Environmental Impact Assessment.* Uppsala, EWTEC.

Khan, M. J., Bhuyan, G., Iqbal, M. T. & Quaicoe, J. E., 2009. Hydrokinetic energy conversion systems and assessment of horizontal and vertical axis turbines for river and tidal applications: A technology status review. *Applied Energy,* Volume 86, pp. 1823-1835.

Kolmogorov, A. N., 1941. On degeneration of isotropic turbulence in an incompressible viscous liquid. *Comptes Rendus (Doklady) de l'Academie des Sciences de l'U.R.S.S.,* Volume 31, p. 538–540.

Lalander, E., 2009. *Numerical modeling of a river site for in-stream energy converters.* Uppsala, EWTEC.

Lalander, E. & Leijon, M., 2009. *Numerical modeling of a river site for in-stream energy converters.* Uppsala, EWTEC.

Large, W. G., Mc Williams, J. C. & Doney, S. C., 1994. Oceanic Vertical Mixing - a Review and a Model with a Nonlocal Boundary-Layer Parameterization. *Reviews of Geophysics,* Volume 32(4), pp. 363-403.

Lawrence, J., Kofoed-Hansen, H. & Chevalier, C., 2009. *High-resolution metocean modelling at EMEC's (UK) marine energy test sites.* Uppsala, EWTEC.

Ledwell, J. R., Watson, A. J. & Law, C. S., 1993. Evidence for slow mixing across the pycnocline from an open-ocean tracer-release experiment. *Nature,* 364(6439), pp. 701-703.

Lee, S. H. et al., 2009. A numerical study for the optimal arrangement of ocean current turbinegenerators in the ocean current power parks. *Current Applied Physics.*

Legrand, C., 2009. Assessment of tidal energy resource. In: *Marine Renewable Energy Guides.* London: The European Marine Energy Center.

Li, Y. & Calisal, S., 2010. Estimating Power Output from a Tidal Current Turbine Farm with First-Order Approximation of Hydrodynamic Interaction between Turbines. *International Journal of Green Energy,* 7(2), pp. 153-163.

MacLeod, A., Barnes, S., Rados, K. & Bryden, I., 2002. *Wake effects in tidal current turbine farms. Tech. Report.,* IMAREST.

Maganga, F. et al., 2009. *Experimental Study to Determine Flow Characteristic Effects on Marine Current Turbine Behaviour.* Uppsala, EWTEC.

Mc Combes, T., Johnson, C. & Grant, A., 2009. *Unsteady 3DWake Modelling for Marine Current Turbines.* s.l., Uppsala.

McCann, G. N., 2007. *Tidal current turbine fatigue loading sensitivity to waves and turbulence - a parametric study.* s.l., EWTEC.

Mellor, G. L. & Yamada, T., 1974. A hierarchy of turbulence closure models for planetary boundary layers. *Journal of Atmospheric Sciences,* Volume 31, pp. 1791-1806.

Monin, A. S. & Obukhov, A. M., 1954. Osnovnye zakonomernosti turbulentnogo peremesivanija v prizemnom sloe atmosfery. *Trudy Geofiz.,* Volume 24(154), pp. 162-187.

Myers, L. & Bahaj, A. S., 2009. *Near wake properties of horizontal axis marine current turbines.* Uppsala, EWTEC.

Myers, L. E. & Bahaj, A. S., 2010. Experimental analysis of the flow field around horizontal axis tidal turbines by use of scale mesh disk rotor simulators. *Ocean Engineering,* Volume 37, pp. 218-27.

Myers, L. E. & Bahaj, A. S., 2012. An experimental study of flow effects within 1st-generation marine current energy converter arrays. *Renewable Energy,* 7(1), pp. 28-26.

Myers, L. E., Keogh, B. & Bahaj, A. S., 2011. *Experimental investigation of inter-array wake properties in early tidal turbine arrays.* Santander, OCEANS 2011.

Neill, S. P., Emmer, L. J., Couch, S. J. & Davies, A. G., 2009. The impact of tidal stream turbines on large-scale sediment dynamics. *The impact of tidal stream turbines on large-scale sediment dynamics,* Volume 34, p. 2803–2812.

Neill, S. P., Jordan, J. R. & Couch, S. J., 2012. Impact of tidal energy converter (TEC) arrays on the dynamics of headland sand banks. *Renewable Energy,* Volume 37, pp. 387-397.

O'Doherty, T. et al., 2009. *Experimental and Computational Analysis of a Model Horizontal Axis Tidal Turbine.* Uppsala, EWTEC.

Peters, H., Gregg, M. C. & Toole, J. M., 1988. On the parameterization of equatorial turbulence. *Journal of Geophysical Research,* Volume 93, pp. 1199-1218.

Pham, C.-T. & Martin, V. A., 2009. *Tidal current turbine demonstration farm in Paimpol-Bréhat (Brittany): tidal characterisation and energy yield evaluation with Telemac.* Uppsala, EWTEC.

Pingree, R. D., 1978. The formation of the Shambles and other banks by tidal stirring of the seas. *J. Mar. Biol. Assoc,* Volume 58, p. 211–226.

Polagye, B., Bedard, R. & Previsic, M., 2007. *Tidal in-stream energy conversion survey and characterization of snopud project sites in Puget Sound, Tech. Report EPRI-TP-003*.

Polagye, B. L., 2009. *Hydrodynamic Effects of Kinetic Power Extraction by In-Stream Tidal Turbines,* Seatle: University of Washington.

Polagye, B., Malte, P., Kawase, M. & Durran, D., 2008. Effect of large-scale kinetic power extraction on time-dependent estuaries. *Journal of Power and Energy,* Volume 222, pp. 471-484.

Prandtl, L., 1945. The Role of Viscosity in the Mechanism of Developed. *GOAR 3712.*

Previsic, M., Bedard, R. & Polagye, B., 2008. *System level design, performance, cost and economic assessment – Admiralty Inlet, Washington tidal in-stream power plant 2008 update,Tech. Report EPRI-TP-003*.

Rados, K. G. et al., 2009. *CFD modeling issues of wind turbine wakes under stable atmospheric conditions. EWEC*.

Réthoré, P.-E. & Sorensen, N. N., 2008. *Actuator disc model using a modified Rhie-Chow/SIMPLE pressure correction algorithm.* Brussels, EWEC.

Réthoré, P.-E., Sørensen, N. N., Bechmann, A. & Zhale, F., 2009. *Study of atmospheric wake turbulence of a CFD actuator disc model.* Marseille, EWEC.

Robertson, I., Sherwin, S. J. & Graham, J. M. R., 2004. Comparison of wall boundary conditions for numerical viscous free surface flow simulation. *Journal of Fluids and Structures,* Volume 19(4), pp. 525-542.

Roc, T., Conley, D. C. & Greaves, D., 2010. *Accounting for Turbulence in a Regional Numerical Model for Tidal Current Farm Planning.* Bilbao, ICOE.

Roc, T., Conley, D. C. & Greaves, D., 2011. *Turbulence Correction Terms for Representing Tidal Current Turbines in a Regional Ocean Model for Array Planning and Impact Assessment.* Maui, ISOPE.

Roc, T., Conley, D. C. & Greaves, D., 2013. Methodology for Tidal Turbine Representation in Ocean Circulation Model. *Renewable Energy (in press).*

Roc, T., Thyng, K. M. & Conley, D. C., 2012. *Applying a decision-making tool for tidal current turbine (TCT) planning projects to the Puget Sound estuary - Early results.* Southampton, EWTEC.

Ross, O. N. & Sharples, J., 2008. Swimming for survival: A role of phytoplankton motility in a stratified turbulent environment. *Journal of Marine Systems,* Volume 70, pp. 248-262.

Salter, S. H., 2009. *Correcting the Under-estimate of the Tidal-Stream Resource of the Pentland Firth.* Uppsala, EWTEC.

Sanz, C., 2003. A note on k-ε modeling of vegetation canopy air-flows. *Boundary-Layer Meteorology,* Volume 108, pp. 191-197.

Sforza, P. M., Sheering, P. & Smorto, M., 1981. Three dimensional wakes of simulated wind turbines. *AIAA Journal,* 19(9).

Shchepetkin, A. F. & Mc Williams, J. C., 2003. A method for computing horizontal pressure-gradient force in an oceanic model with a nonaligned vertical coordinate. *Journal of Geophysical Research,* 108(C3), p. 3090.

Shchepetkin, A. & Mc Williams, J. C., 2009. Computational Kernel Algorithms for Fine-Scale, Multi-Process, Long-Time Oceanic Simulations. *Handbook of Numerical Analysis,* Volume 14, pp. 121-183.

Shcheptkin, A. F. & Mc Williams, J. C., 2005. The Regional Oceanic system (ROMS): a split-explicit, free-surface, topography-following-coordinate oceanic model. *Ocean Modelling,* Volume 9, pp. 347-404.

Shields, M. A., Dillon, L. J., Woolf, D. K. & Ford, A. T., 2009. Strategic priorities for assessing ecological impacts of marine renewable energy devices in the Pentland Firth (Scotland,UK). *MarinePolicy,* Volume 33, p. 635–642.

Smagorinsky, J., 1963. General circulation experiments with the primitive equations: I. The basic experiment. *Monthly Weather Review,* Volume 91, pp. 99-164.

Smith, T. H. E. & Scott, B. E., 2009. *Bridging the gap between biology (a rock) and physics (a hard place) for tidal energy research.* Upsala, EWTEC.

Sorensen, J. N. & Shen, W. Z., 2002. Numerical Modeling of Wind Turbine Wakes. *J. of Fluids Engineering,* 124(2), pp. 393-399.

Sun, X., Chick, J. P. & Bryden, I. G., 2008. Laboratory-scale simulation of energy extraction from tidal currents. *Renewable Energy,* 33(6), pp. 1267-1274.

Sun, X., Chick, J. P. & Bryden, I. G., 2008. Laboratory-scale simulation of energy extraction from tidal currents. *Renewable Energy,* Volume 33, p. 1267–1274.

Sutherland, G., Foreman, M. & Garrett, C., 2007. Tidal current energy assessment for Johnstone Strait, Vancouver Island. *Journal of Power and Enery,* 221(A2), pp. 147-157.

The Crown Estate, 2012. *UK Wave and Tidal Key Resource Areas Project,* London: The Crown Estate.

Thyng, K. M., 2012. *Numerical Simulation of Admiralty Inlet, WA, with Tidal Hydrokinetic Turbine Siting Application,* Seattle: University of Washington.

Thyng, M. K. & Riley, J. J., 2010. *Idealized Headland Simulation for Tidal Hydrokinetic Turbine Siting Metrics.* Seattle, OCEANS.

Trigo-Teixeira, A. & Rebordao, I., 2009. *An assessment of tidal energy potential. The Lima estuary.* Uppsala, EWTEC.

Turner, N. E. & Owen, A., 2009. *The Effect of Boundary Conditions on Performance Prediction Model Results for Tidal Turbines.* Uppsala, EWTEC.

Umlauf, L. & Burchard, H., 2001. A generic length-scale equation for geophysical turbulence models. *Journal of Marine Research,* Volume 61(2), pp. 235-265.

Umlauf, L., Burchard & Hutter, K., 2003. Extending the k-ω turbulence model towards oceanic applications. *Ocean Modelling,* Volume 5, pp. 195-218.

Vermeer, L. J., Sorensen, J. N. & Crespo, A., 2003. Wind turbine wake aerodynamics. *Progress in Aerospace Sciences,* 39(6-7), pp. 467-510.

Warner, J. C., Armstrong, B., He, R. & Zambon, J. B., 2010. Development of a Coupled Ocean-Atmosphere-Wave-Sediment Transport (COAWST) modeling system. *Ocean Modeling,* 35(3), pp. 230-244.

Warner, J. C., Sherwood, C. R., Arango, H. G. & Signell, R. P., 2005. Performance of four turbulence closure models implemented using a generic length scale method. *Ocean Modelling,* 8(1-2), pp. 81-113.

Whelan, J. I., Graham, J. M. R. & Peiro, J., 2009. *Inertia Effects on Horizontal Axis Tidal-Stream Turbines.* Uppsala, EWTEC.

Whelan, J., Thomson, M., Graham, J. M. R. & Peiro, J., 2007. *Modelling of free surface proximity and wave induced velocities around an horizontal axis tidal stream turbine.* Porto, EWTEC.